Creep and Fatigue of a single crystal nickel base superalloy

Paul Bates

Doctor of Philosophy

The University of Aston in Birmingham

October 1987

The University of Aston in Birmingham

Creep and fatigue of a single crystal nickel base superalloy

Paul Bates
Doctor of Philosophy
1987

The introduction of single crystal casting techniques has led to the development of existing nickel-base superalloys to produce materials with optimum mechanical properties in the single crystal condition. As single crystals are known to be anisotropic,a study is needed to determine the general mechanical properties of these materials, and determine the effects of crystal orientation upon them.

A study has been carried out to identify the effect of orientation and temperature on the creep and fatigue properties of a development single crystal superalloy, SRR 99. Creep testing and crystal rotation experiments have been made on SRR 99 and an earlier development alloy, SRR 9. Fatigue experiments at elevated temperatures have been carried out on both notched and un-notched specimens of alloy SRR 99. To aid in this analysis, several analytical techniques have been employed including Laue x-ray orientation analysis, measurement of strain by photographic methods and microstructural examination.

Crystal rotation experiments have indicated that shear of γ' precipitates by {111}<112> slip systems is operative during primary creep deformation at temperatures of 750°C and 850°C. The effect of orientation variation obtained by standard casting practices was not found to be significant. Creep rupture was found to be associated with multiple crack initiation from micropores.

Fatigue crack initiation in un-notched specimens was found to be related to microporosity and microstructural defects. Failure was predominantly by crystallographic crack growth on {111} planes.

The use of linear elastic fracture mechanics to describe fatigue crack propagation in alloy SRR 99 was found to be acceptable at temperatures up to 850°C. Variation of temperature, frequency and crystal orientation was found to have only moderate effect upon crack propagation rates.

KEYWORDS Single crystal, Nickel-base superalloy, Creep
Crystal rotation, High temperature fatigue

DEDICATION

To mother,father and sister. In acknowledgement of their considerable support during the production of this thesis

ACKNOWLEDGEMENTS

I wish to thank my initial supervisor, Professor J. T. Barnby for his advice and guidance, Dr A. S. Nadkarni for his help and friendship, and my current supervisor Mr L. W. Crane for his assistance in the latter stage of this work.

I wish to acknowledge the assistance given by the Metallurgy Department technicians, J. Jeffs, E. Watson, J. Foden, R. Howell and especially Mr P. Cox who is responsible for printing the photographs contained in this thesis.

I wish to thank Mrs J. Hooker and Dr D. Driver of Rolls-Royce Ltd for the supply of test material, and Rolls-Royce Ltd and the Science and Engineering Research Council for their financial support.

CONTENTS

TABLES

FIGURES

1 INTRODUCTION

The thermodynamic efficiency of a gas turbine engine is related to the maximum allowable temperature at the turbine inlet stage, thereby producing a great demand from engine manufacturers for materials with higher working temperatures. The limiting design factor is the properties of the material used for components situated in the hottest part of the engine, that is the static guide vanes and turbine blades. The fluctuating stresses imposed on the rotating turbine blades and the cyclic thermal stresses experienced coupled with the requirement of dimensional stability make the choice of turbine blade material of paramount importance.

The major advances in turbine blade technology in the past 10 years has not been in the development of new materials but through continuous refinement of the existing blade materials, for example the nickel-base superalloys.

Significant advances came with the adoption of blade cooling, where air from a cooler part of the engine is passed through internal channels machined in the blade thus reducing the effective gas temperature around the blade. The effectiveness of blade cooling together with the difficulties and expense in forging and machining high temperature materials has produced a change in production techniques from wrought and machined blades to the use of investment casting. This has enabled complex cooling channels to be made by the use of ceramic cores.

In recent years casting techniques have been modified to allow control over the crystal structure during solidification. This allows the production of directionally solidified (D.S) blades, where the blade consists of longitudinally oriented columnar grains, and by the use of a helix crystal selector (1,2) to produce single crystal blades.

The introduction of single crystal techniques has led to major improvements in high temperature properties. Creep properties are greatly improved by the removal of high angle boundaries thus reducing the production and mobility of vacancies, lowering diffusional creep and preventing the formation of cavities by grain boundary sliding. Removal of grain boundary strengthening elements simplified alloy design and increased solution temperatures enabling a higher degree of chemical homogeneity and the precipitation of higher volume fractions of strengthening particles, thus increasing resistance to creep. The removal of grain boundaries and the brittle phases used to pin them has also improved resistance to fatigue.

Single crystal technology has given rise to two main areas of research. Firstly, existing alloy compositions are being modified to develop a material with optimum casting and mechanical properties in the single crystal state. Secondly, due to the preference for dendrites in an alloy having a face centered cubic (FCC) structure to grow in a <100> crystal orienation,(3) standard casting

procedure is to produce castings with this longitudinal crystal direction. Currently this axis is controlled to within 7 degrees of the <001>, but no control is placed on the transverse direction. This, with the allowed deviations in the longitudinal direction may include most of the possible directions within a <001>,<011>,<111> stereographic triangle. As the mechanical properties of superalloy single crystals are known to be anisotropic,(4) research is needed to discover the effect of orientation upon the mechanical properties of the new alloys.

The object of the present work was to investigate the mechanical properties of a development single crystal superalloy SRR 99. Creep studies using specimens produced to a nominal <001> orienataion was undertaken to indicate the effect of orientation within specimens cast to standard orientation tolerances. The effect of temperature and orientation has been investigated on both fatigue crack propagation and fatigue failure of un-notched specimens. Some creep work has been carried out on an earlier development alloy, SRR 9, and this has been compared to the present alloy.

2. Literature survey

2.1 Alloy development

Nickel-base superalloys were developed during the 1930's to meet the demands of jet engine researchers for a wrought material with a higher temperature capability than the existing stainless steels (5). The first alloys were modifications of the existing 80 wt% nickel, 20 wt% chromium alloy employing additions of titanium and aluminium to achieve age hardening by precipitation of the coherent, face centered cubic intermetallic phase γ', which has the basic composition of $Ni_3(Al,Ti)$. This feature is the basis of the superalloys used today.

The basic microstructure of a modern cast alloy such as Mar-M200 consists of a FCC solid solution matrix, carbides, and the coherent intermetallic phase γ'. The FCC matrix is based upon nickel and contains a high percentage of solid solution elements such as cobalt, chromium, molybdenum and tungsten. Molybdenum and tungsten are slow diffusing elements in this matrix and also have a beneficial effect of lowering the diffusivity of titanium and chromium. Aluminium and chromium provide oxidation resistance by the formation of Al_2O_3 and Cr_2O_3 rich scales at the surface of the component. The carbides found in high performance cast alloys tend to be of the MC type, that is the metal elements M are in equal proportion to the

carbon. These are primary carbides formed shortly after freezing and are normally based on titanium or tantalum but may also contain tungsten (5). During heat treatment and in service these may decompose to form M_6C and $M_{23}C_6$ carbides which populate the grain boundaries.

Aluminium and titanium are added to form γ' although phase extraction experiments have discovered that tungsten, chromium and cobalt may also be present in certain alloys (6). Cobalt is added to raise the γ' solvus temperature and thus improve the temperature capability of the alloy. Small additions of boron and zirconium have been found to be effective in strengthening grain boundaries (5) and additions of hafnium have been used to maintain good creep ductility at intermediate temperatures for high strength alloys such as Mar-M200.

With the advent of single crystal production, the main problem of grain boundary strengthening has been eliminated. With the removal of the grain boundary strengthening elements; carbon, boron, zirconium and hafnium, alloys can be developed which have an incipient melting temperature above that of the γ' solvus allowing a full solution treatment to be carried out. The reduction of carbon levels and the use of full solution treatments has produced a smaller volume of fine carbides and an increase in the volume fraction of γ' precipitates.

Tantalum has been added to prevent the casting defect called 'freckling' which has been identified (7) as the presence of small random equiaxed grains in the casting. It also has the added effect of increasing the stability of MC carbides at high temperatures. Table 2.1 gives the compositions of conventional and single crystal casting alloys.

Table 2.1 Compositions of nickel-base cast superalloys

Alloy	Element (weight percent)									
	Cr	Co	W	Ta	Cb	Al	Ti	C	B	Zr
Equiaxed										
Mar-M200	9	10	12	--	1	5	2	.15	.015	.05
Single crystal										
Alloy 454(1)	10	5	4	12	-	5	1.5	-	-	-
SRR 99	8	5	9	2.5	-	5	2	-	-	-
	Nickel balance									

2.2 Dislocation theories

2. 2.1 Slip processes in Gamma prime

The compatibility between the gamma prime FCC crystal structure and lattice parameter, with that of the high nickel content matrix, γ, allows homogeneous nucleation of a precipitate with low surface energy and long term stability. The cubic morphology of γ' found in single crystal casting alloys have been found to have a lattice mismatch of around 0.5-1.0% (8). $Ni_3(Al,Ti)$ is an ordered, intermetallic phase with a superlattice based upon the FCC $L1_2$ crystal structure (9). The nickel atoms occupy the face centre (A) sites and the secondary elements (cobalt and other elements may substitute for aluminium) occupy the corner lattice or (B) sites. The symmetry is lowered to simple cubic and antiphase domain boundaries (APB) may exist, where ordering of the two types of atoms is disrupted.

It is well known that perfect dislocations in the unordered FCC lattice may dissociate into pairs of imperfect or partial dislocations. These are dislocations which individually do not recreate the original lattice arrangement upon moving. The driving force of the dissociation is the lowering of the overall energy of the system. A stacking fault (SF) is created between the two partial dislocations, where the stacking arrangement of the atoms in the crystal has been altered. The stacking fault may be intrinsic (ISF) and occur over one atomic plane, or extrinsic (ESF) and occur over two planes. Many

investigators have shown (10,11) that the spacing of the extended dislocation is related to the stacking fault energy of the material thereby having a strong effect upon the mechanicl properties of the material.

In the case of an ordered lattice, Cottrell (12) pointed out that perfect dislocations from the unordered lattice are only partial dislocations in the superlattice due to the formation of an APB in their wake, and must either combine to to form large dislocations with Burgers vectors equal to a primitive translation of the superlattice or occur in pairs connected by a strip of APB. This is shown in figure 2.1.

Marcinkowski et al (13) investigated the crystallographic nature of the superlattice dislocations found in the $L1_2$ structure by use of the alloy $AuCu_3$. The Fcc lattice may be represented by four interpenetrating simple cubic sublattices corresponding to each of the four atoms per unit cell.

Figure 2.2 shows the unit rhombus which connects four atoms from each of the sublattices which lie in the same plane i.e Ia, IIa, IIIa and IVa. Sites Ib to IVb are lattice sites which are initially occupied by atoms in the moveable plane above A prior to slip.

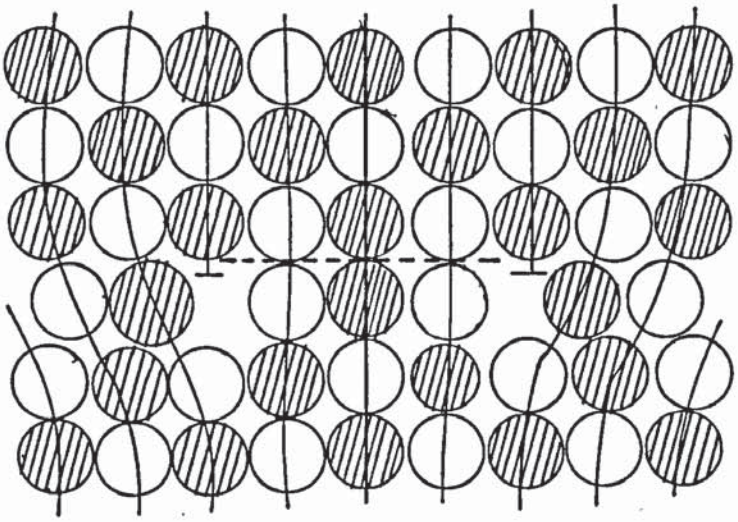

Figure 2.1 Dislocation pair in superlattice (9)

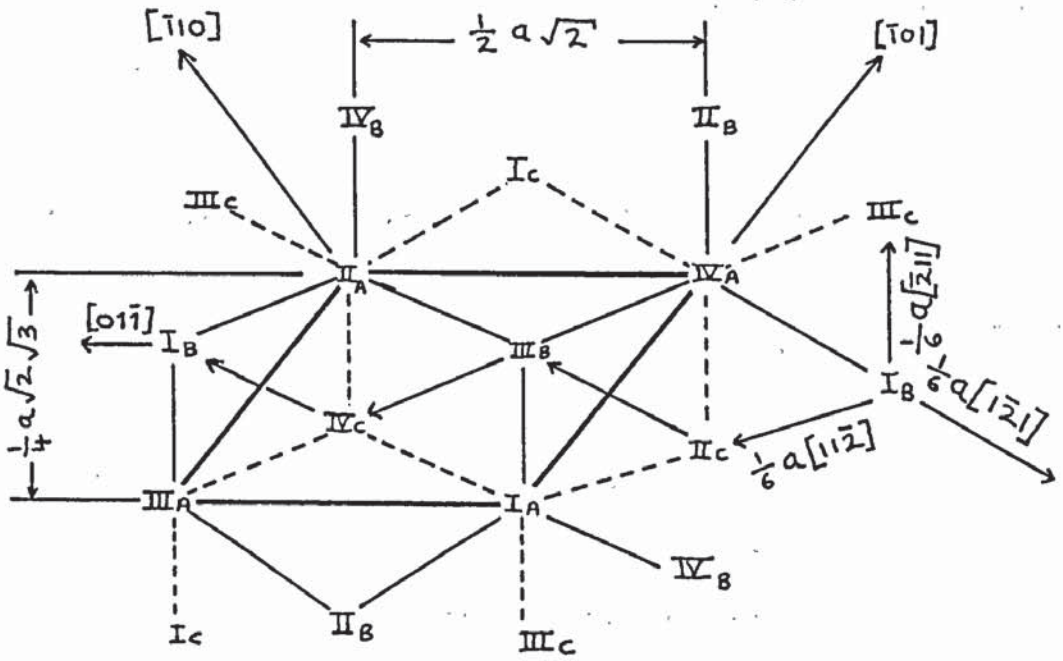

RHOMBUS CONNECTING SITES OF TYPE I_A- IV_A THAT LIE IN PLANE OF THE DRAWING (PLANE A)

BONDS CONNECTING NEAREST NEIGHBOUR SITES ACROSS SLIP PLANE

I_B-IV_B , I_C-IV_C ATOM SITES LYING IN PLANE B JUST ABOVE PLANE A

Figure 2.2 Variation in bond types across slip plane due to slip displacements of a/6 <112> (13)

Sites Ic to IVc are sites twice removed from plane A in the lattice and also represent alternate sites for atoms when the B plane has created a stacking fault by slipping an amount a/6<112>. Consider a [01$\bar{1}$] dislocation which consists of four partial dislocations :

a/6[11$\bar{2}$] ; a/6[$\bar{1}$2$\bar{1}$] ; a/6[11$\bar{2}$] ; a/6[$\bar{1}$2$\bar{1}$]

When plane B is displaced by a/6[11$\bar{2}$], an atom at stationary site Ia gains a nearest neighbour from a Ib site, Ib goes to the position of IIc and looses a nearest neighbour. The total change for the a/6[11$\bar{2}$] partial is given in table 2.2

Table 2.2 Change in nearest neighbour bonds

Site	Change in nearest neighbour bonds
Ia	+(Ia-Ib)-(Ia-IIb)
IIa	+(IIa-IIb)-(IIa-Ib)
IIIa	+(IIIa-IIIb)-(IIIa-IVb)
IVa	+(IVa-IVb)-(IVa-IIIb)

Table 2.2 can be simplified by observing that physically there are only two atom sites in an ordered superlattice; wrong sites or right sites; i.e, in order or out of order. This may be used to simplify table 2.2 by designating a Ib site as a I site, and IIb,IIIb and IVb sites as II sites. Applying the above process to all four partial dislocations, the disorder caused by the a[01$\bar{1}$] dislocation may be assessed and is shown in table 2.3.

Table 2.3 Net change in bonding

Site	Change in nearest neighbour bonds
$a/6[11\bar{2}]$	(I-I)+(II-II)- 2(I-II)
$a/6[\bar{1}2\bar{1}]$	0
$a/6[11\bar{2}]$	0
$a/6[\bar{1}2\bar{1}]$	-(I-I)-(II-II)+2(I-II)

Examination of table 2.3 shows that the first partial alters the crystal lattice and the middle partials have no further effect. The passing of the final partial produces an opposite change in nearest neighbour bonds when compared to the first partial and therefore recreates the original lattice. The $a[01\bar{1}]$ superlattice dislocation is shown in figure 2.3 . The authors found that table 2.3 is invarient with respect to the choice of <110> dislocation and the order of its partial dislocations.

An alternate slip process has been proposed by Kear, Giamei and co-workers (14,15,16). They consider that a superlattice dislocation of net translation vector 2BA can dissociate according to two basic schemes:

$$2BA \longrightarrow \underset{(B\delta+\delta A)}{BA} + \underset{(B\delta+\delta A)}{BA} \quad \ldots\ldots (2.1)$$

$$2BA \longrightarrow \underset{(\delta A+B\delta+\delta C)}{2B\delta} + \underset{(C\delta+\delta A+B\delta)}{2\delta A} \quad \ldots\ldots (2.2)$$

Where the Burgers vectors of the dislocations are defined using the notation of Thompson (17) as shown in figure 2.4. Equation 2.1 illustrates the case envisaged by Marcinkowski (13) where two extended dislocations are linked via an antiphase area. In the case described by equation 2.2, the authors used a dislocation interaction mechanism propounded by Hirth (18), where two total dislocations with Burgers vectors at 60° may react to form intrinsic/extrinsic stacking fault pairs bounded by three partial dislocations having the same Burgers vector, as shown in figure 2.5 . They calculated that equation 2.2 would be the preferred mode of dissociation in materials of high APB energy.

A larger dissociated dislocation with a net shear vector of 6Bδ was proposed for the $L1_2$ lattice containing stacking faults rather than APB . This configuration shown in figure 2.6 was found to have a net Burgers vector of a<112>.

2.2.2 The mechanical properties of Gamma prime

The excellent high temperature mechanical properties of nickel-base superalloys have been attributed to the unusual high temperature mechanical properties of the γ' phase,namely the increase in flow stress with temperature between -196°C and about 800°C (9,19). Additions substitution of titanium or niobium for aluminium has the effect of raising the flow stress significantly without altering the temperature effect (20).

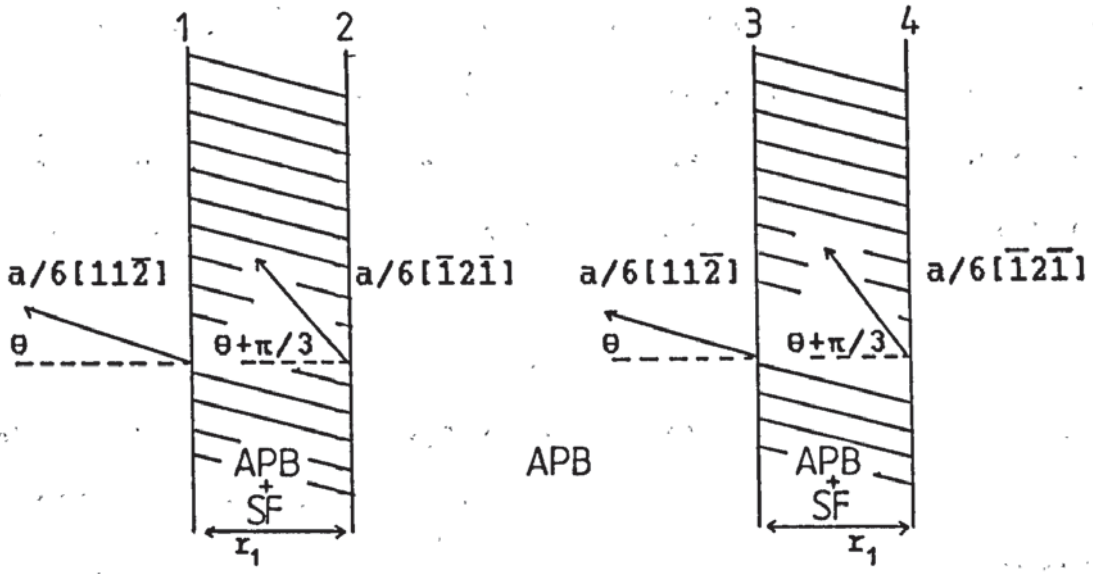

Figure 2.3 a[011] superlattice dislocation in AuCu3 (13)

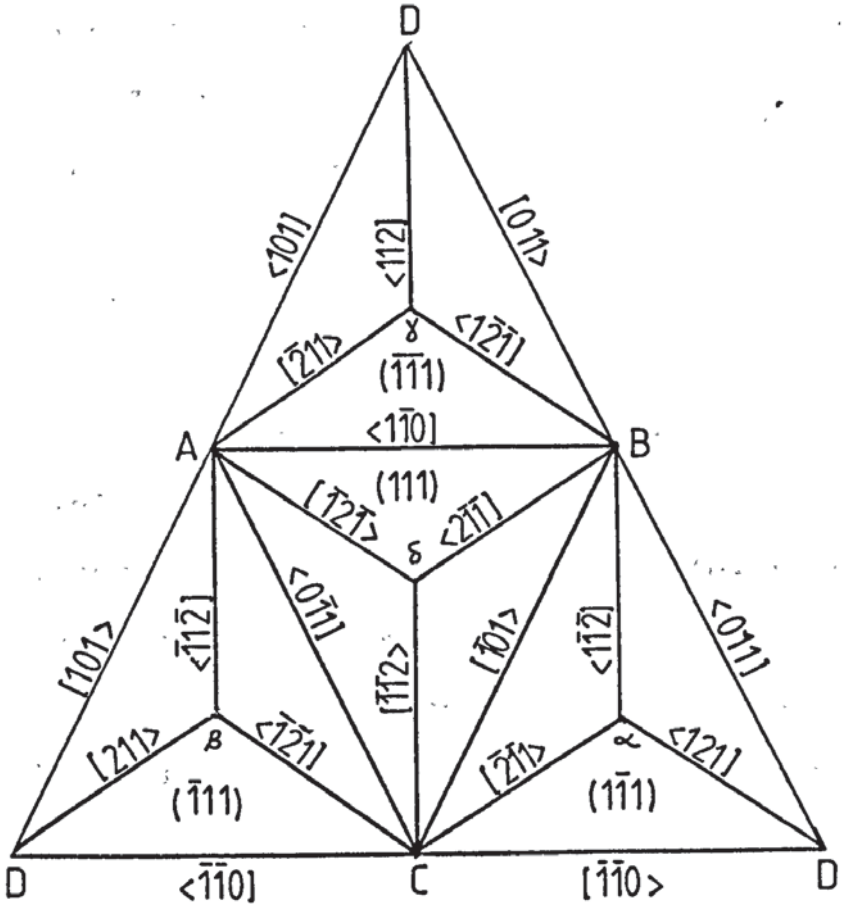

Figure 2.4 Thompson tetrahedron showing possible {111} dislocations for FCC materials (17)

Flinn (9) suggested that the increase in flow stress was attributable to the diffusion controlled climb of superlattice dislocations. He argued that the driving force for the leading dislocation to climb was the transfer of the APB from {111} to {001}. These planes have the lowest APB energy due to the absence of incorrect nearest neighbour bonds. The splitting of the dislocation pair onto different planes makes movement difficult, since each dislocation now produces an APB as it moves. Several investigators have reported the presence of the {001}<110> system at temperatures above 400°C (19,21).

An explanation of the flow stress, temperature dependence based upon the increase of {001} slip causing dislocation debris due to cross slip, was brought into question after Copley and Kear (21) found that the critical resolved shear stress (CRSS) for {111}<110> slip in <001> oriented crystals showed the same temperature dependency, the CRSS for {001}<110> being zero for <001> crystals. The current debris hardening model incorporates the earlier model by Flinn (9). When the CRSS on the {001}<110> system is low, the increase in flow stress is thought to be due to an increased ability for locked screw dislocations to cross slip back onto {111} under the influence of local stress inhomogeneities. At temperatures

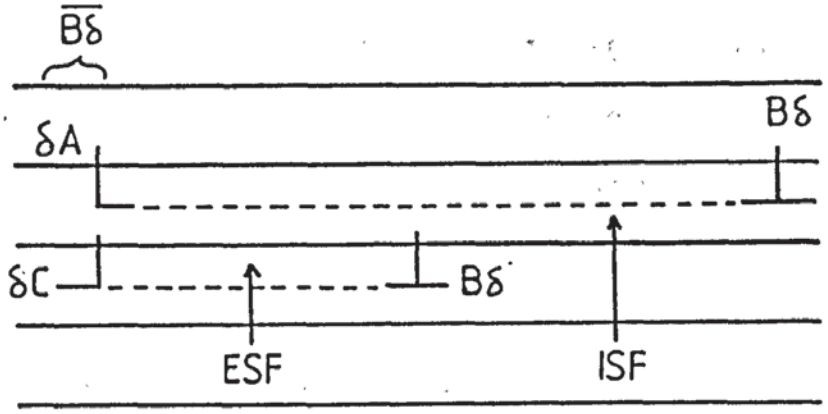

Figure 2.5 Intrinsic/extrinsic fault pair (15)

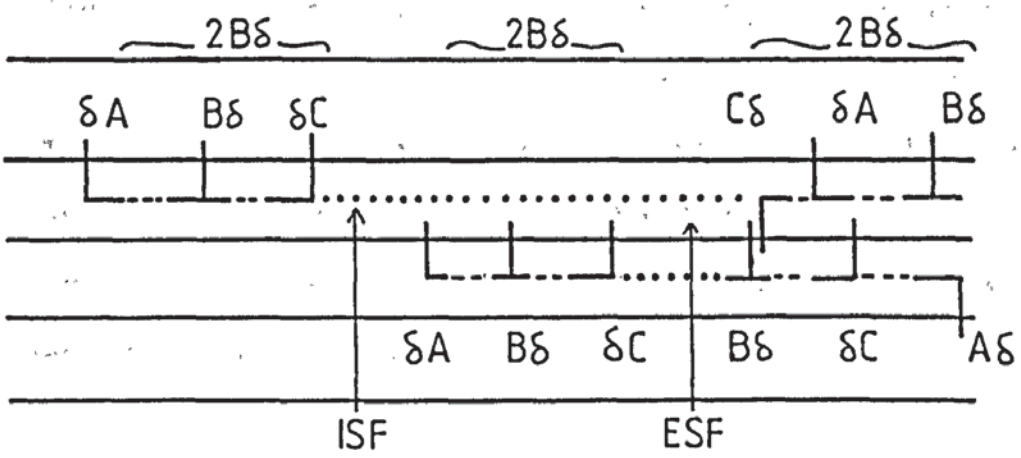

Figure 2.6 Possible $L1_2$ superlattice dislocation (16)

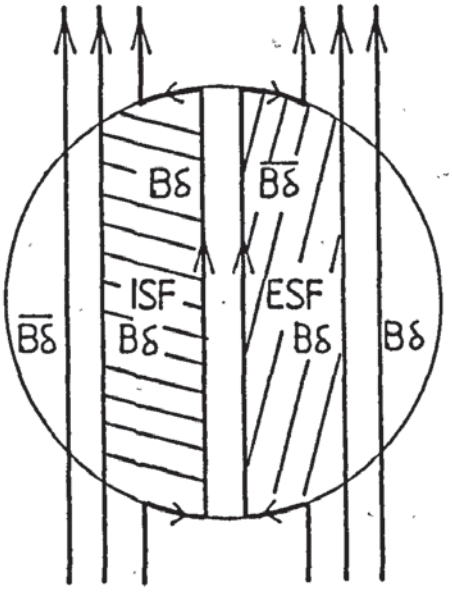

Figure 2.7 Proposed γ' shearing model (16)

above 400°C, in orientations where {001}<110> slip becomes favorable,cross slip from the sessile {001}<110> to the glissile {111}<110>is possible,the macroscopic flow stress being controlled by the rate of debris formation.

2.2.3 Dislocation interactions with γ' particles

Kear et al have used their model for a superlattice dislocation containing intrinsic/extrinsic stacking faults to propose a theoretical model for the shearing of γ' precipitates in a nickel-base superalloy (15,16). They concluded that an interaction of the dislocation with a γ' particle would lead to the configuration shown in figure 2.7. They reasoned that this configuration would be the most favorable as it allowed the 3bδ dislocations to enter and pass through the particle in a relaxed array, without the need for constriction.

The authors have used thin foil examination by transmission electron microscopy to investigate the interaction of dislocations with γ' precipitates in single crystals of Mar-M200 tested in primary creep at 778°C under a stress of 586 MPa (22). Intrinsic/extrinsic stacking fault pairs were observed which were found to have a net Burgers vector for the fault pair of a<112>. The results were found to be in agreement with the <112> type shearing model,however the configuration shown in figure 2.7 is idealised, the real situation being determined by the size and distribution of the γ' particles.

The observed shearing process extended over at least two particles. The position of the dislocations is dependent upon the elastic interactions between neighbouring dislocations,the energy of the stacking faults and the dislocation drag stresses.

In summary it can be seen that there are several possible slip mechanisms in nickel-base superalloys containing a high (>50%) volume fraction of γ'. {111}<110> slip is possible in the matrix,γ. Interactions of these dislocations with the particles may produce <112> type shear. At high temperatures, dislocations within the γ' may be impeded by debris formation due to climb or cross slip onto {001}.

2.3 Strengthening mechanisms in nickel-base superalloys

The factors affecting the strength of nickel-base superalloys may be categorised as follows:

1) Solid solution strengthening of γ and γ'
2) Coherency strain effects
3) Interaction of dislocations with particles
4) Bypassing of particles by dislocations
5) Dimensional stability of γ'

2.3.1 Solid solution strengthening

The effectiveness of elements in strengthening the matrix, γ , has been analysed with respect to their difference in atomic diameter from that of the nickel atom, and their position in the periodic table as defined by the electron vacancy number, N_v (23).

Pelloux and Grant (24) using nickel-base binary alloys, related the increase in size of the solute elements to the change in room temperature yield strength per unit of lattice constant change. They concluded that hardening is directly related to the amount of lattice expansion produced.

Beeston et al (25) have examined the effect of solute elements on the change in stacking fault energy, $\Delta\gamma_{sfe}$. Elements with a high N_v have a larger effect on the reduction in stacking fault energy produced per percent solute. Strengthening is by lowering the stacking fault

energy, producing a wider spacing between partial dislocations. This makes cross-slip more difficult and thereby reduces the possibility of dislocations bypassing particles. The total effect of each element may be assessed in figure 2.8.

At high temperatures (>0.6 T_m) strengthening of the matrix becomes diffusion dependent, therefore slow diffusing elements such as molybdenum and tungsten have a higher beneficial effect than shown in figure 2.8.

Guard and Westbrook (26) have investigated the solid solution strengthening of γ'. They found at temperatures up to 400°C, chromium molybdenum and titanium increase the flow stress of γ'. At 800°C, the effect of titanium, niobium and tantalum was more significant. Phillips (27) suggested that an increase of titanium in γ' as well as producing the increase in friction stress proposed by Guard and Westbrook (26), may also have an important influence on its APB energy. Any significant alteration in APB energy will have a major effect on the dislocation mechanisms in γ' as discussed previously in section 2.2

2.3.2 Coherency strain effects

Decker and Mihalisin (28) have isolated and measured coherency strain effects in nickel-aluminium based ternary alloys. An increase in the γ-γ' mismatch from <0.2% to 0.8% doubled the peak aged hardness. Experimental results

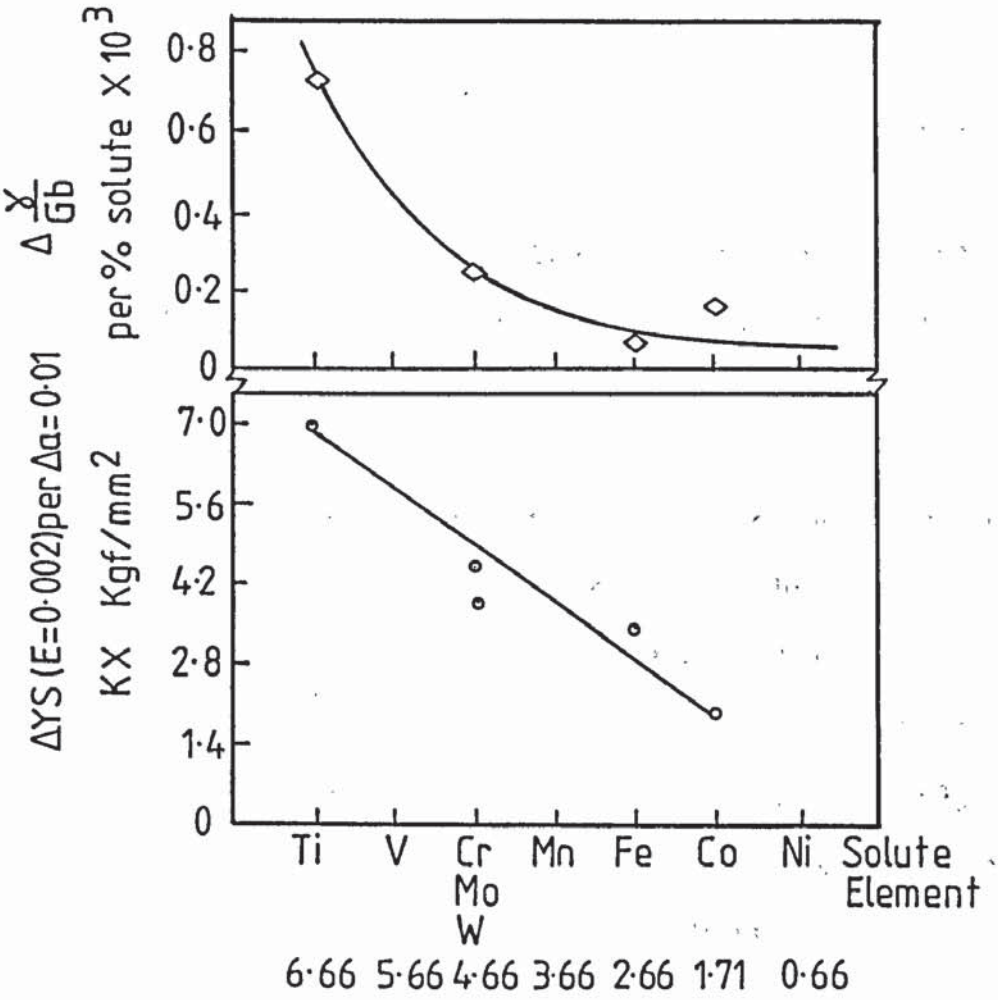

Figure 2.8 Effect of solute position in periodic table and solute N_v in nickel base binary alloys (23)

were found to confirm the relationship proposed by Gerold and Haberkorn (29) for the increment of critical resolved shear stress (CRSS) arising from coherency strains; $\Delta\tau_{cs}$.

$$\Delta\tau_{cs} = 3G\varepsilon^{3/2}\left(\frac{hf}{2b}\right)^{1/2} \qquad \ldots\ldots(2.3)$$

Where G is the γ shear modulus, ε is the constrained lattice strain, h is the mean particle diameter and f is the volume fraction of γ'.

Equation 2.3 predicts that the coherency strain component of the CRSS will increase with coherency strain, the volume fraction of γ', and the size of the γ' particles. Due to compositional effects, coherency strains will only be significant in superalloys with low molybdenum content and a high titanium/aluminium ratio, or alloys containing significant additions of niobium.

2.3.3 Dislocation interaction

When a dislocation encounters an array of obstacles, the dislocation must bend to an angle ϕ which is determined by the strength of the obstacle. For weak obstacles only slight bending is required and ϕ is in the region of 180° whereas strong obstacles forces the dislocation to almost double back on itself and ϕ becomes near zero. As ϕ decreases from 180° the dislocation bows out and intercepts more obstacles, the number of obstacles per unit length being critically dependent upon ϕ.

The basic case of interaction is obstruction by spherical, discrete, non-ordered particles. If the dislocation is bent between obstacles in the slip plane by an applied stress τ, it will assume a configuration where its radius of curvature at every point is given by:

$$r = \frac{T}{\tau b} \qquad \ldots\ldots (2.4)$$

Where b is the Burgers vector and T is the line tension, or the energy per unit length of the dislocation and has a value given approximately by (30):

$$T \approx \frac{Gb^2}{2} \qquad \ldots\ldots (2.5)$$

Where G is the shear modulus. In the case of weak obstacles the dislocation does not depart much from a straight line and the force on the obstacle is given by:

$$F = 2T \cos\left(\frac{\phi}{2}\right) \qquad \ldots\ldots (2.6)$$

If the critical breaking angle is ϕ_c then the stress required to break the particle τ_c is:

$$\tau_c = \frac{2T}{Lb} \cos\left(\frac{\phi}{2}c\right) \qquad \ldots\ldots (2.7)$$

Where L is the interparticle spacing, shown in figure 2.9

If the obstacle is very strong so that it does not break even at $\phi=0$, then the dislocation reaches an unstable

semicircular (Frank-Read) configuration and slip occurs by dislocation multiplication leaving dislocation loops around the obstacle. The critical stress τ_b for bowing past unbreakable obstacles as proposed by Orowan (31) is given by putting ϕ =0 in equation 2.7 or r=L/2 in equation 2.4 to give:

$$\tau_b = \frac{2T}{Lb} = \frac{Gb}{L} \qquad \ldots\ldots(2.8)$$

A more accurate calculation using an equation for the dislocation curvature and type has been made for the case of strong obstacles (32). The critical stress required to reach the circular configuration is the stress that makes the bow small enough to slip between the two particles with the Burgers vector held in the appropriate direction:

$$\tau_c = A(\theta) \frac{Gb}{2\pi L} \ln\left(\frac{L}{r_o}\right) \qquad \ldots\ldots (2.9)$$

Where r_o is an inner elastic energy cut off radius which is approximately equal to b. A(θ) has a value of 1 for Burgers vectors perpendicular to the dislocation line ie an edge dislocation, and a value of 1/(1-ν) for a parallel Burgers vector or screw configuration. ν is the value of Poissons ratio.

The effect of increasing the volume fraction f for a given particle size is to decrease L, leading to equation 2.9 predicting an increase in strength. Strengthening may also occur by increasing particle size, due to the increase

in line tension T. This may be accomplished by either increasing the size of discrete particles or by coherency strains producing a larger effective particle diameter.

2.3.3.1 Effective obstacle spacing

In the previous models the obstacles were assumed to be regularly spaced and have identical size and strength. Several models have been proposed to find the value of L appropriate to obstacles of a given strength; L', is the effective obstacle spacing.

Friedel (30) has given an analysis for weak point obstacles with a square lattice spacing $L=n^{-\frac{1}{2}}$, where n is the number of particles per unit area. The process is shown in figure 2.10, where the dislocation BOC bows out slightly (α,β,δ are all small) before releasing itself from O; the dislocation sweeps through area A before reaching a new equilibrium along BPC. Friedel's model assumes that on average just one new obstacle is encountered and that this 'average' obstacle may be considered to lie on BPC ie:

$$An = 1 \qquad \ldots\ldots (2.10)$$

A is calculated with the assumption that OB=OC=L':

$$A = \tfrac{1}{2} \phi'^{3}_{c} \, r^2 \qquad \ldots\ldots (2.11)$$

Where ϕ'_c is the angle through which the dislocation turns at an obstacle, and r is given by equation 2.4. Using

equations 2.4,2.10 and 2.11 Friedel produced equations for critical release rate and effective obstacle spacing:

$$\tau_c = \frac{2T}{bL}\left(\cos\frac{\phi_c}{2}\right)^{3/2} \qquad \ldots\ldots (2.12)$$

$$L' = L\left(\frac{\phi'_c}{2}\right)^{-\frac{1}{2}} \qquad \ldots\ldots (2.13)$$

At low stresses or when dislocations are nearly straight, the effective obstacle spacing is much greater than the square lattice spacing.

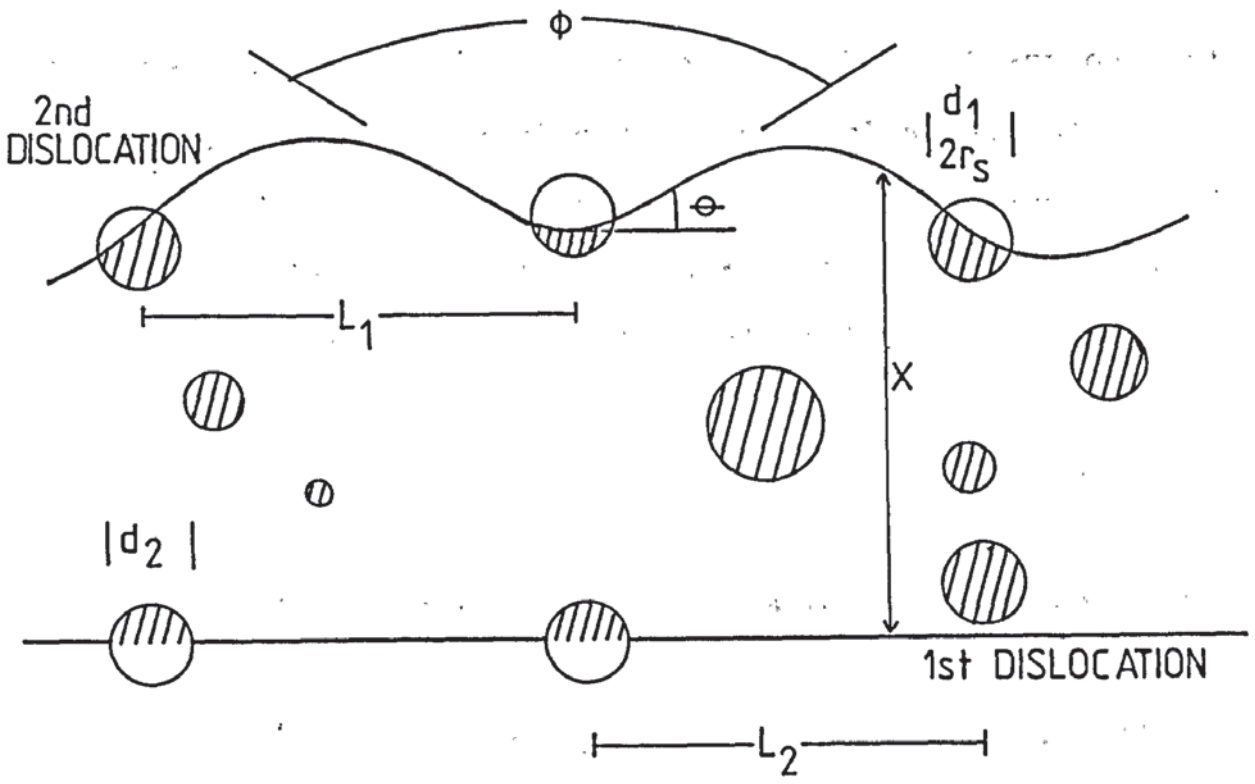

Figure 2.9 Dislocation interaction with obstacles

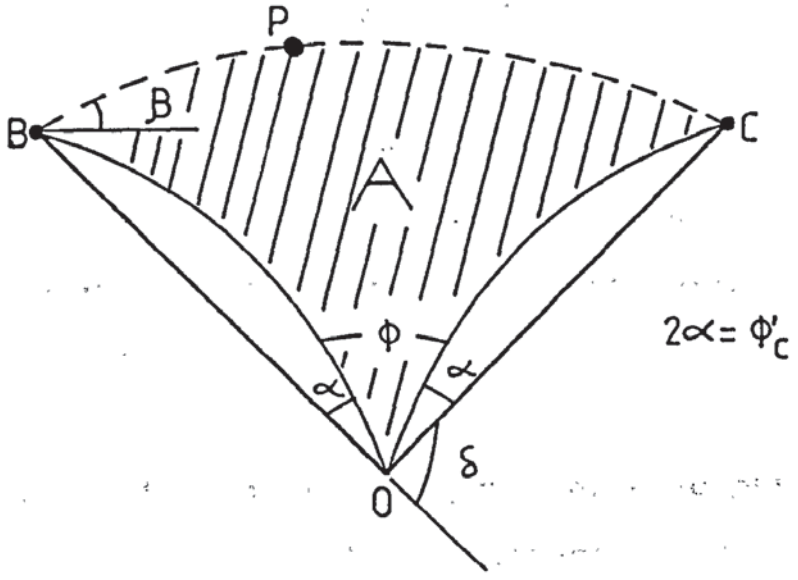

Figure 2.10 Friedel model for the effective obstacle spacing (30)

For materials containing a high volume fraction of particles, models assuming point obstacles may still be used if the particles are sufficiently equiaxed to be approximated as spheres of radius r. The mean radius r_s of the circular section in any given plane is :

$$r_s = (2/3)^{\frac{1}{2}} r \qquad \ldots\ldots (2.14)$$

The number of obstacles per unit area may be obtained by:

$$n = \frac{f}{\pi r_s^2} \qquad \ldots\ldots (2.15)$$

Where f is the volume fraction of particles. For strong particles where the Orowan process dominates, the square lattice spacing is given by:

$$L = \left[(\pi/f)^{\frac{1}{2}} - 2 \right] r_s \qquad \ldots\ldots (2.16)$$

In the case of the Friedel model for weak particles, allowance would have to be made for the size of the particles when calculating the swept area by use of equations 2.4 and 2.11.

2.3.3.2 Dislocation interaction with ordered particles

Ham (33) has studied the interaction of a single dislocation with an ordered particle. Neglecting particle-matrix interfacial energy, he proposed that a force per unit length τb on the dislocation must balance the APB energy created. With reference to figure 2.9:

$$\text{APB energy created} = \frac{2r_s \gamma_o}{L_1} \qquad \ldots\ldots (2.17)$$

Where γ_o is the specific APB energy. Therefore at equilibrium:

$$\tau_1 = \frac{2r_s\gamma_o}{L_1 b} \qquad \ldots\ldots (2.18)$$

By rearranging equation 2.13, the effective obstacle spacing for a random array of point obstacles may be given by:

$$L_1 = \frac{2T\ \pi r_s^2}{f\tau_1 b} \qquad \ldots\ldots (2.19)$$

Where the subscript represents the first dislocation in figure 2.9. Substitution of equation 2.19 into 2.18 gives the stress necessary to force the dislocation through the particle:

$$\tau_1 = \frac{\gamma_o}{b}^{3/2} \left(\frac{4fr_s}{\pi T} \right)^{\frac{1}{2}} \qquad \ldots\ldots (2.20)$$

At a constant volume fraction, the stress required to cut the particle increases with r_s. The fraction of dislocation line cutting particles and touching the APB is limited by the onset of Orowan bowing, ie when $r_s = T/\gamma_o$ and $L_1 = L$. Above this critical fraction the stress required to shear a particle becomes:

$$\tau_1 = \frac{\gamma_o}{b} \left(\frac{4f}{\pi} \right)^{\frac{1}{2}} \qquad \ldots\ldots (2.21)$$

which must be below the stress needed for Orowan bowing given by equation 2.9

Brown and Ham (34) extended this case to the interaction of superlattice dislocation pairs with ordered particles, using principles developed by Gleiter and Hornbogen (35). The process is illustrated in figure 2.10. The first dislocation is just shearing the particles and the second dislocation is being pulled forward by the APB energy in the particles cut by the first dislocation. Provided that the dislocations assume the same shape and that the separation between the two dislocations is small but larger than r_s, the second dislocation may lie outside all the particles. At equilibrium the forward stress on the second dislocation τ_2, balances the repulsive force between the dislocations. For shear of particles by the first dislocation to occur, the forward stress on the second dislocation is given by :

$$\tau_2 = \frac{\gamma_o}{2b}\left(\frac{4f}{\pi}\right)^{\frac{1}{2}} \qquad \ldots\ldots (2.22)$$

Comparing equations 2.21 and 2.22 it can be seen that the applied stress necessary to cut the particles for a dislocation pair where the second dislocation avoids the obstacles is half that necessary for cutting by single dislocation.

A more realistic process has also been analysed, where the second dislocation does come into contact with the APB

area and assumes a nearly straight configuration. Assuming $r_s > T/\gamma_o$ and the applied stress is less than the bowing stress, the applied stress necessary to produce obstacle cutting is:

$$\tau = \left[\frac{\gamma_o}{2b}\left(\frac{4f}{\pi}\right)^{\frac{1}{2}} - f\right] \quad \ldots\ldots (2.23)$$

When $r_s < \pi T f/4\gamma_o$, $\tau=0$ since both dislocations touch the same fraction of APB. As more APB is touched the flow stress will drop.

By the electron microscopic examination of Mar-M200 specimens, Copley and Kear (36) identified the rate controlling step for plastic deformation was that of dislocations moving from the matrix into γ'. The dislocation pairs were found to behave differently to the above model, the first dislocation wrapping around the particle until forced in by the following dislocation. Using a dynamic approach involving the stress dependence on the dislocation velocity, they argued that the critical resolved shear stress τ_c for the dynamic model may be approximated by:

$$\tau_c = \frac{\gamma_o}{2b} - \frac{T}{br_o} + \frac{K}{2}(\tau_o + \tau_p) \quad \ldots\ldots (2.24)$$

Where r_o is the uniform sphere radius, τ_o is the friction stress of the matrix, τ_p is the friction stress of the particle and K is a constant.

2.3.4 Dislocation bypass models

2.3.4.1 Athermal processes

The strengthening mechanisms reviewed so far have not been thermally activated. In nickel-base alloys containing a high volume fraction of γ' however, the increase in strength of γ' with temperature may impart a similar although reduced effect in the alloy (37,38). The effect of temperature on the tensile properties of two single crystal casting alloys supplied by Rolls-Royce Ltd is shown in table 2.4. The compositions and heat treatments for the alloys is given in section 3.

Table 2.4 Tensile properties of Rolls-Royce single crystal casting alloys (39)

Temperature	SRR9 -ALLOY- SRR99			
°C	UTS(MPa)	0.2%PS(MPa)	UTS(MPa)	0.2%PS(MPa)
20	976	896	--	1051
600	1038	884	--	--
700	1088	910	--	--
750	--	--	1177	1071
800	1103	816	--	--
850	--	--	1111	809
900	910	538	--	--
950	--	--	908	577

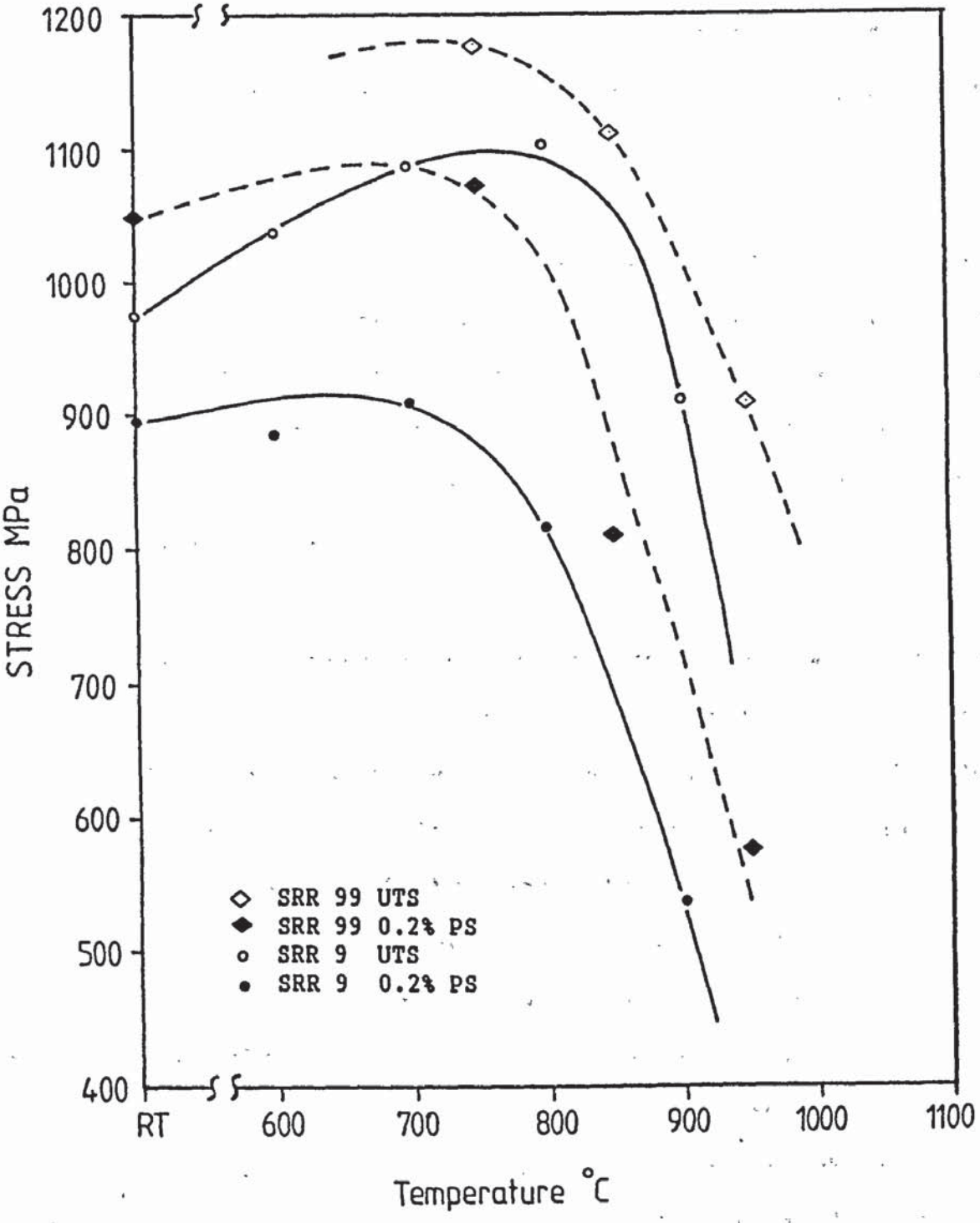

Figure 2.11 Tensile data for Rolls-Royce single crystal superalloys

The data is represented graphically in figure 2.11 and shows that the 0.2% proof stress is constant or slightly increasing from room temperature to temperatures of 700°C-800°C. This is opposite to most engineering alloys which normally exhibit a continual reduction of flow stress with temperature.

Copley and Kear (36) related the drop in flow stress above 700°C to the reduction of the first term of equation 2.24 by lowering of the specific APB energy due to local diffusion in the vicinity of the APB fault. The peak observed at 700°C-800°C was considered to be attributable to τ_p, the strength of the γ' particle.

An athermal mechanism for the bypass of particles by dislocations is by the process of cross slip (34). Both edge and screw may cross slip when a portion of the bow becomes oriented parallel to the Burgers vector and the cross slip plane. If the local stresses are sufficient, the dislocation will glide into the cross slip plane and move far enough to clear the particle. Further cross slip may then occur to link the cross slip segments freeing the dislocation and leaving behind a residual prismatic loop. The ease of cross slip is a function of the stacking fault energy, becoming more difficult as the energy is lowered due to the difficulty in constricting the partial dislocations.

2.3.4.2 Thermal processes

At high temperatures processes involving mass transfer become operational. These are slower than athermal processes due to the time dependency of diffusion and therefore when athermal processes can occur they will have a dominant effect. When athermal processes are inhibited however, ie the applied stress is low producing slow strain rates or at a temperature high enough for an appreciable rate of diffusion ; then time dependent, thermally activated deformation called 'creep' may become important.

2.4 Creep mechanisms

In the case of single crystal nickel-base superalloys complications such as grain boundaries acting as vacancy sources and sinks need not be considered. The two major mechanisms which may be present are creep controlled by the rate of recovery of dislocation networks and the thermally assisted climb of dislocations around the γ'precipitates.

2.4.1 The friction stress concept

At temperatures greater than about one third of the melting point, materials may deform by the movement of dislocations such that a steady strain rate $\dot{\varepsilon}_s$ is reached, which has been found to obey a relationship of the type:

$$\dot{\varepsilon}_s = A \frac{D_v G b}{kT} \left(\frac{\sigma}{G}\right)^n \qquad \ldots\ldots (2.25)$$

Where D_v is the bulk self-diffusion coefficient, k is Boltzmans constant, T is the absolute temperature, A and n are material constants. The relationship has been found applicable for a wide range of materials (40) but is still largely empirical and only attempts to model the basic material properties.

A model using recovery, based upon the rate of dislocation network coarsening due to jog-controlled climb under the driving force of dislocation line tension within the network, has been developed by Gittus (41). He derives the secondary creep rate as:

$$\dot{\varepsilon}_s = \frac{D_V C_j}{\alpha^3} \frac{Gb}{kT} \left(\frac{\sigma}{G}\right)^n \quad \ldots\ldots (2.26)$$

The material constants of equation 2.25 being evaluated as $A=C/\alpha^3$ and $n=3$. C_j is the temperature dependent jog concentration and α is a constant with a value near unity.

Generally the above equations and simple power law equations:

$$\dot{\varepsilon} = A\sigma^n \exp(-Q_c/RT) \quad \ldots\ldots (2.27)$$

Where Q_c is the activation energy for creep and R is the Gas constant, when applied to pure metals and simple alloys give values of n of ~4 and Q_c is approximately the activation energy for self diffusion. For solid solutions and multiphase alloys however, the values obtained for A,n and Q_c are much higher. Several authors (42,43) have sought to rationalise these differences by expressing the power law, equation 2.27, in terms of an effective stress σ_e:

$$\sigma_e = \sigma - \sigma_o \quad \ldots\ldots (2.28)$$

Where σ is the applied stress and σ_o is a 'friction' or resisting stress which for nickel-base superalloys may be related to the critical threshold stress τ_c required to cut or bypass obstacles.

The methods proposed for the measurement of σ_o depend upon the interpretation of transient effects following load or strain rate changes. Parker and Wilshire (44) produced an experimental method based on 'stress drop' measurements. The method consists of producing a constant strain rate in a creep specimen, then lowering the applied stress a small amount. This produces an instantaneous contraction followed by a time dependent contraction and a period of constant strain (incubation period), during which creep is not detected, after which creep recommences at a reduced rate. Further stress reductions are made until the change in stress $\Delta\sigma$ leads to an infinite incubation period. σ_o is determined by finding the asymptotic value in the plot of the incubation period, Δt, versus the remaining stress σ_r.

McLean (45) discussed the serious difficulties in identifying the asymptotic value of a slowly changing function. He argued that the inherent resolution of the strain measuring equipment will mean that creep appears to have ceased when it can no longer be measured. Consequently, visual inspection of the data will always over estimate σ_o, with the error involved being dependent upon the test conditions.

In alloys strengthened by both precipitates and solid solution elements, the measured friction stress will be the sum of all the friction stresses from the operating strengthening mechanisms (43) ie:

$$\sigma_s = C\,(\sigma - \sigma_p) \qquad \ldots\ldots\ (2.29a)$$

$$\sigma_o = \sigma_s + \sigma_p \qquad \ldots\ldots\ (2.29b)$$

Where σ_o is the total friction stress, σ_s is the friction stress due to solid solution strengthening, σ_p is the friction stress due to particle strengthening and C is a constant.

2.4.2 Bypass of obstacles by dislocation climb

Stevens and Flewitt (43) have derived an expression for σ_p when climb is the only possible dislocation by-pass mechanism. The authors used a closely packed arrangement of regular sized spheres with the effective radius and area of precipitate on the slip plane being estimated. They argued that when the dislocation climbs a particle, its length will increase. The total increase in length is governed by the effective particle radius R_s and the effective particle spacing L. The authors related the rate of change of line length as the dislocatiom climbs, dl/dz to the back stress acting over a dislocation of length L. The threshold shear stress for climb is:

$$\tau_{back} = \frac{Gb}{2L}\left(\frac{dl}{dz}\right)_{max} \qquad \ldots\ldots\ (2.30)$$

Where (dl/dz)max is computed by evaluating dl/dz from the point the dislocation first touches the particle to the position of the climbing dislocation when its points of intersection become normal to the glide plane.

Brown and Ham (34) have considered the climb of dislocations over cubic obstacles. In this case, if the dislocation moves forward an amount δx an additional line length $\sqrt{2}.dx$ is created. If the effective particle spacing is L, the flow stress is given by:

$$\tau_{climb} = \frac{1}{\sqrt{2}} \frac{Gb}{L} \qquad \ldots\ldots (2.31)$$

Assuming that the line energy of the dislocation is approximated by equation 2.5,equation 2.31 may be related to the general condition for Orowan bowing τ_{ob},equation 2.8 such that:

$$\tau_{climb} = \frac{\tau_{ob}}{\sqrt{2}} \qquad \ldots\ldots (2.32)$$

This illustrates that when the temperature is high enough for appreciable diffusion of vacancies, climb will be more favourable than bypass by bowing. The above process envisages climb over individual obstacles,commonly termed 'local climb'. It has been stated however (46) that 'general climb' may occur, where dislocations climb over arrays of obstacles. This can occur with a smaller increase in dislocation length when all the dislocation climbs out of the glide plane. The threshold stress for general climb τ_{gc} is dependent upon the effective mean spacing of obstacles which varies with the stress level .

For superalloys containing a high volume fraction of regularly spaced particles, the friction stress for general climb is given by:

$$\tau_{gc} = \tau_{ob} f^{\frac{1}{2}}/2^{\frac{1}{4}} \quad \text{For high stress} \quad \ldots\ldots (2.33a)$$

$$\tau_{gc} = \tau_{ob} f^{\frac{1}{2}}/2^{\frac{5}{4}} \quad \text{For low stress} \quad \ldots\ldots (2.33b)$$

For a volume fraction of 0.5 the equations yield values of $0.6\tau_{ob}$ and $0.15\tau_{ob}$ respectively which is less than the value predicted by equation 2.32 for local climb. General climb is insensitive to particle size but is strongly dependent on the applied stress.

For low volume fractions of precipitates it is argued that general climb will occur many orders of magnitude more slowly than local climb due to the larger amount of diffusion needed. At volume fractions above 12.5% however the kinetics of the two processes are thought to be similar.

2.5 The stability of Gamma prime

During creep at temperatures above 0.6 T_m, where T_m is the melting point of the alloy; a change in γ' morphology may occur leading to a loss of coherency.

Pearson et al (47) observed the formation of γ' rafts in orientations perpendicular to the applied stress during creep testing at 1038°C of a nickel base superalloy. The driving force for the coalescing of individual γ' particles into lamellar platelets or 'rafts' was considered to be the lowering of the negative γ/γ' lattice misfit assisted by the applied stress. The authors found that in <001> oriented specimens, the formation of finely spaced rafts produced a 4-fold increase in creep rupture life.

Recently, Ebert and co-workers (48,49,6) have found that the production of lamellar γ' improved the creep resistance of Nasair 100 at 1000°C but found little benefit at 925°C although γ' coalescence was still taking place.

Using experimental alloys it was found that cobalt retarded the coarsening rate of γ' in the unstressed condition but rafting perpendicular to an applied stress was rapid in all compositions. At 1000°C coarsening was completed during the first 10 percent of the creep life whereas at 925°C it was not completed until secondary or tertiary creep stages.

The improvement in creep properties for <100> crystals at 1000°C is considered to be due to the lamellar γ' morphology suppressing climb bypass thus forcing dislocations to shear γ'. Misfit dislocations at the γ/γ' interface retard the penetration of dislocations into γ'.

As most benefit is obtained by the early formation of a stable finely spaced raft network, the absence of improved creep properties at 925°C may be explained by the slow rate of γ' coarsening at this temperature.

2.6 Creep properties of nickel-base superalloys

Creep curves associated with nickel-base superalloys may have several differences when compared to the general type of curve which occurs for the majority of engineering alloys. The general curve as shown in figure 2.12a consists of three stages:

(a) The primary stage, when relatively rapid extension takes place but at a decreasing rate.

(b) The secondary or steady state stage, where the creep strain rate $\dot{\epsilon}$ is fairly constant.

(c) The tertiary stage, where the creep strain rate accelerates and finally leads to rupture.

The two main differences seen in creep curves for nickel-base superalloys are shown in figure 2.12b. Firstly, the primary creep stage may be replaced by an incubation period, A, where the strain rate is zero or very slow. Secondly the non linear tertiary period may be extended to cover over 50 percent of the total life with little or no secondary creep stage present.

2.6.1 The incubation period

In superalloy single crystals, the incubation period is not always observed. Analysis of dislocation structures in creep specimens identified the presence of an incubation period to be due to a low density of mobile dislocations.

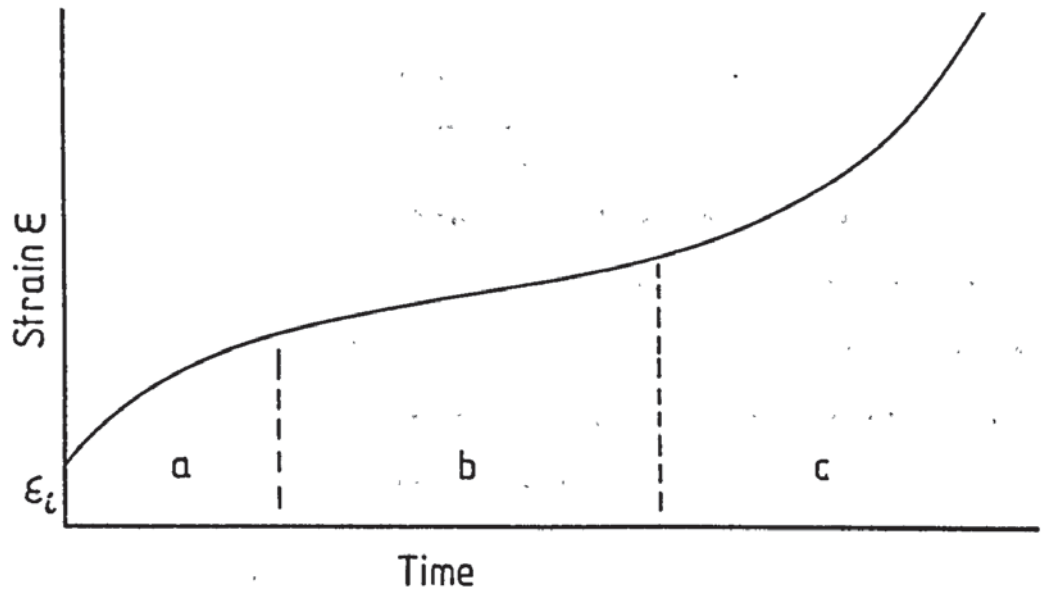

Figure 2.12a Main features of general creep curve

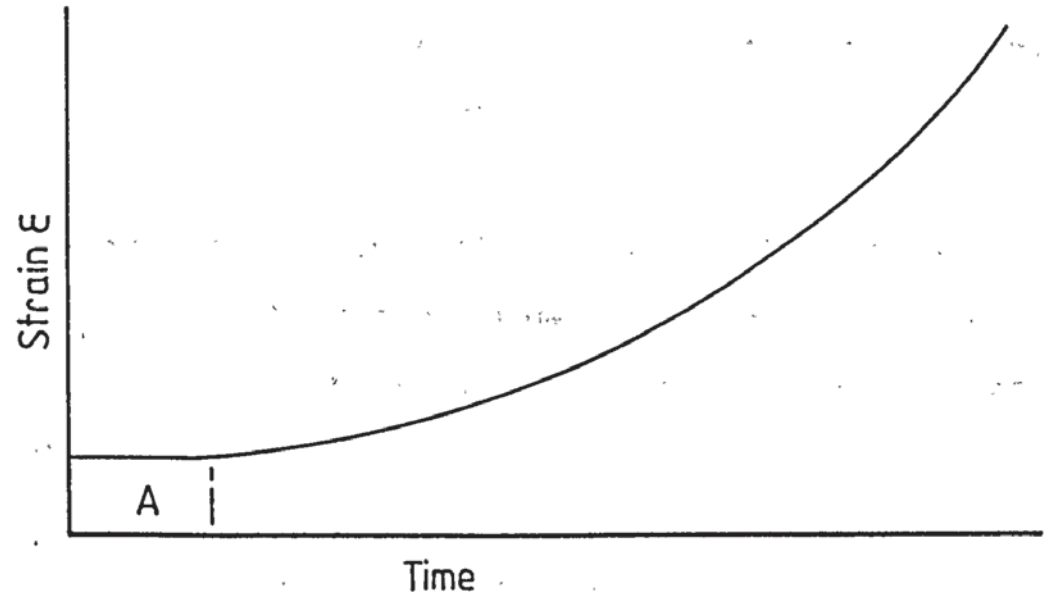

Figure 2.12b Main feature of creep curve observed with nickel-base superalloys

Carry and Strudel(50) related the number of mobile dislocations to the lattice misfit parameter δ:

$$\delta = 2\,\frac{a_p - a_m}{a_p + a_m} \qquad \ldots\ldots (2.34)$$

Where a_p and a_m are the lattice parameters of the precipitates and of the matrix respectively. In superalloys where the γ' precipitates are much less than one micron in size the lattice misfit is accommodated by elastic strains. Where the precipitates are larger, networks of interfacial dislocations develop.

The authors found that full solution treatments and precipitation of γ' cuboids of less than 0.25 micron in size may confine dislocations to subgrain boundaries. This produces a lower density of mobile dislocations compared to misfit dislocation networks containing dislocations having all six possible a/2<110> Burgers vectors.

Webster and Piearcey (51) showed that deformation of specimens prior to creep, namely lathe machining, may remove the incubation period by the production of mobile dislocations.

2.6.2 The prolonged tertiary period

The progressively increasing strain rate following the transient stage, where the rate of increase is greater with increasing applied stress, has been attributed by several authors (42,43) to the coarsening of γ' throughout the

creep tests, leading to a steady decline in σ_o.

Dyson and McLean (52) reviewing the above models noted that they could not explain the improvement of creep properties due to γ' rafting (47), and suggested that plastic strain would be a more important parameter than time in determining the degree of acceleration of strain rate in these alloys. They concluded that a new model which envisages the mobile dislocation density being directly proportional to strain may be applicable.

Recently, Henderson and McLean (53) examined the variation of σ_o during creep using a mathematical model for the stress decrement behaviour:

$$\Sigma\Delta t = \frac{G^2b^2}{K} \quad (\sigma_r-\sigma_o)^{-2} - (\sigma_i-\sigma_o)^{-2} \quad \ldots\ldots (2.35)$$

Where K is a kinetic constant, σ_r is the remaining stress and σ_i is the initial stress. They found that σ_o:

(a) Decreases slightly with increasing γ' cuboid size but much less than predicted by bowing or climb models.

(b) Is insensitive to applied stress.

(c) Decreases slightly with increasing temperature.

(d) Remains fairly constant during creep, decreasing more in an alloy with fine γ' particles than in an alloy with stable γ' cuboids.

(e) Is associated with the threshold stress for local climb in alloy IN738LC.

Using the values obtained for the constant K in equation 2.45 to model the dislocation recovery kinetics, it was found that recovery kinetics:

(a) Are generally insensitive to γ' cuboid size.

(b) Increase with increasing initial applied stress and therefore creep rate.

(c) Increase significantly with increasing temperature.

The increase in recovery kinetics was found to be in proportion to the gradual increase in creep rate that is exhibited in nickel-base superalloys. In specimens examined by transmission electron microscopy (TEM), the authors found that the dislocation network spacing at the semi-coherent γ/γ' interfaces decreased with increasing strain.

They proposed that this network affects the dislocation climb kinetics and thus causes the progressive increase in creep rate, and may also be responsible for the observed slight fall in σ_o.

2.7 Effects of temperature, strain rate and orientation on mechanical properties

2.7.1 Single crystal rotation analysis

It is well known that slip in single crystals occurs on planes with the most closely packed atoms, and nearly always along the most closely packed direction. For a given crystal structure the operative slip systems may be identified by the use of x-ray diffraction techniques.

The slip planes may be identified by two trace analysis (54), where square sectioned crystals with electropolished faces are utilised. The orientation of the two faces are determined by the Laue back reflection x-ray technique (55). Slip lines are produced by straining the crystal a small amount. Measuring the angle a slip line makes with the two faces, enables a stereographic projection to be produced which may be indexed to discover the type of plane making the slip lines.

The slip direction may be revealed using the fact that the active slip direction in a crystal rotates towards the tensile axis during uniaxial loading (56). Use of the Laue x-ray technique allows the determination of the tensile axis direction in the crystal to be determined prior to and after extension. The crystal rotation is portrayed by considering the rotation of the tensile axis relative to the crystal, ie the opposite of the real case.

Schmid (56) found that the operating slip system may be determined theoretically by finding the system in which the resolved shear stress is a maximum. The cross sectional area of the specimen shown in figure 2.13 is designated A. The cross sectional area of the slip plane may be calculated by noting that the angle between the two planes is the same as the angle between the two plane normals, which is designated ϕ, then:

$$A_{sp} = \frac{A}{\cos\phi} \qquad \ldots\ldots (2.36)$$

For a tensile specimen, ϕ is also the angle between the applied force P, and the slip plane normal. The component of force P which is a shear force acting parallel to the slip direction OD is:

$$P_{sp} = P \cos\lambda \qquad \ldots\ldots (2.37)$$

Where λ is the angle between the tensile axis and the slip direction. The resolved shear stress in the slip direction τ_{sd} is given by dividing the resolved force by the area of slip plane:

$$\tau_{sd} = \frac{P}{A} \cos\phi \cos\lambda \qquad \ldots\ldots (2.38)$$

Where P/A is the applied stress σ, and $\cos\phi\cos\lambda$ is called the Schmid factor.

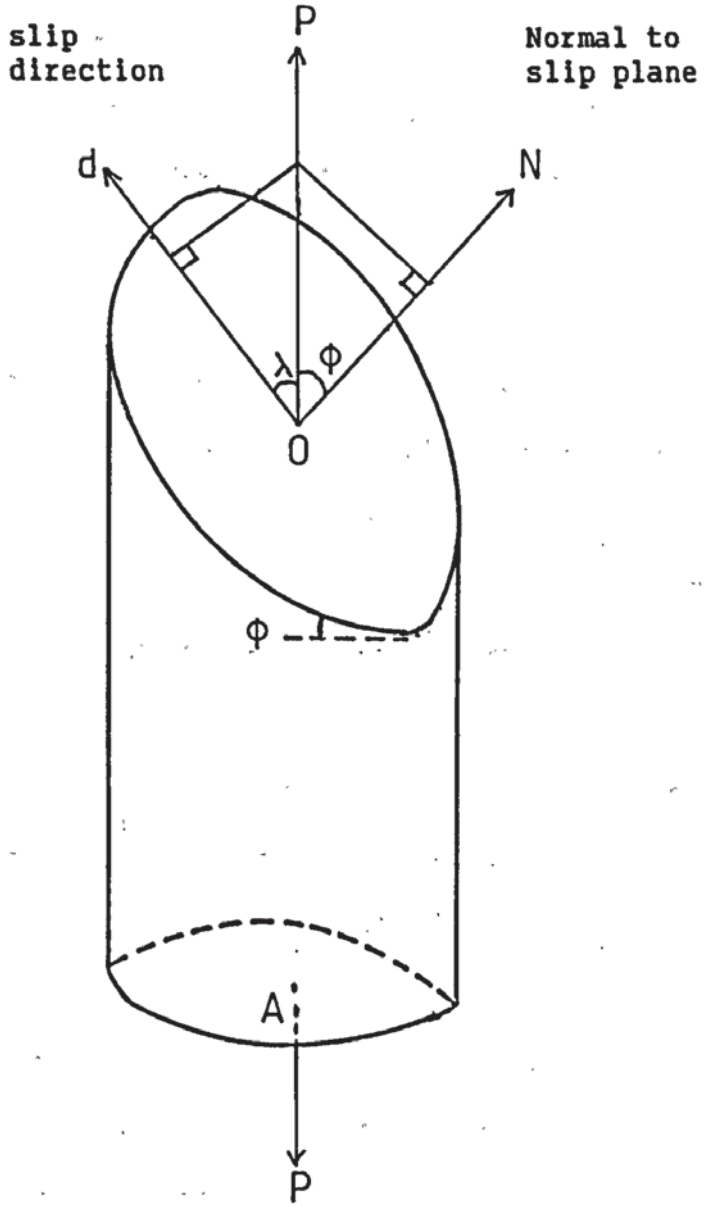

Figure 2.13 Determination of Schmid's law

2.7.2 Effect of strain rate and temperature on creep properties

Kear and co-workers (57,58) have examined the effect of orientation upon the tensile and creep properties of Mar-M200 single crystals. They found that tensile properties may be explained with reference to Schmid factors and lattice rotations for slip on the {111} or octahedral planes, as shown in figure 2.14. Specimens oriented for slip on the {111}<110> having maximum ductility and minimum work hardening index. During creep and stress rupture tests, the operative deformation mechanism was found to be dependent upon temperature and strain rate. During creep at 760°C and 690 MPa, the observed properties could not be explained by consideration of the {111}<110> system. Use of TEM analysis showed that primary creep occurred by glide of loosely coupled intrinsic/extrinsic dislocation pairs with a net Burgers vector of a<112>, as considered previously (15,16). The observed crystal rotations were in accordance with figure 2.15 which shows the effect of the most highly stressed {111}<112> slip systems. At high strain rates and during secondary creep, the mechanism reverts back to shear of the γ' by a/2<110> superlattice dislocation pairs.

At 850°C the {111}<110> was found to be dominant in both primary and secondary creep. The high temperature deformation mechanism for Mar-M200 was considered to be as follows:

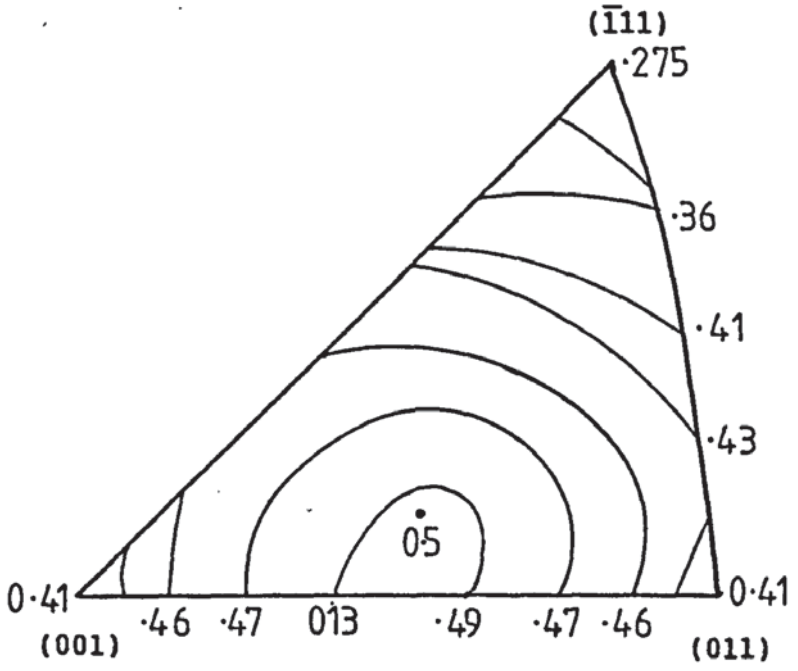

Figure 2.14a Schmid factor contours for (111)[1̄01] slip

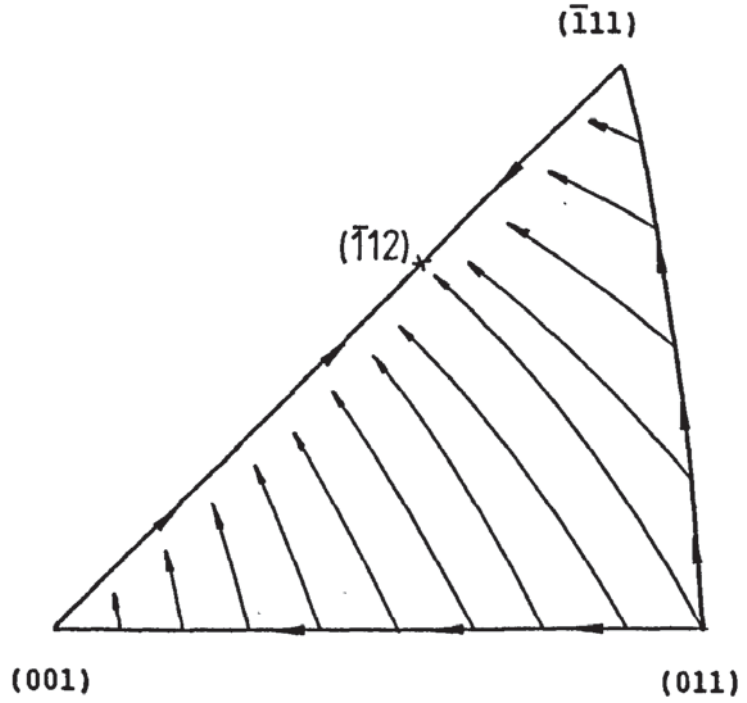

Figure 2.14b Crystal rotations for (111)[1̄01] slip

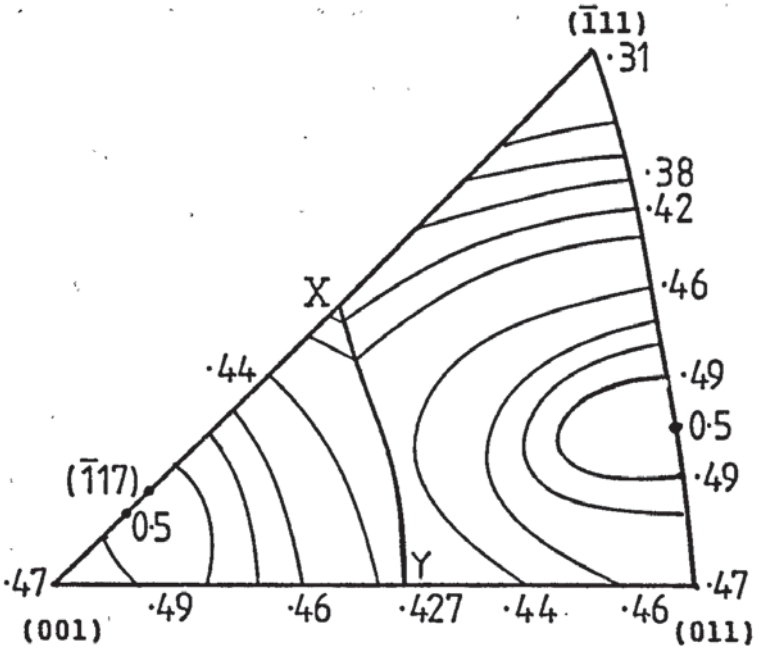

Figure 2.15a Schmid factor contours for {111}<112> slip

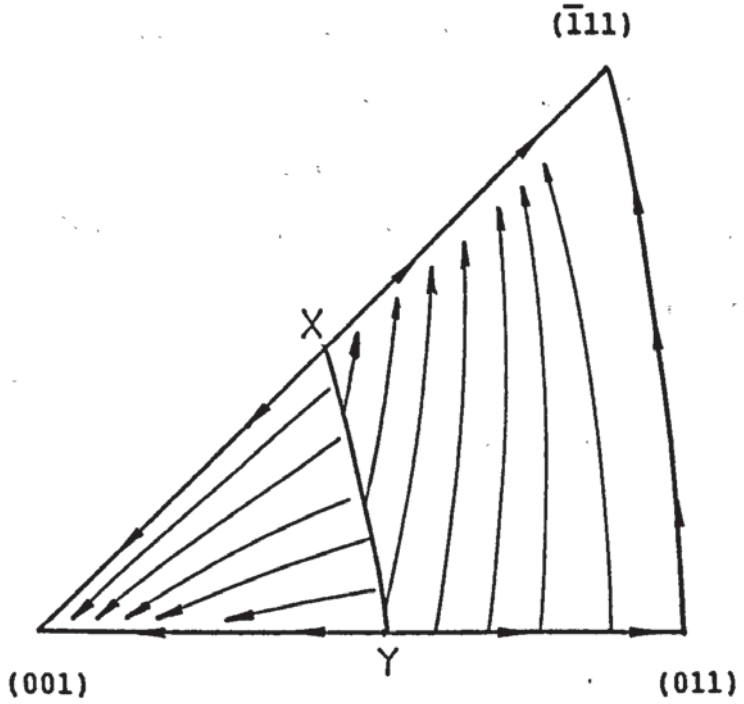

Figure 2.15b Crystal rotations for {111}<112> slip

During primary creep at intermediate temperatures, shear of γ' by complex arrays of partial dislocations having a net Burgers vector of a<112> occurs until multiple slip produces strain hardening by the formation of dislocation networks. At the onset of secondary creep, movement of dislocations through the γ/γ' dislocation networks and the unordered matrix is easier for a/2<110> superlattice dislocation pairs. The lowering of APB energy with temperature reduces the advantage of forming a<112> dislocations which incorporate stacking faults rather than APB. As the movement of a<112> dislocations is a viscous slip process requiring diffusion, this deformation mode is not observed at high strain rates.

2.7.3 The effect of orientation on creep properties

Several workers have examined the effect of single crystal orientation upon creep properties. Leverant et al (59) found that at 870°C specimens with orientations at [001] or along the [001]-[$\bar{1}$11] boundary had longer creep lives than orientations along the [001]-[011] boundary, considered to be due to a greater stability of the γ/γ' interfacial dislocation networks producing a lower number of mobile dislocations.

At 750°C to 870°C the creep properties of both Mar-M200 (58) and Mar-M246 (60,61) were found to be related to {111}<112> slip with creep rate increasing with orientation in the following order:

[001], tensile axis along [001]-[011], tensile axis between [001]-[011] and [001]-[$\bar{1}$11] and tensile axis along [001]-[$\bar{1}$11].

When {111}<112> slip is operative the [001]-[011] produces long creep lives due to multiple slip on ($\bar{1}$11)[1$\bar{1}$2] and (111)[$\bar{1}\bar{1}$2] systems. This is opposite to the dependency of orientation for {111}<110> slip where the [001]-[$\bar{1}$11] is a multiple slip orientation. The [$\bar{1}$11] orientation gives the longest creep lives at both temperatures due to this being a multiple slip orientation for {111}<110> and having a lower Schmid factor than [001].

Winstone and Northwood (2) confirmed the above results using alloy Mar-M002 and stated that for optimum creep and thermal fatigue properties the tensile axis should be near [001] lying in a {001} plane. They also found that creep properties in the transverse [010] direction were similar to [001] properties showing that dendritic structure has little effect on creep behaviour. This is in agreement with the findings of Kear and Piearcey (57).

2.8 FATIGUE

Turbine blades in service are subject to fluctuating stresses caused by thermal gradients set up during the start up and shutdown periods of the engine, together with the centrifugal stresses imposed on the blade. the magnitude of the transient stresses depends upon the physical constants of the material, such as its thermal conductivity and co-efficient of thermal expansion. if sufficient transient stresses are encountered to produce reversed yielding in the surface layers of the blade, probably at a stress concentration; then a small fatigue crack may be initiated.

The resistance of the material to fatigue depends both on enviromental and metallurgical conditions. As fatigue in turbine blades occurs at elevated temperature, the addition of creep stress to the cyclic load fluctuations is of great importance.

2.8.1 Metallurgical aspects of fatigue

Fatigue failure under cyclic conditions takes place by the initiation and growth of one or more cracks until specimen failure occurs. In a review on metallography, Plumbridge and Ryder (62) examined a multistage model proposed by Forsyth and Ryder (63). A three stage process has been defined as:

STAGE I — The initiation of cracks in slip bands or regions of local strain controlled by shear stress, followed by slip band crack growth.

STAGE II — Crack growth becomes normal to the applied stress controlled by the continuum response of the material, primarily by the stress intensity at the crack tip.

STAGE III — When local crack tip deformation reaches the order of the material inhomogeneities, static fracture ie hole growth contributes to crack advance and leads to final fracture.

The amount of crack growth in each stage depends upon the applied strain level. At high strain levels, stage II is dominant and covers almost the entire fracture surface. At low strain levels stage I may dominate. Stage III becomes important in less ductile materials tested at high strain levels.

2.8.1.1 Crack initiation and stage I crack growth

Generally fatigue crack initiation occurs at a free surface, although subsurface initiation can occur in some materials. At ambient temperature, fatigue crack initiation studies have identified the formation of cracks at a free surface by the appearance of persistent slip bands PSB (64). These are formed due to the lack of

constraint at the surface allowing the accumulation of fine reverse slip movements to extend from the surface. Within the PSB, the irreversibility of the slip process causes thin regions of metal approximately 10 micron by 1 micron thick to protrude from the surface ie. extrusions, and associated crevices of the same dimensions also form ie. intrusions. An intrusion may act as a notch root of atomic dimensions where fatigue cracks may form.

Observation of the development of persistent slip bands and microcracks has led to the following considerations (62,5):

1. The tendency of a material to disperse slip throughout the crystal determines to a large extent the number of cycles required to produce a microcrack.
2. Cross slip is an important factor in fatigue crack initiation. It is well known that hexagonal close packed (HCP) crystals which do not favour cross slip exhibit high fatigue to static strength ratios.
3. Materials with a tendency for dislocation substructure formation during fatigue have shown early fatigue crack initiation. The tendency for cross slip and substructure formation is related to stacking fault energy. There is evidence to suggest that cross slip is essential to the formation of intrusions and extrusions and hence alloys with high stacking fault energy where cross slip is easy, favors the initiation of cracks by the intrusion/extrusion mechanism.

4. Microcracks may form from surface discontinuities such as pores or inclusions which produce areas of high stress concentration. Subsurface nucleation is also possible where discontinuities produce a local resolved shear stress higher than that present on the surface.

The criterion for stage I crack growth is the resolved shear stresses on the slip plane. The tip of the intrusion or microcrack becomes a very active dislocation source, crack growth occurs by the emission of dislocations from the tip of the crack. Stage I crack growth ends when the slip band (crystallographic) cracks eventually link up to produce dominant cracks, which start to extend on a plane normal to the applied stress. The transition from stage I to stage II is supposed to occur due to the reduction in the ratio of shear to normal stress at the crack tip.

2.8.1.2 Stage II fatigue crack growth

This mode of crack growth generally occupies the largest area of a cross-section, and often shows macroscopic progression marks. Forsyth et al (65) identified two types of striation:

TYPE A "Ductile" striations lying on irregular non-crystallographic plateau.

TYPE B "Brittle" striations lying on crystallographic planes.

It is generally accepted that striation formation involves alternate blunting and resharpening of the crack tip. The mechanism of plastic blunting proposed by Laird (66) is illustrated in figure 2.16.

The notch tip at the end of a sharp crack concentrates deformation along planes at 45° under the application of a tensile load (figure 2.16b). The crack widens to its maximum extension as the load increases and growth occurs by plastic shearing, the crack tip blunting at the same time (figure 2.16c).

The load reversal also reverses the slip direction and the crack faces are crushed together. Part of the newly created surface folds resharpening the crack (figure 2.16d,e).

The amount or presence of "ductile" or "brittle" striations is dependent upon material properties, temperature and enviroment. At high values of stress intensity factors near net section yielding, large scale steps may form caused by microvoid coalescence or by micro clevage determined by the ductility of the material.

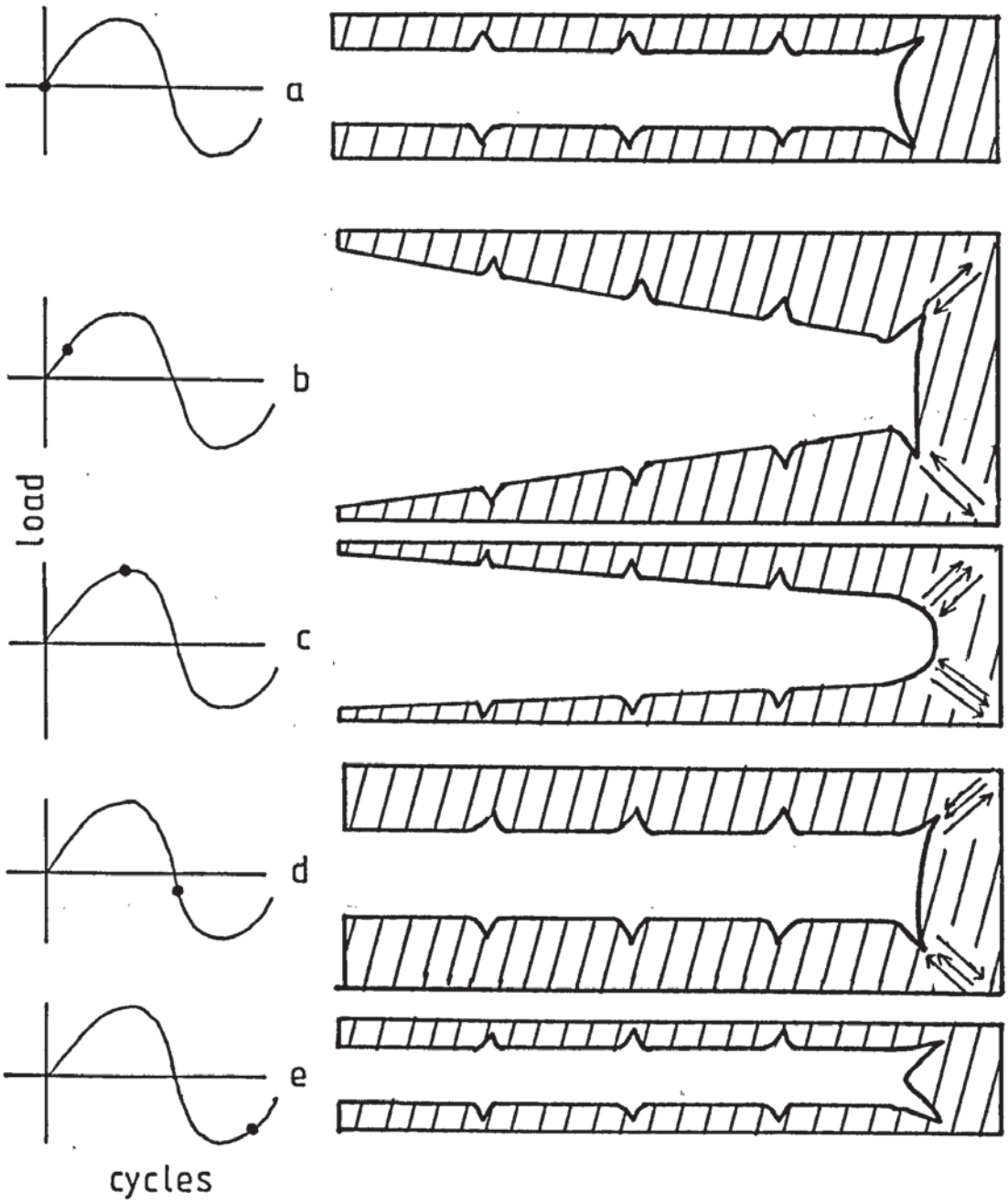

Figure 2.16 Plastic blunting model of fatigue crack growth in stage II

2.8.2 The engineering approach to fatigue

The engineering analysis of fatigue is based upon the measurement of cycles to final failure in smooth specimens, related to the applied nominal stresses and strains. The approach is valid as until the formation of an engineering crack from a smooth specimen, the stresses and strains remain essentially unchanged.

The data is represented by correlating the stress amplitude ΔS with the number of cycles to failure N_f, which is commonly called an S-N curve. Normally a logarithmic scale is used for N_f in order to allow a wide variation of cycles to be plotted. The two basic types of S-N curve are illustrated in figure 2.17. In some materials such as mild steel, there is a stress below which fatigue never occurs called the fatigue or endurance limit. In materials not exhibiting a fatigue limit, an arbitrary life time of 10^7 cycles is used for the purpose of comparison.

At low stresses, the number of cycles corresponding to the fatigue limit represents the initiation life primarily, whereas the number of cycles to crack initiation is negligible. The errors involved in the use of S-N curves to predict crack initiation increase with decreasing N_f. This is described by Basquin's relationship (67):

$$S^a N_f = \text{Constant} \qquad \ldots\ldots (2.39)$$

With the exponent in the range 8 to 20 and S being the stress amplitude about the mean stress σ_m, which is equal to half the total stress range $\Delta\sigma$.

The S-N curve is considered to have two regions. Endurance beyond 10^4 cycles is termed high cycle fatigue (HCF), where the bulk of the specimen is elastically deformed and stage II crack growth occupies only 10% or so of the total fatigue life. In the case of low cycle fatigue (LCF), where the endurance is less than 10^4 and the nominal stress exceeds the yield stress Basquin's law no longer applies. Manson and Coffin (68) proposed a relationship for low cycle fatigue:

$$\Delta\varepsilon' N_f^b = \text{Constant} \qquad \ldots\ldots (2.40)$$

Where $\Delta\varepsilon$ is the applied strain range and the exponent b is in the range of 0.5 to 0.6.

The above relationships apply for cycling about a zero mean stress. If a non zero mean stress is used, it may be related to the stress range for failure in the same number of cycles using a zero mean stress $\Delta\sigma_o$, by use of Goodmans rule (67):

$$\Delta\sigma_{\sigma_m} = \Delta\sigma_o \left(1 - \frac{|\sigma_m|}{\sigma_{uts}}\right) \qquad \ldots\ldots (2.41)$$

Where $\Delta\sigma_{\sigma_m}$ is the stress range required to produce failure in N_f cycles using a mean stress of σ_m, and σ_{uts} is the

ultimate tensile strength. A more acceptable and conservative estimate proposed by Soderberg is to replace σ_{UTS} in equation 2.41 with the yield stress of the material, σ_y.

2.8.3 The fracture mechanics approach to fatigue

The empirical laws considered previously are based upon the assumption that stress and strain remain fairly constant for the majority of the fatigue life. However, when a stress concentration such as a notch or fatigue crack is present, the local stress and strain at the end of the discontinuity is different from those applied.

At first, strain controlled LCF of smooth specimens was used to estimate the fatigue life for a notched component by attempting to simulate the plastic conditions at the crack tip. With the advent of fracture mechanics the conditions at the crack tip may be calculated, allowing more accurate analysis of fatigue crack growth.

2.8.3.1 Linear elastic fracture mechanics (LEFM)

The fundamental relationships used in linear elastic fracture mechanics were laid down by Griffith (69). Griffith noted that when a crack is introduced into a stressed plate of elastic material, a balance must be attained between the decrease in potential energy (caused by the release of stored energy and work done by movement of the external loads), and the increase of surface energy resulting from the presence of the crack.

Crack growth occurs if the necessary additional surface energy is supplied by the system. Griffith's relationship for a central crack in an infinite plate is:

$$\sigma = \sqrt{\frac{2E\gamma_s}{\pi a}} \qquad \ldots\ldots (2.42)$$

Where E is Young's modulus, a is the half crack length, γ_s is the specific surface energy and σ is the applied stress. Irwin (70) applied the Griffith relationship to materials capable of plastic deformation. Instead of γ_s, Irwin chose to use the energy source term du/da which is the elastic energy per unit crack length increment. This term may also be denoted as G, the strain energy release rate, so that Griffith's relationship for plastic materials is:

$$\sigma = \sqrt{\frac{EG}{\pi a}} \qquad \ldots\ldots (2.43)$$

Where $G= 2(\gamma_s+\gamma_p)$ and γ_p is the plastic deformation energy.

The fracture of flawed components has been analysed using elastic theory. Using analytical methods described by Westergaard (71), Irwin (72) published solutions for crack tip stress distributions for three different forms of loading:

MODE I	Tensile
MODE II	Sliding or in-plane shear
MODE III	Tearing or pure shear

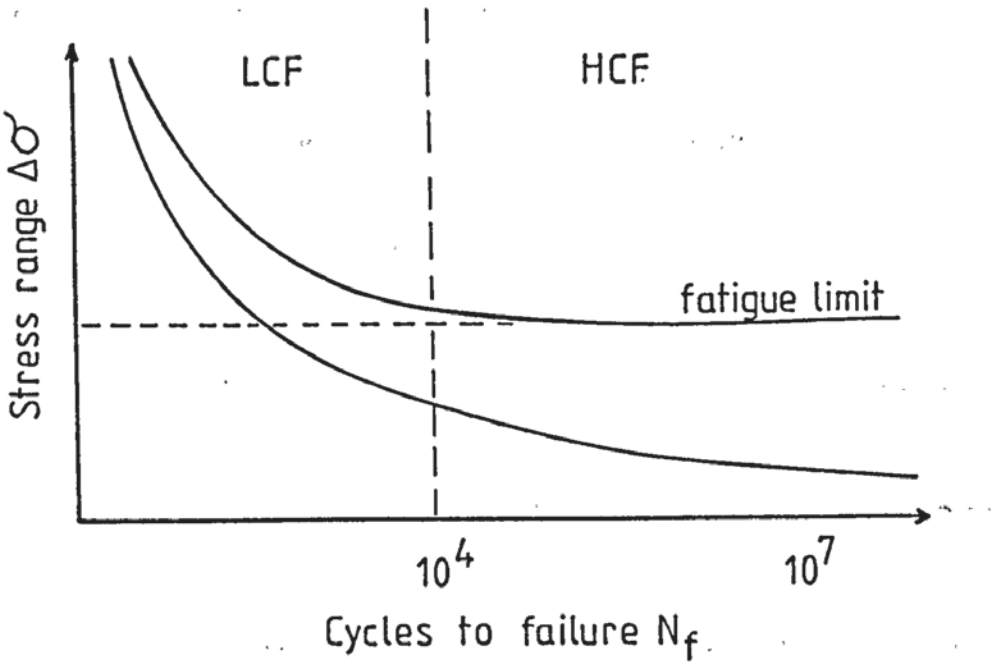

Figure 2.17 Schematic of an S-N Curve

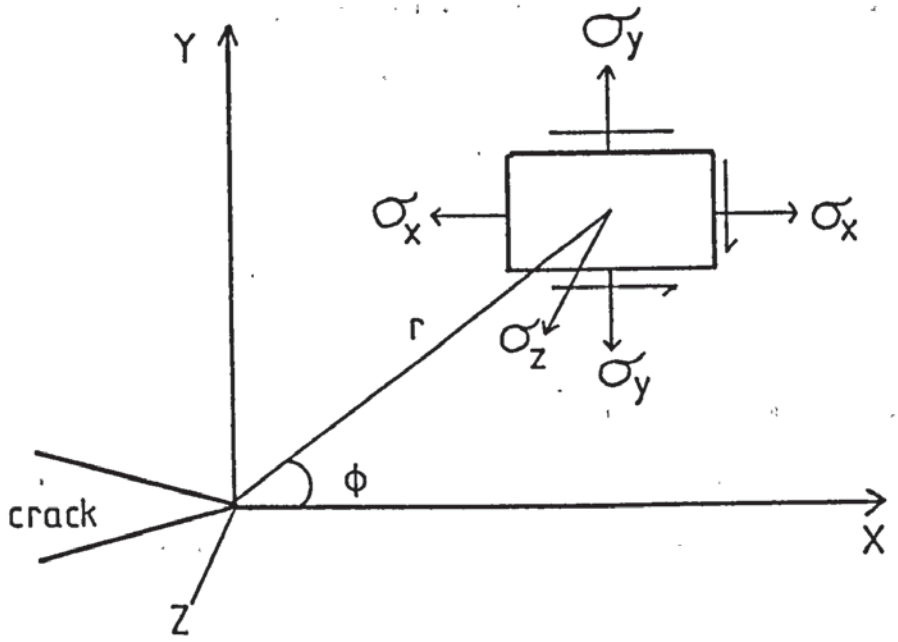

Figure 2.18 Distribution of stresses near a crack tip

For Mode I, using the notation shown in figure 2.18, the crack tip stresses are given by:

$$\sigma_{xx} = \frac{K}{\sqrt{2\pi r}} \cos\frac{\theta}{2} \left[1-\sin\frac{\theta}{2} \sin\frac{3\theta}{2} \right] \quad \ldots\ldots (2.44a)$$

$$\sigma_{yy} = \frac{K}{\sqrt{2\pi r}} \cos\frac{\theta}{2} \left[1+\sin\frac{\theta}{2} \sin\frac{3\theta}{2} \right] \quad \ldots\ldots (2.44b)$$

$$\tau_{xy} = \frac{K_I}{\sqrt{2\pi r}} \sin\frac{\theta}{2} \cos\frac{\theta}{2} \cos\frac{3\theta}{2} \quad \ldots\ldots (2.44c)$$

The stress distribution around any crack in a structure depends only on the parameters r and θ. The difference between one cracked component and another lies in the magnitude of the stress field parameter K, defined as the stress intensity factor :

$$K_I = \sigma \sqrt{2\pi r} \quad \ldots\ldots (2.45)$$

Where K_I is the stress intensity factor for mode I loading and r is the distance ahead of the crack tip. Comparing equations 2.43 and 2.45, it can be seen that:

$$K = \sqrt{EG} \quad \ldots\ldots (2.46)$$

Analytical solutions for laboratory test specimens and commonly encountered crack configurations can be found in various handbooks (95,96), in the form of:

$$K = \sigma\sqrt{\pi a} \, . Y \quad \ldots\ldots (2.47)$$

Y is usually a polynomial function of a/W, where a denotes the crack length and W is the width of the specimen. It is commonly called the stress intensity calibration factor or the compliance calibration. Calibration of non-standard specimens may be done by experiment using photoelastic or compliance measurement techniques (73) or theoretically using finite element stress analysis or numerical methods.

When the stress in the crack tip region exceeds the yield strength of the material, a plastic zone is developed near the crack tip. As the presence of the plastic zone makes the material behave as though the crack is longer than actually measured, knowledge of the size of the plastic zone size is important for obtaining the effective length of the crack. Re-arranging equation 2.45:

$$r_y = \frac{K_I^2}{2\pi\sigma_y^2} \qquad \text{(Plane Stress)} \qquad \ldots\ldots (2.48)$$

Where the subscripted y variables denote the plastic zone radius and the value of stress respectively at yielding condition. This equation however leads to a low estimate of r_y because the redistribution of stress from yielding leads to an increase in plastic zone size.

For conditions of plane strain, ie constraint in the thickness direction, Irwin (74) considered the increase in uniaxial yield stress σ_y caused by the plane strain elastic constraint. Taking a value of the constrained yield stress

of $\sqrt{2\sqrt{2}}$ times the uniaxial yield stress and substituting for σ_y in equation 2.45, then :

$$r_y = \frac{1}{5.6\pi}\left[\frac{K_I}{\sigma_y}\right]^2 \qquad \ldots\ldots (2.49)$$

The above value for r_y is only approximate as the plastic zone size is assumed to be circular; in fact the plastic zone has been found to be dumbell shaped, being larger near the free surfaces of the body.

As the size of the plastic zone is dependent upon the level of stress triaxiality, as the thickness of the specimen is increased, the size of the plastic zone diminishes. This has the effect of lowering the fracture toughness of the specimen, as the amount of material capable of deforming plastically is reduced as shown in figure 2.19.

Once the thickness is large enough to generate the maximum triaxial stress, the value of fracture toughness becomes independent of specimen geometry. This allows the value of plane strain fracture toughness to be used as a conservative lower limit of material toughness.

The ASTM standard for the fracture toughness testing of metallic materials (75) gives the following requirements to ensure plane strain conditions:

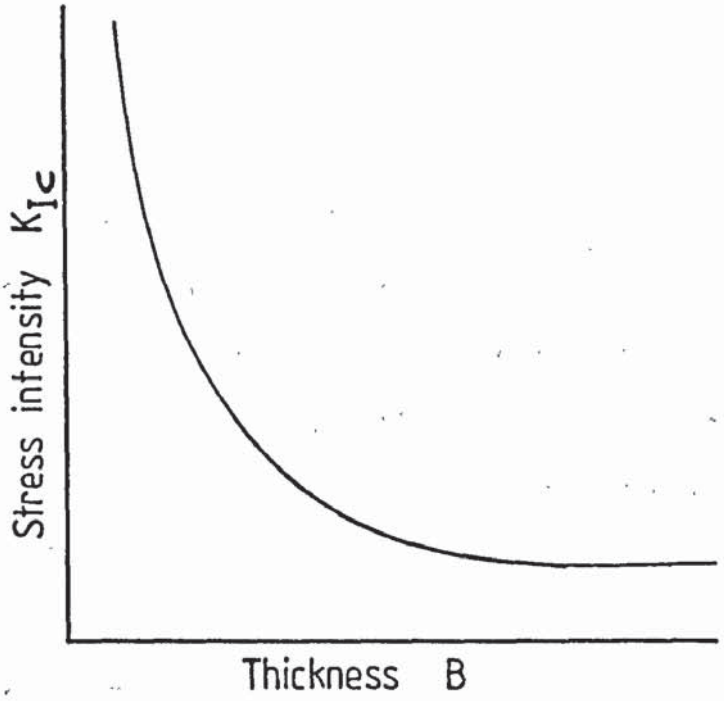

Figure 2.19 The effect of thickness on fracture toughness

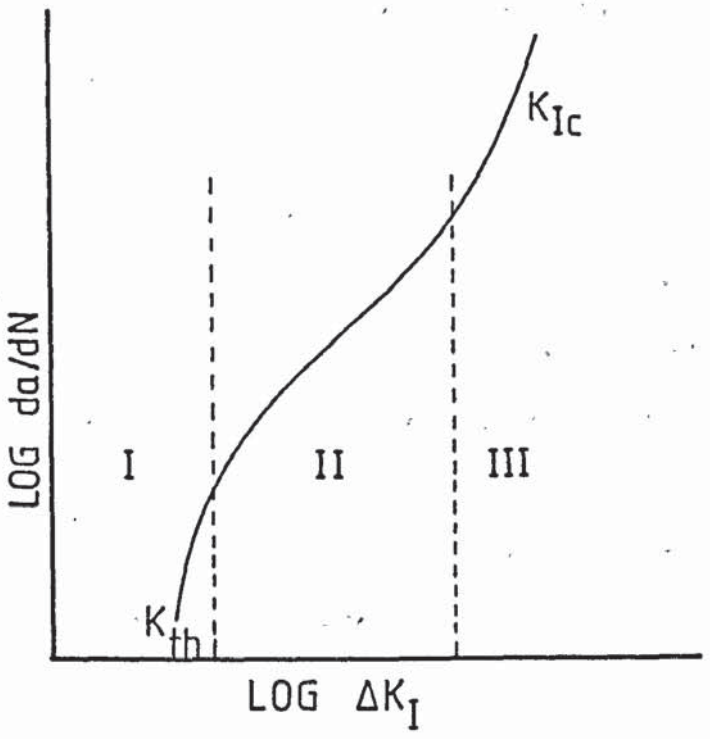

Figure 2.20 Schematic representation of fatigue crack growth behaviour

$$a, B > 2.5\left(\frac{K_{Ic}}{\sigma_y}\right)^2 \qquad \ldots\ldots (2.50a)$$

$$W > 5.0\left(\frac{K_{Ic}}{\sigma_y}\right)^2 \qquad \ldots\ldots (2.50b)$$

Where B is the specimen thickness and K_{Ic} is the critical stress intensity factor for fast fracture during mode I loading. For specimens meeting the above requirements, the plastic zone size is approximately 1/50th of the thickness ensuring that the plastic zone is contained within an elastic stress field.

2.8.3.2 Application of LEFM to fatigue

The above parameters can be modified to account for cyclic loading. In this case crack propagation can occur even though the maximum load is less than that required to exceed the K_{Ic} value. The stress intensity factor range ΔK, where $\Delta K = K_{max} - K_{min}$, is used for correlation of crack growth rates.

During the tension cycle in fatigue the plastic zone size will be given by equation 2.48 for a plane stress condition. During the reverse cycle, for symmetry, the yield stress in compression is equal to the tensile yield stress. Thus the formation of a reverse plastic zone requires an imposed stress of $-2\sigma_y$. Substituting for σ_y in equation 2.48 gives:

$$r_{ry} = \frac{1}{2\pi}\left(\frac{\Delta K}{2\sigma_y}\right)^2 \qquad \ldots\ldots (2.51)$$

Leading to a reversed plastic zone size one quarter of the maximum plastic zones size.

Fatigue crack propagation behaviour for metals may be illustrated by plotting the increment of crack growth per cycle da/dN, versus the stress intensity factor range ΔK. This is illustrated in figure 2.20. Many materials exhibit three ranges of behaviour.

Stage I is a region where a small drop in ΔK leads to a large reduction in crack growth rate, and exhibits a fatigue threshold cyclic stress intensity factor ΔK_{th} below which cracks do not propagate. Stage II is stable crack propagation which may be represented by the Paris law (76):

$$\frac{da}{dN} = A(\Delta K)^n \qquad \ldots\ldots (2.52)$$

A and n are constants, the value of n being approximately 3 to 6. In stage III unstable behaviour occurs at high ΔK levels and results in a rapid increase in crack growth rate, just prior to complete failure of the specimen.

Crack closure effects, which are sensitive to loading conditions, become predominant at the near threshold region, producing the effect of a threshold stress intensity level. Due to the low values of ΔK and therefore crack tip plasticity, there is an increased likleyhood of faceted crack growth.

The main limiting factor for the application of LEFM techniques is the size of the plastic zone. Linear elastic fracture mechanics is not valid unless the region of plasticity surrounding the crack tip is small in comparison to both the crack length and remaining ligament of uncracked material.

It is apparent that, in stage III crack growth, or at elevated temperatures where the decrease in yield strength which occurs in certain engineering materials, together with the emergence of creep effects, can give rise to situations where analysis by non-linear parameters is preferred.

2.8.4 Non-Linear parameters

An equivalent parameter to K, the path-dependent J integral, has been proposed by Rice (77). Values of J may be determined from load versus load point deflection curves. At a given deflection δ, the potential change caused by a small increase in crack length da is related to J as follows:

$$J = \frac{-1}{B} \frac{dU}{da} \qquad \ldots\ldots (2.53)$$

Where B is the specimen thickness, and dU is the area between the two load versus deflection curves. Deflections δ are measured simultaneously with the applied load. Load versus deflection curves for several different crack lengths may be employed with equation 2.53, to determine empirical relationships between J and deflection at various values of crack length, a similar method to the compliance method of measuring G, the strain energy release rate. If the load/deflection lines measured are linear, then J reduces to G which is related to the stress intensity K:

$$J = G = \frac{K^2}{E} \qquad \ldots\ldots (2.54)$$

The mathematical theory leading to the J-integral implies that for elastic-plastic materials, the concept is valid when deformation theory applies. As the deformation theory does not account for plasticity effects on unloading, there is a question regarding the use of the J-integral to cyclic loading.

2.8.4.1 Experimental measurement of cyclic J;ΔJ

Rice et al (78) have developed approximations to allow J values to be determined from a single load versus deflection curve. This approximation is only valid for deeply notched (a/W>0.6) compact tension and bend bar specimens. The approximate J value at a given deflection is related to the area under the load versus deflection curve:

$$J = \frac{2}{Bb} \int_0^{\delta_o} P \, d\delta \qquad \ldots\ldots (2.55)$$

Where b is the uncracked ligament of the specimen.

Dowling and Begley (79) used the above technique on compact tension specimens to demonstrate that cyclic J-integral values, ΔJ, could be determined under displacement controlled conditions. They used deflection controlled to a sloping line, shown in figure 2.21, to avoid ratcheting effects caused by using pure load or displacement control. The estimate of J was made using the Rice et al approximation (78), but deleted the portion of the hysteresis loop which was considered to have occurred under crack closure. Sadananda and Shahinian (80) have studied the use of J integral under the more relevant and popular testing condition of load controlled fatigue. They investigated two different techniques of data reduction from the load versus displacement hysteresis loops.

In figure 2.22, N represents the cycle number, a represents crack length , d represents the cumulative

displacement at the minimum load as a result of cycling, and o represents the extrapolation of the loading part of the loop to zero displacement, which is defined as the displacement at zero load in the first cycle.

In the first technique, the loading portion of the loops are transposed to a common point of origin, as shown in figure 2.22b. The second technique argues that d_1 and d_2 are the reference points since only that part of the curve between the the two limiting loads represent the actual strain energy expended in each cycle. This method is shown in figure 2.22c.

The authors used the compliance method of data reduction, the load-displacement curve being approximated by polynomials using regression techniques and then integrated numerically. They found that ΔJ determined by the first technique was not consistent with linear elastic behaviour, whereas the second technique seemed more appropriate.

The poor results obtained by Dowling and Begley (79) using load controlled fatigue was considered to be due to the Rice et al approximation (78)being inadequate. Merkle and Corten (81) have produced a new approximation for compact tension specimens which takes into account the loading geometry:

$$\Delta J = \frac{2}{Bb} \quad (\alpha_1 U - \alpha_2 P\delta m) \qquad \ldots\ldots (2.56)$$

Where α_1 and α_2 are correction coefficients derived as a function of a/W. The equation has been used to measure crack growth rates in Udimet 700 at 650°C with results comparable to the more time consuming compliance technique (80).

2.8.4.2 Creep effects during High temperature fatigue

The fatigue of turbine blade material is commonly tested using a trapezoidal waveform to simulate loading, unloading and periods of constant load. At high temperatures creep crack growth may occur during these hold times which may have a significant effect on the standard high temperature fatigue properties.

Figure 2.23 shows a schematic of the plastic deformation zones formed ahead of a crack subject to load in the creep regime. The size of the plastic zone may be determined by use of equation 2.49 . A larger zone, the K zone schematically shows the the region around the crack tip where deformation theory and LEFM conditions apply. If the plastic zone becomes comparable with the K zone then K looses its significance and the crack tip stresses and strains must be characterised by the use of the J integral.

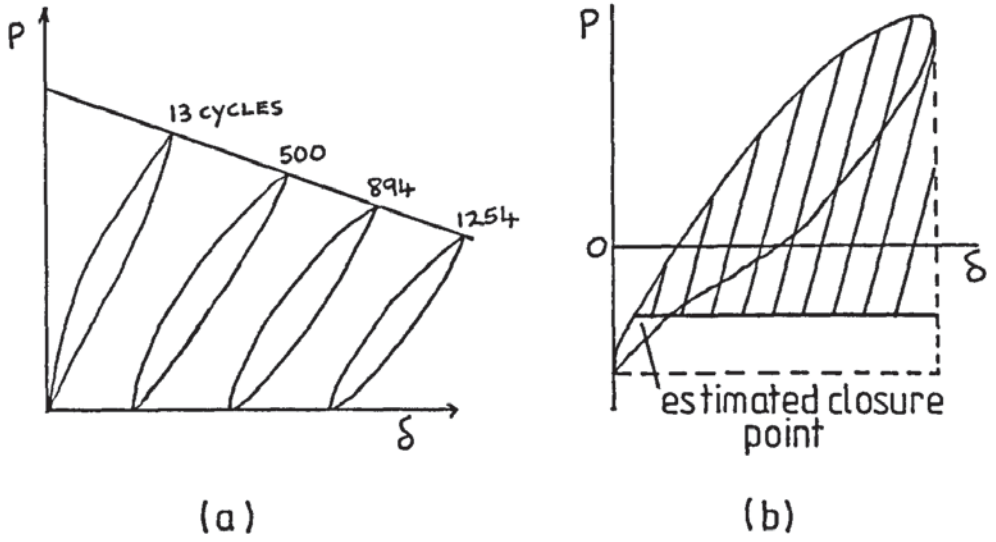

Figure 2.21 Determination of cyclic J (79)

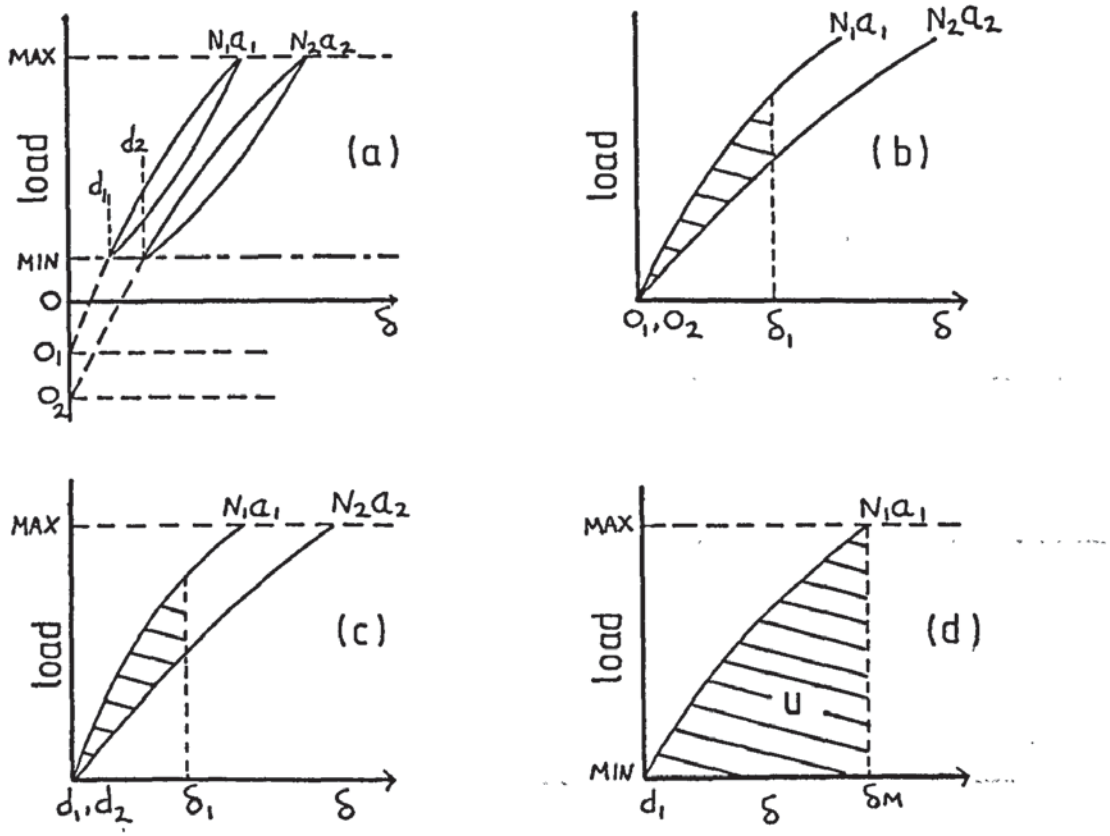

Figure 2.22 Determination of J integral during load controlled fatigue (80)

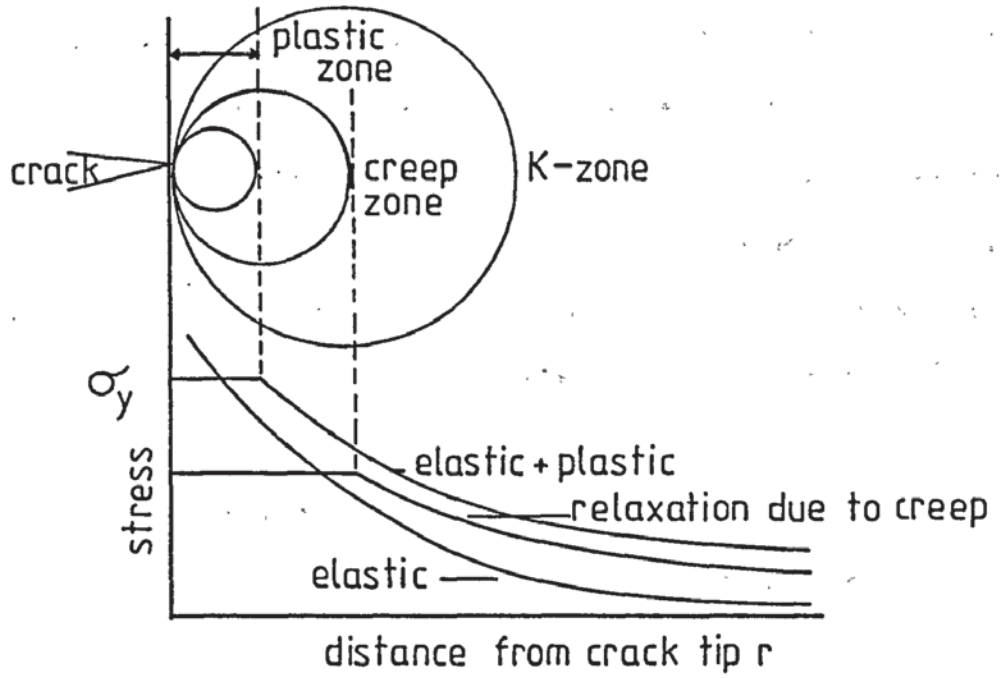

Figure 2.23 Deformation zones ahead of a crack tip at elevated temperature (88)

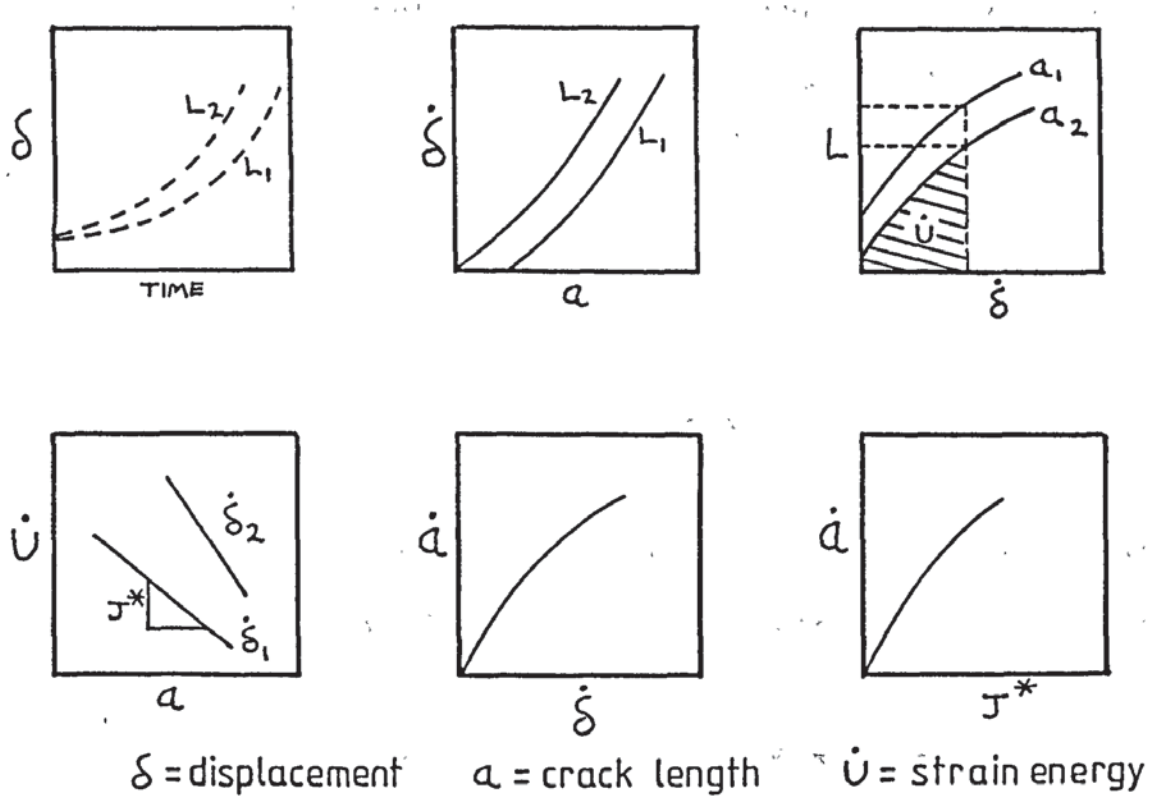

Figure 2.24 J^* Data reduction procedure

If creep conditions are introduced, then with time the stresses in the vicinity of the crack tip will begin to relax due to creep deformation. The size of the relaxation zone increases with time. If this zone becomes comparable with the K zone, neither K or J will completely characterise the stresses and strains at the crack tip.

Although Sadananda and Shahinian have found that creep resistant materials, namely nickel-base superalloys may be characterised using LEFM techniques as high as 850° C (80,82,83), new parameters have been developed for use where plasticity and creep effects become dominant.

For time dependent crack growth, the elastic-plastic parameter corresponding to K_{max} is J_{max}. This may be determined from ΔJ by:

$$J_{max} = \Delta J/(1-R) \qquad \ldots\ldots (2.57)$$

Where R is the ratio of minimum to maximum load.

As J_{max} or ΔJ determination involves the use of load-displacement curves for a given crack length, it is impossible to determine them without introducing cyclic load effects. This problem and that of stress relaxation due to creep has lead to the development of the J^* parameter (84,85). Other parameters of similar function are C^*, and the $\dot{J}$ integral

The J integral is defined by:

$$J^* = \frac{-1}{B}\frac{d\dot{U}}{da}\Big|_{\dot{\delta}} \qquad \ldots\ldots (2.58)$$

Where $\dot{U}$ and $\dot{\delta}$ are the strain energy rate and the displacement rate respectively. J^* may be calculated by the data reduction procedure shown in figure 2.24, or may be estimated by an analytical procedure which assumes the material undergoes power law creep, equation 2.27. This assumption is generally valid for uniformally stressed specimens creeping at a steady state. Koterazawa and Mori (87) have produced expressions for various geometries, the expression for compact tension specimens being:

$$J^* = \frac{2P\dot{\delta}}{Bb} \qquad \ldots\ldots (2.59)$$

and by Sadananda and Shahinian (87) as:

$$J^* = \frac{2(n-1)}{(n+1)}\frac{P\dot{\delta}}{Bb} \qquad \ldots\ldots (2.60)$$

Where b= (W-a) and n is the exponent in equation 2.27.

The C^* parameter is analogous to J^*, however many investigators prefer the C notation to describe the energy rate line integral to avoid confusion with the $\dot{J}$ parameter (dJ/dt) .

Saxena (88) found that for type 304 stainless steel, values obtained from the data reduction technique varied

from 8 to 40 percent compared to the graphical procedure. Sadananda and Shahinian (89), however found that both techniques gave J^* values which were mutually compatible for creep crack growth in type 316 stainless steel. The authors examined two types of specimen geometry, compact tension and centre-notched, and found that although J^* values for the compact tension were higher than for the centre-notched plate there appeared less spread in the data than when the stress intensity factor K was used.

2.9 Hold time effects in fatigue

Saxena et al (90) have developed a model to explain hold time effects in fatigue. The model follows the Riedel and Rice analysis (91), that under small scale creep conditions, stresses and crack growth rates are a function of K^2/t. The time dependent component is :

$$\frac{da}{dt} = b\left(\frac{K^2}{t}\right)^p \qquad \ldots\ldots (2.61)$$

Where b and P are material constants which depend upon the material and temperature. The model is only valid for hold times that are in the transient region where K characterises the crack tip conditions.

If the load or stress history experienced by a turbine rotor is considered to be as indicated in figure 2.25, the the total crack growth per cycle may be given by:

$$\left(\frac{da}{dN}\right)_h = \left(\frac{da}{dN}\right)_o + \int_o^{t_h} \left(\frac{da}{dt}\right) dt \qquad \ldots\ldots (2.62)$$

Where t_h is the hold time, and $(da/dN)_o$ is the crack growth rate for the same loading/unloading rates but no hold time which may be represented by the Paris law (76), equation 2.52. Substituting equation 2.61 into 2.62, the authors obtained:

$$\frac{da}{dN} = C(\Delta K)^n + A'(\Delta K)^{2p} . t_h^{(1-p)} \qquad \ldots\ldots (2.63)$$

$$\text{Where } A' = \frac{b}{1-p} \cdot \frac{1}{(1-R)^{2p}}$$

R is the ratio of minimum to maximum load, and ΔK may be calculated from:

$$K_{max} = \left(\frac{\Delta K}{1-R}\right) \qquad \ldots\ldots (2.64)$$

Where K_{max} is the value of K during hold time. The evaluation of the constants in equation 2.63 is done by obtaining the da/dN versus ΔK behaviour for no hold time and at least one hold time. The no hold time data gives the constants c an n, the constants A' and p are determined from the graphical method shown in figure 2.26.

The advantage of the graphical method is that it takes into account any creep-fatigue interaction for the hold cycle in question and interpolates it for other hold times.

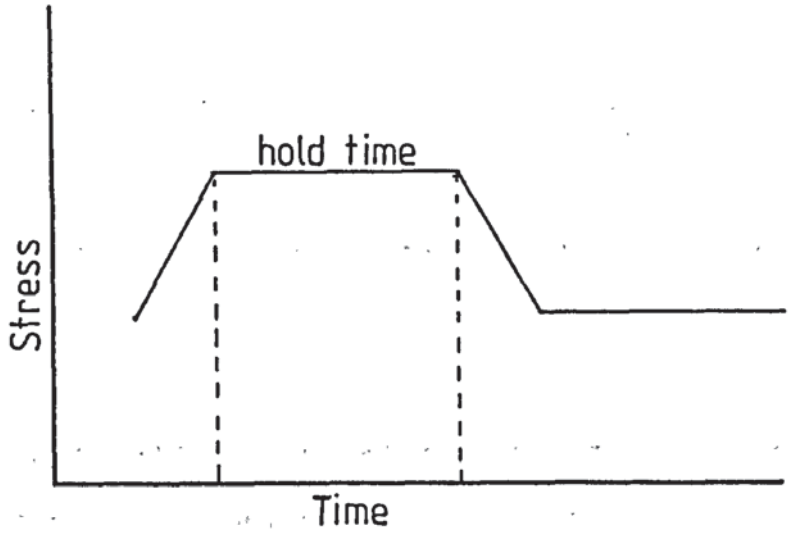

Figure 2.25 Waveform for modelling the service history of a turbine blade.

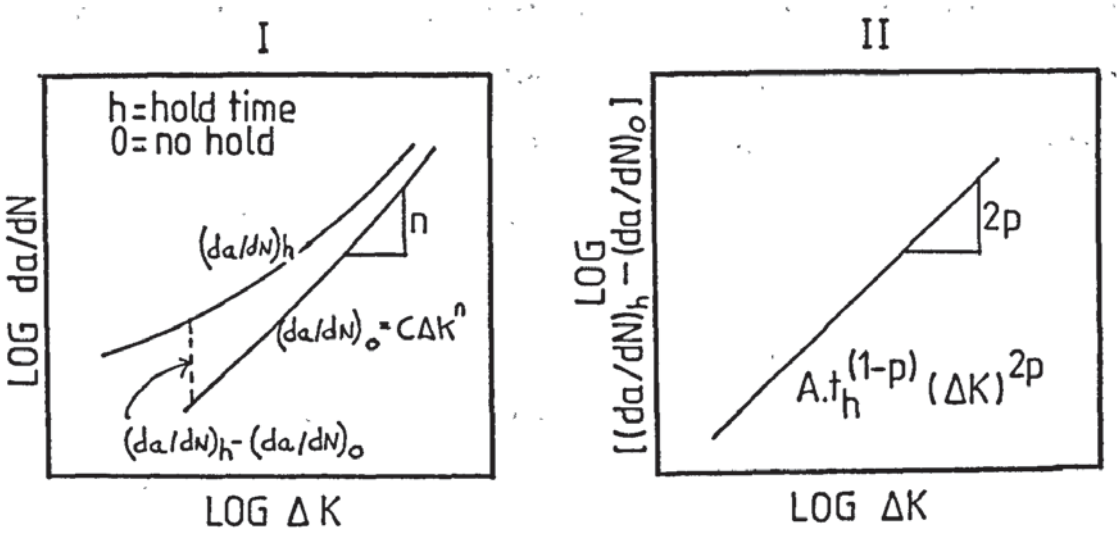

Figure 2.26 Determination of constants for equation 2.63 from reference (90).

For long hold times and high temperatures where creep is extensive, the authors modify equation 2.63 to:

$$\left(\frac{da}{dN}\right)_h = C(\Delta K)^n + A'(\Delta K)^p \cdot (t_h)^{1-p} + C'(C^*)^q (t_h - t_1) \quad (2.65)$$

Where t_1 represents the transition time for small scale to large scale creep (91).

The choice of parameter to model fatigue crack growth at high temperatures is dependent upon the physical properties of the material. For high creep resistant materials such as nickel-base superalloys crack growth may still be cycle dependent even with the presence of small hold times at intermediate temperatures and therefore ΔJ or ΔK may be acceptable.

If creep is not dominant, the choice between J or K will depend upon the reduction of yield stress with temperature and the size of the specimens, (ie the usable crack growth before general yield of the remaining ligament) for the load range used.

Where significant plasticity is encountered, the use of the elastic-plastic parameter for cyclic loading, ΔJ is to be preferred.

3. Experimental Procedure

3.1 The materials

Two nickel-base superalloy single crystal casting alloys supplied by Rolls-Royce Ltd: SRR 9 and SRR 99, were used for this experimental programme.

The compositions, as supplied by Rolls-Royce Ltd are presented in table 3.1. The material was supplied in the form of finished machined specimens in the heat treated condition. The heat treatments were as follows:

SRR 9 Solution treatment: 4 Hrs at 1300°C, Air cool.
Ageing treatment: 16 Hrs at 870°C.

SRR 99 Solution treatment: 1 Hr at 1280°C, 2 Hrs at 1290°C, 1/2 Hr at 1300°C, 1/2 Hr at 1305°C, then gas fan quench at greater than 100°C/min.
Ageing treatment: 16 Hrs at 870°C.

Table 3.1 Composition of material supplied by Rolls-Royce Ltd

	Element Wt%						
ALLOY	Cr	Co	Al	Ti	W	Ta	C
SRR 9	8.55	4.89	5.32	1.5	8.82	2.03	0.03
SRR 99	7.95	4.98	5.17	2.11	9.23	2.63	---
	Nickel Balance						

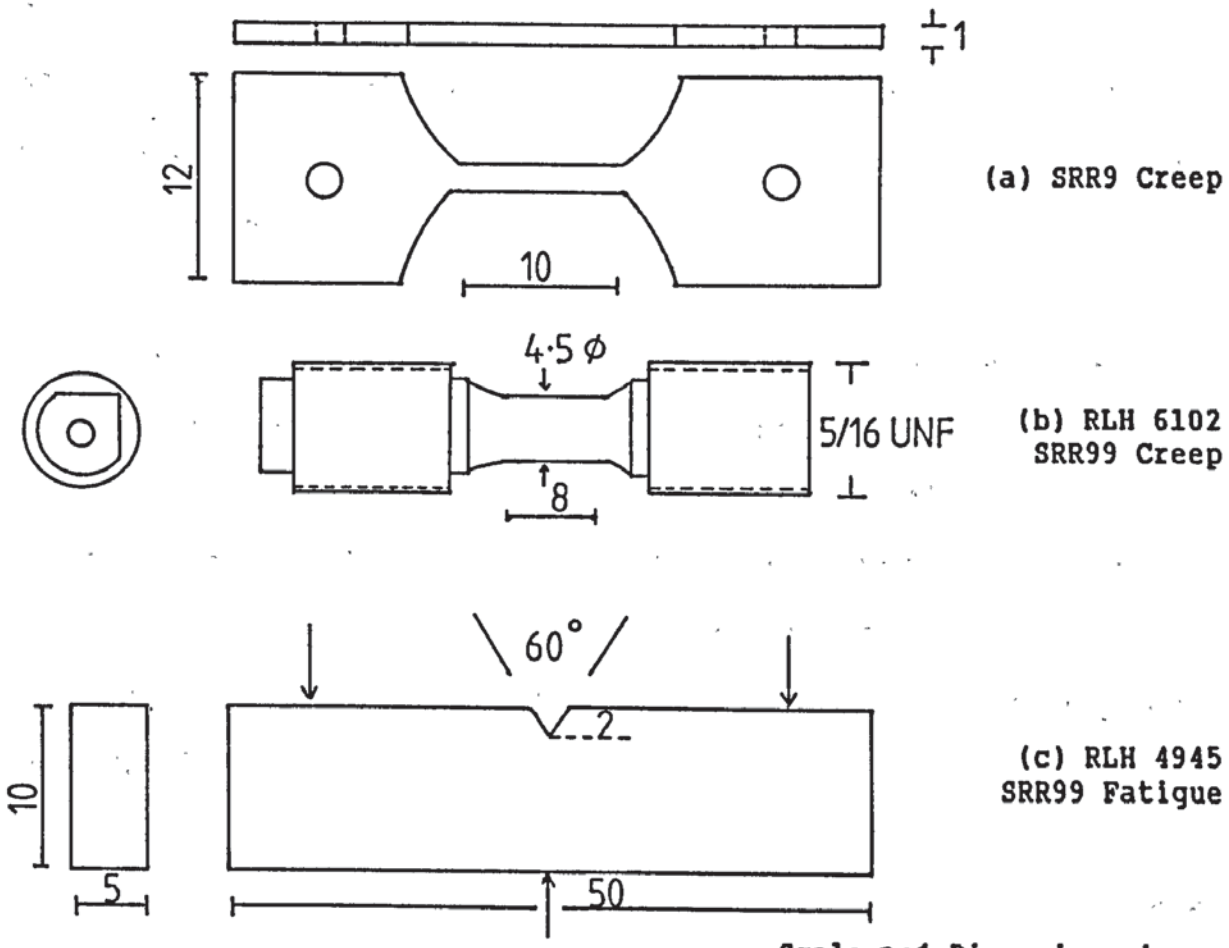

Figure 3.1 Test specimen geometries.

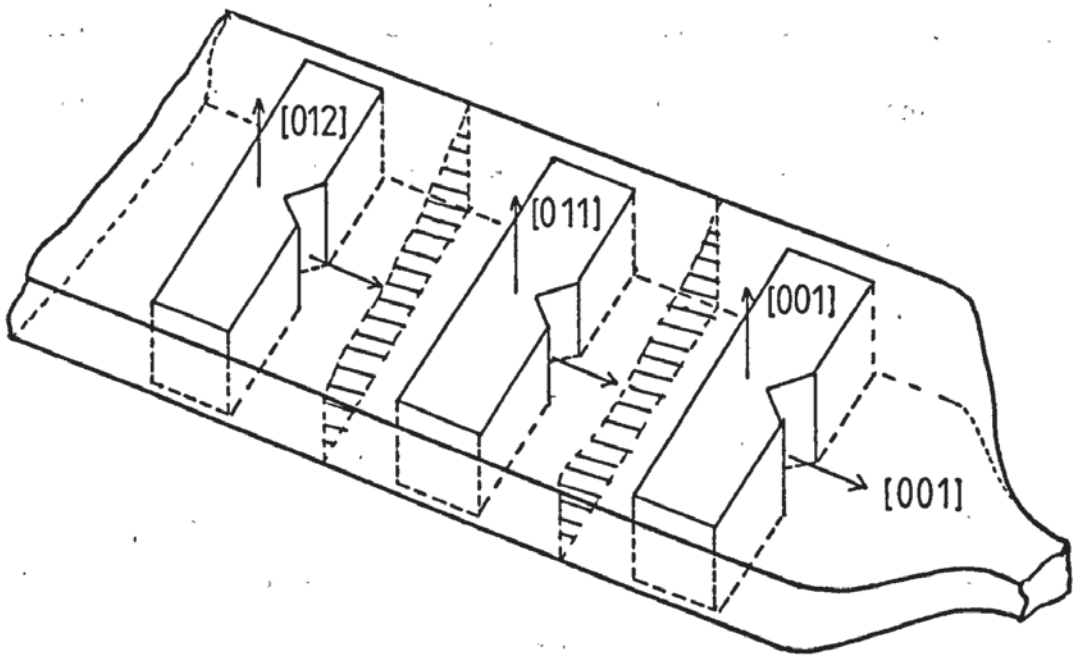

Figure 3.2 Chosen fatigue specimen orientations.

3.2 Specimen details

All single crystal specimens were cast and machined by Rolls-Royce Ltd, Elton Road, Derby. Three types of specimen were supplied, as shown in figure 3.2.

$2mm^2$ rectangular sectioned creep rupture specimens having a nominal tensile axis orientation of <001> were supplied in alloy SRR 9; an early development single crystal alloy based on Mar-M200, an investment casting alloy. These specimens were used for early experimental trials, and as a comparison to the latest development alloy, SRR 99.

$16mm^2$ circular cross-section, threaded, RLH 6102 creep rupture specimens with a nominal <001> tensile axis, were supplied in alloy SRR 99. The specimens have a three part identification, for example, DP2103 B1/2. The first term refers to the cast, B1 represents one of the cast bars in the mould, and 2 refers to the position of the specimen machined from the bar. Three specimens were machined from each bar, POS1 denoting the specimen nearest the pig-tail. An x-ray cylinder was produced from the end of the bar: a short square ended section with 90° locating flats matching those machined on the specimens. This is used to determine the tensile axis orientation for the bar in relation to the machined flats by use of 'SCORPIO', the computerised single crystal orientation analysis system used by Rolls-Royce Ltd.

Unnotched fatigue crack initiation and notched fatigue crack propagation specimens designated RLH 4945, were supplied by Rolls-Royce Ltd to the dimensions shown in figure 3.1c. The chosen orientations are shown in figure 3.2.

In some cases, the seed crystals failed and the orientation of the slabs were not sufficiently close to the desired orientation for the specimens to be cut normally. For each of the single crystal slabs which did not match the desired orientations, a stereographic projection was drawn using the values for the characteristic angles supplied using 'SCORPIO', as defined by Rolls-Royce Ltd; (92). This was accomplished by the manner shown in figure 3.3.

Firstly, the pole of the (001) was located using the values of γ and δ, then a great circle was drawn passing through the (001) pole to the position defined by the angle α. A construction line intersecting the (001) pole and the centre of the projection was drawn, and a position 90° from the (001) pole along the construction line was marked. The great circle corresponding to this position was then drawn. From the position X, a distance equal to the angle rho ρ is marked clockwise along the dotted great circle to define the pole of the (010). The corresponding (100) plane can be marked at the intersection of the great circles, as shown in figure 3.3. The (010) and (001) are linked with a great circle to complete the definition of the projection.

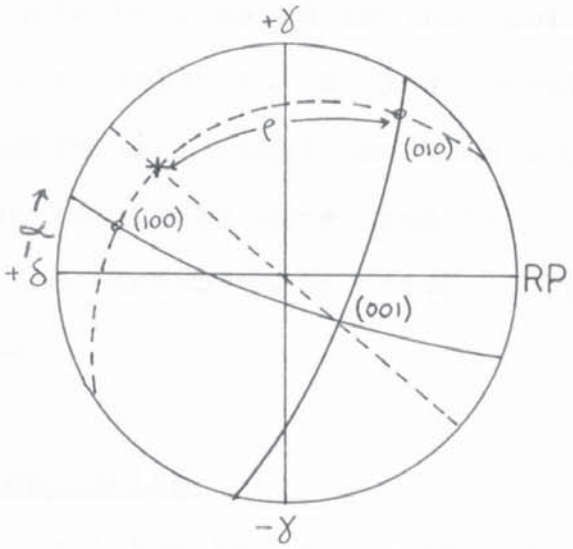

Figure 3.3 Construction of a stereographic projection from characteristic angles.

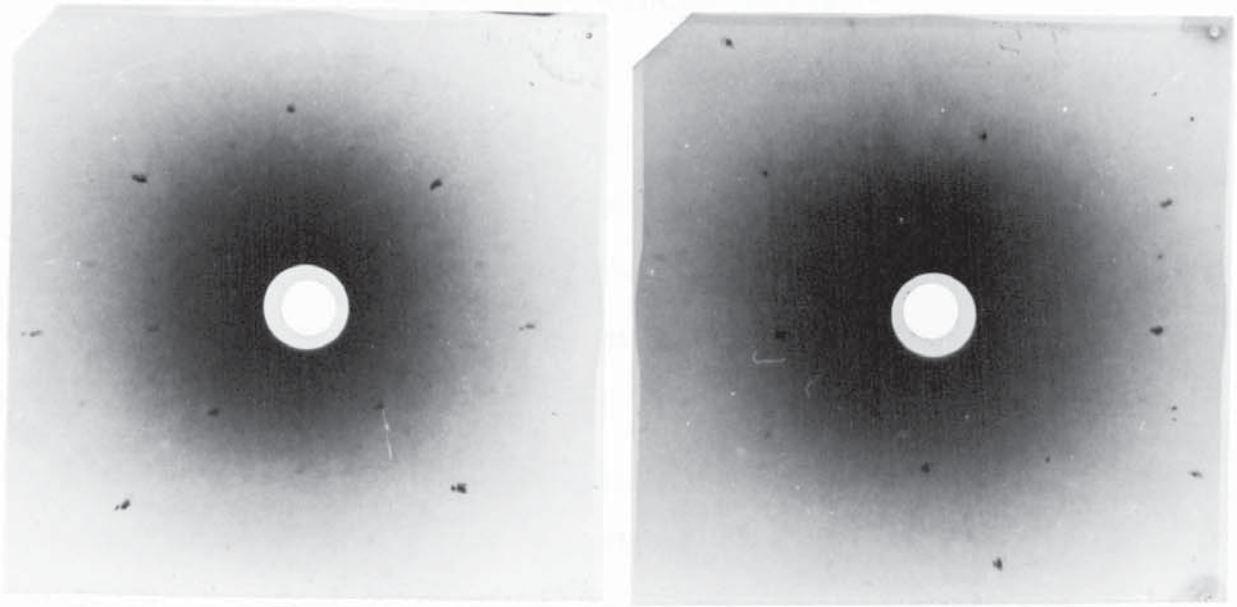

(a)<001> (b)<210>

Figure 3.4 Examples of Laue back reflection photographs

As the through thickness dimensions of the slabs used were close to the required specimen thickness, slabs were chosen which could be rotated to the correct orientation without a large rotation in the vertical plane. To produce the specimens, rotations were supplied to Rolls-Royce Ltd. The rotations were used to offset the slab in relation to the machining table prior to the manufacturing of the specimens.

3.3 Specimen preparation

Before testing, all the top face and a portion of the side face of both the notched and smooth fatigue specimens were electropolished. This was to facilitate Laue orientation analysis and to enable the investigation of fatigue crack initiation from a smooth surface. Electropolishing was also carried out on the gauge lengths of the two types of creep specimens in order to remove any surface defect which may give rise to local stress concentrations.

A 5% solution of perchloric acid in industrial methylated spirits was used for polishing, using a stainless steel beaker to act as the cathode. Due to the explosive nature of the solution, the temperature was maintained between 0°C and 15°C by the use of a bath of methylated spirits cooled by liquid nitrogen, and stirring of the electrolyte. A potential of 20 volts was used, giving a current density of approximately 1 A/cm^2, the specimens being polished for 1.5-2 minutes.

3.4 Laue single crystal orientation analysis.

Crystal orientation was determined by the use of the Laue back reflection x-ray method (55). In this method, a beam of white radiation is allowed to fall onto the crystal, thus fixing the Bragg angle θ for every set of planes in the crystal. Each set of planes diffracts the portion of the incident radiation with a wavelength which satisfies Bragg's law, equation 3.1, for the values of d and θ involved. The beams which are diffracted backwards are recorded on the film.

$$n\lambda = 2d \sin \theta \qquad \ldots\ldots (3.1)$$

These beams form an array of spots on the film, as shown in figures 3.4a and 3.4b. The spots can be seen to lie along hyperbolas. The spots lying on one curve are reflections from planes belonging to one zone.

Orientation is determined by finding the orientation of the normal to the planes causing each spot, as the plane normal always bisects the angle between incident and diffracted beams. The directions of the plane normals can be plotted on a stereographic projection, the angles between them measured, and the planes identified by comparison with a list of known interplanar angles for the crystal involved.

3.4.1 Film production

3.4.1.1 Specimen alignment

In the case of the $2mm^2$ stress rupture specimens and the RLH 4945 fatigue specimens, the specimen holder shown in figure 3.5 was used. This held the specimen parallel with the plane of the film and allowed the specimen to be rotated until the specimen long axis was vertical, ie parallel to the sides of the film. This was accomplished by use of a simple gauge.

When possible, the initial orientations of the RLH 6102 circular cross-section SRR 99 specimens were obtained from Rolls Royce Ltd, where the orientation was determined by use of the x-ray cylinder. If this information was not available or the specimen was to be used for crystal rotation analysis, then the following procedure was used.

The RLH 6102 creep specimens were aligned by placing them on a 3 axis goniometer with their gauge length parallel to the x-ray beam and the two locating flats (figure 3.1b) parallel to the edges of the film holder. Again, a simple gauge made from sheet steel was used to ensure the locating flats were square to the base of the x-ray unit and was also located at the correct height. As the specimens contained a centre drilled hole in each end, the specimen was aligned slightly below centre to ensure that the x-ray beam impinged on the electropolished annulus.

3.4.1.2 Producing the film

The unit was fitted with an x-ray tube containing a tungsten target and the filter dial on the tube tower was set to give no filtration in order to produce the widest range of wavelength and so produce the largest number of spots.

A piece of high contrast double sided x-ray film was loaded into the film holder with a piece of aluminium foil on either side, in order to reduce the amount of general fogging of the film by reflected x-rays. In order to reduce parallax error, the film was marked by removing the top right corner (when viewed from the specimen) and by an arrow at the bottom left of the film holder producing a shadow upon exposure. This defines the film in relation to the specimen and allows the film to be read from the correct side, that is the side nearest the x-ray source.

After placing the film holder in position and setting the specimen holder to give a specimen to film distance of 3cm, the film was exposed using a potential of 35 Kv and a current of 15ma for a period of 15 minutes.

The film was developed for a period of 4 minutes, washed for 1 minute, fixed for 2 minutes in standard hardener, then transferred into fixer containing hardener solution for a further 3 minutes. The film was washed using running water for 20 minutes then dried.

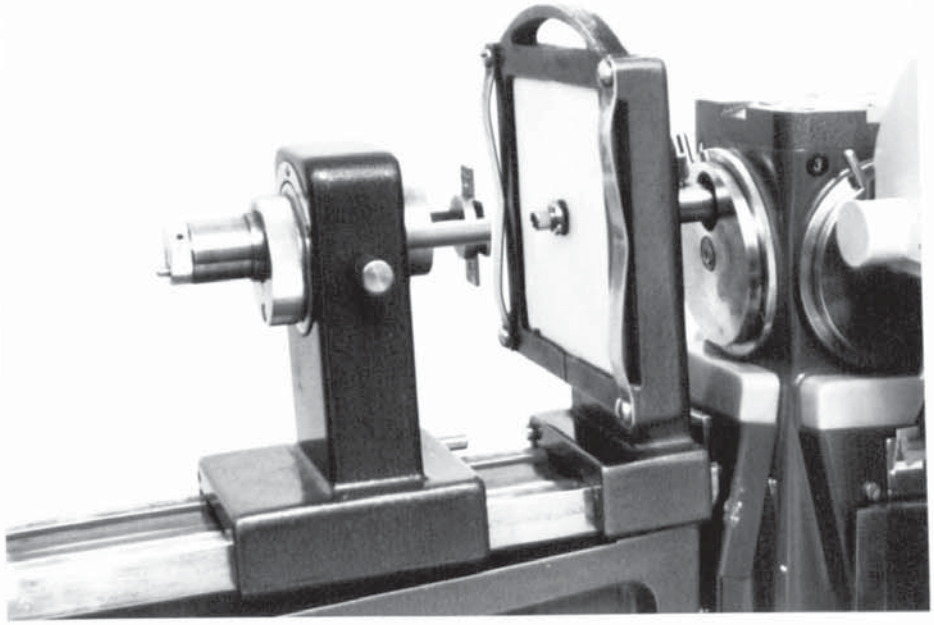

Figure 3.5 Back reflection Laue camera.

3.4.2 Analysing the film

Several techniques were utilised for the transfer of information from film to the stereographic projection.

The first technique is a graphical procedure introduced by Greninger (93), who developed a chart, when placed on the film gives values of γ and δ co-ordinates corresponding to any diffraction spots. The procedure which is well documented (55), is shown in figure 3.6

The second technique utilised the equations of Greninger (93) to enable digitised x,y co-ordinates for the spots to be converted into γ and δ values for the production of a stereographic projection. The program, written for a Tektronix 4020A computer, is given in appendix 1.

Once the γ and δ values had been obtained, they were transferred onto the stereographic projection by the procedure shown in figure 3.6 With the Wulff net oriented so that it's meridians ran horizontally, the position of each spot was marked. With the aid of the Wulff net and with reference to the hyperbolas observed on the film, great circles were drawn through the various sets of poles.

Indexing of the resultant projection was carried out by measuring the angles between several points and comparing the values with a table of interplanar angles for

cubic crystals, noting especially those points that lie 90°, 45° and 55° apart. Once the main spots (ie those at the intersection of two or more great circles) had been indexed, the angles between lesser points were checked to ensure correct indexing. As most of the orientations examined were close to three main orientations: <001>, <012>, and <023>, knowledge of the Laue patterns for these orientations as shown in figure 3.4 reduced the amount of trial and error needed to index the projections.

In the case of fatigue and RLH 6102 creep specimens, indexing gave directly the crack growth direction and the tensile axis respectively. However for SRR9 creep specimens, the Laue photograph was produced with the normal to the tensile axis in the direction of the x-ray beam and consequently the tensile axis of the specimen was at the top of the projection. By measuring the angle between the true tensile axis point and the [001] and [011] poles on the projection, the position may be transferred onto a standard cubic projection based on [001] by use of the [100] and [110] poles at the circumference of the projection, as shown in figure 3.7.

The position of the centre of the projection or tensile axis was related to the unit triangle which surrounded it. The position was given by it's distance from the [001], θ, and the angle from the [001]-[011] boundary, ϕ, in accordance with Rolls-Royce convention (92).

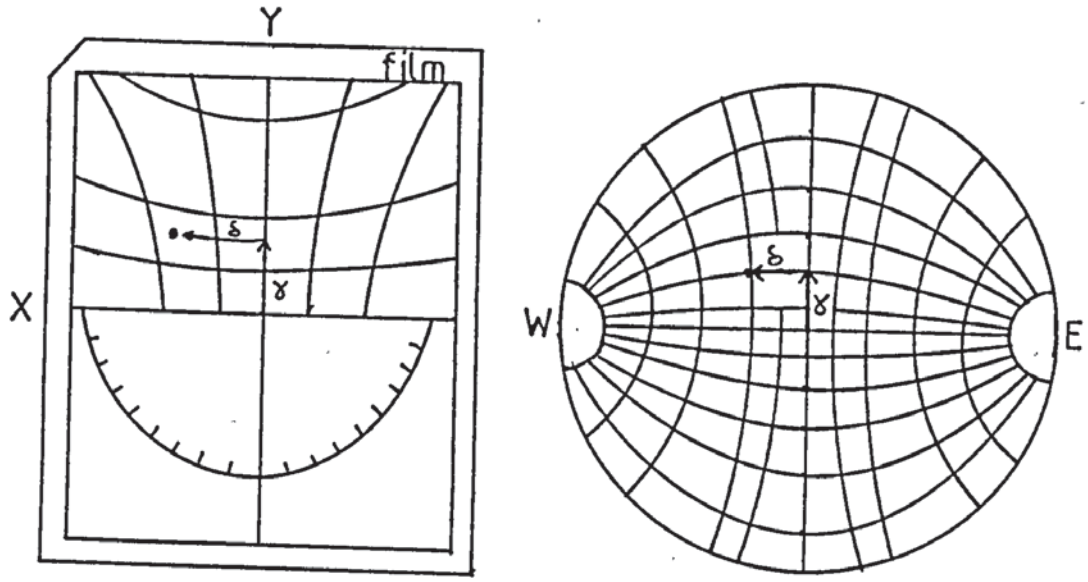

Figure 3.6 Plotting the pole of a reflecting plane onto a stereographic projection (55)

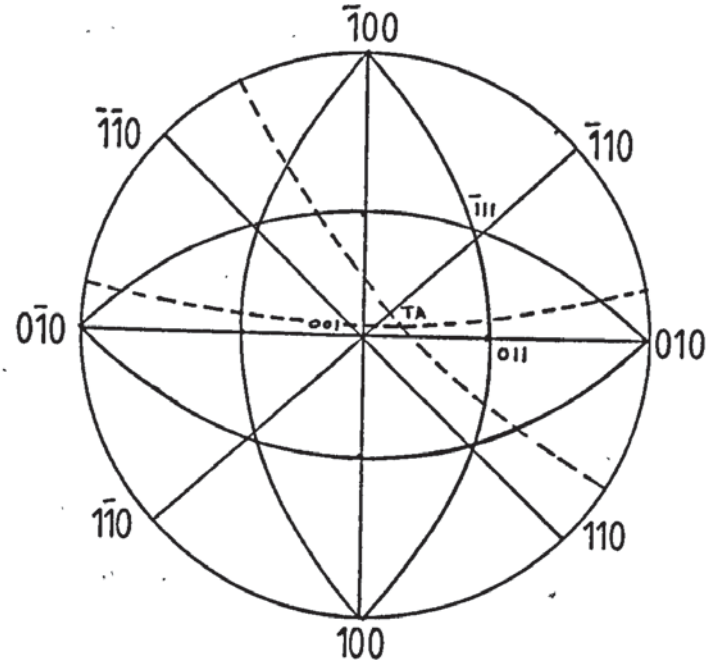

Figure 3.7 Determination of the tensile axis for SRR9 creep specimens.

A third technique was examined in the later stages of the project. In a recent paper, Kosel (94) discussed the use of computer programs for stereographic projection analysis and derived simplified equations for use in such programs.

By use of these equations, a program incorporating the film digitising technique has been produced and is presented in appendix 2.

The program allows immediate transfer of the spots on the film onto a stereographic projection and allows the user to specify the two points to be joined by a great circle. In this manner, a complete projection may be plotted.

Dummy indexing of the main points and great circle intersections (if a digitised spot is not present) by assuming the centre of the projection to be [001], enables the main angles needed for indexing to be printed by entering the number of the two points in question.

The program was designed to produce the hard copy of the projection with a diameter of 18cm, which is a standard Wulff net size and hence allows the projection to be indexed and checked by the conventional method.

3.5 Creep Testing

The specimen to be tested was measured to determine accurate dimensions for the width and thickness of the gauge length. The creep tests were carried out on a constant load, single lever creep testing machine with a lever arm ratio of 25:1. The load required was calculated as for the example below:

SRR 9 Creep specimen

Cross sectional area = Width x Thickness

$2.032mm^2 = 1.881mm \times 1.08mm$

For a stress of 850MPa, the loading is:

$850MPa \times 2.032mm^2 = 1727.23N$

But there is a lever arm ratio of 25:1, hence:

$1727.23N / 25 =$ 69.1 N loading

The specimen to be tested was placed in the grips of the machine, and the lower ram raised until the loading pan rested on the back of the of the machine, which was the loaded with the correct weights. Small weights were manufactured from lead sheet to obtain a precise weight, as any error may become significant when multiplied by the lever system. The specimen and grips were rotated until the gauge length was parallel to the observation window in the furnace wall. The furnace was then closed and the top and bottom openings of the furnace filled with Kaowool. The strain recording equipment was set up as shown in figure 3.8.

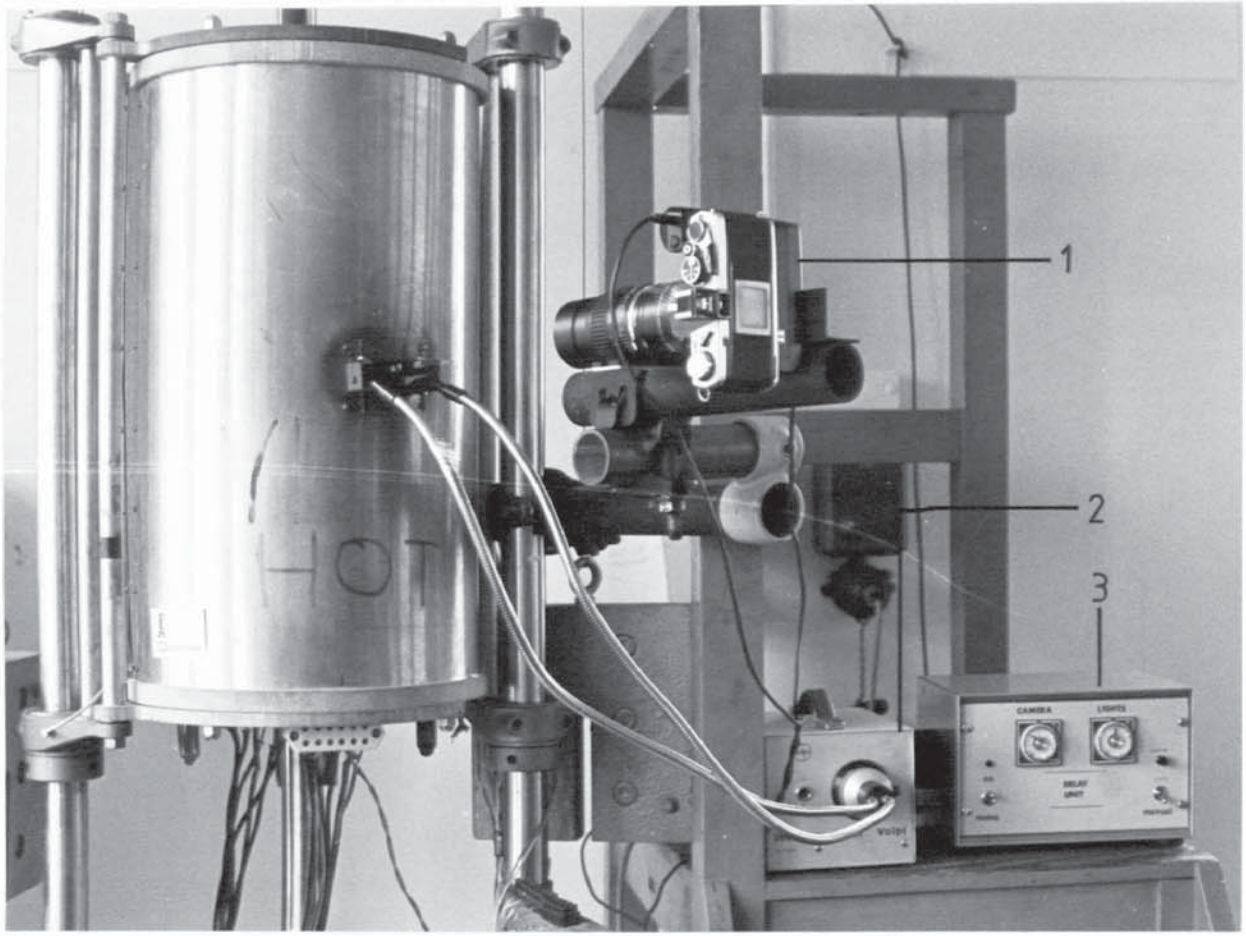

KEY

1. Camera unit
2. Light source
3. Electronic timer

Figure 3.8 Strain measuring equipment.

This equipment consists of:

(1) An Olympus OM2n camera fitted with autowinder, 135mm lens and extension tubes. This is attached directly onto the frame of the creep machine to avoid vibration and accidental movement.

(2) A twin boom fibre optic light unit, used to provide contrast between specimen and background, and to reduce exposure times.

(3) An electronic interval timer. This can be set to take one frame every 15 seconds to one frame every 30 hours. A second timer switches the light source on as the shutter is fired, for a period of 5 seconds. The equipment also provides power for the light unit and the camera's autowinder.

3.5.1 Creep testing procedure

Before use, the camera timer was adjusted to a selected time duration between photographs, dependent upon the expected time to rupture of the specimen. The creep furnace was switched on and allowed to attain a constant operating temperature for a period of 2 hours. The camera was then focused on the specimen and a photograph taken to record the specimen's initial gauge length.

The creep machine was then set to automatic, to slowly apply the load over a period of 5-10 minutes. A second photograph was taken as soon as the load was fully applied, to give a measurement of initial creep strain. The interval timer was then reset and the camera set to automatic. The equipment was left untouched until the end of the film or test.

3.5.2 Analysis of data

After the test, the film was processed and dried. In the case of flat SRR 9 creep specimens, a two stage process was employed. Firstlly, the film was placed in an enlarger and projected onto a piece of paper, then the position of the specimen shoulders were marked as shown in figure 3.9. Secondly, the distance between the shoulders imaged on each negative was measured using the digitising tablet of the Tektronix 4020A computer. For each specimen, readings were taken at the top, middle and bottom of the marks, an average of the three results being taken as the final value.

For the SRR 99 RLH 6102 specimens, the lengths were measured directly from the negatives by use of a Nikon Measurescope. Photographs of the recorded data are shown in figure 3.10, and the Nikon Measurescope is shown in figure 3.11.

True strains were calculated using the distance measured in frame 1 as L_o. Creep curves of true strain versus time were produced from the data.

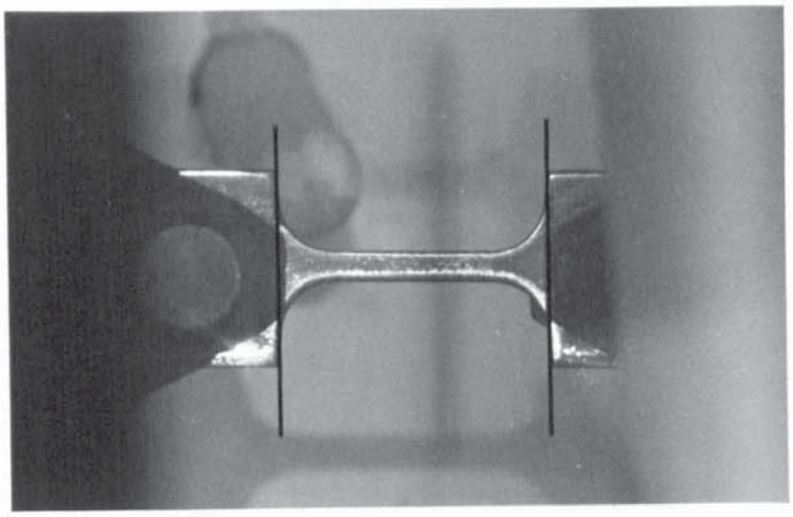

9L/4
L_o

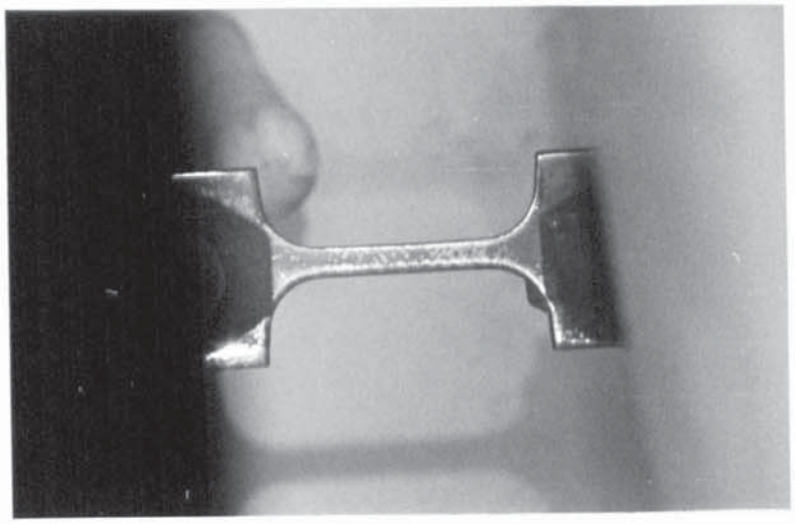

8Hrs

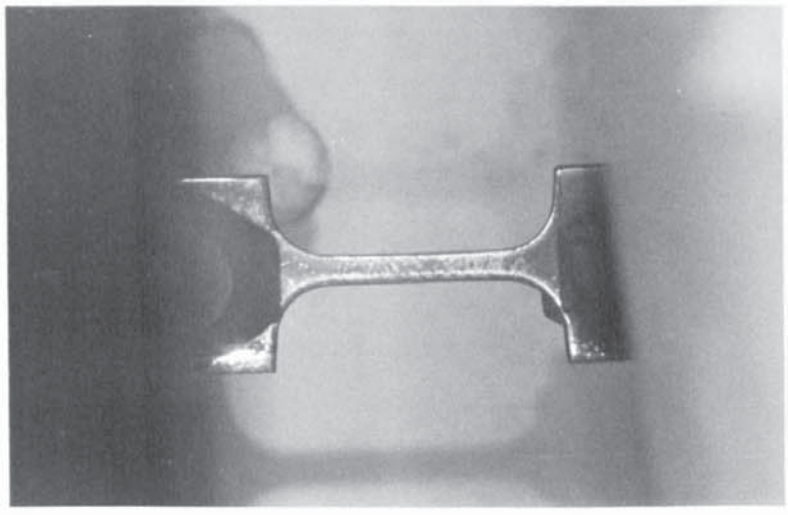

16Hrs

Figure 3.9 Measurement of strain from photographs for SRR9

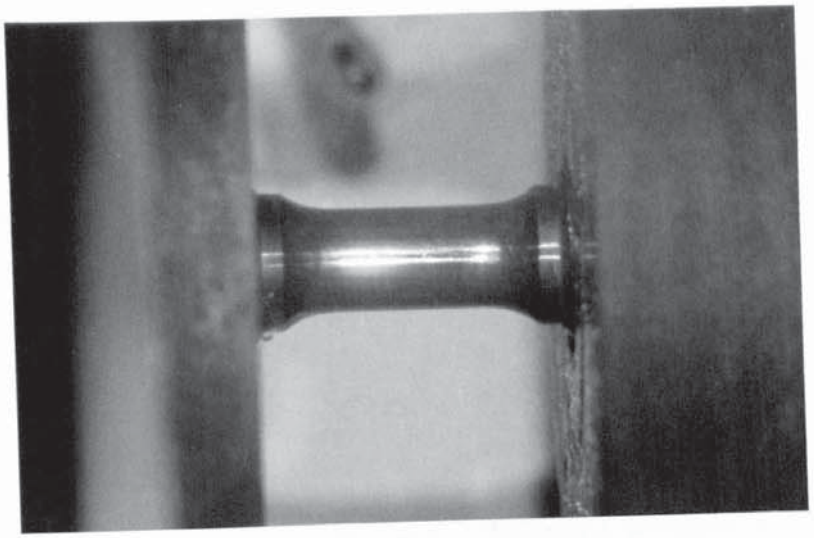

DP2103 F3/1

L_o

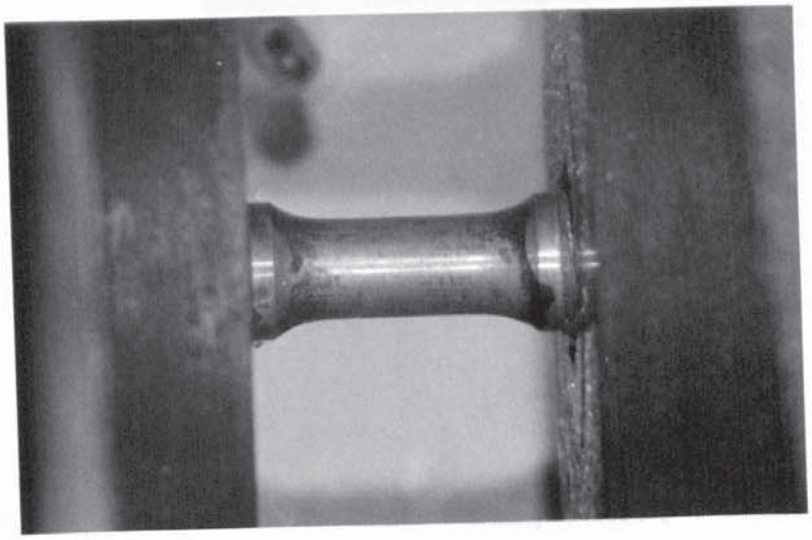

45 Hrs

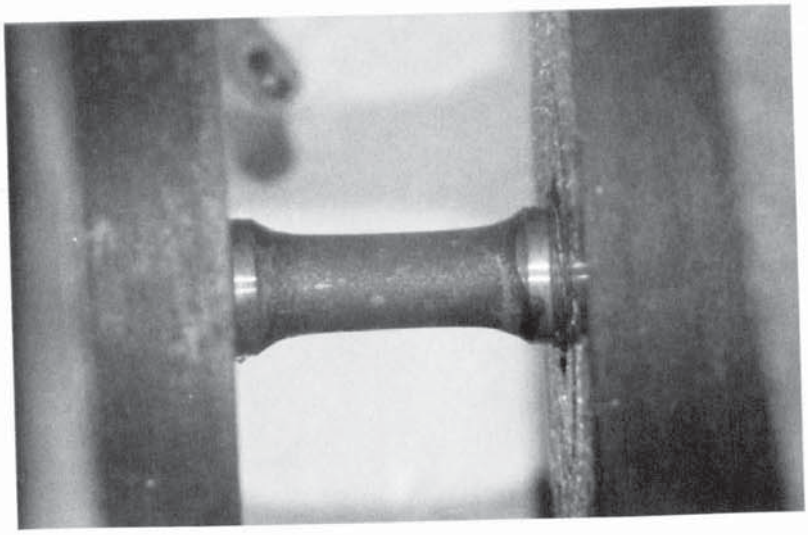

90 Hrs

Figure 3.10 Measurement of strain from photographs - SRR99

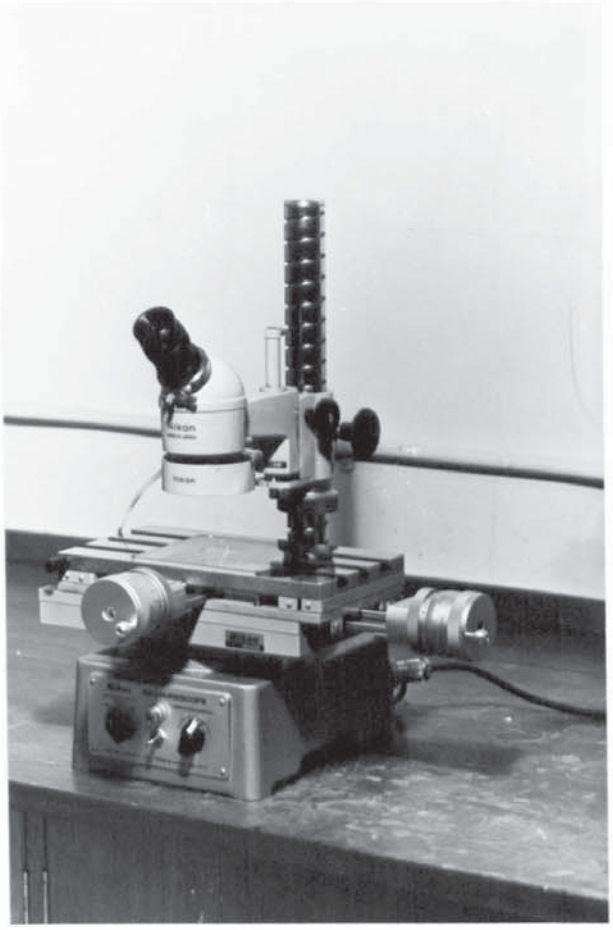

Figure 3.11 Nikon Measurescope used for film measurement

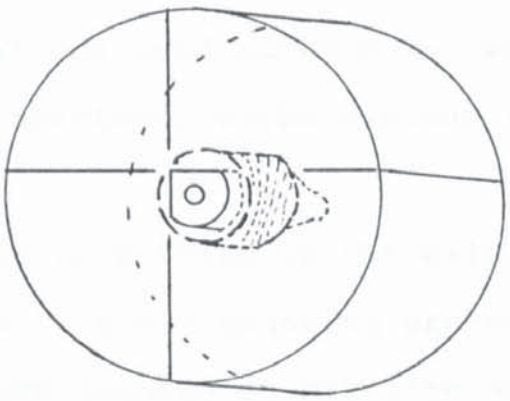

Figure 3.12 Schematic of mounted SRR99 specimen for rotation analysis

3.6 Crystal rotation analysis

For flat SRR 9 specimens; oxide was removed from the gauge length of one half of the broken specimen, by light manual polishing, care being taken not to distort the crystal. A Laue photograph was produced from a region on the gauge length a few millimeters away from the fracture, with the crystal in the same orientation with respect to the film as the initial Laue photograph.

The position of the tensile axis after deformation was superimposed onto the unit triangle containing the initial tensile axis position; the direction of rotation was then examined with respect to possible slip systems.

In the case of RLH 6102 SRR 99 specimens, the fracture surface of the half of the specimen containing the locating flats was removed by electro-discharge machining and retained for metallographic examination. The flat surface of the specimen was then ground and polished to a 1μm finish, then electropolished. Care was taken to ensure that the final polished surface was well within the gauge length of the specimen, where maximum rotation would occur.

Difficulty in setting up the half specimen on a 3-axis goniometer led to a new mounting procedure being developed. The specimen was mounted in bakelite using a Metaserv hot mounting press with it's polished end face on the ram ie visible after mounting.

As the specimen was screwed into a square sectioned holder for electro-discharge machining, this ensured that the specimen would be aligned vertically in the mounting compound. The back of the mount was lathe machined until the locating flats became visible. These locating lines were extended to the end of the back face by use of a scribing block and vee block.

The mounted specimen was the placed into position on the x-ray set by use of the specimen holder shown in figure 3.5, the specimen being rotated until the locating marks were square to the film. The mounted specimen is shown schematically in figure 3.12.

3.7 Smooth bar fatigue testing

Smooth bar fatigue testing was carried out using un-notched RLH 4945 specimens with electropolished top surfaces. Three specimen orientations were tested, as shown in figure 3.2. Testing was carried out in three point bending in air at temperatures of 750°C and 850°C, with a sinusoidal waveform having a stress ratio R, of 0.1 and a frequency of 40 Hz.

After preliminary trials it was discovered that the use of D.C potential drop for crack initiation monitoring was not desirable due to the tendency for initiation from the spot welds connecting the monitoring wires. Testing was therefore carried out to specimen failure.

The testing equipment is shown in figures 3.13 and 3.14. Sintered alumina rollers were used in order to prevent flattening of the contact area due to the influence of temperature and load, and also to provide insulation of the specimen from the test rig when potential drop (P.D) crack monitoring is used. Two thermocouples were used. The bottom thermocouple was connected to the three zone furnace controller, the top thermocouple was connected to an over-temperature policeman. Both were connected to a multi-channel temperature indicator in order that the temperature range across the specimen could be monitored. The furnace zone controls were adjusted to reduce the temperature range across the 12cm gap between the thermocouples to 5-8°C.

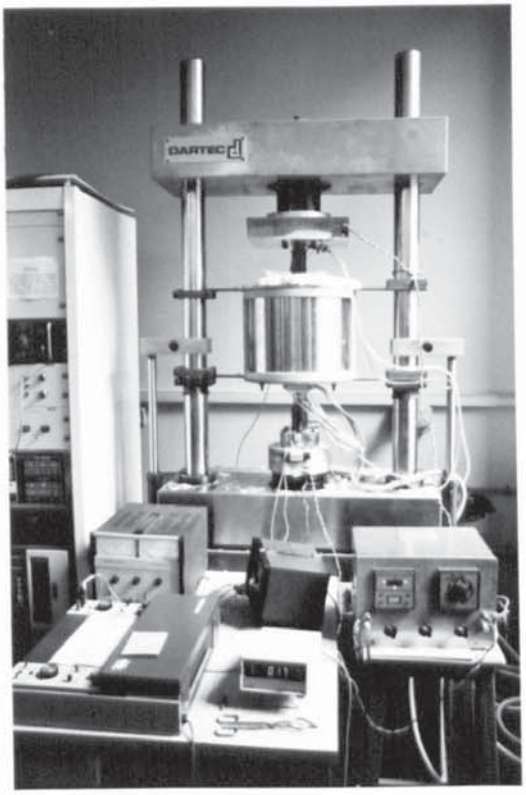

Figure 3.13 Dartec servohydraulic fatigue machine and D.C potential drop crack monitoring equipment

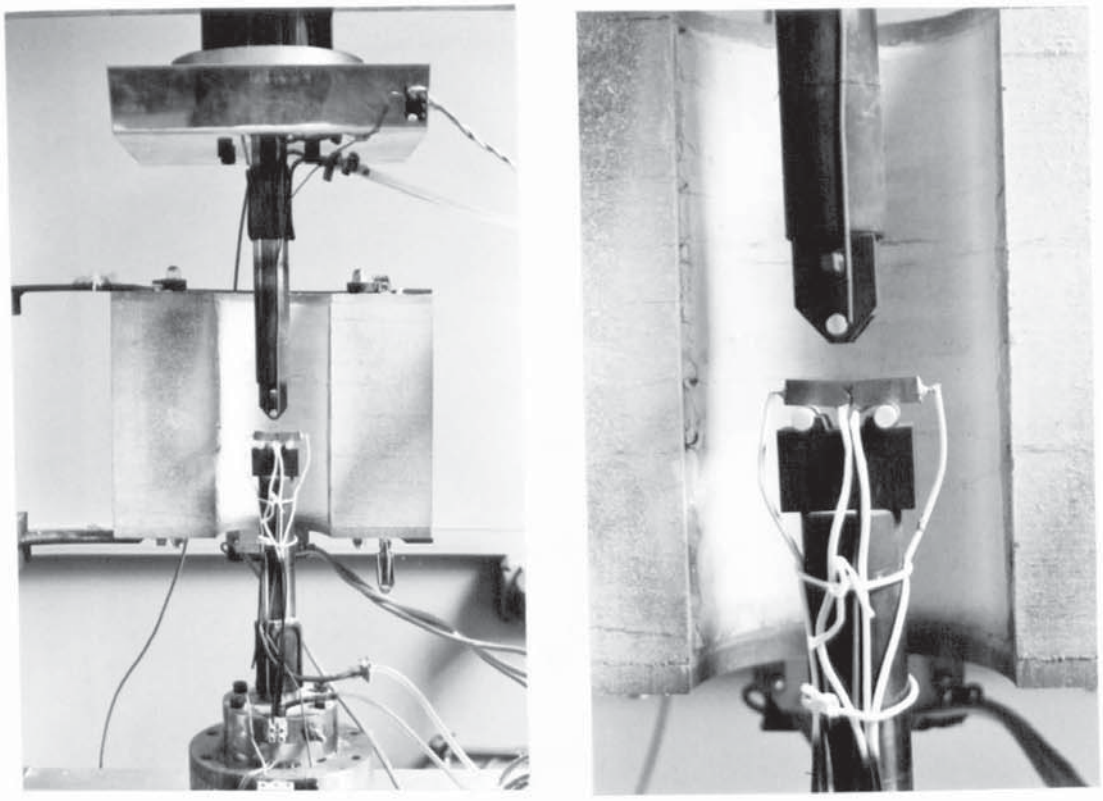

Figure 3.14 3 point bend rig and thermocouple positio

Copper cooling coils were used around the IN 108 columns to prevent conduction of heat to the load cell, and a heat shield was used to prevent convection.

The testing procedure was as follows. The specimen was placed centrally on the base of the bend rig. The machine was set to straining unit and the ram raised until contact was made with the top rig, the machine limiting the applied load to 1KN. The load was reduced manually until the specimen could be moved and the specimen was repositioned to ensure central loading. The control mode was changed to load control and the load increased to 2KN. The furnace was closed and the openings were filled with Kaowool. The cooling water and furnace was switched on. The stress range required was calculated by using classical bending theory:

$$\frac{\sigma}{Y} = \frac{M}{I} \qquad \ldots\ldots (3.2)$$

For three point bending:

$$\text{Moment} = M = \frac{PS}{4}$$

Where S = full span = 30.31mm

$$\text{Second moment of area} = I = \frac{BW^3}{12}$$

$$\text{Neutral axis} = Y = \frac{W-a}{2}$$

Substituting the above into equation 3.2 gives:

$$\Delta\sigma = \frac{3\Delta PS}{2B\ W^2} \qquad \ldots\ldots (3.3)$$

The maximum and minimum load values were calculated by using an R value of 0.1 and the fact that $\Delta P = P_{max} - P_{min}$ and that :

$$\frac{P_{max}}{P_{min}} = R = 0.1 \qquad \ldots\ldots (3.4)$$

After the furnace had reached a stable temperature, the load was increased to maximum load and then back to mid-load manually in order to ensure free movement of the ram. The required maximum and minimum loads and trip conditions were entered via the computer terminal and the machine was switched to load controlled cyclic mode. The load was monitored using the computers terminal display of the actual maximum and minimum loads, and corrections were made to the load gain and bias controls until the actual values matched those desired.

The test was terminated on failure of the specimen, the machine automatically tripping on sudden change of compliance or ram displacement. The cycles to failure were read from the computer terminal.

3.8 Fatigue crack propagation testing

Notched RLH4945 specimens of the dimensions shown in figure 3.1c were used, the nominal root radius being 0.076mm giving an approximate Kt value of 6.

Three transverse orientations, as shown in figure 3.2 were tested using temperatures of 750°C and 850°C . Two waveforms were utilised. Firstly, the standard Rolls-Royce trapezoidal waveform, consisting of a 0.4 second rise time, a hold time at maximum and minimum load of 1.6 seconds and a decay time of 0.4 seconds. Secondly, a triangular waveform of 0.4 seconds rise, 0.4 seconds decay time was use to produce base line data for the comparison of hold time effects.

Due to the size limitations imposed by the investment casting process, and the internal bore of the furnace; the three point bend specimens could not be made long enough to conform to standard stress intensity calibrations, and the following methods were used to develop an accurate K-calibration for the specimen geometry.

3.8.1 Stress intensity calibration

A stress intensity (or K) calibration was produced for three point bend specimens by use of 'PAFEC', a finite element program running on a Vax-B minicomputer. The analysis was conducted using a two dimensional idealisation and plane strain conditions, using the mesh and program shown in Appendix 3.

The analysis was carried out on two specimen sizes; the first having a half span to width ratio of 3:1 to model the fatigue specimens obtained; the second with a ratio of 4:1 to enable the calibration to be compared with standard published calibrations (95,96). The value of K for the inputted material constants and load was obtained by using the displacement of the node immediately behind the crack tip position in the UY direction (see figure A3.1). The displacement is related to K by Westergaard's equations (71); transposing equation 3.5 :

$$U = \frac{K_I}{G}\left[\frac{r}{2\pi}\right]^{\frac{1}{2}} * \cos\theta\,[\,2-2\nu + \sin^2\theta/2] \quad ....(3.5)$$

For $\theta = 180°$

$$U = \frac{K_I}{G}\left[\frac{r}{2\pi}\right]^{\frac{1}{2}} * (2-2\nu) \quad ..... (3.6)$$

Now, using the fact that $G=E/2(1+\nu)$:

$$K_I = \frac{UE}{4(1-\nu^2)} * \left[\frac{2\pi}{r}\right]^{\frac{1}{2}} \quad ..... (3.7)$$

Where r and θ are defined in figure 2.18, E is Young's modulus and ν is Poisson's ratio. U is the displacement of the node immediately behind the crack tip in the Y direction.

3.8.2 Fatigue crack monitoring by the direct current (D.C) potential drop system.

Several methods are available for detecting fatigue crack initiation and measurement of a growing crack. These are:

1) Optical measurement
2) Acoustic emission
3) Strain gauges
4) Ultrasonic measurement
5) Plastic replica techniques
6) Electrical potential methods

Crack monitoring at elevated temperatures precludes the use of acoustic emission, ultrasonic and strain gauge techniques due to the difficulty in obtaining probes capable of withstanding high temperature.

Plastic replica techniques may only be used by interruption of the test, producing temperature cycling effects. Also the build up of oxide on the surface of the component will lead to difficulties in obtaining accurate results.

The most popular technique in early, high temperature fatigue investigations was optical measurement by travelling microscope. This is only effective on large size specimens, where crack growth occurs over several millimetres, due to the resolution of the measuring system.

There are also the added problems of oxide build up on the surface of the specimen, and the introduction of a viewing port in the furnace wall without creating problems with temperature stability. In these conditions, the electrical potential drop technique offers a more convenient and sensitive technique with the added advantage of continuous and automatic monitoring of crack length.

The direct current electrical potential method is based on the fact that a growing crack in a metal body alters the potential distribution. By passing a constant current through the specimen, the change in potential distribution may be measured in terms of the potential difference across the crack faces. A calibration may be established relating the potential difference to the instantaneous crack length. The calibration may be produced experimentally (98), or by theoretical methods (99,100).

3.8.2.1 Crack measurement procedure

A schematic of the circuit used is shown in figure 3.15, and can be seen in figures 3.13 and 3.14. The specimen was electrically insulated from the test machine by the use of ceramic rollers. A direct current of 1 ampere was introduced by use of 1.5 mm diameter Nichrome wires spot welded onto the end faces of the specimen, supplied by a Farnell 12V/10 A bench power supply. The potential was measured by 0.25 mm. 80 wt% Ni / 20 wt% Cr wires welded either side of the notch, as shown in figure 3.15.

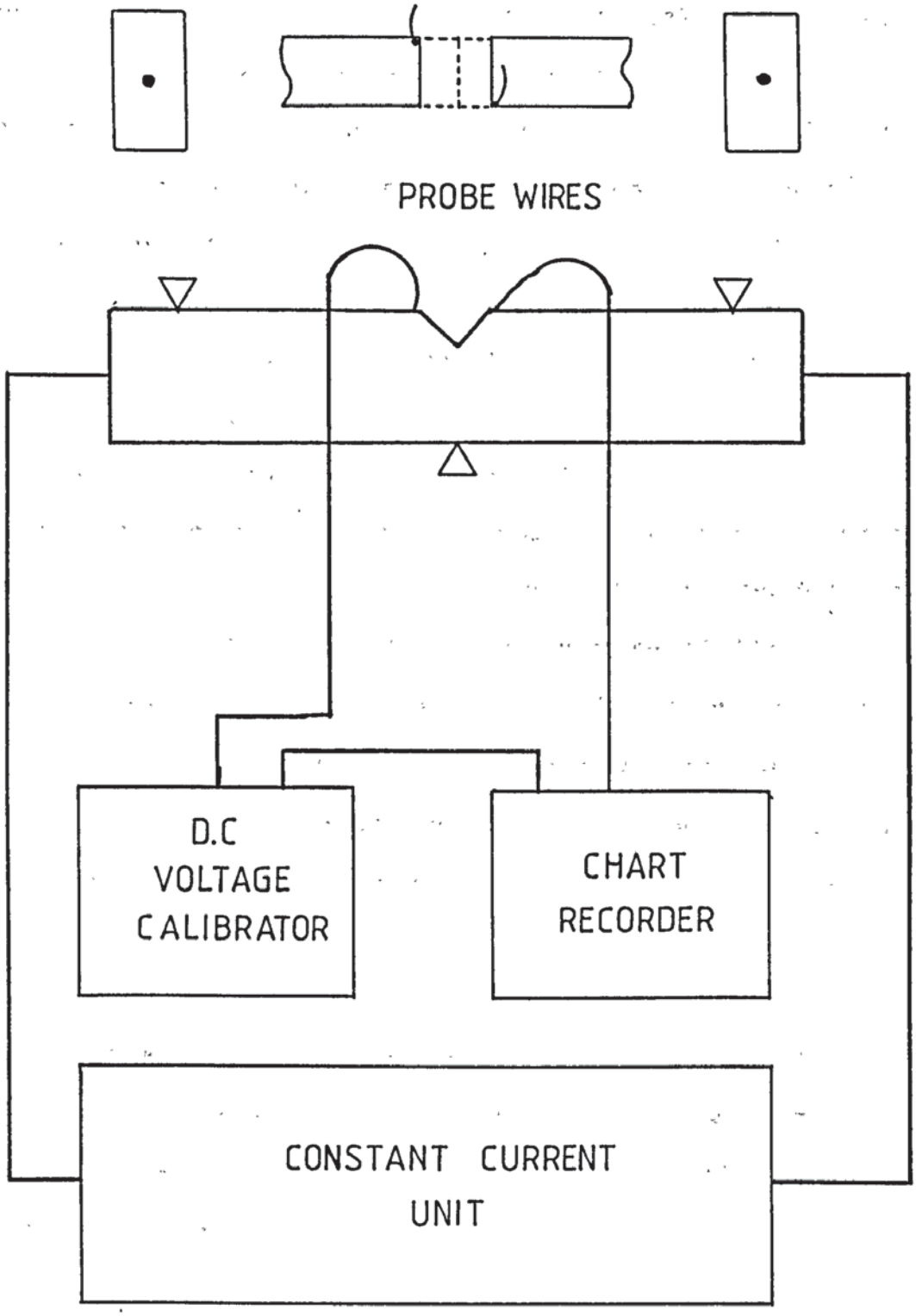

Figure 3.15 Circuit diagram for the potential drop crack measurement system

The electrical potential from the probe wires was measured using a D.C chart recorder (Tekman 200) which has a maximum sensitivity of 0.5μV and a 50μV full scale deflection. In order that the maximum sensitivity of the chart recorder could be used, the potential was opposed by a voltage from a voltage calibrator (0.006% grade)

A potential drop calibration was produced by spark machining 0.2mm wide slits into notched RLH 4945 specimens to give a range of a/W from 0.2 (unnotched) to 0.7. Measurements were taken at room temperature, after allowing time for the specimens to reach a stable temperature, and at 750°C and 850°C. The results were plotted as suggested by Saxena (88) and Johnson (100) in terms of $\Delta a/a$ against $\Delta V/V$, where V is the initial voltage from an initial crack length a, taken to be the length of the notch. ΔV is the change in potential caused by a change in crack length of Δa.

3.8.3 Fatigue crack propagation testing procedure

The load range for propagation tests was calculated by first estimating the value of the threshold stress intensity factor range ΔK_{th} (101) :

$$\Delta K_{th} = 0.9 \times \sigma_{uts} \cdot \sqrt{\rho} \qquad \ldots\ldots (3.8)$$

The equation is obtained for structural steels having a yield strength between 400-1000 MPa tested under 3 point bending at a stress ratio of 0.1.

Using values for SRR99 of σ_{uts} = 1111 MPa, ρ = notch root radius = 0.076mm gives a threshold stress intensity factor range of approximately 9 MPa$\sqrt{m}$.

The minimum load range however was found to be determined by the control limit of the fatigue machine. As a servohydraulic machine with a 100KN capacity was used for the tests, difficulty was encountered using small minimum loads, due to the inability to maintain a constant load range and machine tripping . It was decided to use a starting ΔK value of approximately 20 MPa$\sqrt{m}$.

The specimens to be used were measured using a micrometer and the initial notch depth was measured by use of a Nikon shadowgraph giving a magnification of 50X. As the crack was allowed to grow a short distance away from the notch root to avoid stress intensity effects, the initial crack length was assumed to be approximately 2.06mm; ie an a/W of 0.206.

Using the Pafec calibration (figure 4.26):

$$\Delta P = \frac{\Delta K_I \, BW}{Y'} \qquad \ldots\ldots (3.9)$$

Where Y' is a function of a/W = 0.26

hence:

$$\Delta P = \frac{20 \times 0.005 \times 0.01}{0.265}$$

$$\Delta P = 3.8KN$$

Now stress ratio R = 0.1

So $\frac{P_{min}}{P_{max}} = \frac{0.42KN}{4.2KN} = 0.1$

Gives a ΔP of 3.78KN.

The specimens were installed in the machine as shown in figure 3.14 and as described in section 3.7. The potential drop measuring equipment was switched on with the furnace to allow the components to achieve a stable operating condition. Testing was started when a stable temperature had been achieved, tests being carried out at 750°C and 850°C.

Initiation of a fatigue crack was carried out using a sinusoidal waveform with a frequency of 40Hz, using a Maximum load of 0.28-3KN ie slightly less than the propagating loads to avoid having to re-initiate the crack through the plastic zone. As the machine had to be stopped to allow the waveform to be changed for the propagation tests it was found that the crack had to be grown to give a deflection of approximately 15-20μV which is equivalent to a crack length of 0.6mm in order that propagation could be recommenced without re-initiation.

When the machine was stopped, the waveform to be used was programmed into the computer using the 'ramp at rates' option and the machine load gain and bias controls altered for the new frequency. The two propagation waveforms are shown in figure 3.16 together with the resultant

frequencies. The stress ratio used for all tests was 0.1. During propagation testing, regular readings were taken of the top and bottom temperature readings for the chamber, the maximum and minimum loads and the number of cycles. These readings were marked on the Tekman chart to act as a check of accuracy and an indication of the conditions throughout the test. The test was stopped on failure of the specimen or upon indications of yielding by a change of compliance or fluctuation in the potential drop reading.

The results were analysed by use of a 7 point polynomial data reduction technique recommended by the American society for testing and materials (102), incorporating an experimental potential drop calibration to convert potential values into crack length, and a Pafec finite element theoretical stress intensity calibration. The program is listed in Appendix 4. Graphs of increment in crack growth per cycle da/dN versus the stress intensity factor range ΔK were produced from the data satisfying linear elastic fracture mechanics conditions.

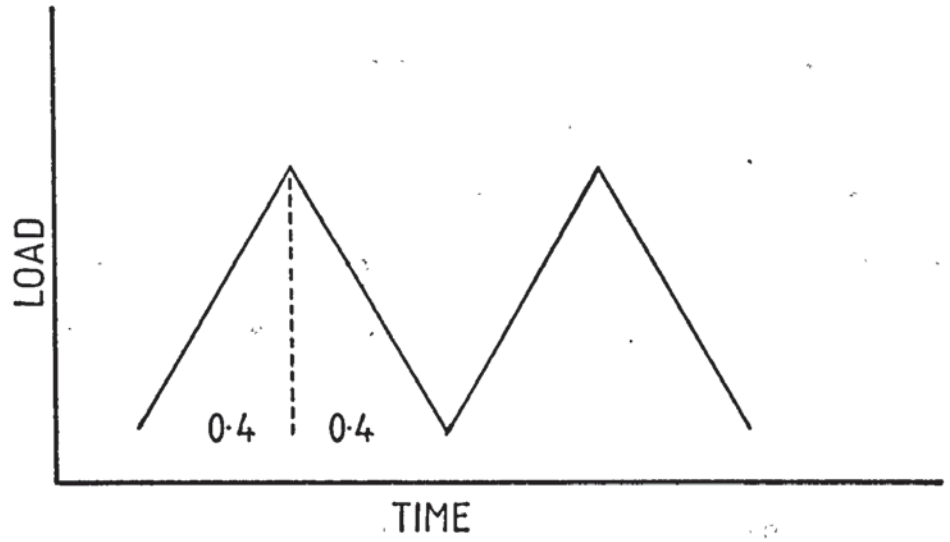

a) 1.25Hz Triangular waveform (no hold time)

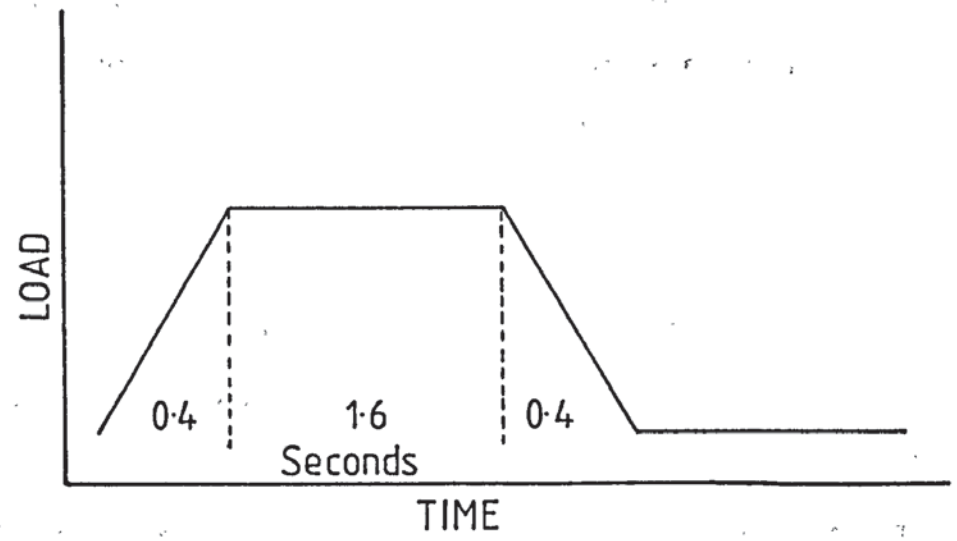

b) 0.25Hz Rolls-Royce trapezoidal waveform

Figure 3.16 Fatigue propagation waveforms

3.9 Metallography and fractography

Samples of the two alloys were prepared to a 1μm diamond polish and etched in a solution of 33% nitric acid, 33% acetic acid, 33% water and 1% hydroflouric acid, for a period of 30 seconds to 1 minute. The specimens were then examined using a scanning electron microscope. In some cases, areas were investigated using a Link system energy dispersive x-ray analysis unit in semi-quantitative mode to identify elements present and give an indication of their concentration.

The fracture surfaces of creep, and fatigue propagation specimens representing each testing condition were examined in the scanning electron microscope.

The fracture surfaces of the smooth bar fatigue specimens were photographed by use of a camera with fitted bellows attachment. As the fracture surfaces were found to be faceted, analysis of the facet orientations was undertaken.

3.9.1 Two trace analysis of crystallographic facets

The specimens were examined by use of a Reichart inverted stage microscope having a angular scale around the stage. Viewing the specimen on a projection screen containing grid lines, the specimen was rotated until the angle between the side face and the facet was traversed. The same procedure was carried out for the same facet and the top face of the specimen.

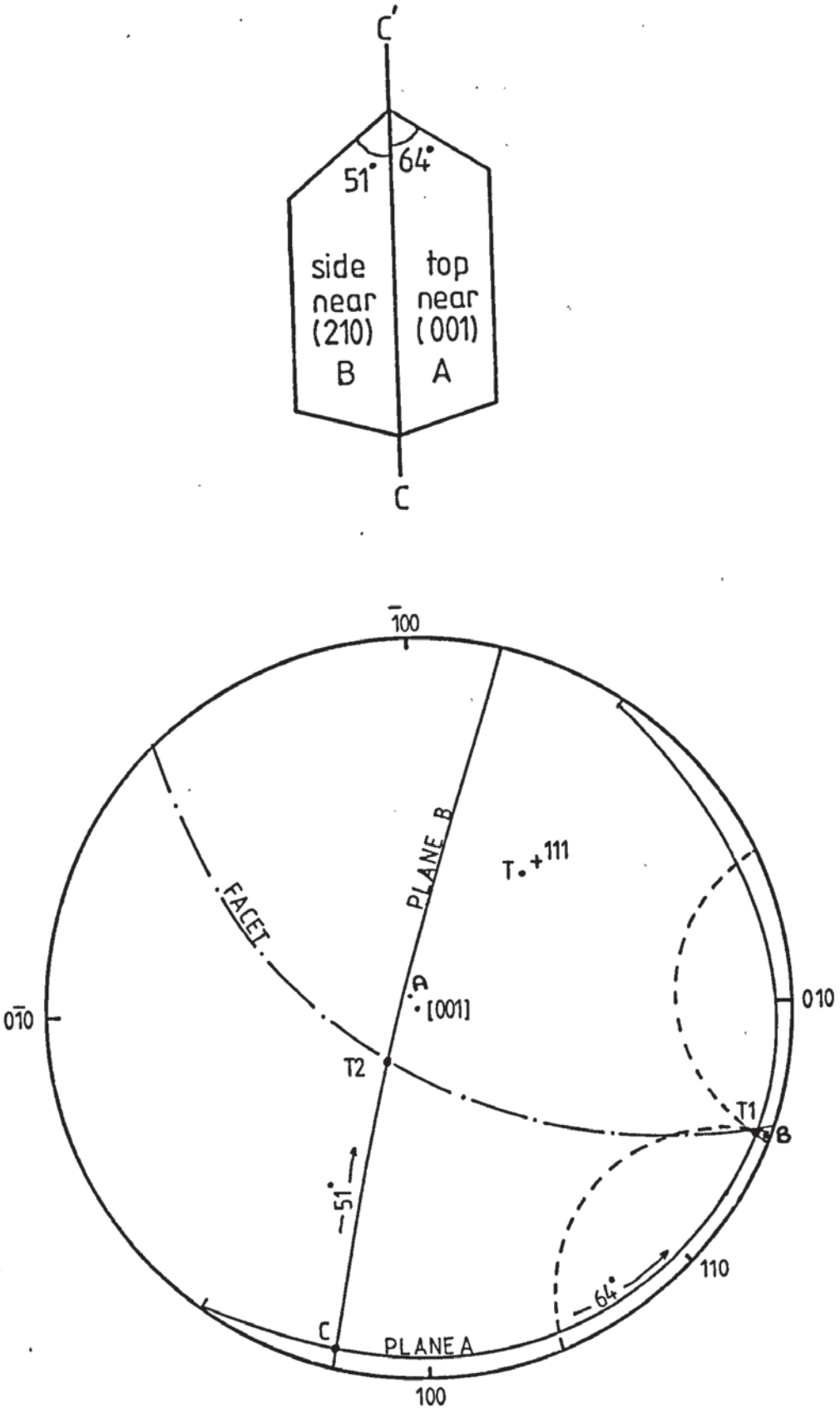

Figure 3.17 Use of two trace analysis to identify orientation of facet

Knowledge of the Miller indices of the side and top face of the specimen enabled the orientation of the facet to be determined (54). The procedure is shown in Figure 3.17. Point A is the orientation of the top face of the specimen ie near [001] and A' is the trace of plane A. Point B is the orientation of the side face of the crystal, and is located by the use of small circles after measuring it's position from the nearest <001> and <011> poles on the original projection. As the two faces are 90° apart, the trace of plane B should pass through or close to point A, as shown in figure 3.17 as B'. The two traces intersect at C which is the common line of intersection for the two faces, labelled C - C' on the schematic of the specimen.

A point T1 is measured 64.3° from C along the trace of plane A, A', T2 is measured 51.5° from C along the trace of plane B, B'. The two points are joined by a great circle which becomes the trace of the facet plane. The orientation of the plane is determined by plotting the pole of the plane 90° from the trace, marked T. The point T may be compared with a standard projection on [001] or plotted inside a stereographic triangle to identify its orientation.

4. Results

4.1 Alloy microstructure

Examination of alloy microstructure was carried out as described in section 3.9. Figure 4.1 shows the general features found in alloy SRR 99. Examination at low magnification revealed the presence of a low percentage of evenly distributed carbides. At higher magnification, the carbides were found to be rounded with no evidence of decomposition products at the carbide/matrix interfaces as shown in figure 4.1a. The matrix was found to consist of a high volume fraction of γ' , having a cuboid morphology with approximate cube dimensions of 0.25-0.5μm. Observation of several fields revealed that γ' was of uniform size with only slight coarsening in interdendritic areas. The matrix is shown in figures 4.1b and c.

The general features of alloy SRR 9 are shown in figure 4.2. The matrix was found to consist of a similar fraction of γ' and of similar size to alloy SRR 99 but was found to be less cuboidal in morhology as shown in figure 4.2a. At lower magnification the dendritic solidification pattern was more apparent. This was discovered to be due to coarser γ' in the interdendritic areas of the matrix. The carbides were found to be evenly distributed but had a greater number of finer particles when compared to alloy SRR 99.

A number of larger particles were observed in alloy SRR 9 and are shown in figures 4.2b and c.

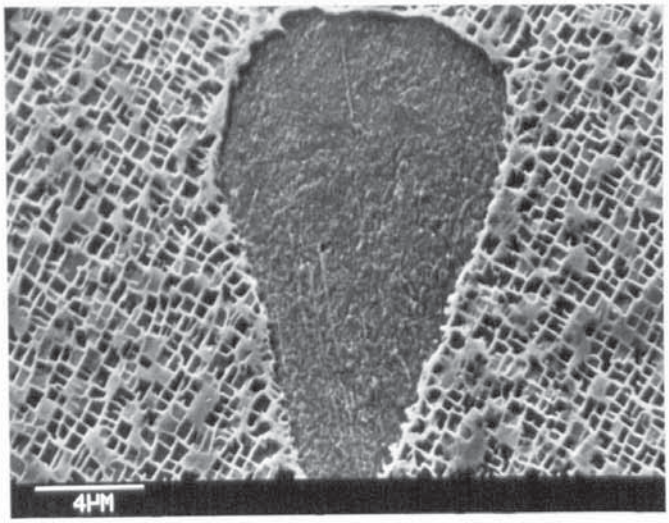

a) Matrix and MC carbide

Mag'n x3500

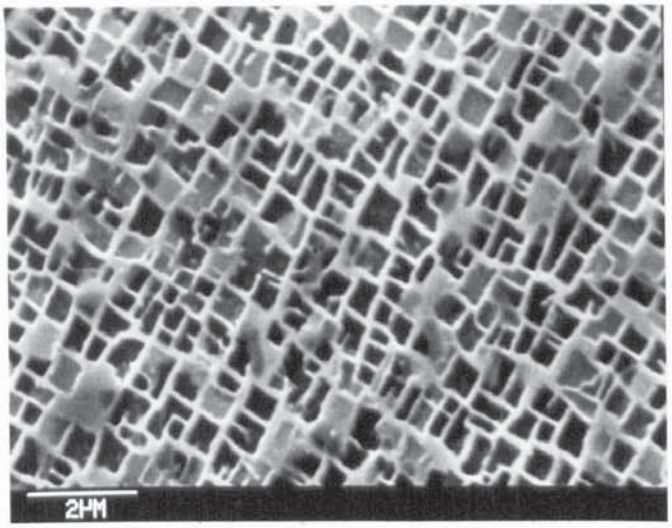

b) Matrix

Mag'n x7000

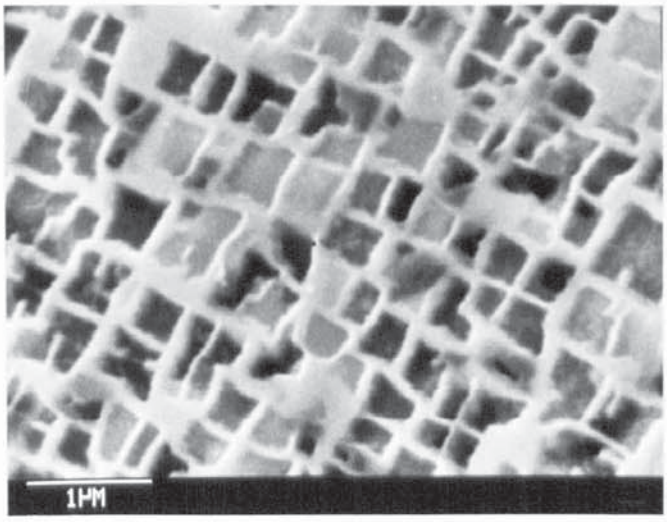

c) Matrix

Mag'n x16000

Figure 4.1 Alloy SRR 99 microstructure

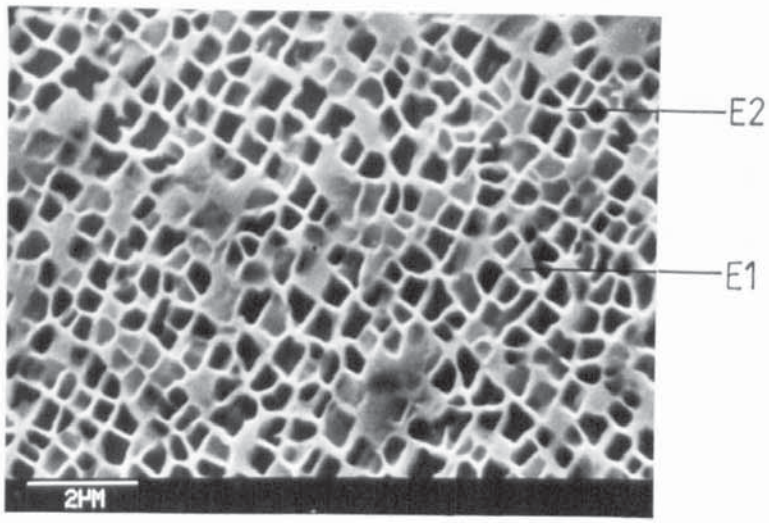

a) Matrix

Magn x 7000

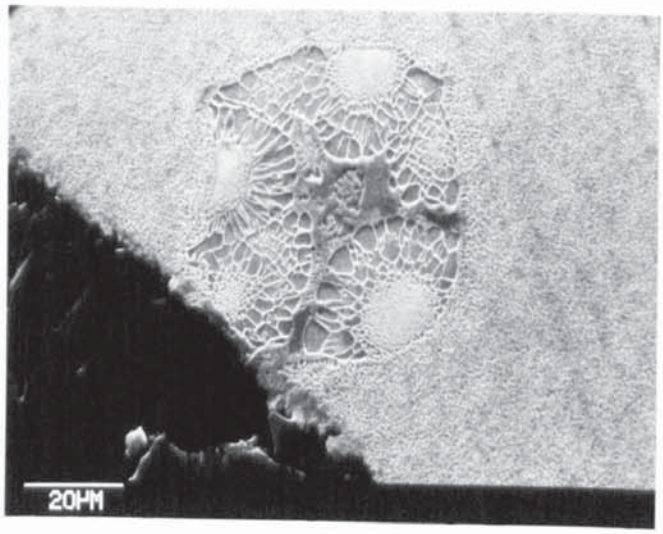

b) Eutectic Nodule

Magn x 650

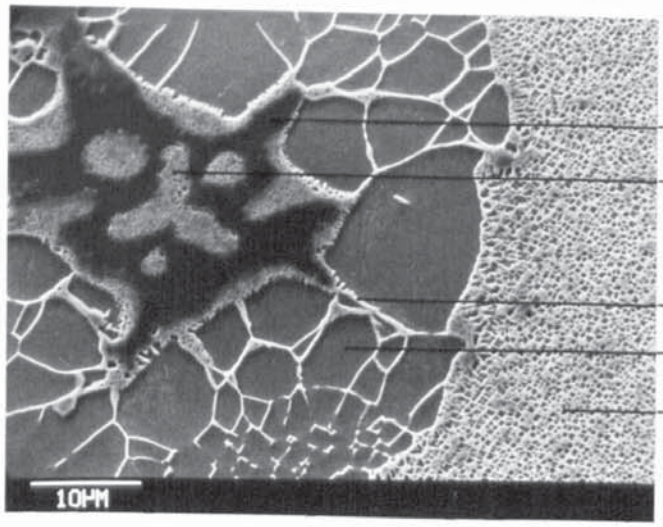

c) Eutectic Nodule

area used for EDAX analysis

Magn x 1400

Figure 4.2 Alloy SRR 9 microstructure

The particles were considered to be eutectic nodules which had not been fully decomposed by the solution treatment. A semi-quantitative analysis was carried out by use of a Link system energy dispersive x-ray analysis unit using the area shown in figure 4.2c. The analysis was used to indicate the presence and relative concentration of elements, determination of accurate composition was not attempted. The results are given in table 4.1.

Table 4.1 Semi-quantitative EDAX analysis of alloy SRR 9

Window label	Al	W	Zr	Ti	Cr	Fe	Co	Ni
Window centre eV	1460	1740	2060	4520	5400	6400	6920	7480
Efficiency factor	0.81	0.80	0.76	0.56	0.62	0.85	1.00	1.19
Position	Element wt%							
A) Dark centre	0.00	10.3	6.15	2.87	4.18	0.81	4.44	71.23
B) Light centre	0.32	3.32	0.00	0.64	11.2	4.93	6.73	72.93
C) Acicular	1.24	4.77	0.00	0.90	8.08	4.43	6.95	73.62
D) Smooth area	1.81	3.50	0.00	1.21	2.30	2.13	4.02	85.03
E1) Gamma prime	0.61	3.44	----	0.92	9.95	1.16	5.81	78.11
E2) Web/Matrix	0.75	3.54	----	1.00	9.96	0.42	6.38	77.95
F) Full raster Matrix	0.51	2.97	----	0.96	8.77	0.70	5.60	80.49

4.2 The creep properties of alloy SRR 9

4.2.1 Creep tests

Creep testing was carried out on specimens supplied as having a tensile axis near [001], under two conditions:

H) 850°C and an applied stress of 550MPa.

L) 750°C and an applied stress of 850MPa

These conditions were specified by Rolls-Royce Ltd as producing a time to rupture for alloy SRR 99 of approximately 100 hours. The same conditions were used for alloy SRR 9 to provide direct comparison of results.

Specimens are identified by the alloy, condition (low and high temperature) and test number; ie 9L/1 relates to a specimen of alloy SRR 9 tested at A temperature of 750°C and an applied stress of 850MPa identified as specimen number 1.

The initial tests ie 9L/1 and 9L/2 were carried out with no glass panel in the observation port as shown in figure 3.8, instead a metal cover was used which had to be removed before a photograph could be taken. This affected the temperature control for these tests. Tests 9L/1 to 9L/3 were tested to failure but due to a problem with the electronic timing device the strain measurements are not complete.

The true strain versus time data obtained is shown graphically in figures 4.3a to 4.3k. Figures 4.3l and 4.3m show compiled test results for the two conditions examined, together with the specimen cast identification . Table 4.2 gives the creep results obtained from the true strain versus time curves for alloy SRR 9.

Table 4.2 SRR 9 creep test results

Specimen I.D	Condition	Initial plastic strain	Linear regression				Time to rupture
	Temp/ stress		points used	intercept	slope min ε	Regression coefficient	
	°C/MPa	ε_i x10^{-2}	Hrs	x10^{-2}	ε_{min} x10^{-3}/Hr	R	Tr Hrs
9L/1	750/850	0.75	2-8	2.58	3.62	0.78	>8
9L/2	750/850	0.50	2-9	2.78	7.71	0.96	>12
9L/3	750/850	0.20	1.5-6	3.05	2.53	0.95	14.7
9L/4	750/850	1.10	2-10.5	2.32	2.13	0.93	23
9L/5	750/850	1.10	2-13	3.33	2.20	0.97	25.4
9L/6	750/850	1.10	2.5-10	0.00	3.90	0.96	19.5
9H/1	850/550	1.4	0.5-4	1.59	10.97	0.99	8.2
9H/2	850/550	0.17	1.5-4.5	-0.29	2.71	0.82	22.4
9H/3	850/550	1.8	1-5.5	1.70	7.18	0.99	11.2
9H/4	850/550	0.40	1-4	0.15	8.15	0.98	8.2
9H/5	850/550	0.5	1-3	-0.57	15.3	0.995	5.3

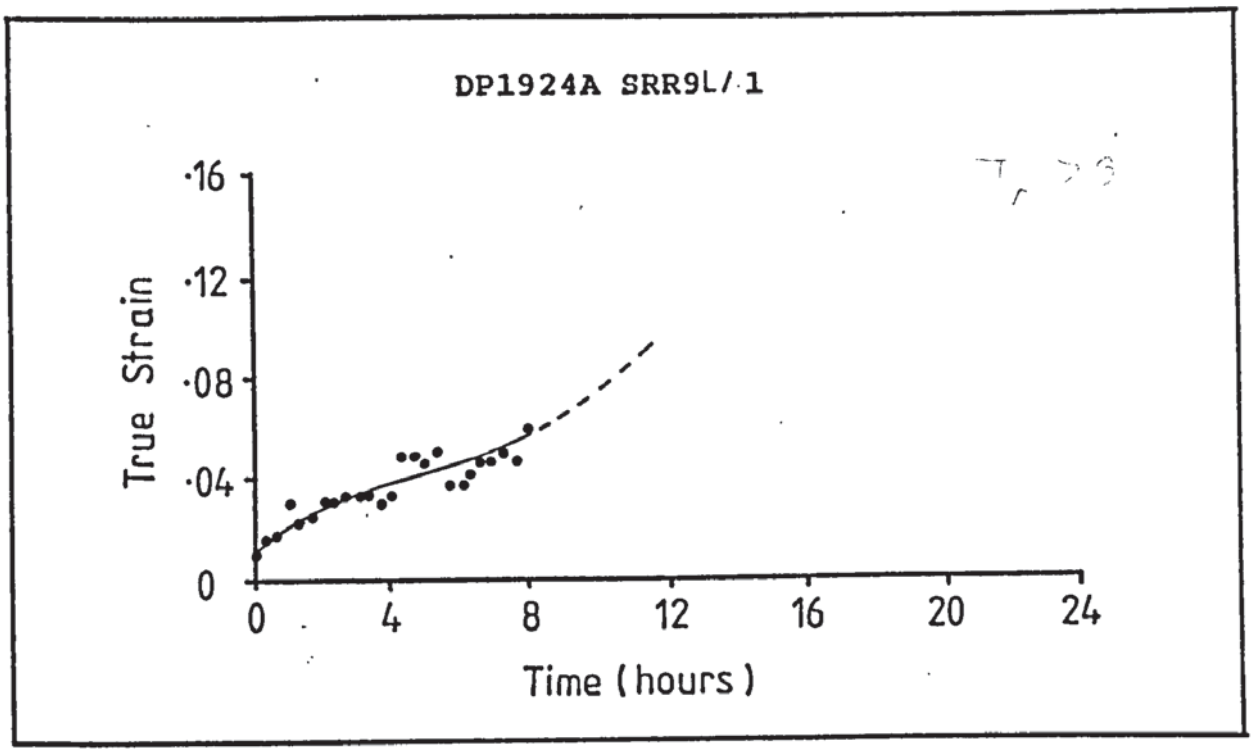

Figure 4.3a SRR 9 Creep tested at 750°C and 850MPa

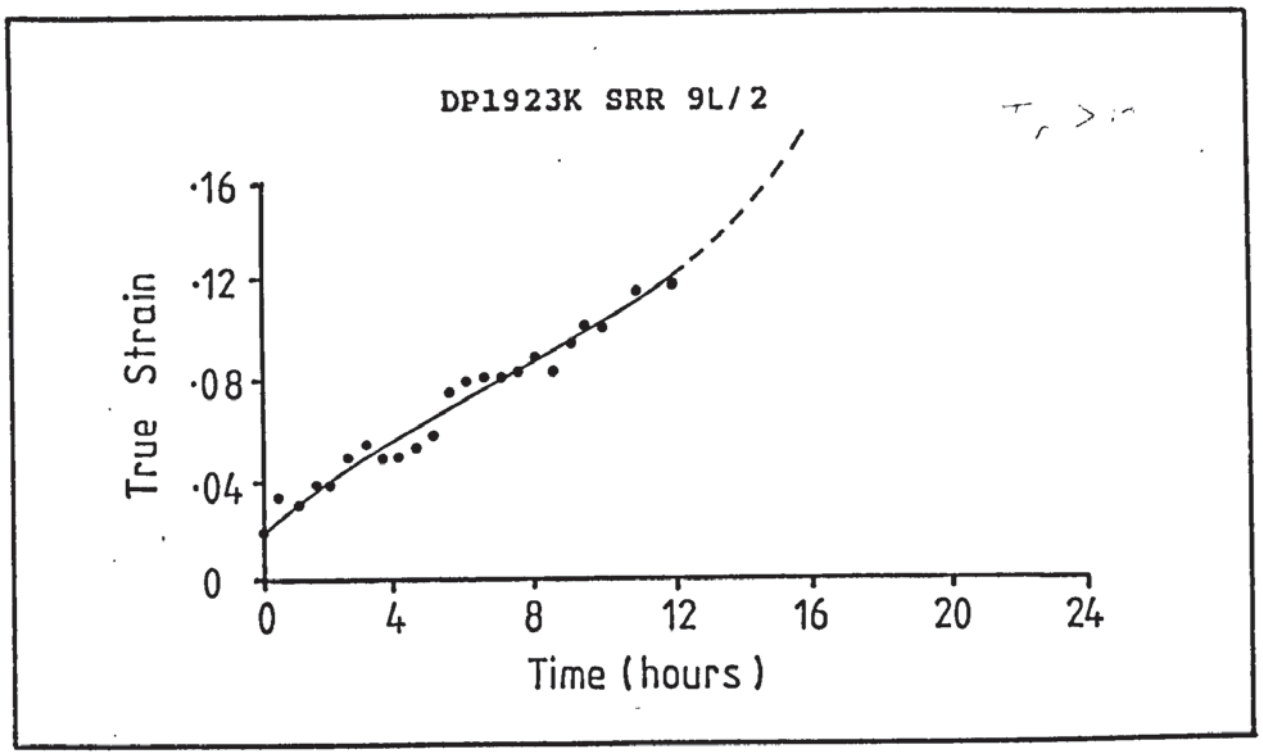

Figure 4.3b SRR 9 Creep tested at 750°C and 850MPa

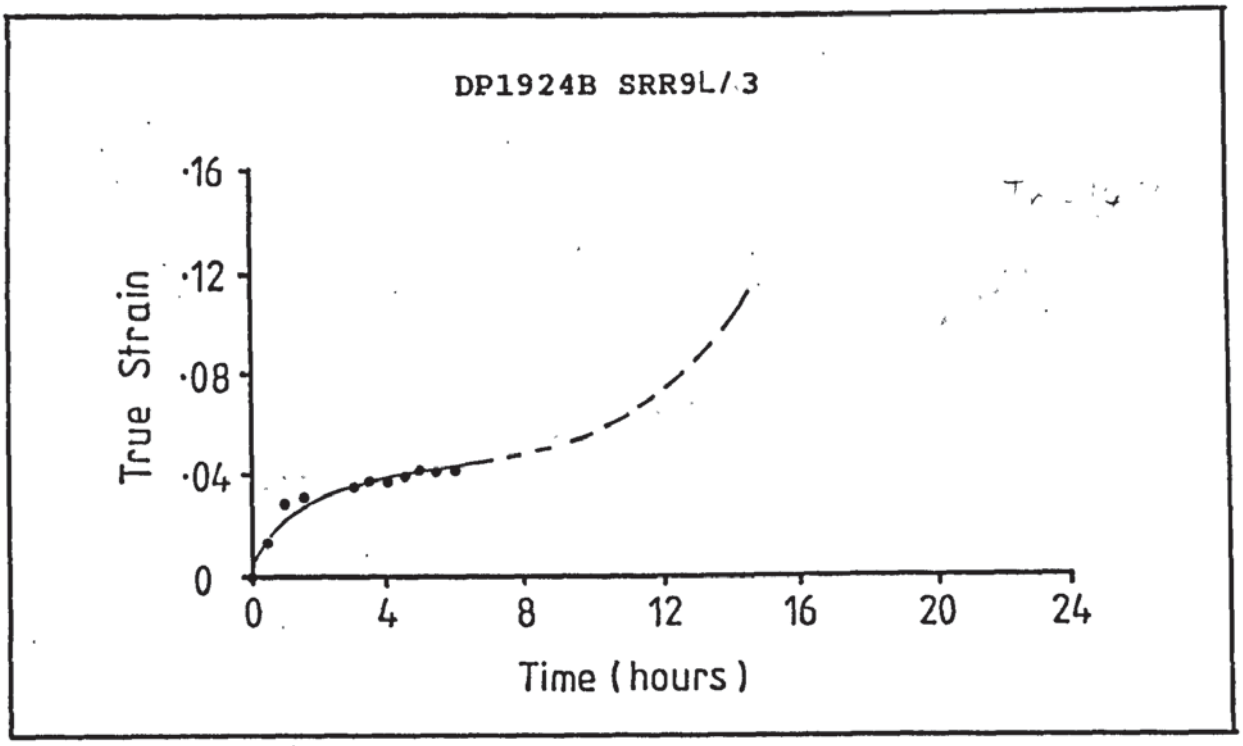

Figure 4.3c SRR 9 Creep tested at 750°C and 850MPa

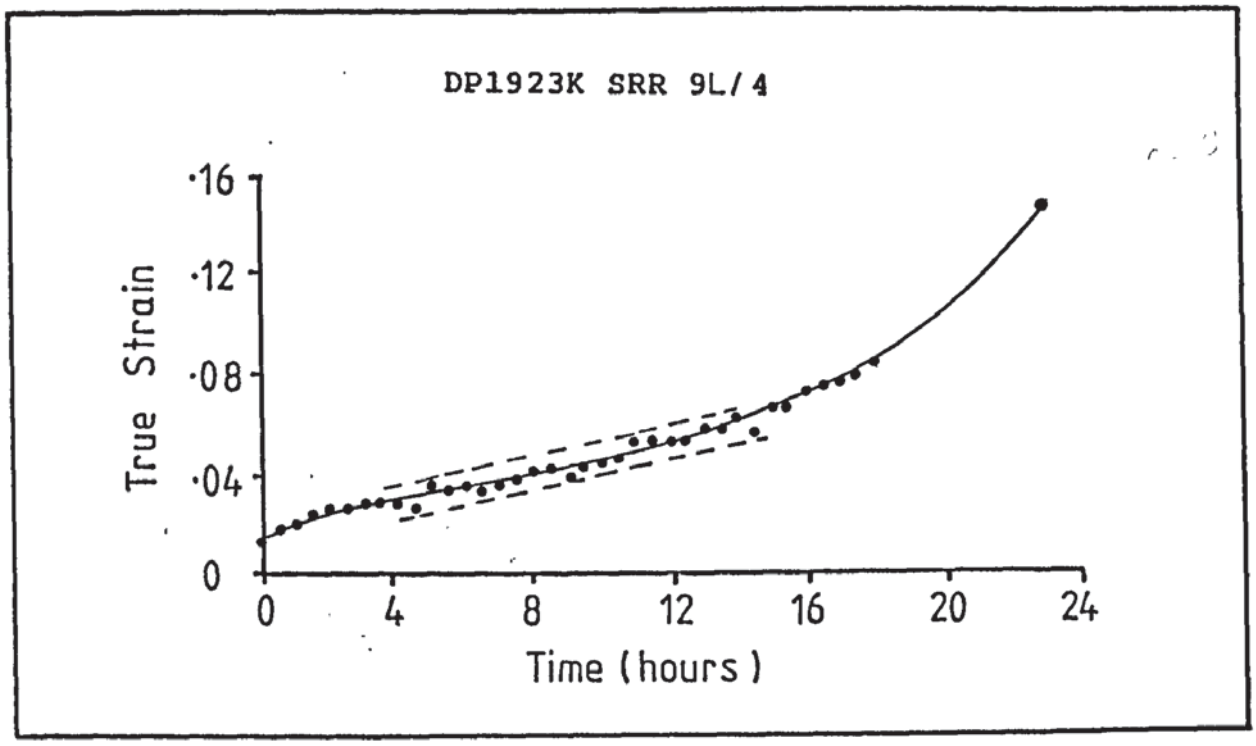

Figure 4.3d SRR 9 Creep tested at 750°C and 850MPa

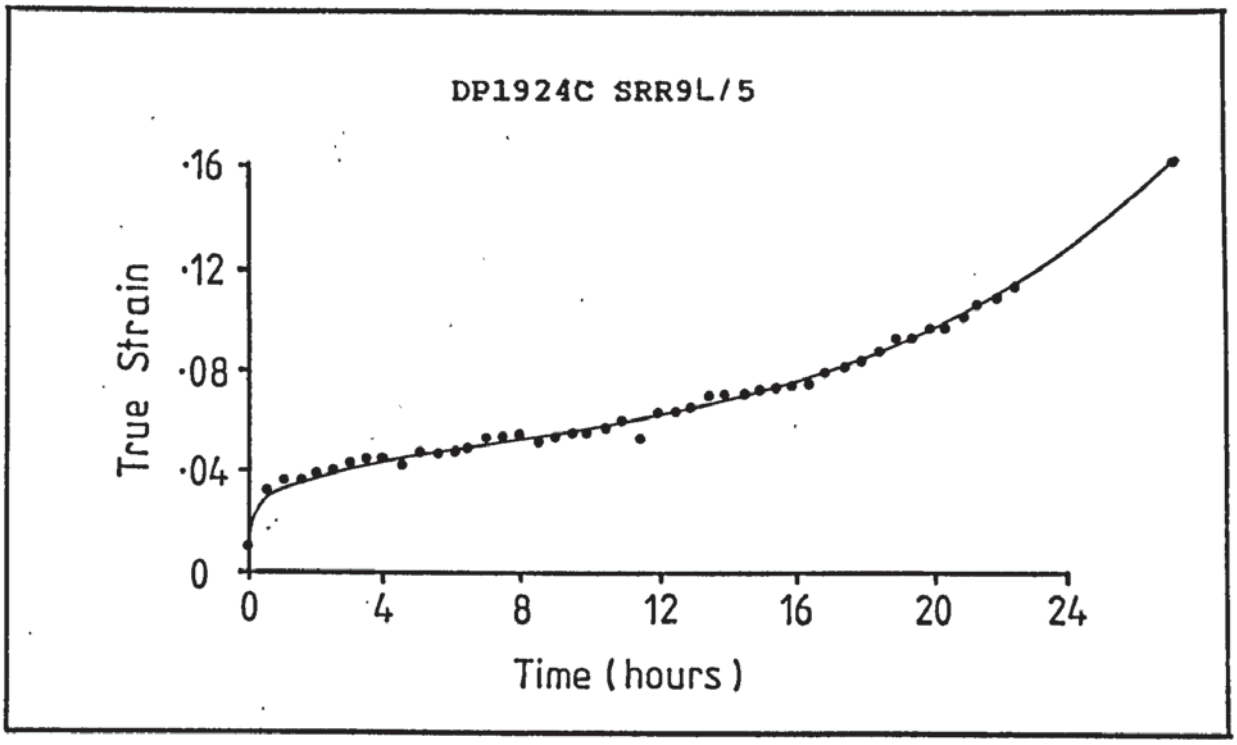

Figure 4.3e SRR 9 Creep tested at 750°C and 850MPa

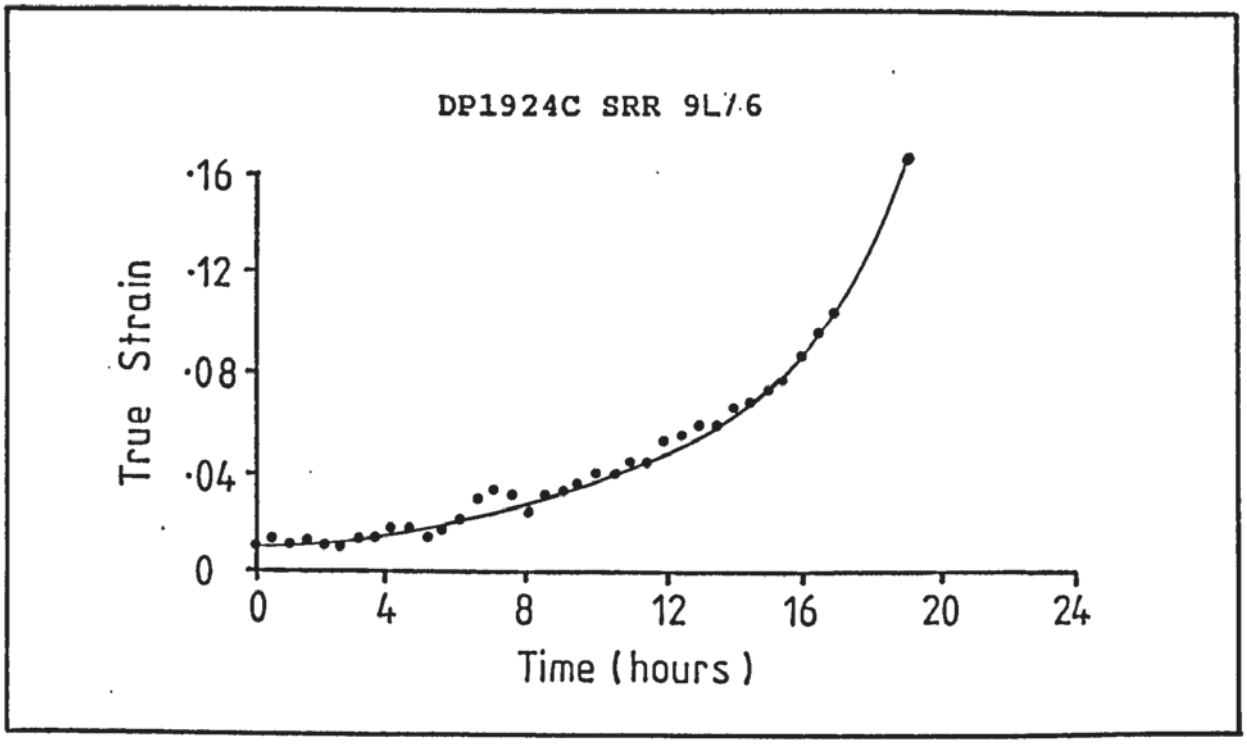

Figure 4.3f SRR 9 Creep tested at 750°C and 850MPa

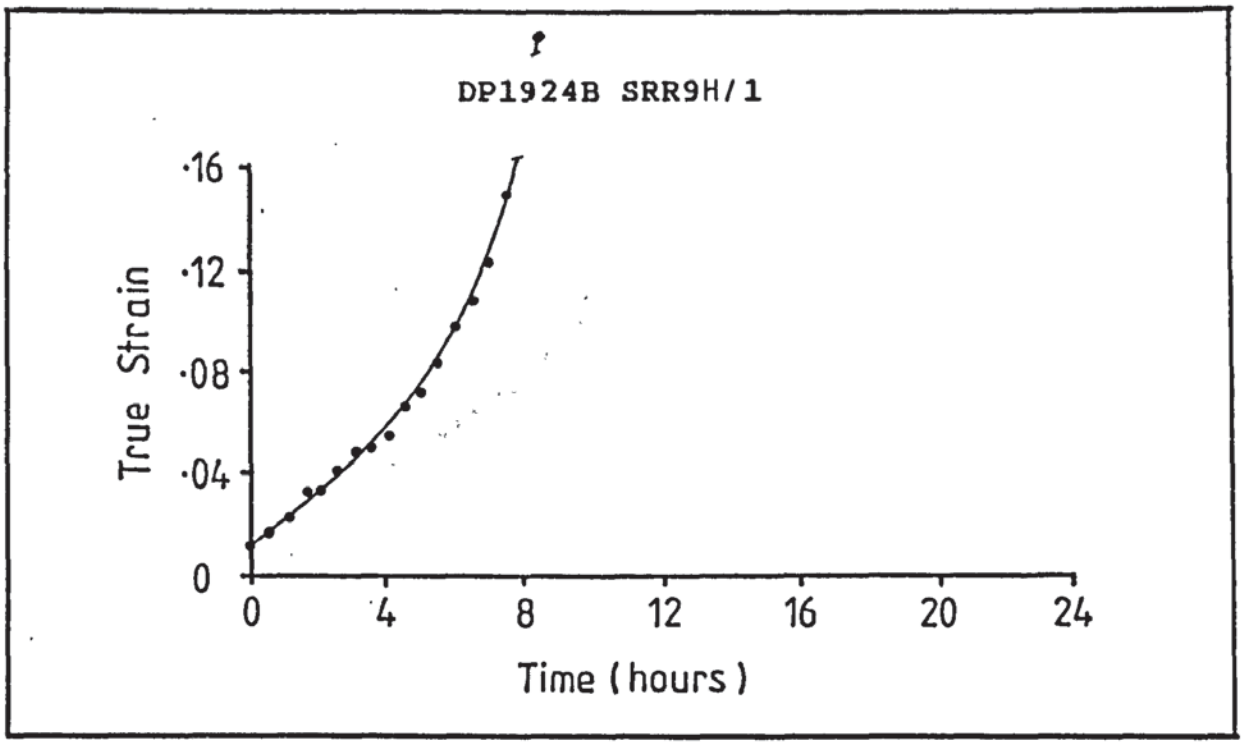

Figure 4.3g SRR 9 Creep tested at 850°C and 550MPa

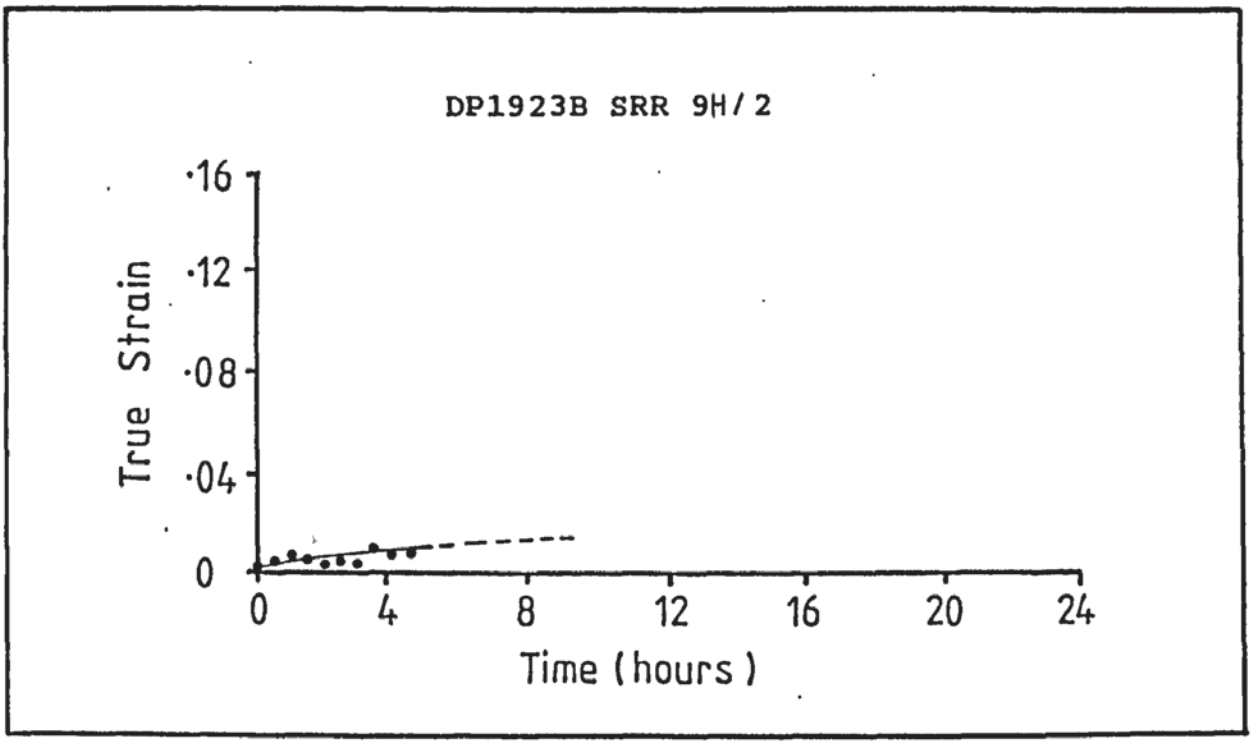

Figure 4.3h SRR 9 Creep tested at 850°C and 550MPa

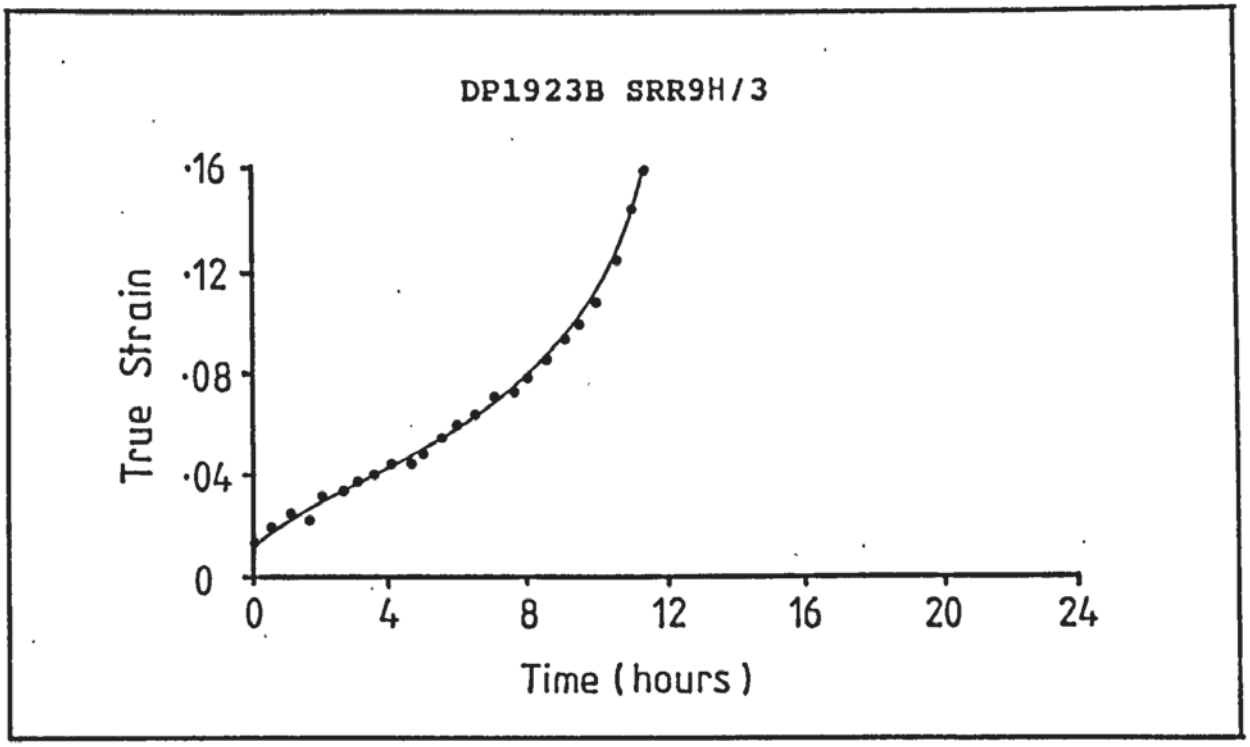

Figure 4.3i SRR 9 Creep tested at 850°C and 550MPa

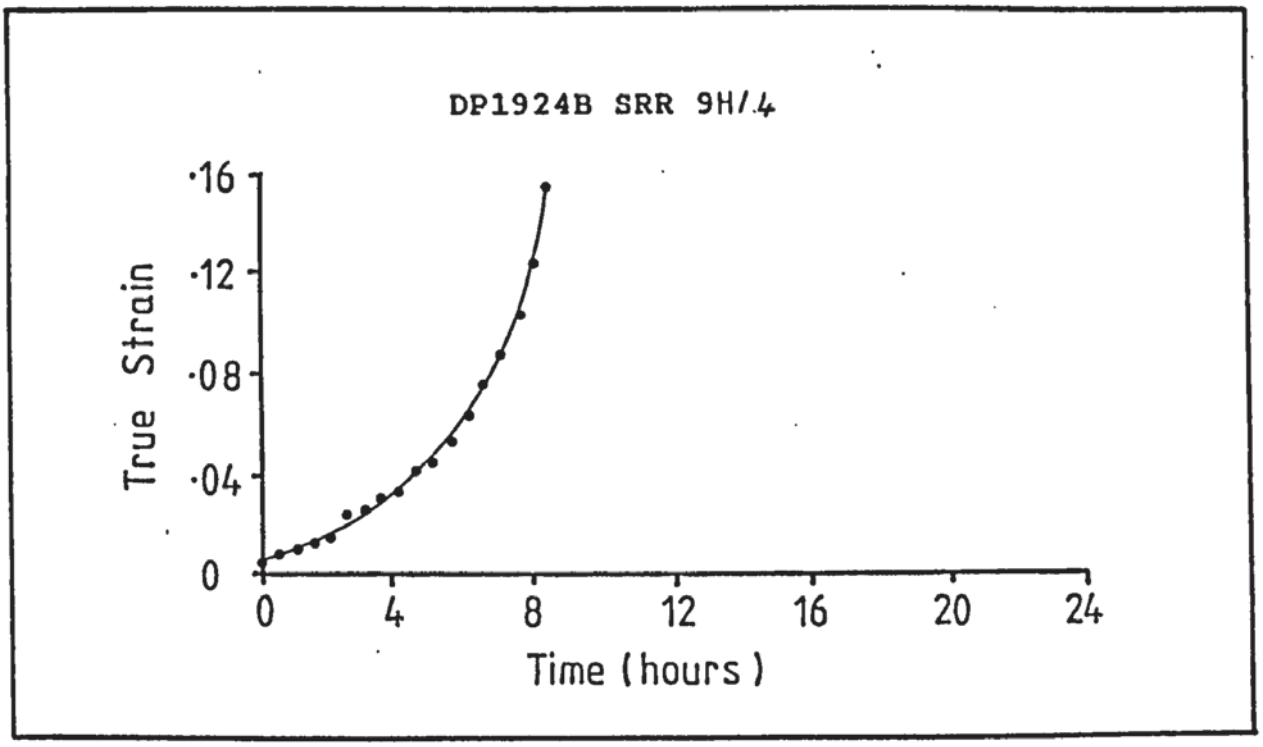

Figure 4.3j SRR 9 Creep tested at 850°C and 550MPa

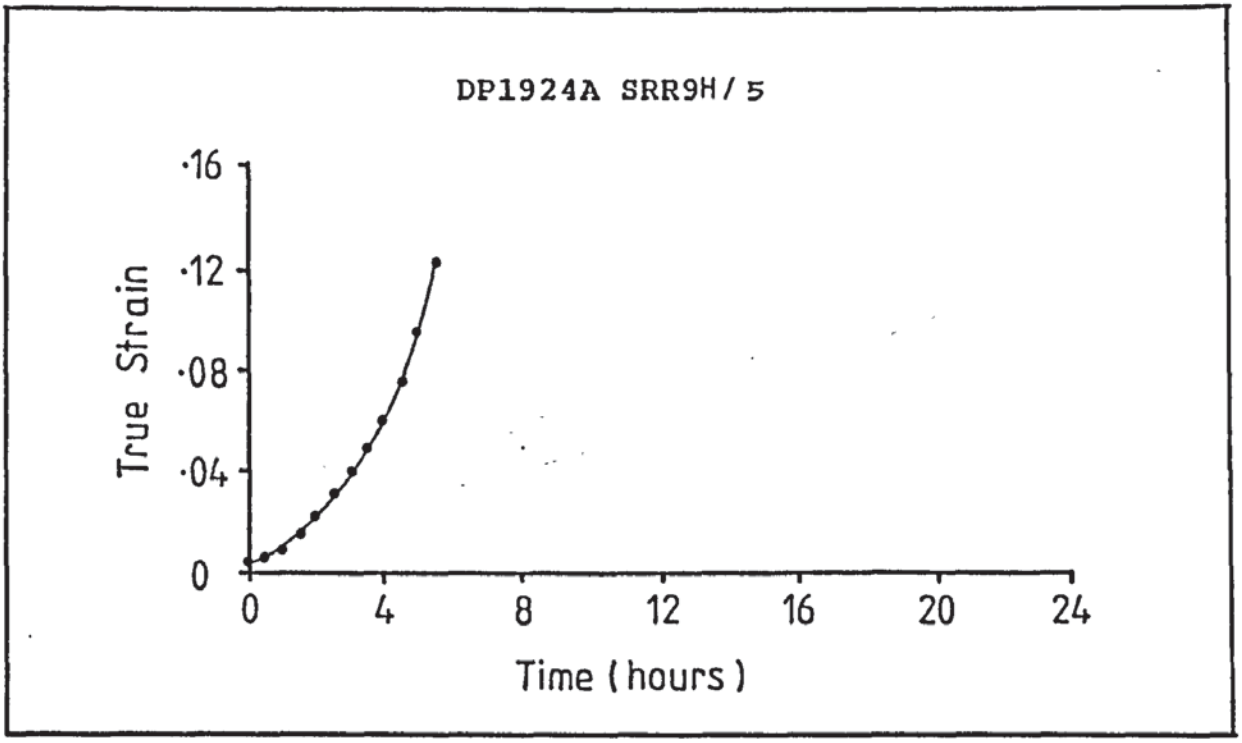

Figure 4.3k SRR 9 Creep tested at 850°C and 550MPa

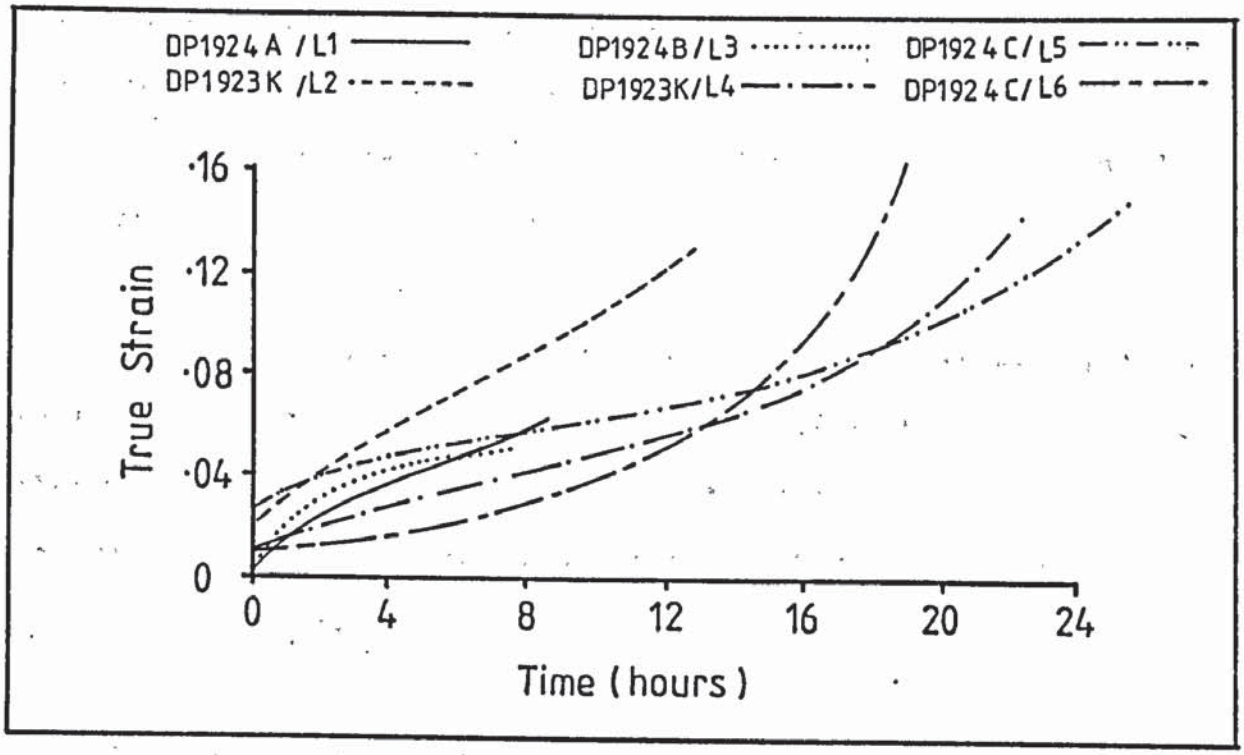

Figure 4.31 SRR 9 Creep tested at 750°C and 850MPa

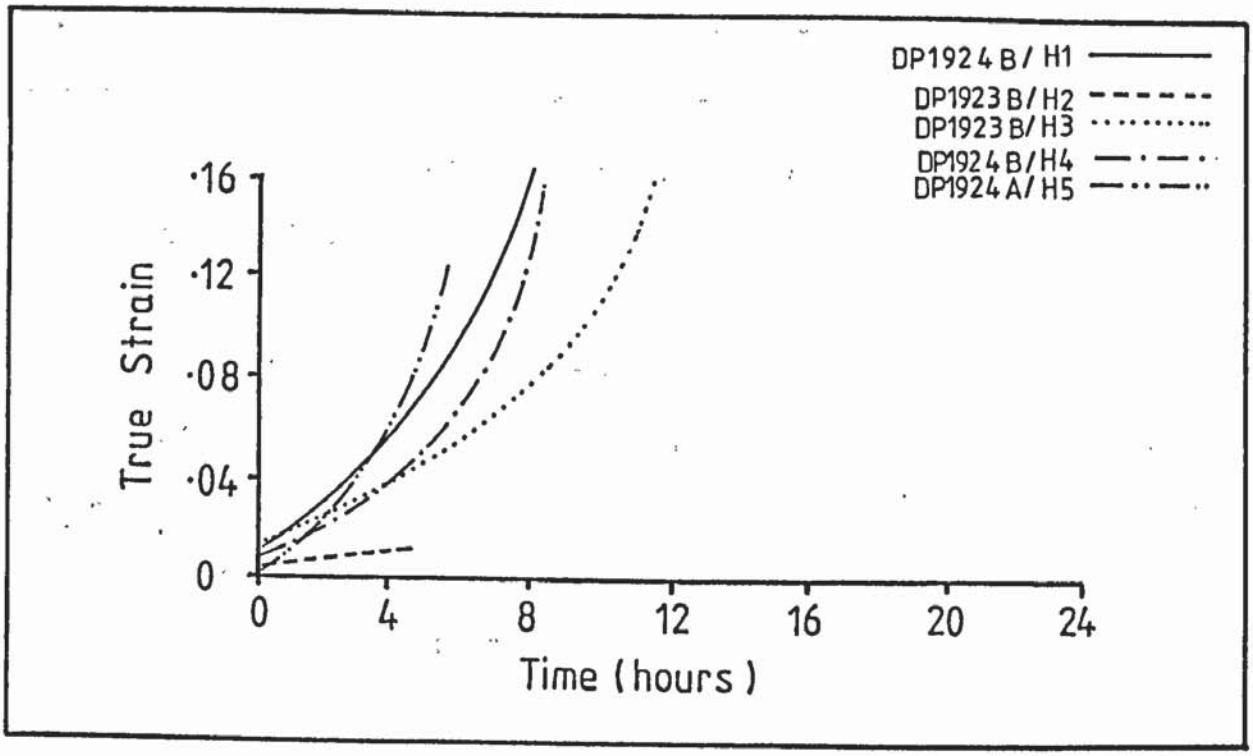

Figure 4.3m SRR 9 Creep tested at 850°C and 550MPa

4.2.2 Examination of SRR 9 creep fractures

All creep tests were carried out until failure of the specimen. Rupture times were found to be short, less than 30 hours as shown in table 4.2.

As the furnace did not switch off on specimen failure, most of the fracture surfaces when examined in a scanning electron microscope were found to have an appreciable oxide coating. This limited examination of the fracture to a relatively low magnification .

Figure 4.4 shows typical creep fractures for specimens tested at 750°C and 850MPa. The fracture faces were found to be square to the gauge length with no distortion of the rectangular section. This is a general indication that multiple slip systems were in operation for the majority of the creep life. Figure 4.4c is a higher magnification view of specimen 9L/6 showing smaller crystallographic facets and crack growth regions associated with microvoids.

Figure 4.5 shows creep fractures from specimens tested at 850°C and 550MPa. The fracture faces were found to be undistorted, again indicating operation of multiple slip systems. The majority of the fractures were smooth indicating crystallographic failure.

An exception was specimen 9H/2, shown in figure 4.5b. This was found to have a significantly different orientation to the other specimens, as discussed in section 4.2.3.

Figure 4.5c shows a feature found on specimen 9H/2. A transverse crack was found in the gauge length, parallel to and approximately 0.3mm from the fracture face. Examination indicated a rosette shaped fracture formation of approximately 50μm diameter.

a)9L/5
Mag'n x60

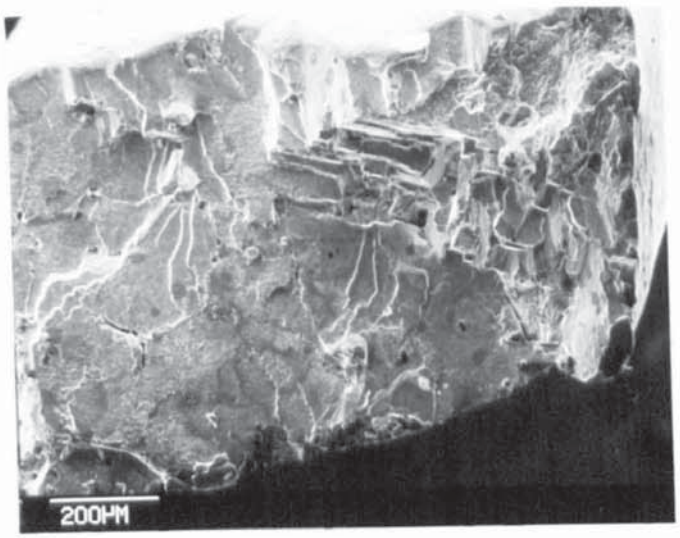

b)9L/6
Mag'n x70

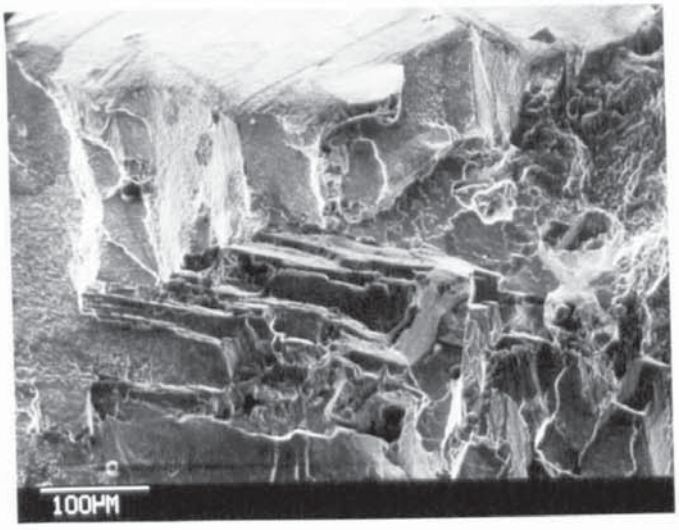

c)9L/6
Mag'n x140

Figure 4.4 Creep fractures for alloy SRR 9 tested at 750°C and 850MPa

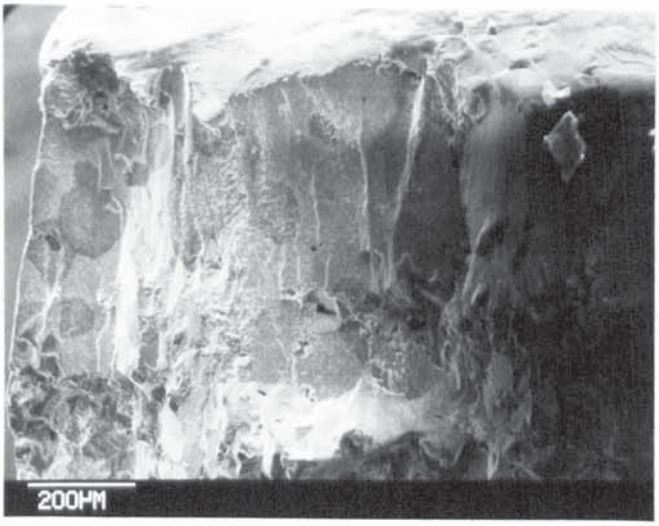

a)9H/1
Mag'n x70

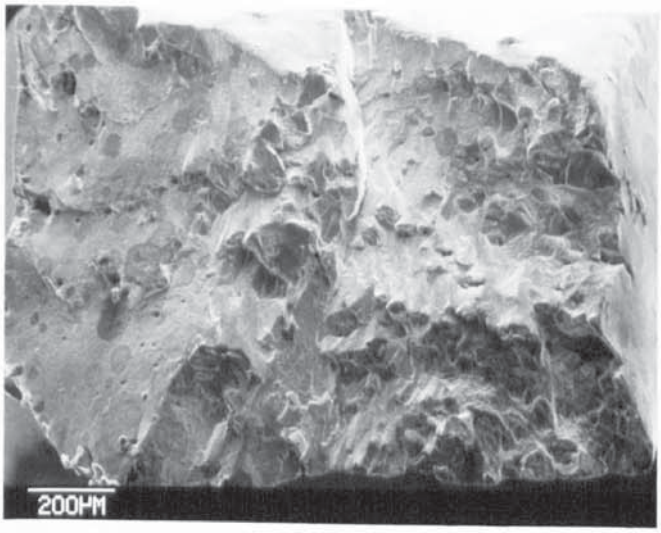

b)9H/2
Mag'n x60

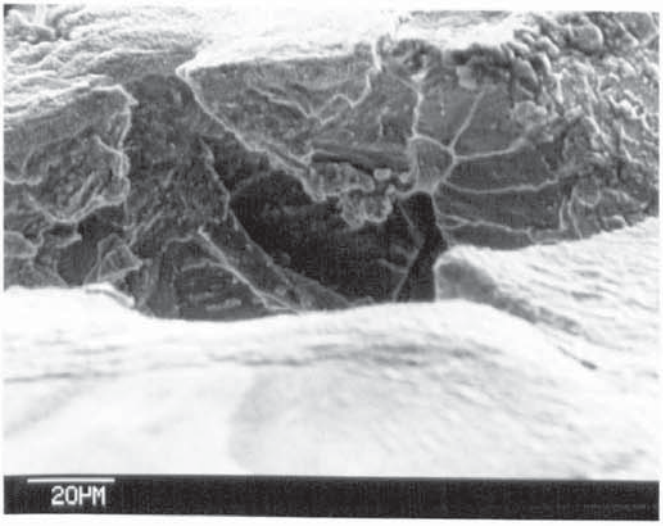

c)9H/2
Mag'n x550

Figure 4.5 Creep fractures for alloy SRR 9 tested at 850°C and 550MPa

4.2.3 The effect of orientation on SRR 9 creep properties

Crystal rotation experiments were undertaken to indicate the type of slip mechanism, and to indicate any effect of temperature and stress upon it. The initial and final tensile axis orientation for SRR 9 creep specimens are shown in table 4.3.

Figure 4.6 portrays the crystal rotation results graphically with reference to a unit stereographic triangle for specimens tested at 750°C and 850MPa. The creep rupture times for the specimens are also given in order to indicate the effect of orientation on creep life. Figure 4.7 portrays the results for specimens tested at 850°C and 550MPa.

Table 4.3 SRR 9 orientation and crystal rotation results

Specimen	Initial		Final	
	θ degrees	ϕ degrees	θ degrees	ϕ degrees
9L/1	3	45	2.5	21
9L/2	1.5	18	0	0
9L/3	8	11	5	9
9L/4	2	17	1	17
9L/5	3	28	4	15
9L/6	2.5	17	1	17
9H/1	4	8	2	8
9H/2	19	37	20	44
9H/3	18	44	14	40
9H/4	5	9	3.5	0
9H/5	2	23	2	0

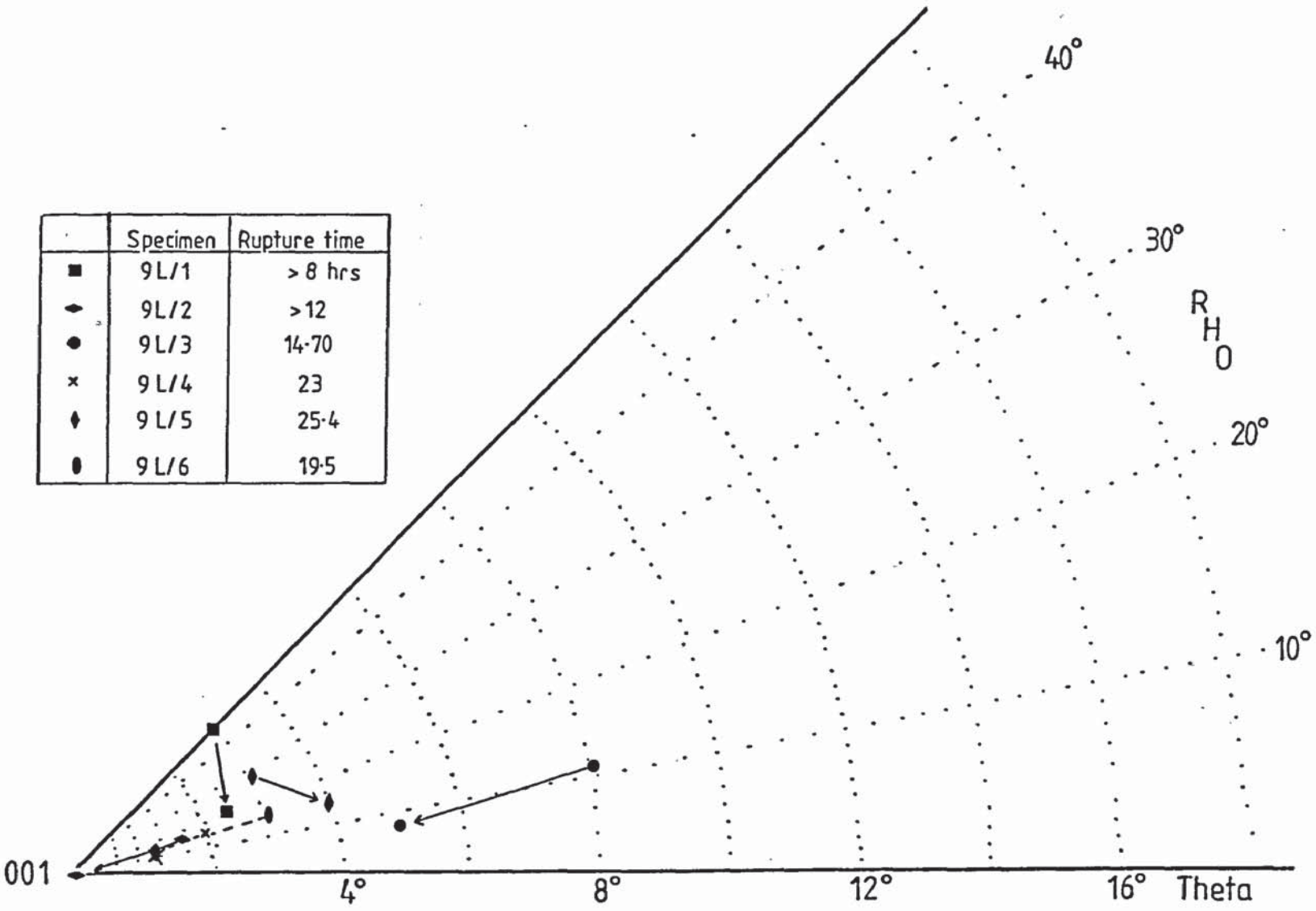

Figure 4·6 Effect of orientation on alloy SRR 9 creep tested at 750°C and 850 MPa

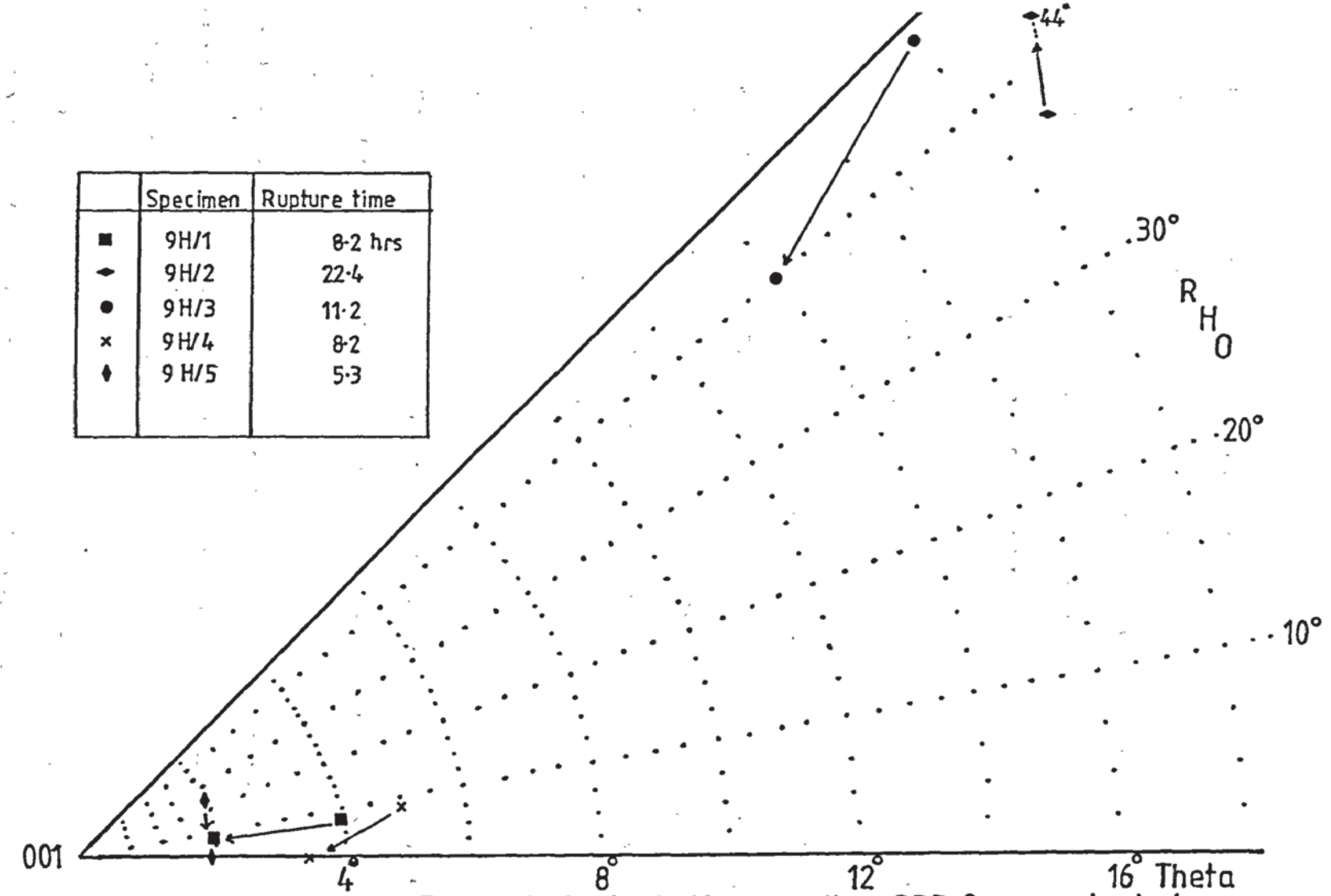

Figure 4·7 Effect of orientation on alloy SRR 9 creep tested at 850°C and 550 MPa

4.3 The creep properties of alloy SRR 99

4.3.1 Creep tests

Creep testing was carried out on specimens supplied as having a tensile axis near [001], under five conditions:

H1) 850°C and an applied stress of 550MPa.

H2) 850°C and an applied stress of 500MPa.

L1) 750°C and an applied stress of 850MPa.

L2) 750°C and an applied stress of 825MPa.

L3) 750°C and an applied stress of 800MPa.

The specimens are identified by the alloy, condition code (as given above) and test number; ie 99H2/1 represents the first specimen to be creep tested at 850°C and an applied stress of 500MPa. The cast code and position of the casting in the mould as described in section 3.2 is related to the specimen code in table 4.5 together with the specimen orientations, and is also displayed in figures 4.8 and 4.9.

The true strain versus time data is shown graphically in figures 4.8a to 4.8i for specimens tested at 750°C, figures 4.8e,h and i being compiled test results for the conditions examined. Figures 4.9a to 4.9h give the creep results for specimens tested at 850°C, figures 4.9g and h being compiled test results.

Table 4.4 gives the creep results obtained from analysis of the creep curves in figures 4.8 and 4.9.

Table 4.4 SRR 99 creep test results

Specimen I.D	Condition Temp/ stress	Initial plastic strain	Linear regression				Time to rupture
			points used	intercept	slope min ε	Regression coefficient	
	°C/MPa	ε_i x10^{-2}	Hrs	x10^{-2}	ε_{min} x10^{-3}/Hr	R	Tr Hr
99L1/1	750/850	0.153	3-81	1.543	0.475	0.990	128.7
99L1/2	750/850	1.10	3-90	2.842	0.37	0.984	150.4
99L1/3	750/850	0.557	18-90	2.395	0.339	0.97	161.0
99L1/4	750/850	1.043	4-33	1.324	0.370	0.996	153.5
99L2/1	750/825	0.030	12-93	1.791	0.37	0.929	--
99L3/1	750/800	3.213	21-117	5.302	0.20	0.978	322.0
99L3/2	750/800	1.12	24-159	1.651	0.28	0.987	--
99H1/1	850/550	1.7	4-38	1.620	0.377	0.986	75.70
99H1/2	850/550	0.07	2-26	0.718	0.287	0.972	96.4
99H1/3	850/550	0.83	10-56	1.065	0.628	0.99	91.1
99H1/4	850/550	0.17	4-44	0.453	0.671	0.985	78.6
99H2/1	850/500	0.442	6-87	0.609	0.30	0.984	175.5
99H2/2	850/500	0.341	12-75	0.42	0.45	0.983	204.0

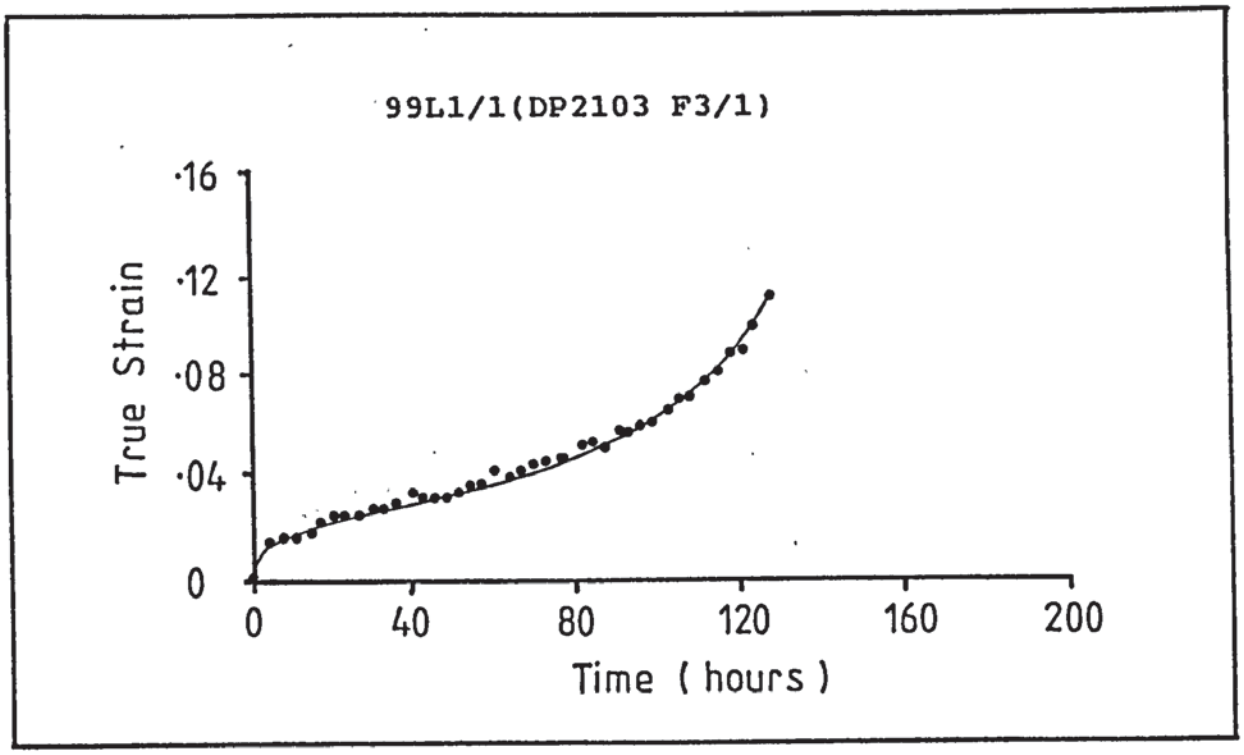

Figure 4.8a SRR 99 Creep tested at 750°C and 850MPa

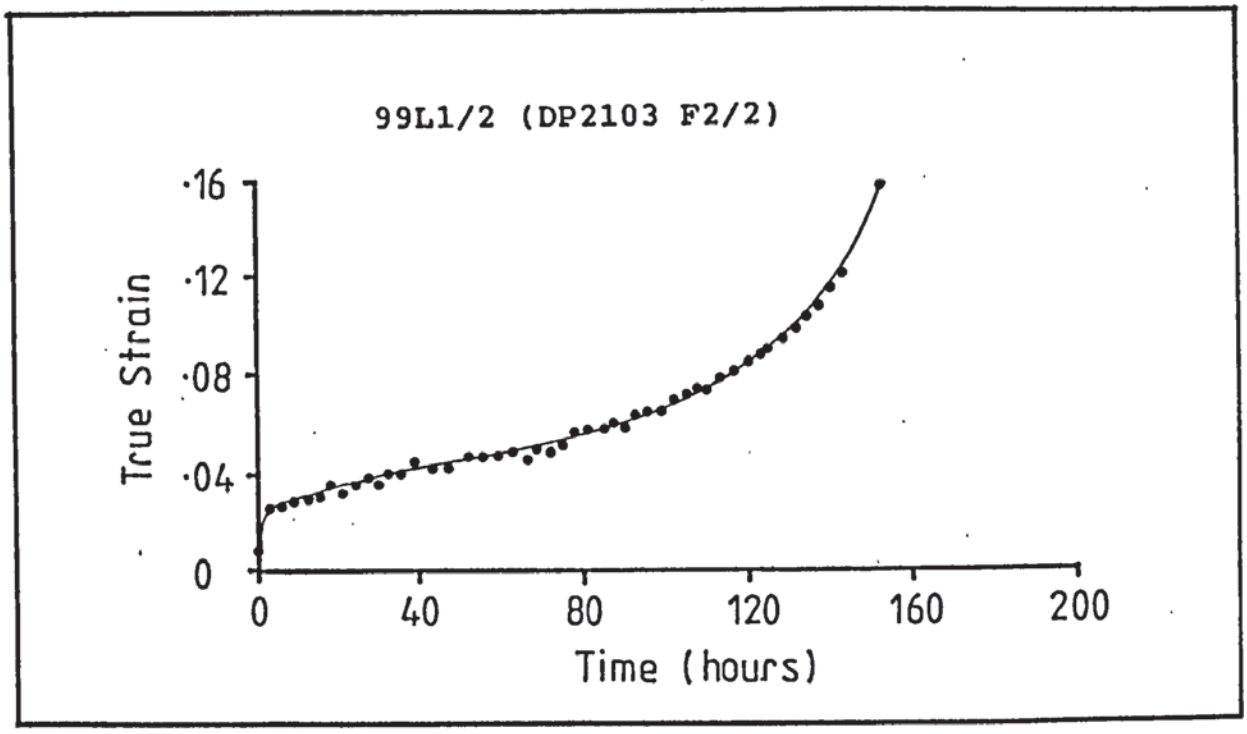

Figure 4.8b SRR 99 Creep tested at 750°C and 850MPa

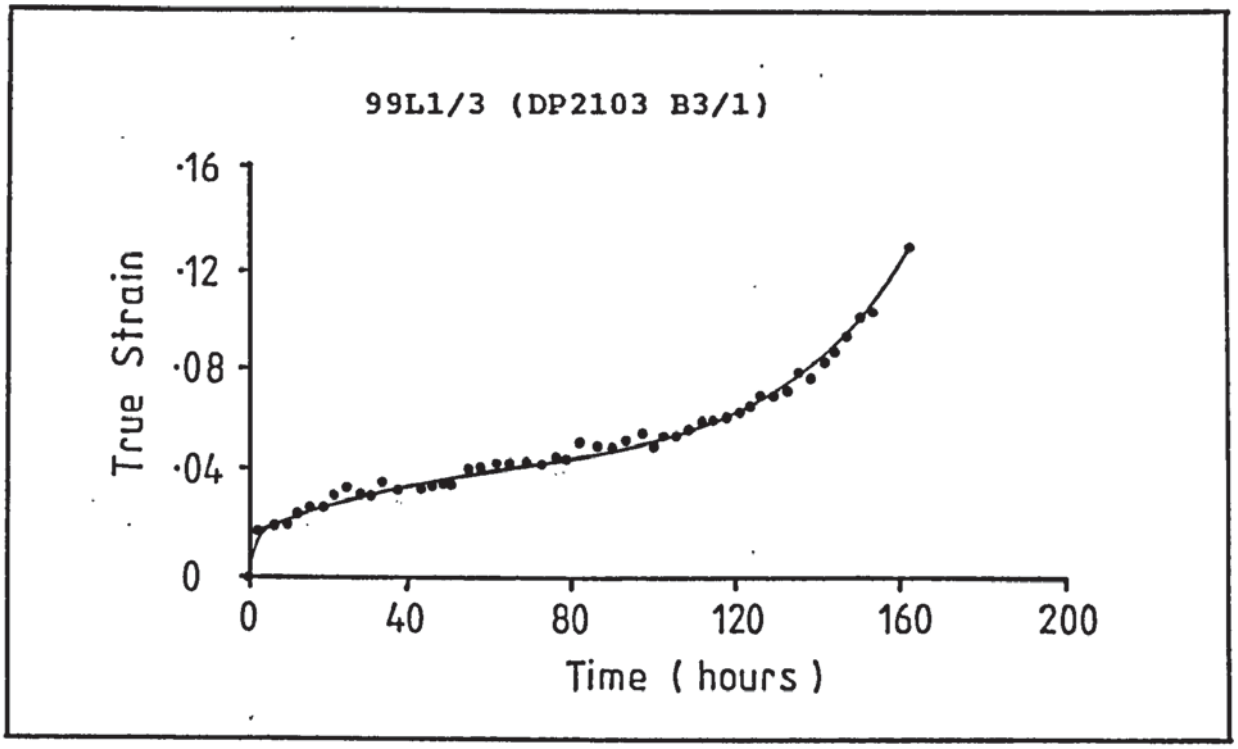

Figure 4.8c SRR 99 Creep tested at 750°C and 850MPa

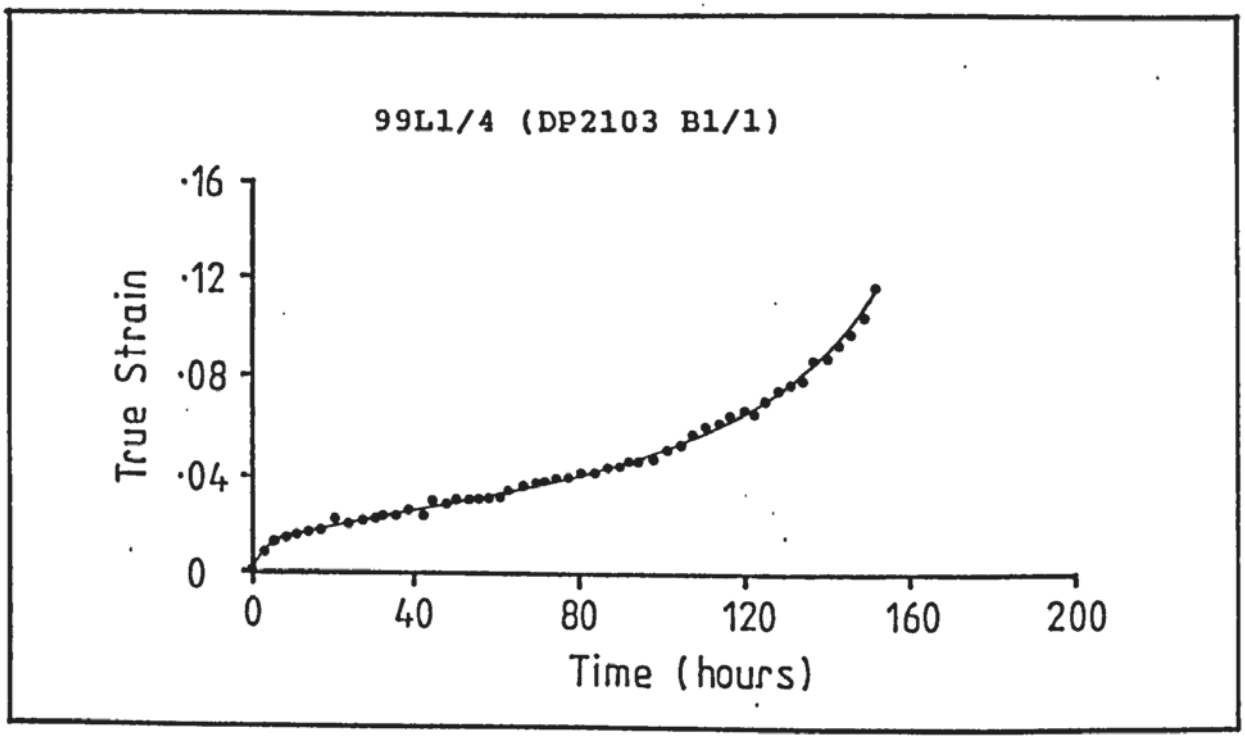

Figure 4.8d SRR 99 Creep tested at 750°C and 850MPa

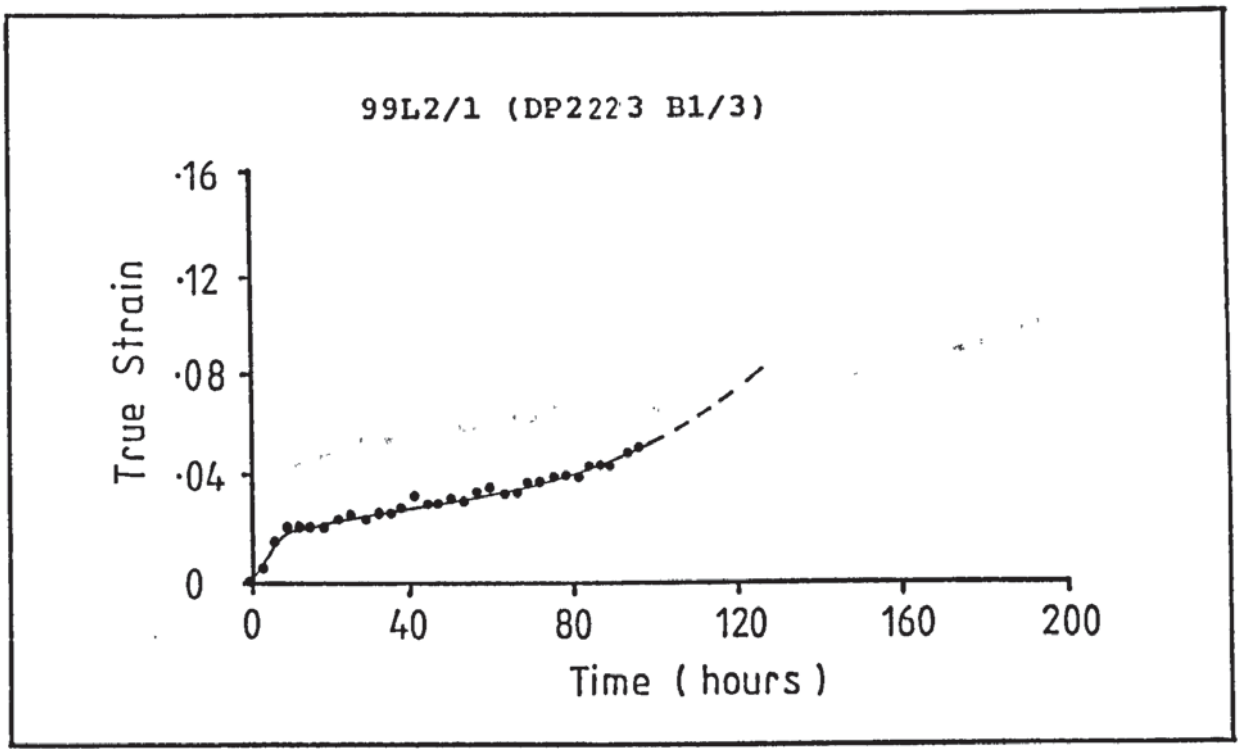

Figure 4.8e SRR 99 Creep tested at 750°C and 825MPa

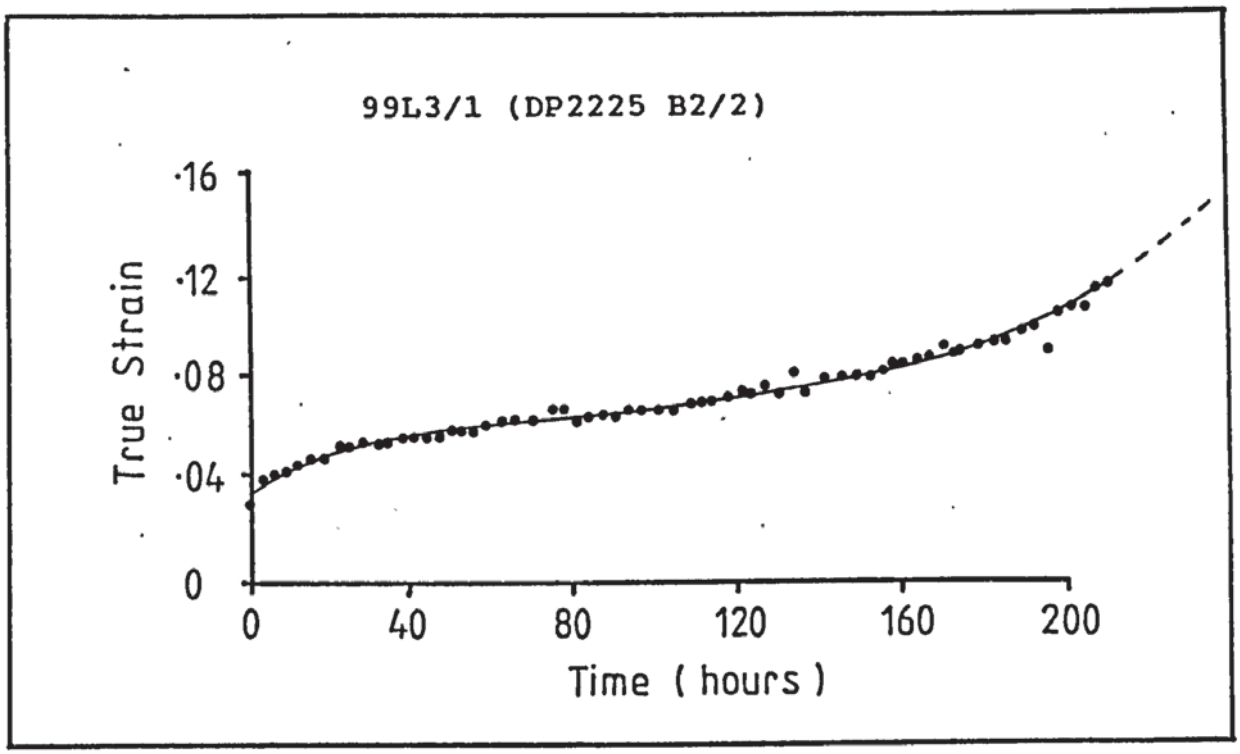

Figure 4.8f SRR 99 Creep tested at 750°C and 800MPa

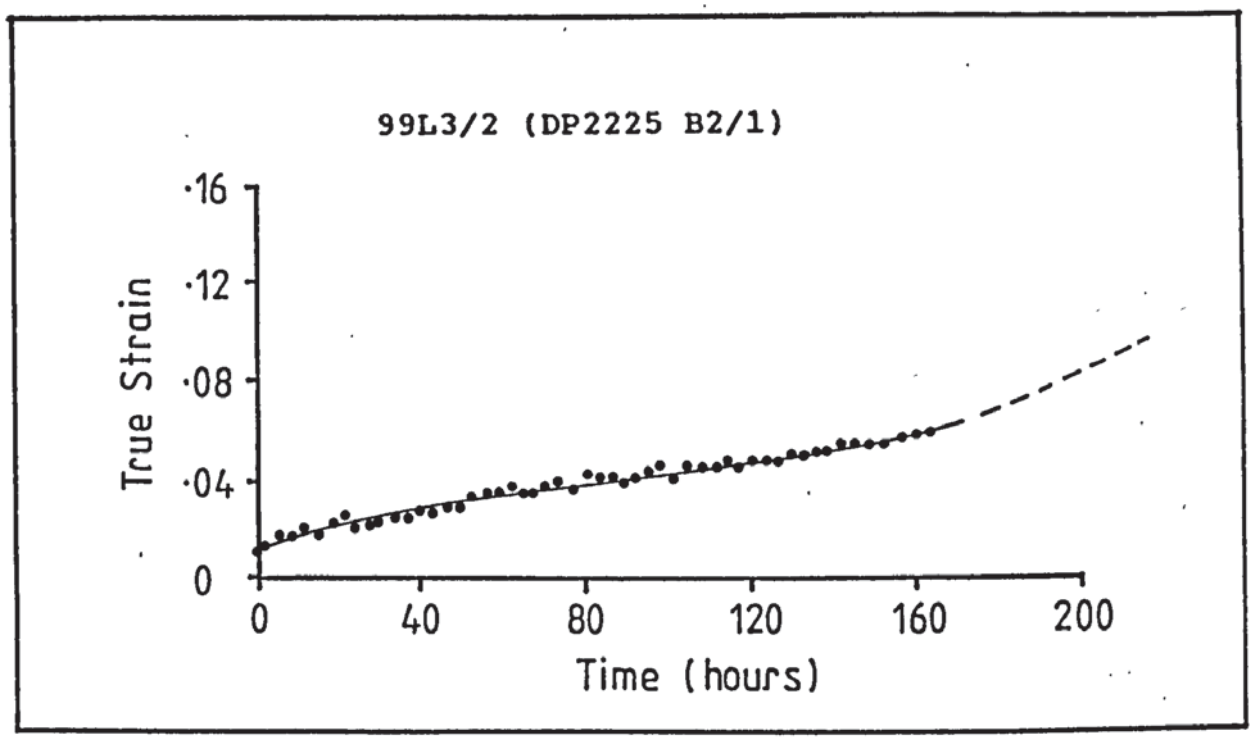

Figure 4.8g SRR 99 Creep tested at 750°C and 800MPa

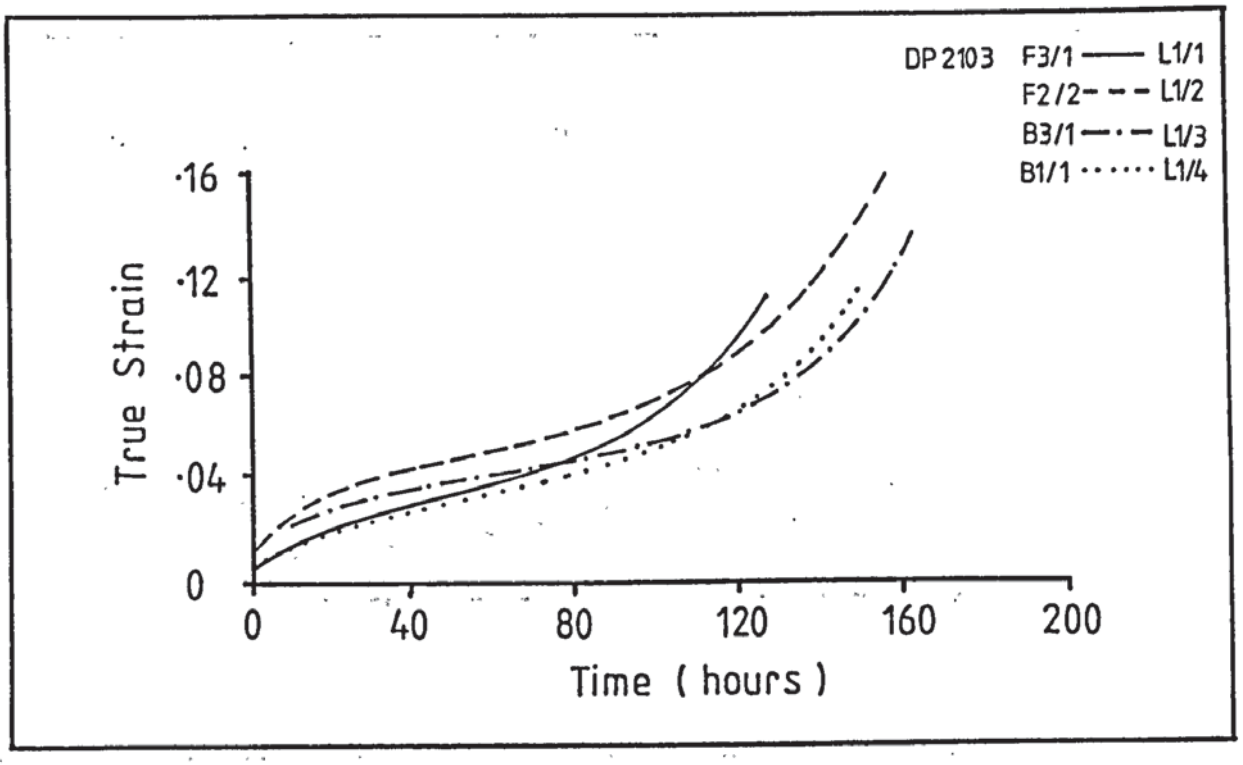

Figure 4.8h SRR 99 Creep tested at 750°C and 850MPa

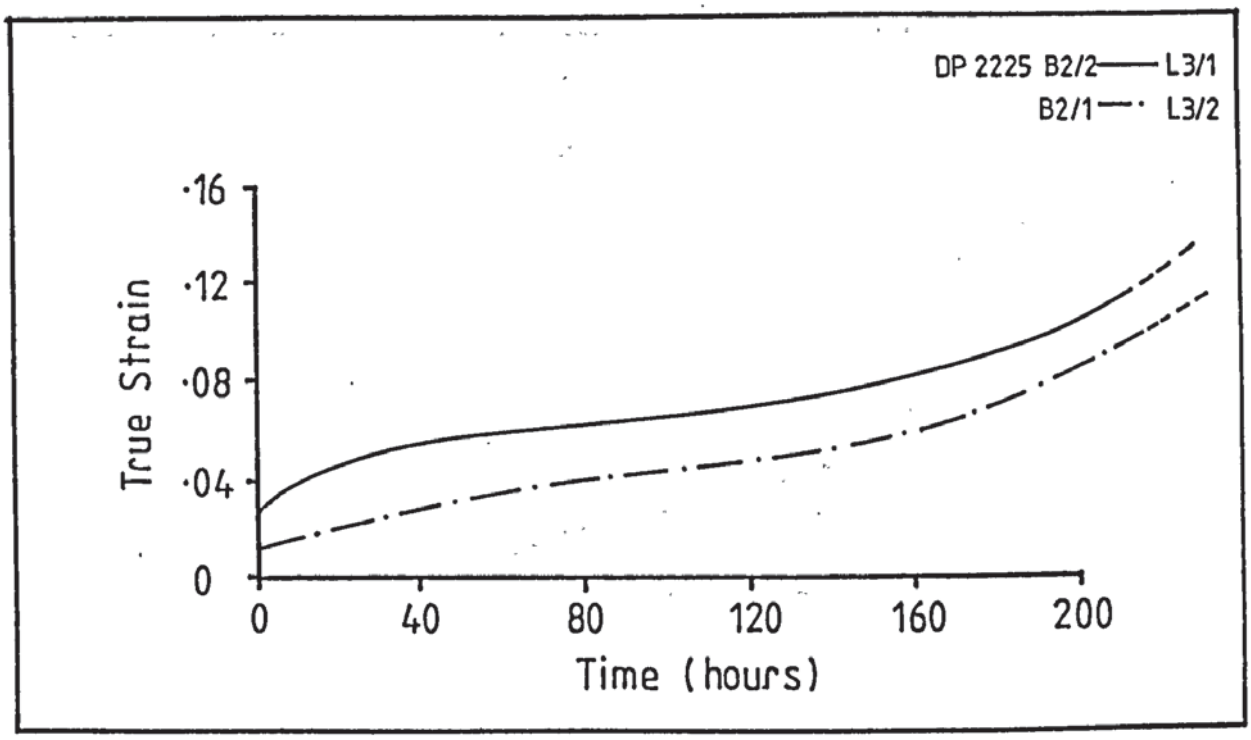

Figure 4.8i SRR 99 Creep tested at 750°C and 800MPa

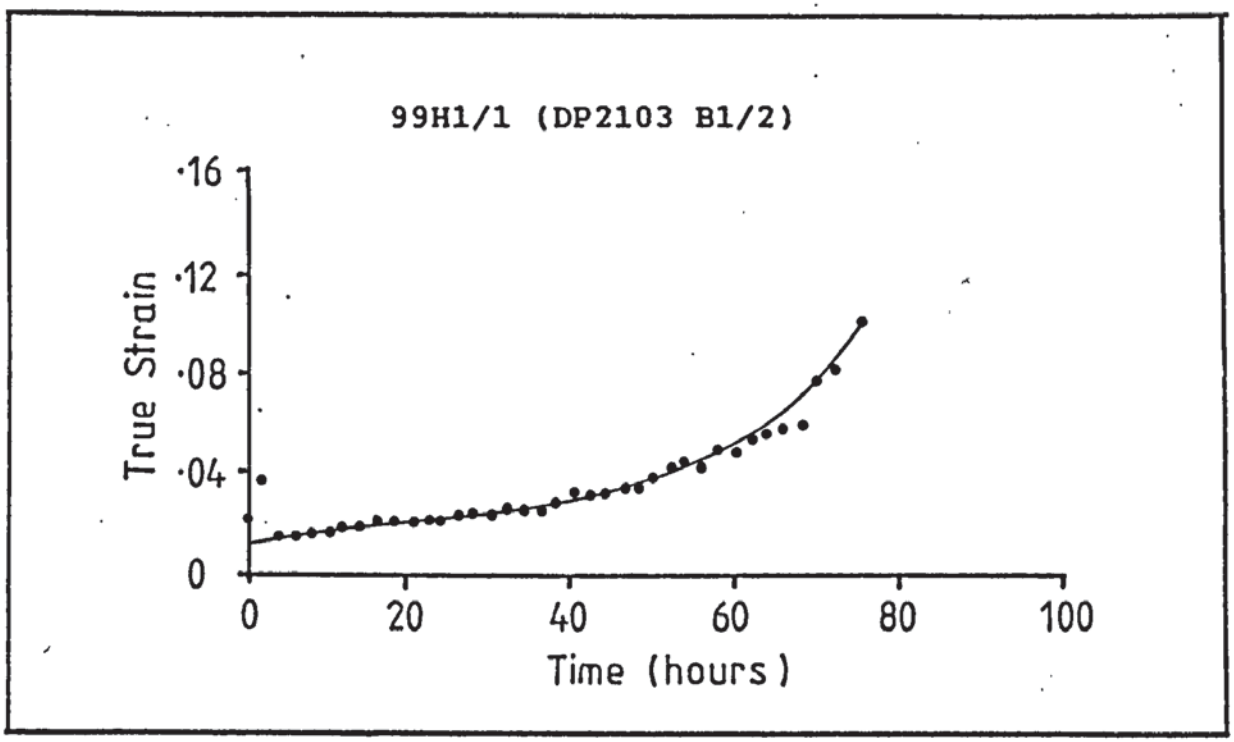

Figure 4.9a SRR 99 Creep tested at 850°C and 550MPa

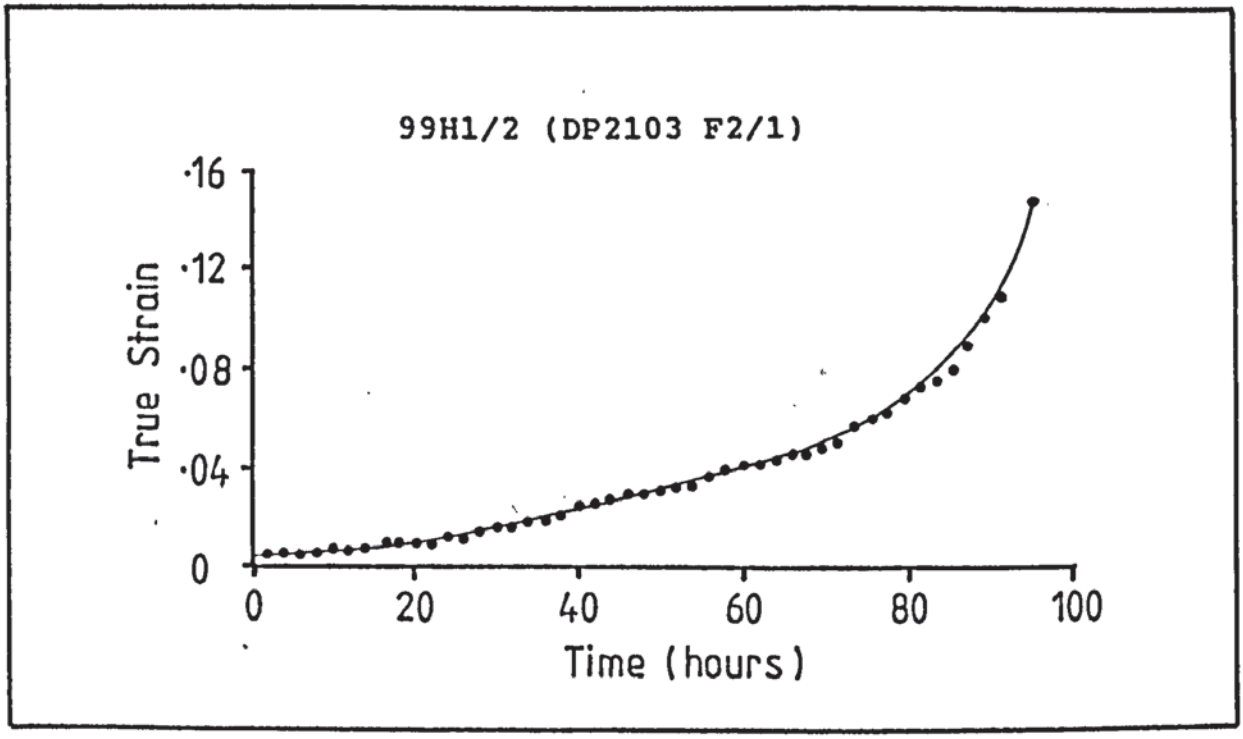

Figure 4.9b SRR 99 Creep tested at 850°C and 550MPa

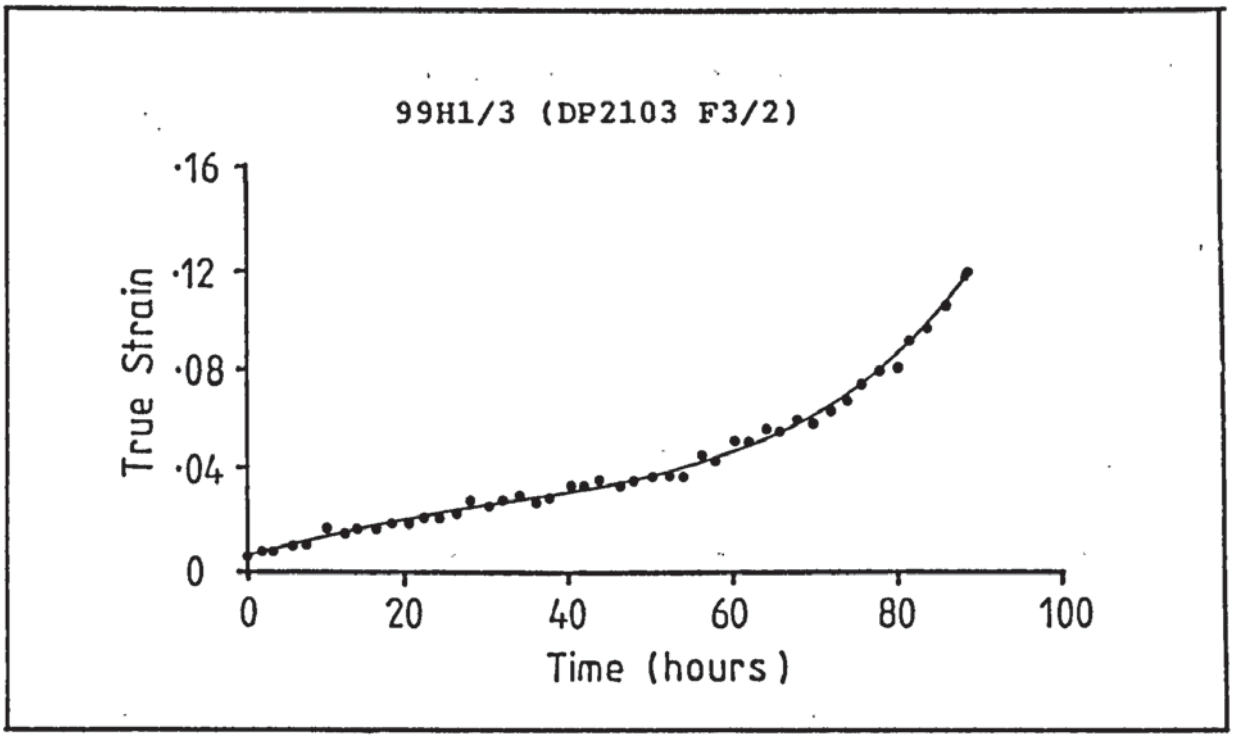

Figure 4.9c SRR 99 Creep tested at 850°C and 550MPa

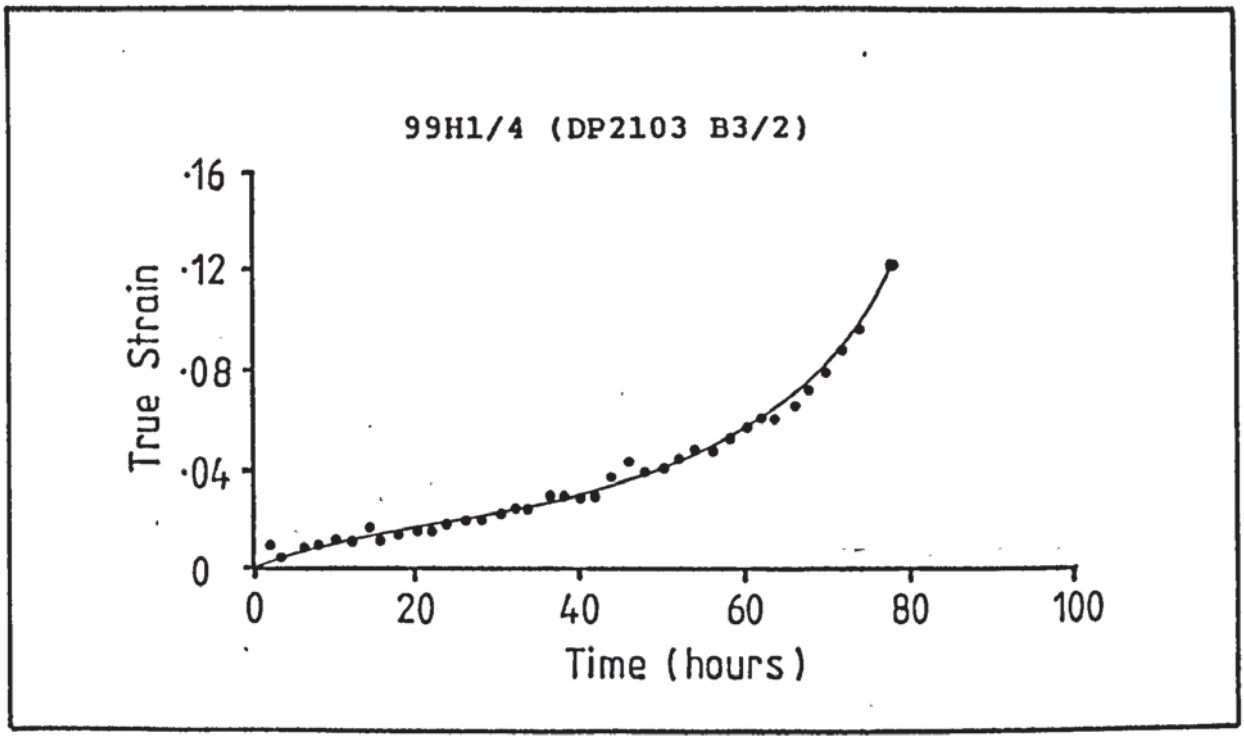

Figure 4.9d SRR 99 Creep tested at 850°C and 550MPa

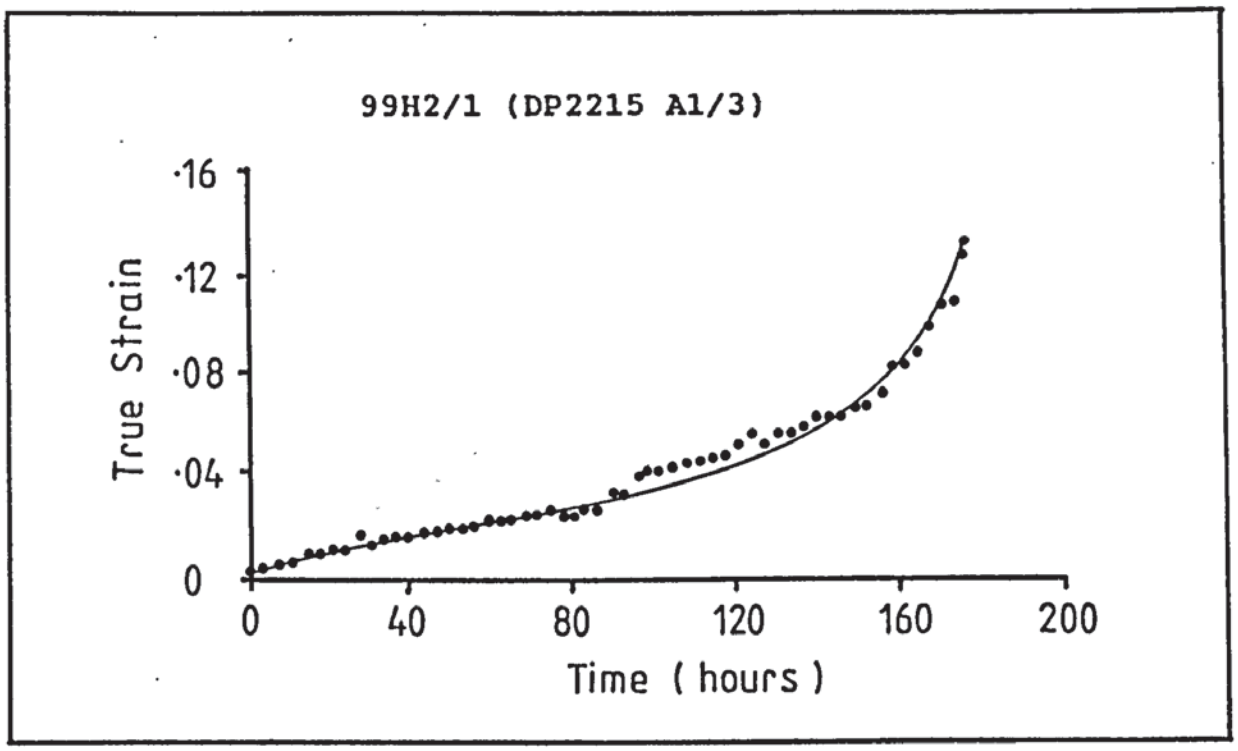

Figure 4.9e SRR 99 Creep tested at 850°C and 500MPa

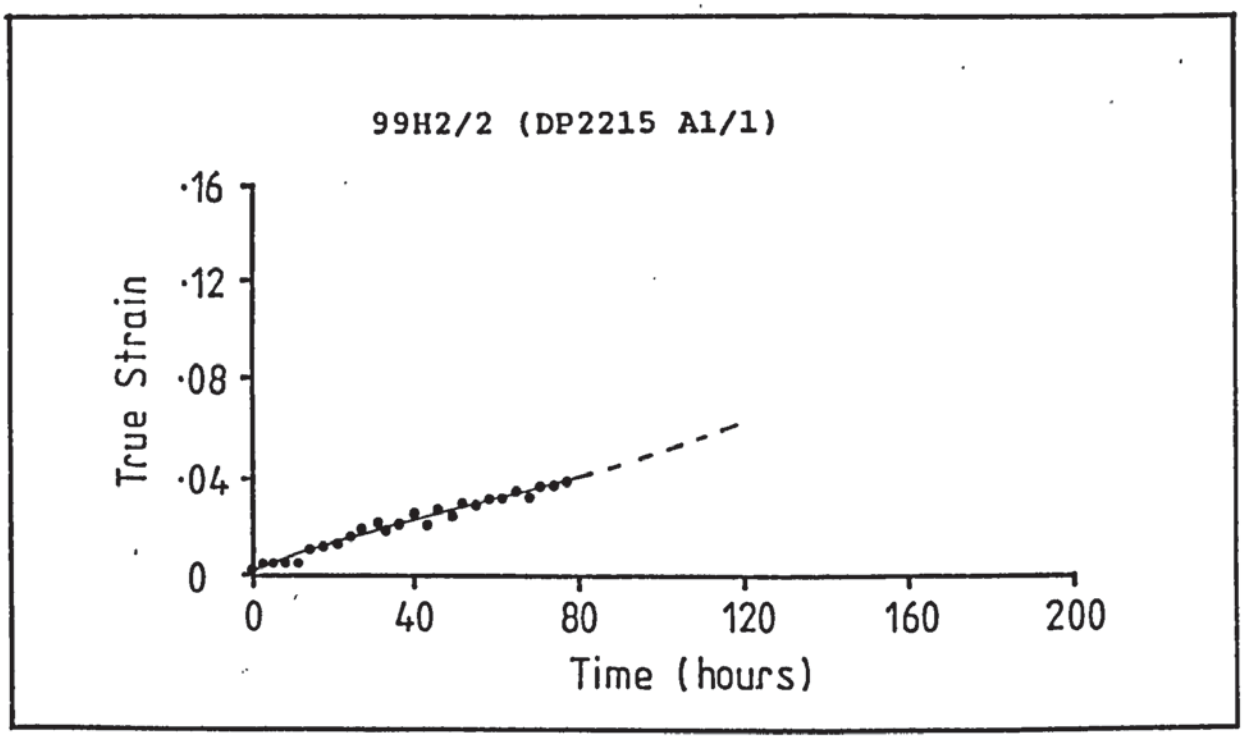

Figure 4.9f SRR 99 Creep tested at 850°C and 500MPa

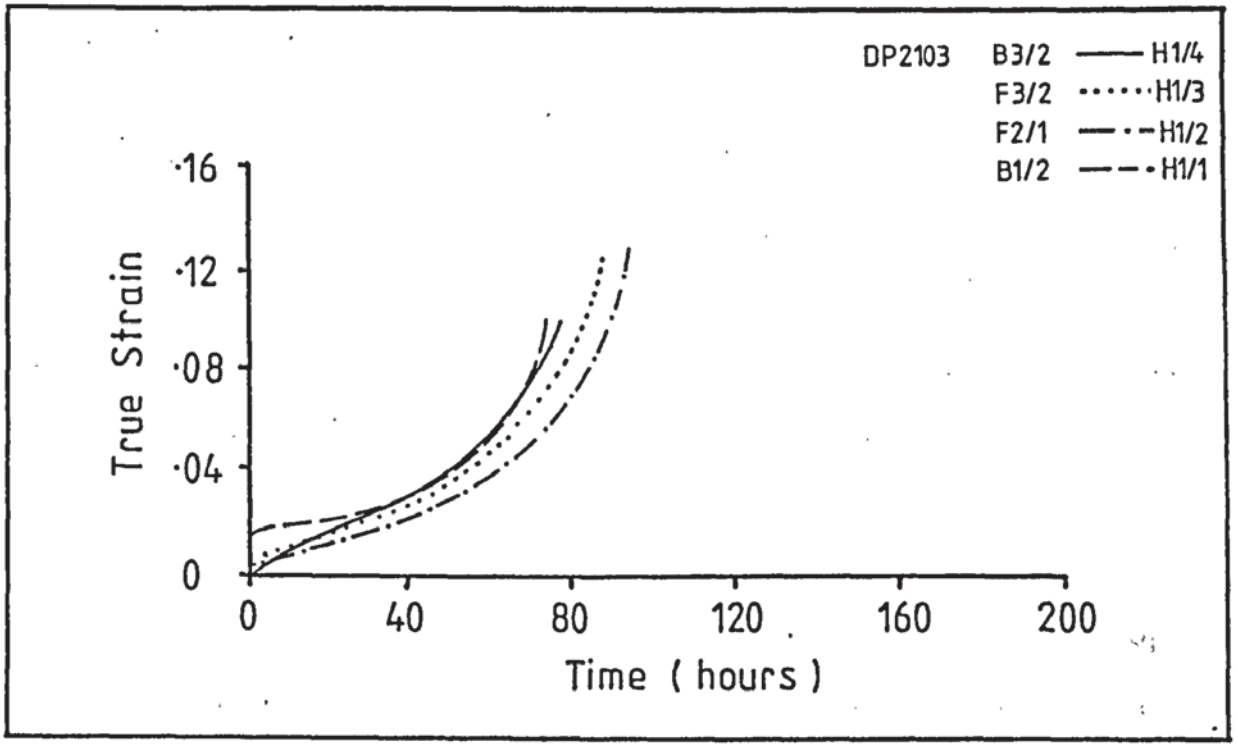

Figure 4.9g SRR 99 Creep tested at 850°C and 550MPa

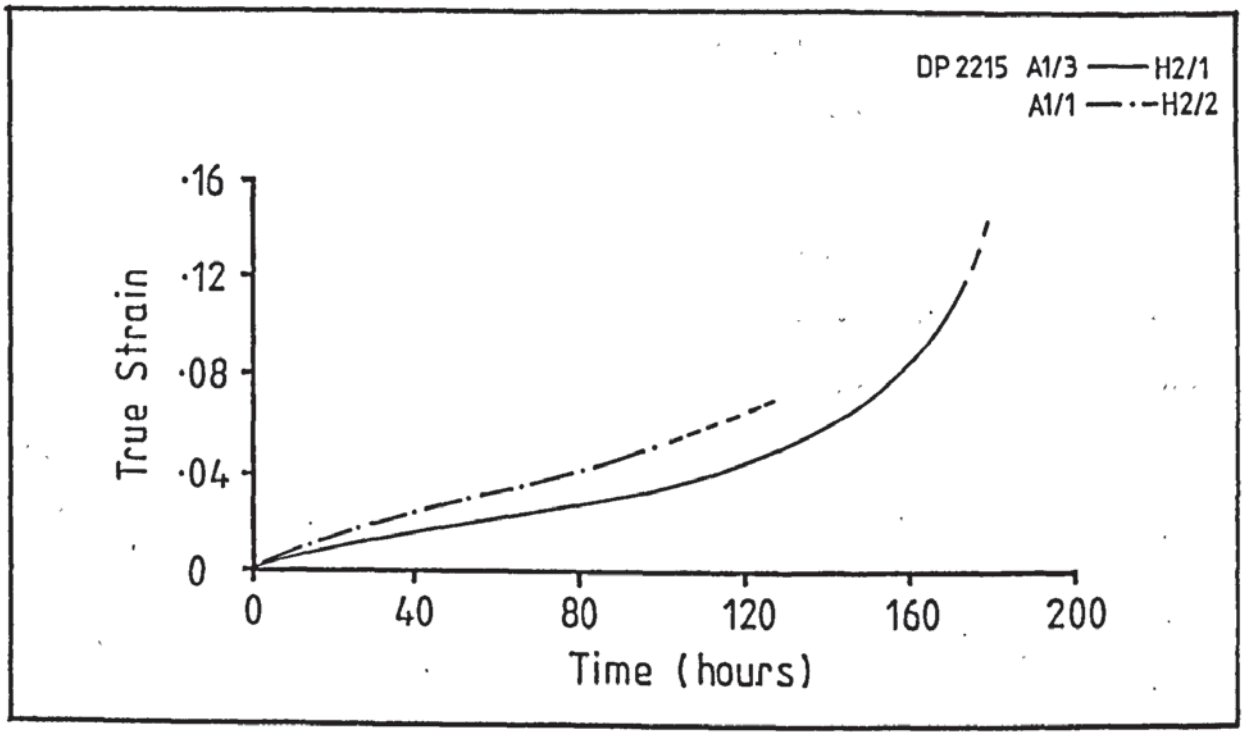

Figure 4.9h SRR 99 Creep tested at 850°C and 500MPa

4.3.2 Examination of SRR 99 creep fractures

Figure 4.10 shows typical creep fractures for specimens tested at 750°C. The fracture faces were found to be circular in cross section and square to the gauge length, indicating that several slip systems were active for the majority of the creep life. Due to the presence of an oxide film on the fracture face, examination was limited to low magnifications.

The creep fractures at both 850MPa and 800MPa exhibited similar features. On specimens which were retrieved from the creep machine shortly after fracture so that oxidation was limited, such as 99L1/1 (figure 4.10a), rectangular planar features were associated with the micropores. These appear to be due to cracks initiating at the pores as a consequence of the stress concentration in their vicinity. The cracks surrounding the micropores are linked by areas of a planar, crystallographic nature.

Figure 4.11 shows typical creep fractures for specimens tested at 850°C. The fractures for both 550MPa and 500 MPa stress conditions were found to be similar and exhibited the same features as for specimens tested at 750°C.

Figure 4.12 shows the features associated with micropores at higher magnification for specimen 99L1/3 tested at 750°C and 850MPa.

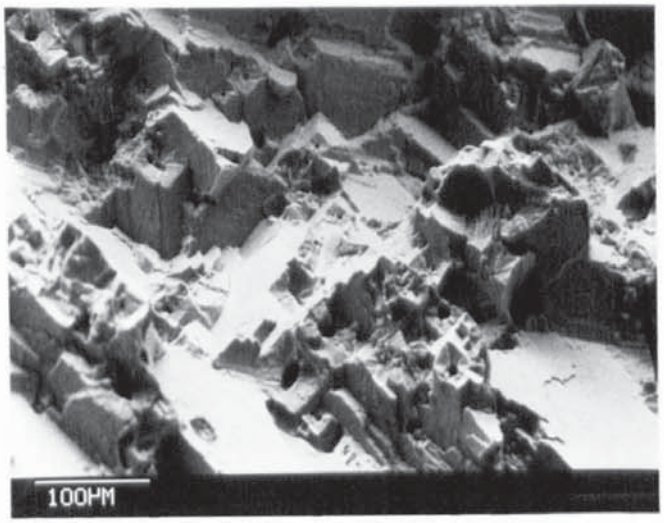

a)99L1/1
850MPa
Mag'n x150

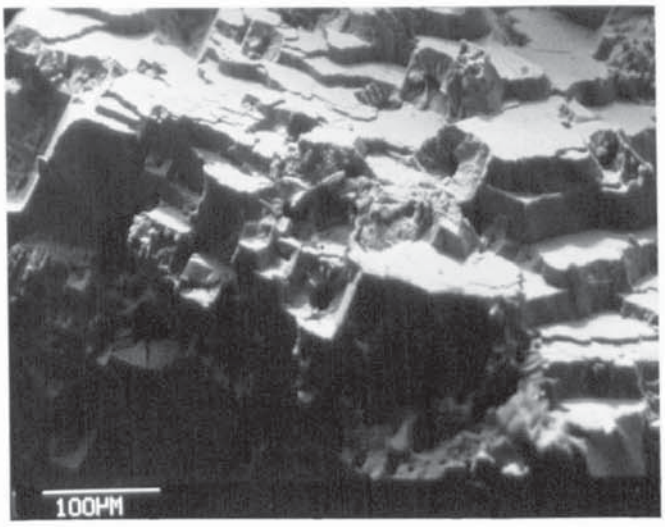

b)99L1/3
850MPa
Mag'n x150

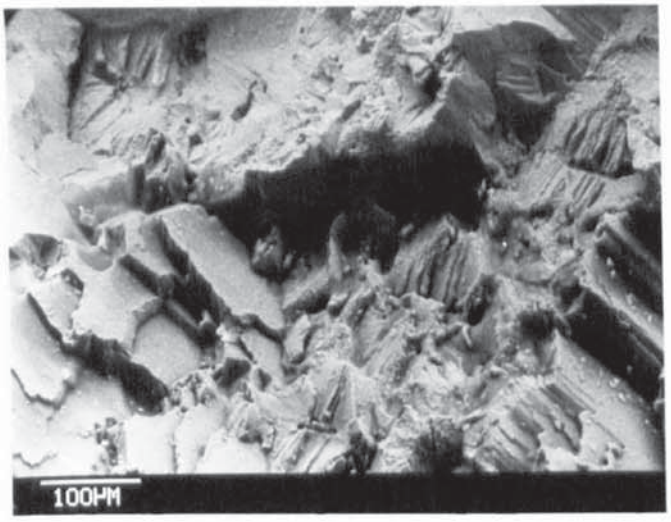

c)99L3/1
800MPa
Mag'n x140

Figure 4.10 Creep fractures for alloy SRR 99 tested at 750°C

a)99H1/2
550MPa
Mag'n x150

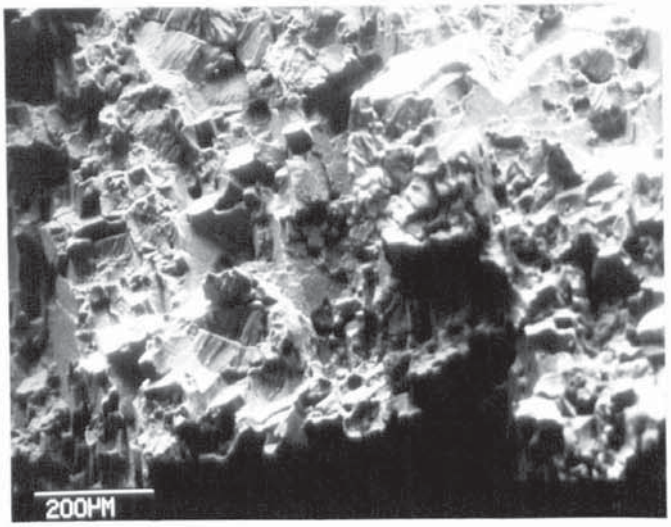

b)99H1/4
550MPa
Mag'n x75

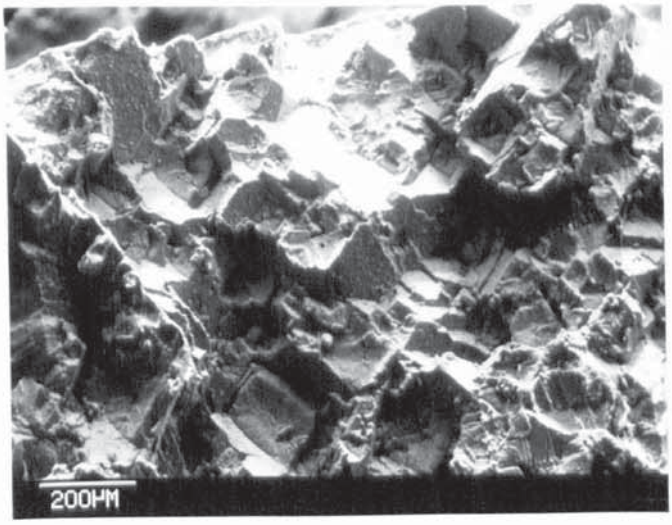

c)99H2/1
500MPa
Mag'n x60

Figure 4.11 Creep fractures for alloy SRR 99 tested at 850°C

a)99L1/3
Mag'n
x1450

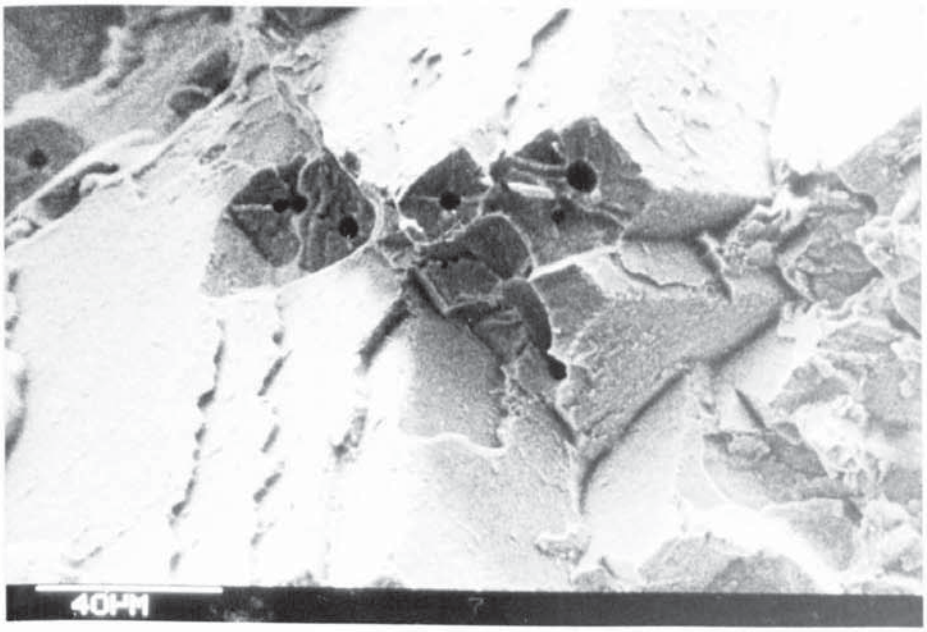

b)99L1/3
Mag'n
x600

Figure 4.12 Creep fractures for SRR 99 tested at 750°C and 850MPa

4.3.3 The effect of orientation on SRR 99 creep properties

Creep properties for SRR 99 were analysed with respect to crystal orientation. Crystal rotation experiments were also undertaken in order to indicate the type of operating slip system. The initial and final tensile axis orientation for SRR 99 creep specimens are shown in table 4.5. The data in brackets was supplied by Rolls-Royce Ltd; using 'SCORPIO', the computerised orientation analysis system.

Figure 4.13 portrays the crystal rotation results graphically with reference to a unit stereographic triangle for specimens tested at 750°C and 850MPa. The creep rupture times for the specimens are also given in order to indicate the effect of orientation on creep life. Figure 4.14 portrays the results for specimens tested at 850°C and 550MPa.

Table 4.5 SRR 99 orientation and crystal rotation results

Specimen	Initial		Final	
	θ degrees	℘ degrees	θ degrees	℘ degrees
99L1/1	3.5 (2.7)	44 (26.4)	3	35
99L1/2	2 (2.1)	6 (7.9)	2.5	0
99L1/3	1.25 (1.2)	18 (15.3)	--	--
99L1/4	5 (4.9)	22 (30.6)	--	--
99L2/1	(4.9)	(30.6)	--	--
99L3/1	(3.4)	(21.1)	--	--
99L3/2	(3.4)	(21.1)	--	--
99H1/1	6 (4.9)	16 (30.6)	1	27.5
99H1/2	3 (2.1)	20 (7.9)	2.5	9.5
99H1/3	2.5 (2.7)	35 (26.4)	--	--
99H1/4	(1.2)	(15.3)	2.5	25
99H2/1	(5.0)	(39.4)	--	--
99H2/2	(5.0)	(39.4)	--	--

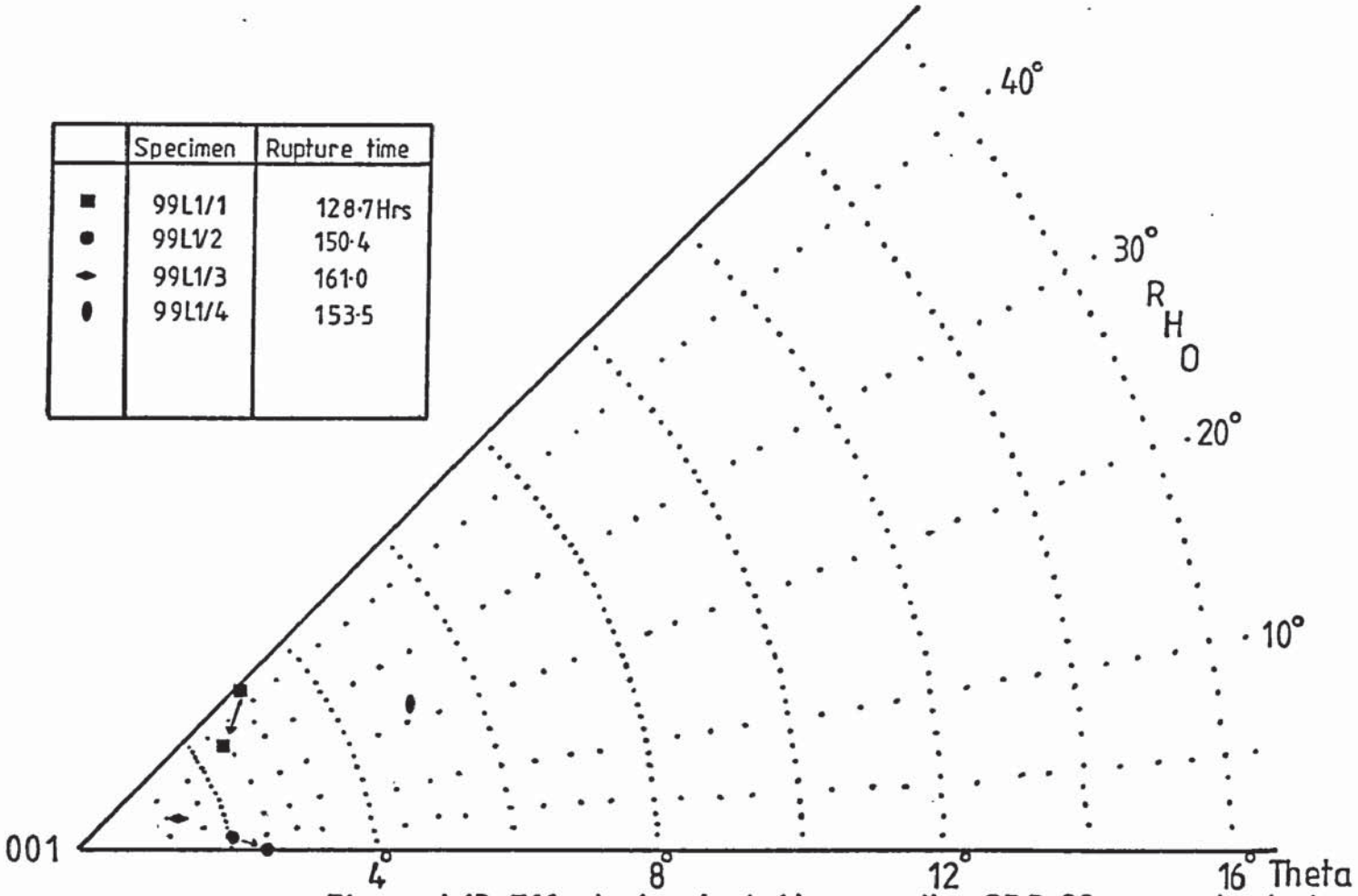

Figure 4·13 Effect of orientation on alloy SRR 99 creep tested at 750°C and 850MPa

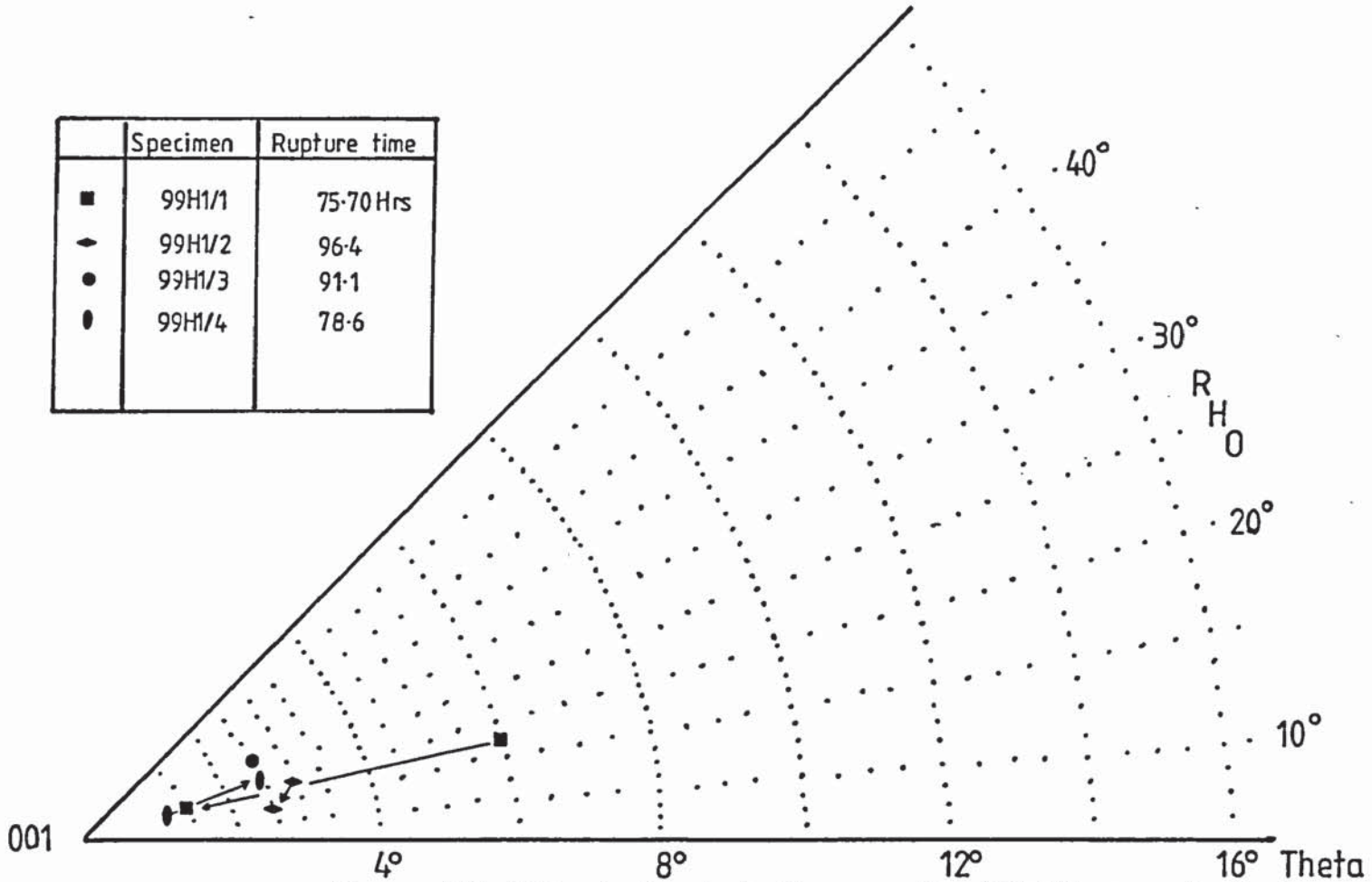

Figure 4·14 Effect of orientation on alloy SRR99 creep tested at 850°C and 550MPa

4.4 Smooth bar fatigue life results.

Smooth bar fatigue life tests were carried out using a sinusoidal waveform at a frequency of 40Hz and temperatures of 750°C and 850°C, as described in section 3.7.

Specimens of alloy SRR 99 were tested with an electropolished initiation surface. Three specimen orientations were tested, as shown in figure 3.2. As previously stated, failure of the seed crystals during casting meant that specimens had to be machined from the cast blocks at an angle to produce the desired orientation. In order to confirm the final orientations, two specimens from each block were examined by the Laue back reflection x-ray method. For each specimen, the top and side faces were analysed to determine the 3 dimensional specimen orientation.

The specimens are denoted by the following codes in order to simplify reference to the results:

FL1	Smooth fatigue tested at 750°C (001)-(100)
FL2	Smooth fatigue tested at 750°C (001)-(210)
FL3	Smooth fatigue tested at 750°C (001)-(110)
FH1	Smooth fatigue tested at 850°C (001)-(100)
FH2	Smooth fatigue tested at 850°C (001)-(210)
FH3	Smooth fatigue tested at 850°C (001)-(110)

Where the orientation is given for the top (initiation) and side (transverse) face respectively. The orientation results are given in table 4.6. Table 4.7 gives the smooth bar fatigue life results.

Figure 4.15 shows the fatigue life results for specimens tested at 750°C graphically in terms of applied stress range versus cycles to failure, figure 4.16 giving the results for specimens tested at 850°C. The results are compiled and shown in figure 4.17 in order that the effect of orientation and temperature on fatigue life may be examined.

Table 4.6 Smooth bar fatigue specimen orientations

Specimen	Cast No	nominal Orientation	Top face		Side face	
			θdegrees	ϕdegrees	θdegrees	ϕdegrees
FL1/2	S38233 8 POS3	(001)-(100)	4.5	6.5	8	36
FH1/2	8 POS5	(001)-(100)	2.0	6.0	6	28
FL2/1	2 POS2	(001)-(210)	2.0	36	21	4
FL2/4	2 POS5	(001)-(210)	4	1.0	20	2
FH3/2	11 POS5	(001)-(110)	4	25	32.5	1
FL3/1	11 POS1	(001)-(110)	6.5	22	33	3
FH3/4	1956J POS10	(001)-(210)	1	24	28	4

Table 4.7 Smooth bar fatigue life results

Temp	Orientation	Specimen No	Cast No	σ_{min} MPa	σ_{max} MPa	$\Delta\sigma$ MPa	cycles $x10^3$	load KN
	(001)-(100)	FL1/1	S38233 8 POS2	87.83	748.81	668.99	510.4	7.63
750°C	(001)-(100)	FL1/2	8 POS3	80.99	878.71	797.73	139.5	8.74
	(001)-(100)	FL1/3	8 POS4	96.29	984.77	888.48	98.41	9.77
	(001)-(100)	FL1/4	8 POS6	83.38	757.63	674.24	459.7	7.33
	(001)-(210)	FL2/1	2 POS2	82.67	854.71	772.04	134.0	8.56
750°C	(001)-(210)	FL2/2	2 POS3	108.15	937.09	828.94	131.61	9.1
	(001)-(210)	FL2/3	2 POS4	93.81	792.67	698.87	264.34	7.67
	(001)-(210)	FL2/4	2 POS5	96.77	885.6	767.79	173.66	8.41
	(001)-(110)	FL3/1	11 POS1	95.47	948.4	858.65	233.45	9.44
750°C	(001)-(110)	FL3/2	11 POS3	82.74	829.0	746.26	359.86	8.21
	(001)-(110)	FL3/3	11 POS7	81.53	906.67	825.14	326.65	8.81
	(001)-(100)	FH1/1	8 POS1	85.13	893.89	808.76	339.18	8.79
850°C	(001)-(100)	FH1/2	8 POS5	81.24	810.94	729.70	1213.0	7.91
	(001)-(100)	FH1/3	8 POS7	89.29	1006.6	917.37	149.63	10.05
	(001)-(210)	FH2/1	1956J POS7	83.72	842.6	750.5	764.19	8.34
	(001)-(210)	FH2/2	POS8	85.54	931.3	840.84	227.34	9.24
	(001)-(210)	FH2/3	POS9	73.71	825.33	751.21	849.21	8.21
850°C	(001)-(210)	FH2/4	POS10	95.10	950.1	855.4	31.91	9.4
	(001)-(210)	FH2/5	S38233 2 POS1	107.9	869.04	761.10	467.47	8.32
	(001)-(210)	FH2/6	2 POS6	107.53	1074.3	966.82	66.67	10.42
	(001)-(210)	FH2/7	2 POS7	89.83	994.53	904.70	176.84	9.87
	(001)-(110)	FH3/1	11 POS4	83.47	867.85	784.38	535.63	8.52
850°C	(001)-(110)	FH3/2	11 POS5	83.31	839.87	756.57	1081.8	8.38
	(001)-(110)	FH3/3	11 POS6	91.29	978.62	898.84	262.88	9.846

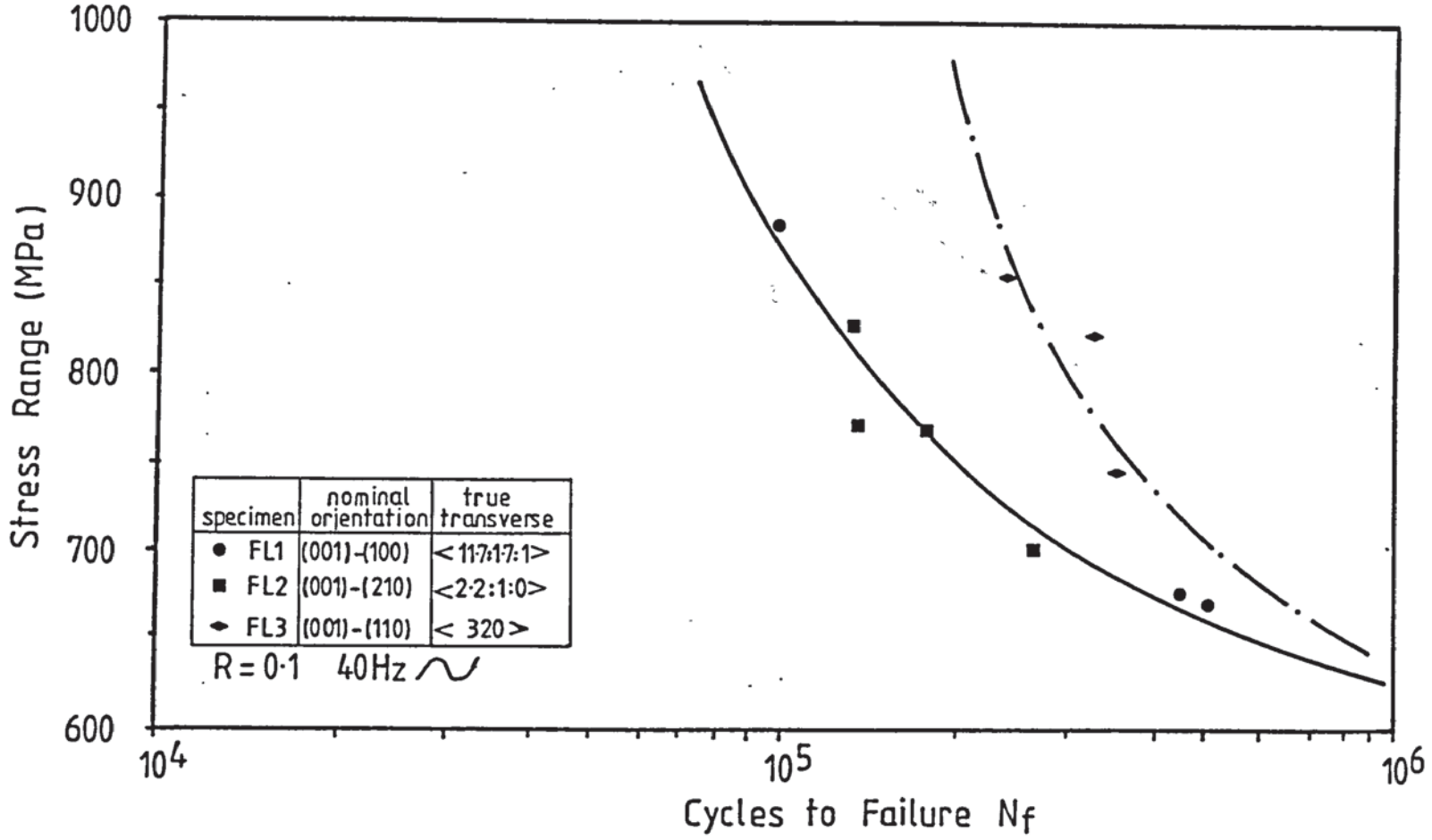

Figure 4·15 Effect of transverse orientation on fatigue life at 750°C

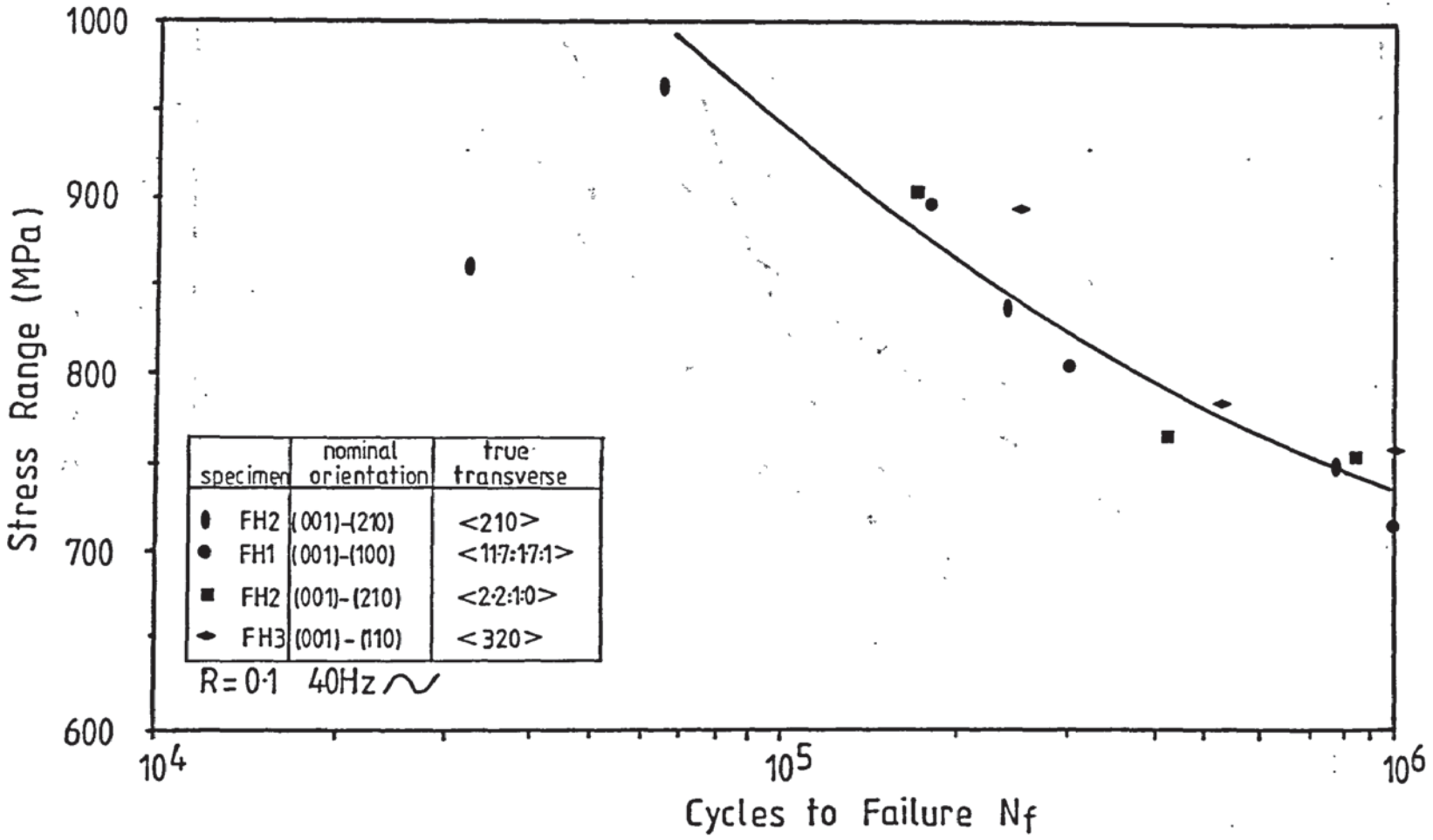

Figure 4·16 Effect of orientation on fatigue life at 850°C

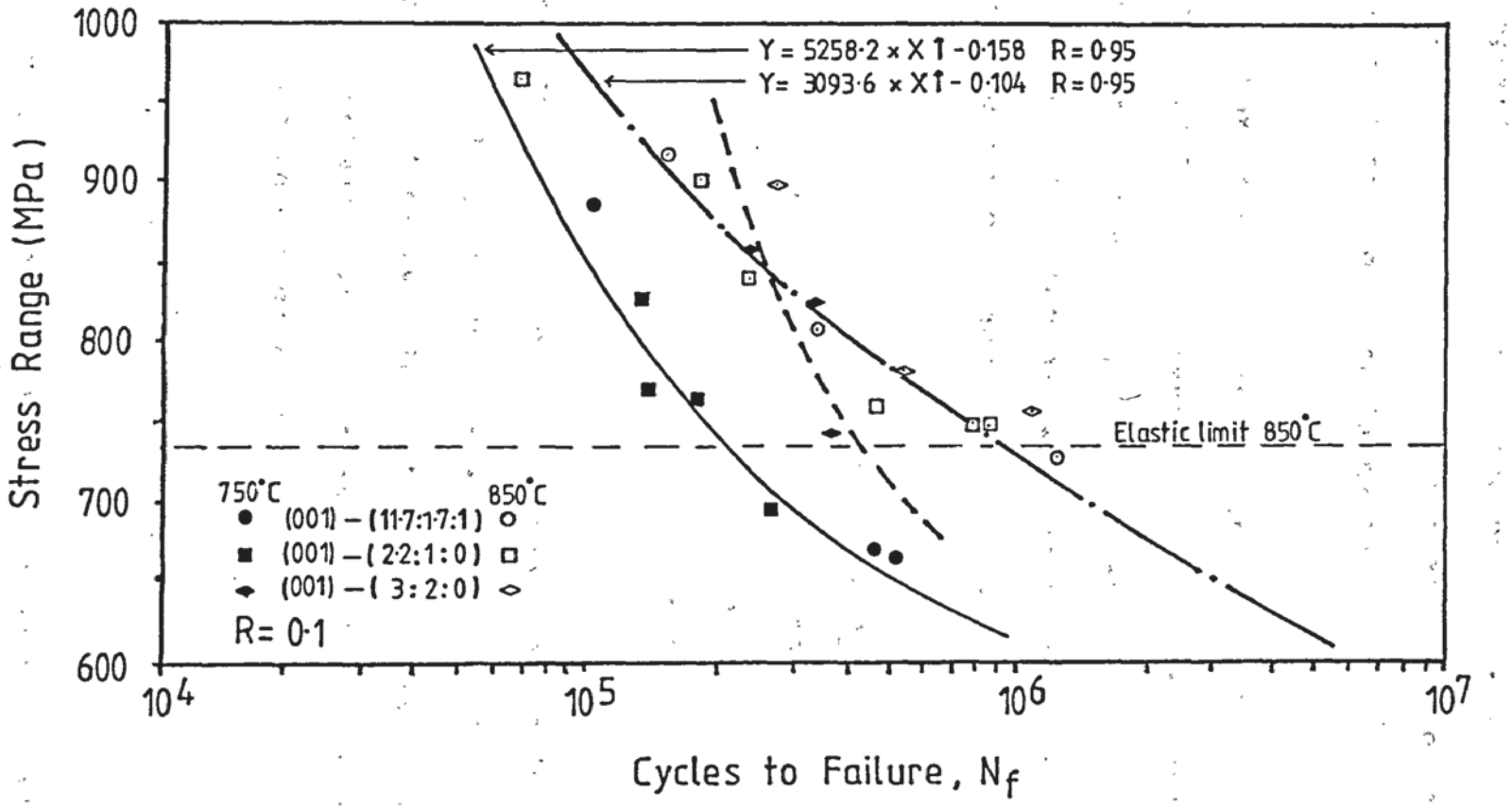

Figure 4·17 Effect of temperature and orientation on fatigue life of SRR 99

4.4.1 Indexing a Laue back reflection orientation result

In order to examine the effect of orientation on fatigue properties, the following procedure was used to produce direction indices for the top and side orientations for the three types of specimens tested.

For the example of specimen FL2/4 (S38233-2 POS5 (001)-(210)); the centre of the strereographic projection produced from the Laue back reflection film from the side face of the specimen was found to be related to a unit stereographic triangle as follows:

spot	distance	Cosθ
(001)	21.5°	0.930
(011)	24°	0.9135
(111)	38.5°	0.7826

As the Laue technique does not produce a specific orientation, a unit triangle of standard indices may be used to simplify calculation. From coordinate geometry the angle between two directions of direction cosines $l_1\ m_1\ n_1$ and $l_2\ m_2\ n_2$ is given by:

$$\text{Cos}\theta = l_1 l_2 + m_1 m_2 + n_1 n_2 \qquad \ldots\ldots (4.1)$$

Where l_i, m_i and n_i are the direction cosines of the plane normals. l_f, m_f, n_f are the direction cosines of the centre of the projection $[U_f V_f W_f]$. Direction cosines may be obtained from direction indices from the formula:

$$l = \frac{U}{\sqrt{(U^2+V^2+W^2)}}, \quad m = \frac{V}{\sqrt{(U^2+V^2+W^2)}}, \quad n = \frac{W}{\sqrt{(U^2+V^2+W^2)}} \quad \ldots (4.2)$$

The direction cosines of the centre of the projection may be related to the three unit triangle indices to produce three equations with three unknowns. These may be written as matrices:

$$\begin{bmatrix} \cos\theta_1 \\ \cos\theta_2 \\ \cos\theta_3 \end{bmatrix} = \begin{bmatrix} l_1 & m_1 & n_1 \\ l_2 & m_2 & n_2 \\ l_3 & m_3 & n_3 \end{bmatrix} \begin{bmatrix} l_f \\ m_f \\ n_f \end{bmatrix} \quad \ldots\ldots (4.3)$$

Rearranging:

$$\begin{bmatrix} l_f \\ m_f \\ n_f \end{bmatrix} = \begin{bmatrix} l_1 & m_1 & n_1 \\ l_2 & m_2 & n_2 \\ l_3 & m_3 & n_3 \end{bmatrix}^{-1} \begin{bmatrix} \cos\theta_1 \\ \cos\theta_2 \\ \cos\theta_3 \end{bmatrix} \ldots\ldots (4.4)$$

For all cases examined, the same unit triangle indices were used. In terms of direction cosines:

$$\begin{bmatrix} l_f \\ m_f \\ n_f \end{bmatrix} = \begin{bmatrix} 0 & 0 & 1 \\ 0 & 0.707 & 0.707 \\ 0.577 & 0.577 & 0.577 \end{bmatrix}^{-1} \begin{bmatrix} \cos\theta_1 \\ \cos\theta_2 \\ \cos\theta_3 \end{bmatrix} \ldots\ldots (4.5)$$

The inverse of this matrix is:

$$\begin{bmatrix} l_f \\ m_f \\ n_f \end{bmatrix} = \begin{bmatrix} 0 & -1.414 & 1.733 \\ -1 & 1.414 & 0 \\ 1 & 0 & 0 \end{bmatrix} \begin{bmatrix} \cos\theta_1 \\ \cos\theta_2 \\ \cos\theta_3 \end{bmatrix} \ldots\ldots (4.6)$$

For the example given:

$$l_f = 0 + (-1.414 \times 0.9135) + (1.733 \times 0.7826) = 0.0646$$
$$m_f = (-1 \times 0.93) + (1.414 \times 0.9135) + 0 = 0.3617 \quad ..(4.7)$$
$$n_f = (1 \times 0.7826) = 0.7826$$

Now let $\sqrt{(U^2+V^2+W^2)}=A$ and rearranging equations 4.2:

$$U = lA,\ V = mA,\ W = nA \text{ therefore } \frac{U}{l} = \frac{V}{m} = \frac{W}{n}$$

$$U = \frac{Vl}{m} \quad \text{But } \frac{U}{l} = \frac{W}{n} \quad \text{therefore } \frac{Vl}{ml} = \frac{W}{n}$$

Let U = 1 then Vl = m

So: $V = m/l = 0.3617/0.0646 = 5.599$

$W = Vn/m = 5.599 \times 0.7826/.3617 = 12.114$

Therefore the indices are:

< 1 : 5.6 : 12.1 >

divide through by 5.6:

< 0.18 : 1 : 2.16 >

ie near <012>. Table 4.8 gives the results for the transverse orientations of the three specimen types. The top face orientation of all three types was found to be near <001>. The orientation results shown in table 4.6 are illustrated in figure 4.18 with respect to a stereographic unit triangle.

Table 4.8 Transverse orientation indices

Specimen No	Cast No	Nominal Orientation	Indices <UVW>
FL1/3	S38233 8 POS3	(001)-(100)	<1 : 1.71 : 11.63>
FL2/4	2 POS5	(001)-(210)	<0.18 : 1 : 2.16>
FL3/1	11 POS1	(001)-(110)	<0 : 1 : 1.6>

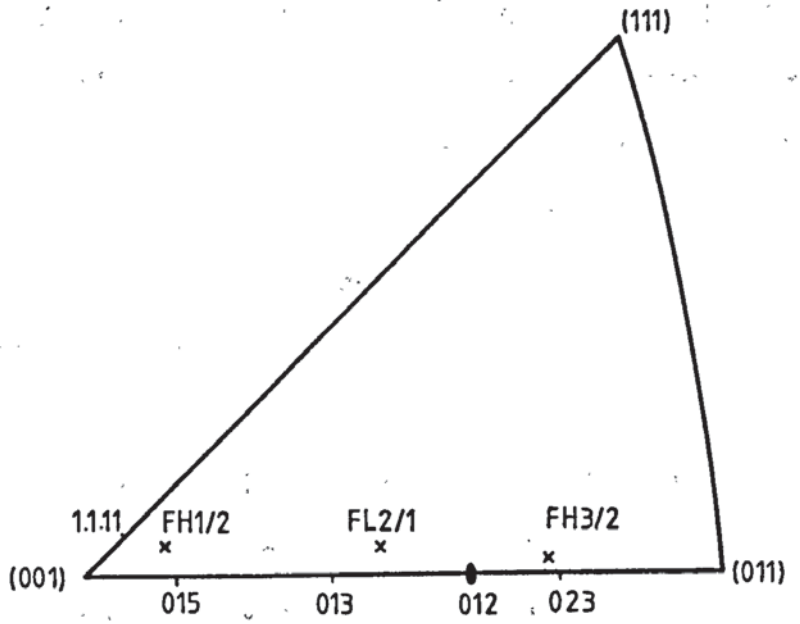

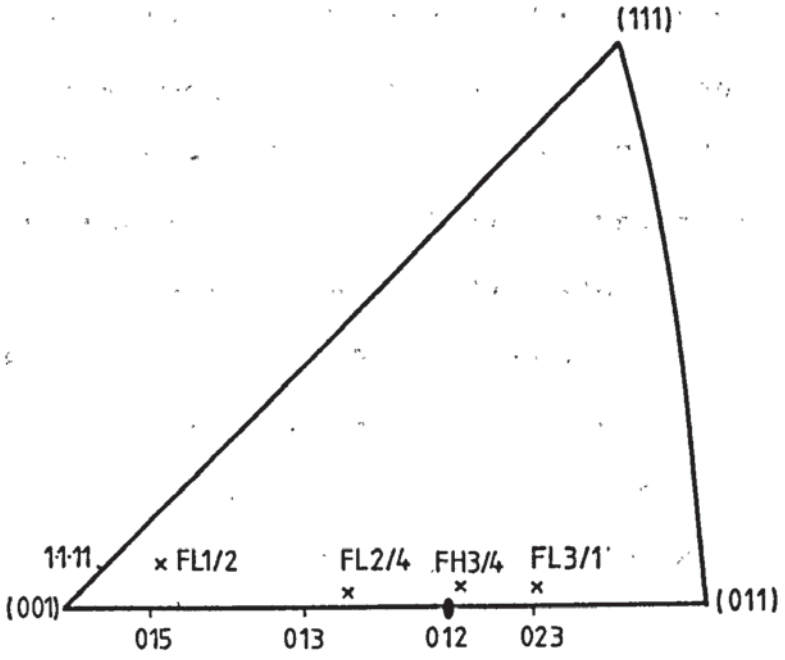

Figure 4.18 Transverse orientations for smooth bar fatigue specimens

4.4.2 Examination of SRR 99 smooth bar fatigue fractures

Figures 4.19 and 4.20 illustrate the fracture surfaces produced by smooth bar fatigue testing using sine wave loading at a frequency of 40Hz. Two specimens for each orientation are shown with the electropolished initiation face at the top of the frame.

The specimens will be referred to as having a transverse orientation near {100},{210} or {320} for convenience , the accurate orientation being given in figure 4.18 and table 4.8.

Figure 4.19 illustrates fatigue fractures for specimens tested at 750°C. Specimens having {11.7:1.7:1} and {2.2:1:0.2} (ie nominal {100} and {210}) side faces) were found to have mainly crystallographic fractures. The {001}-near{100} specimens exhibited more than one facet. Figure 4.19a shows for specimens FL1/1 and FL1/2, initial crack growth started on one plane before transferring to another crystallographic plane for the majority of crack propagation. For {001}-near{210} specimens, initiation and propagation took place on one main crystallographic plane, as illustrated in figure 4.19b. In the case of {001}-near{320} specimens, the fractures were found to be of mixed mode,a proportion of the fracture surface being non crystallographic. This portion was found to be normal to the applied stress. The faceted area was found to be associated with the top surface of the specimen.

Figure 4.20 shows fatigue fractures for specimens tested at 850°C. {001}-near{100} specimens were found to have crystallographic fractures of similar nature to those observed in specimens tested at 750°C. specimens of {001}-near{210} orientation were found to have fracture surfaces containing a lower proportion of facets than specimens tested at 750°C, all the specimens having a mixed fracture mode. {001}-near{320} specimens were also found to have a mixed fracture mode, with the majority of the fracture non crystallographic. Two of the specimens were found to have subcutaneous crack initiation sites, several millimetres from the top surface.

Figures 4.21a to c show examples of the two types of fracture surface observed. Figures 4.21a and b illustrate the nature of the crystallographic facets. These were found to be smooth and in all cases exhibited a dendritic pattern. Boundaries between twodifferently oriented facets were sharp with no transition area discernable.

Figure 4.21c gives an example of a non-crystallographic fracture. The area surrounding the initiation site was smooth, indicating appreciable crack closure during the early stages of crack growth. The main region was found to be planar, running normal to the top face. Distinctive ridges were observed in all cases, running vertically down the face. These appear to be the positions of the main dendrite arms.

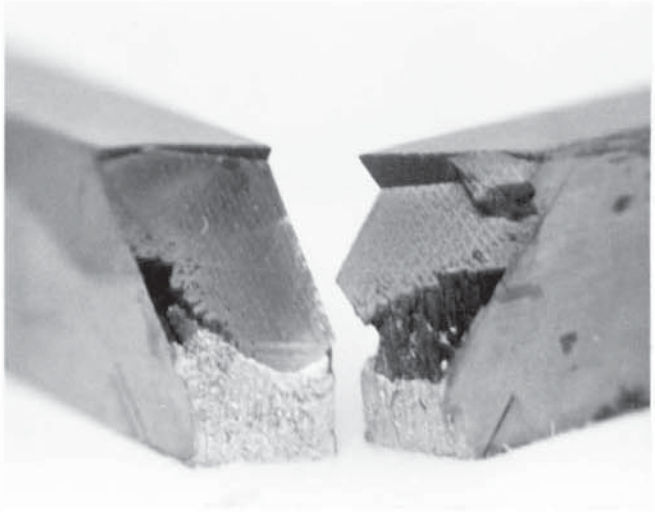

a) FL1/1 FL1/2
{001}-{100}
Mag'n x4

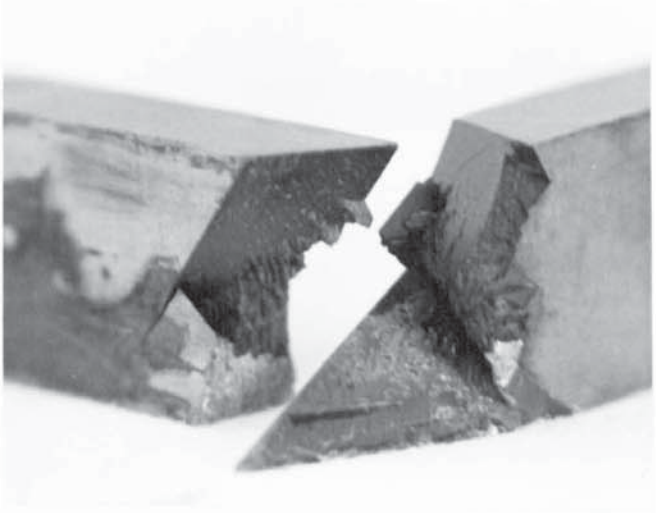

b) FL2/1 FL2/3
{001}-{210}
Mag'n x4

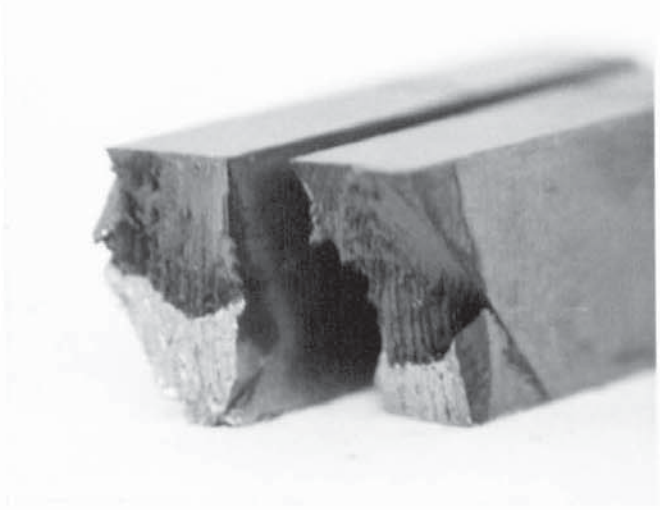

c) FL3/2 FL3/1
{001}-{320}
Mag'n x4

Figure 4.19 Smooth bar fatigue fractures for alloy SRR 99 tested at 750°C

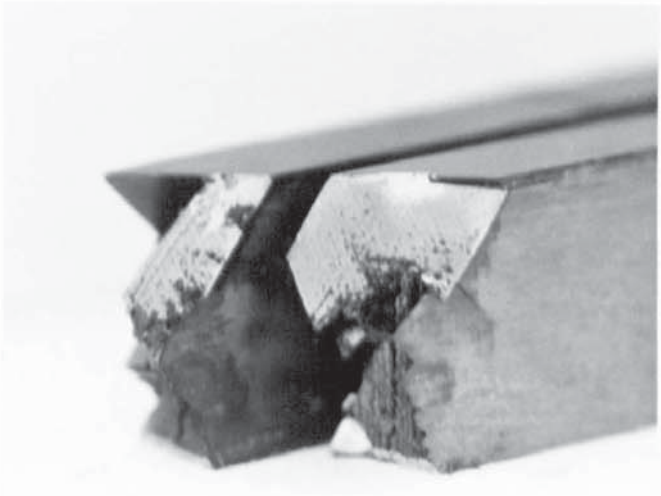

a) FH1/2 FH1/1
{001}-{100}
Mag'n x4

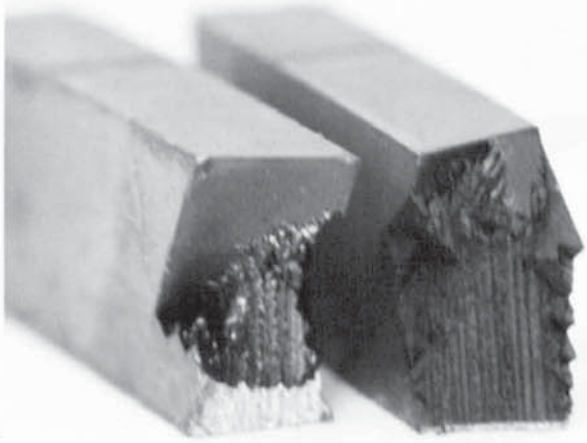

b) FH2/7 FH2/6
{001}-{210}
Mag'n x4

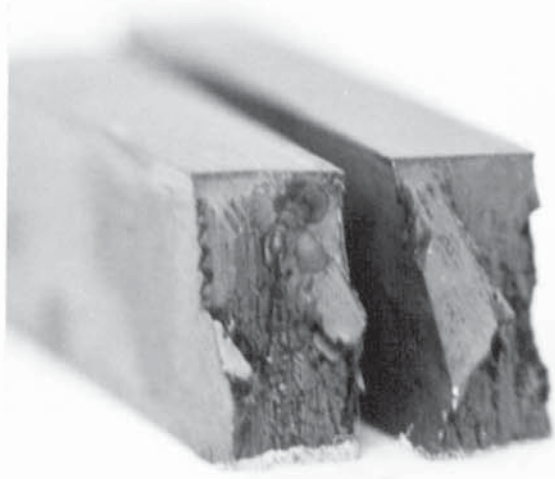

c) FH3/3 FH3/2
{001}-{320}
Mag'n x4

Figure 4.20 Smooth bar fatigue fractures for alloy SRR 99 tested at 850°C

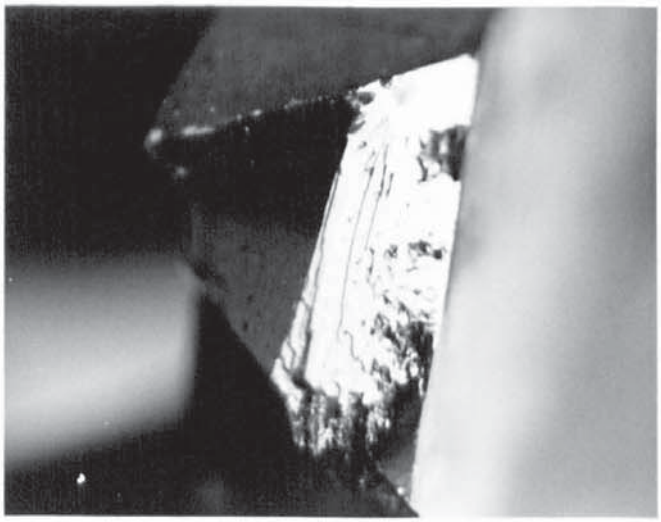

a) FH1/2

{001}-{100}

850°C

Mag'n x7

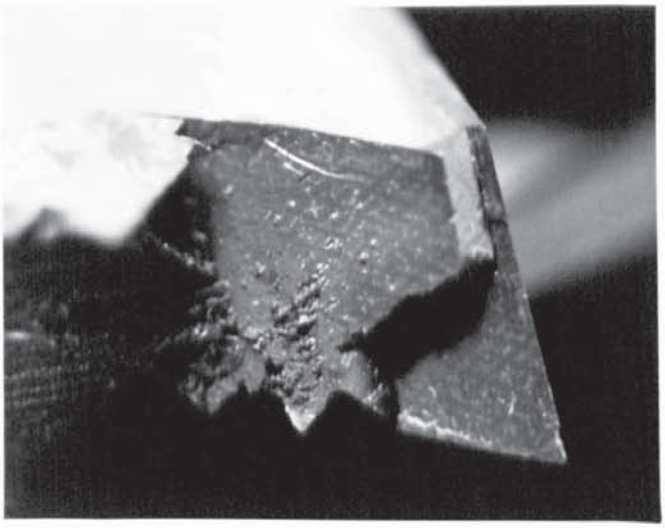

b) FH1/1

{001}-{100}

850°C

Mag'n x7

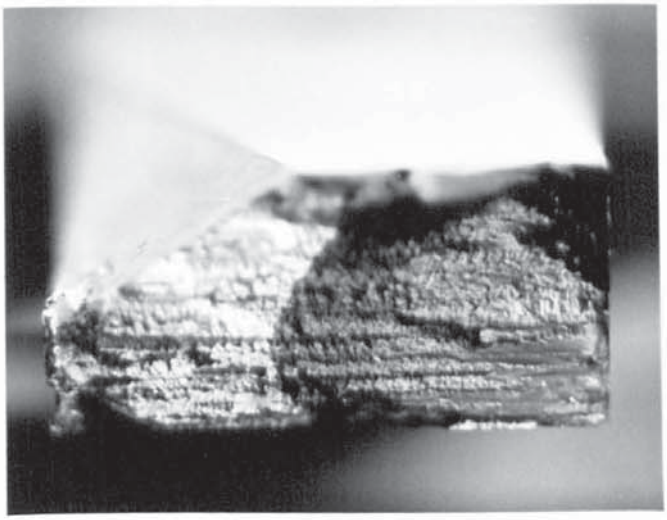

c) FL3/2

{001}-{320}

750°C

Mag'n x7

Figure 4.21 Fracture modes observed in smooth bar fatigue test specimens of alloy SRR 99

Table 4.9 is a summary of the features observed on the fracture surfaces of smooth bar fatigue specimens, noting the position of the initiation site and the presence and number of crystallographic facets. The latter was determined by the number of different crystallographic planes and not the actual number of facets present. The primary failure mode (ie the mode for the first half of the fracture) is denoted as crystallographic, mixed or ductile (C,M,D). The initiation site is identified as being surface, near surface or internal (S,NS,I).

Table 4.9 Details of smooth bar fatigue fracture surfaces

Temperature	specimen	orientation	Stress range MPa	failure mode (C,M,D)	No of facets	initiation site
	FL1/1	{001}-{100}	669	C	2	NS
750°C	FL1/2	{001}-{100}	798	C	2	S
	FL1/3	{001}-{100}	888	C	1	S
	FL1/4	{001}-{100}	674	C	1	S
	FL2/1	{001}-{210}	772	C	1	S
750°C	FL2/2	{001}-{210}	829	C	2	NS
	FL2/3	{001}-{210}	699	C	2	S
	FL2/4	{001}-{210}	768	M	3	NS
	FL3/1	{001}-{320}	859	M	1	S
750°C	FL3/2	{001}-{320}	746	D	1	NS
	FL3/3	{001}-{320}	825	-	-	I
	FH1/1	{001}-{100}	809	C	3	S
850°C	FH1/2	{001}-{100}	730	C	4	S
	FH1/3	{001}-{100}	917	C	2	S
	FH2/1	{001}-{210}	750	M	2	NS
	FH2/2	{001}-{210}	841	M	2	S
850°C	FH2/3	{001}-{210}	751	D	0	S
	FH2/4	{001}-{210}	855	M	1	S
	FH2/5	{001}-{210}	761	M	2	S
	FH2/6	{001}-{210}	967	C	1	S
	FH2/7	{001}-{210}	905	M	2	NS
	FH3/1	{001}-{320}	785	M	2	I
850°C	FH3/2	{001}-{320}	757	M	1	I
	FH3/3	{001}-{320}	899	M	2	NS

4.4.3 Two trace analysis of smooth bar fatigue specimen fracture surface facets

The facets observed on fracture surfaces of Smooth bar fatigue specimens were examined using two trace analysis as described in section 3.9.1. Table 4.10 gives the angles the facet made with the top (near {001}) and side faces of the specimen and the resultant orientation of the normal to the facet plane as related to a unit stereographic triangle as described in section 3.4.2.

Figure 4.22 illustrates the results schematically for each of the specimen orientations examined. The facets were found to have orientations approximately 5 to 7 degrees from {111}.

Table 4.10 Two trace facet analysis results

Specimen	orientation	temperature °C	angle measured on		facet orientation	
			top face	side face	θdegrees	φdegrees
FH1/2	{001}-{100}	850	129	129	46	39.5
FL1/2	{001}-{100}	750	54	55	49.5	45
"	" "	"	52	138	51	37.5
FL2/4	{001}-{210}	750	22.5	28	48	45
FH2/6	{001}-{210}	850	64.5	52	47	38.5
FL3/1	{001}-{320}	750	105	53	48.5	42

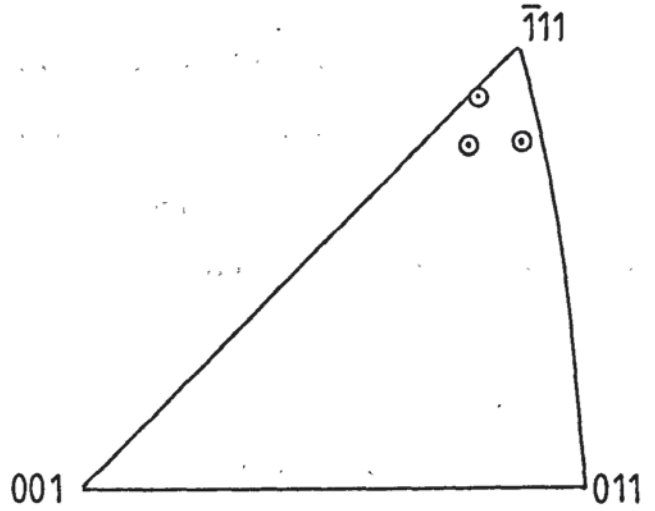

(001) – (1:1·7:11·7)
Specimens

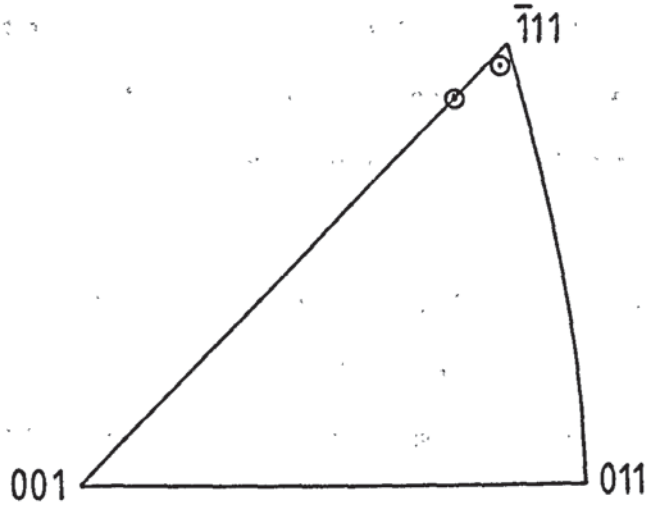

(001) – (0·2:1:2·2)
Specimens

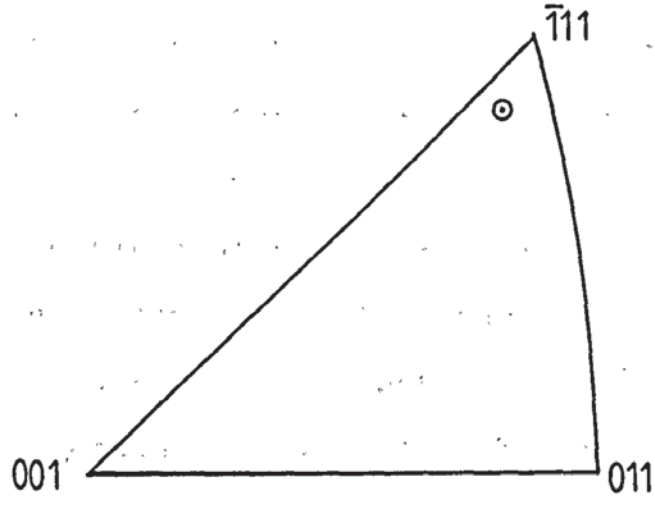

(001) – (320)
Specimens

Nominal orientations given in table 4·8

Figure 4.22 Orientation of facets found on smooth bar fatigue specimen fracture surfaces

4.5 Fatigue crack propagation

Fatigue crack propagation testing was carried out under load controlled conditions for three specimen geometries, shown in figure 3.2. The testing procedure is given in section 3.8.

The specimens used could not be made to conform to standard three point bend geometries due to the dimensions of the cast block and the internal dimensions of the furnace, therefore experimental electrical potential and theoretical stress intensity calibrations were produced.

4.5.1 The electrical potential calibration

An experimental electrical potential drop calibration was produced by use of specimens containing electro-discharged machined 0.2mm wide slits. The measuring procedure was described in section 3.8.2.1. The current and probe wire positions are shown in figure 3.15. Calibration was carried out at three temperatures; room temperature, 750°C and 850°C. The results are shown graphically in figure 4.23 in terms of $\Delta a/a$ versus $\Delta V/V$, where V is the initial voltage from an initial crack length a (the notch depth). ΔV is the change in potential caused by an increase in crack length of Δa. As the electrical potential results for test temperatures of 750°C and 850°C were found to be identical, the 850°C test results were used to produce the mathematical calibration, the results being adequately described by a first degree equation.

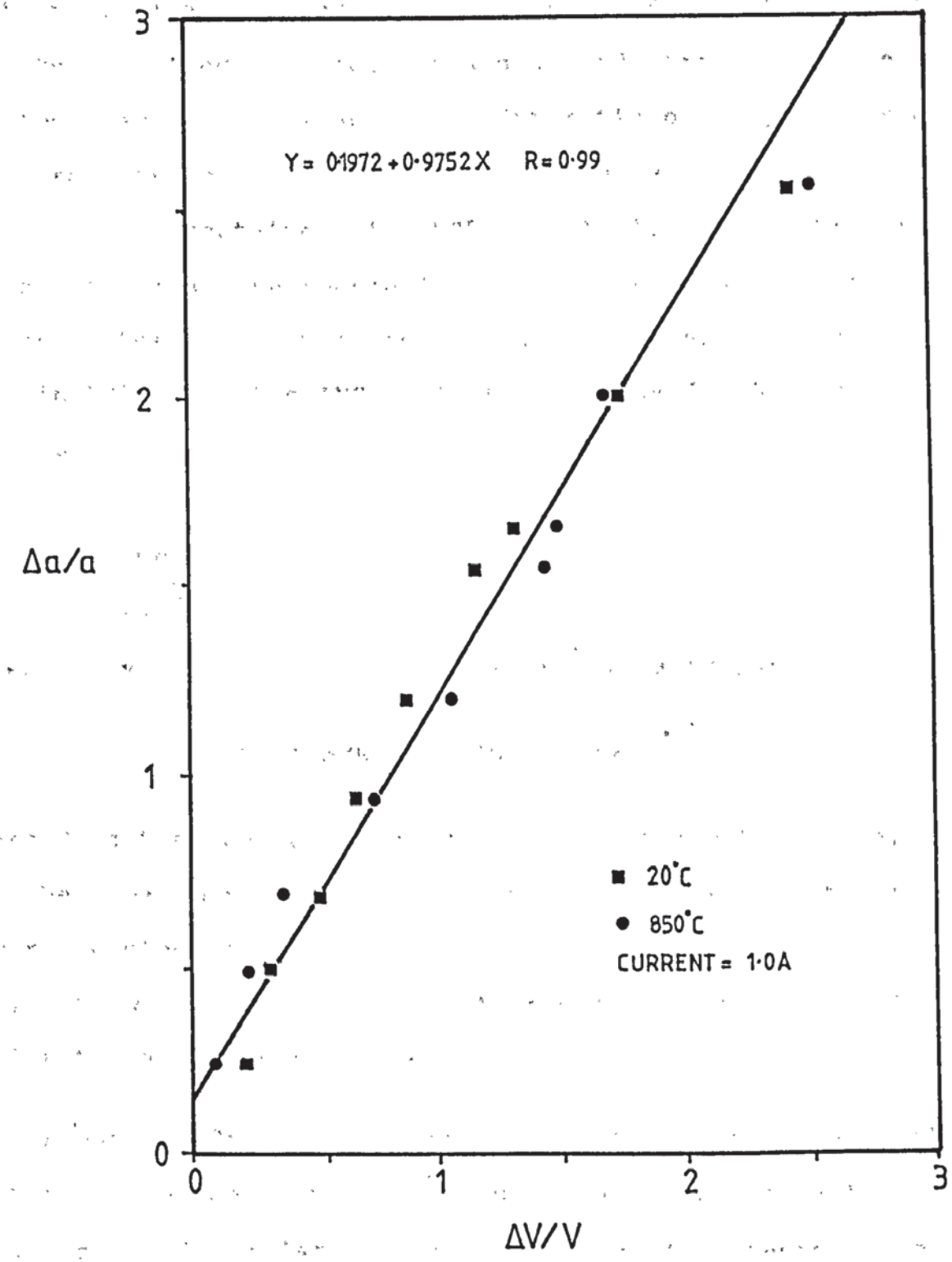

Figure 4.23 Experimental electrical potential calibration for RLH 4945 notched fatigue specimens

4.5.2 Theoretical stress intensity calibration

A theoretical stress intensity calibration was carried out using Pafec, a finite element program, as described in section 3.8.1 and appendix 3. Figure 4.24 illustrates the results obtained by modelling a standard three point bend specimen having a full span to width ratio of 4:1, compared with results obtained by use of the stress intensity calibration contained in BS5447 (103), the British standards institue regulations for plane strain fracture toughness testing. This is equivalent to the calibration used in E399-78, the ANSI/ASTM test standard (75), and is given by:

$$K = \frac{3PS}{BW^{3/2}} \cdot Y' \qquad \ldots\ldots(4.8)$$

Where $$Y' = 1.93(a/W)^{0.5} - 3.07(a/W)^{1.5} + 14.53(a/W)^{2.5} - 25.11(a/W)^{3.5} + 25.80(a/W)^{4.5}$$

Where P is the applied load, B is the specimen thickness, W is the specimen width and S is the span between the two lower loading points. In the range of a/W from 0.35 to 0.6, it was found that the discrepancy between the two calibrations was approximately 2.5%

Figure 4.25 illustrates the Pafec finite element results for a geometry using a full span to width ratio of 3:1, as used for fatigue crack propagation tests. The results are compared with the BS5447 stress intensity calibration given in equation 4.8. It can be seen that the

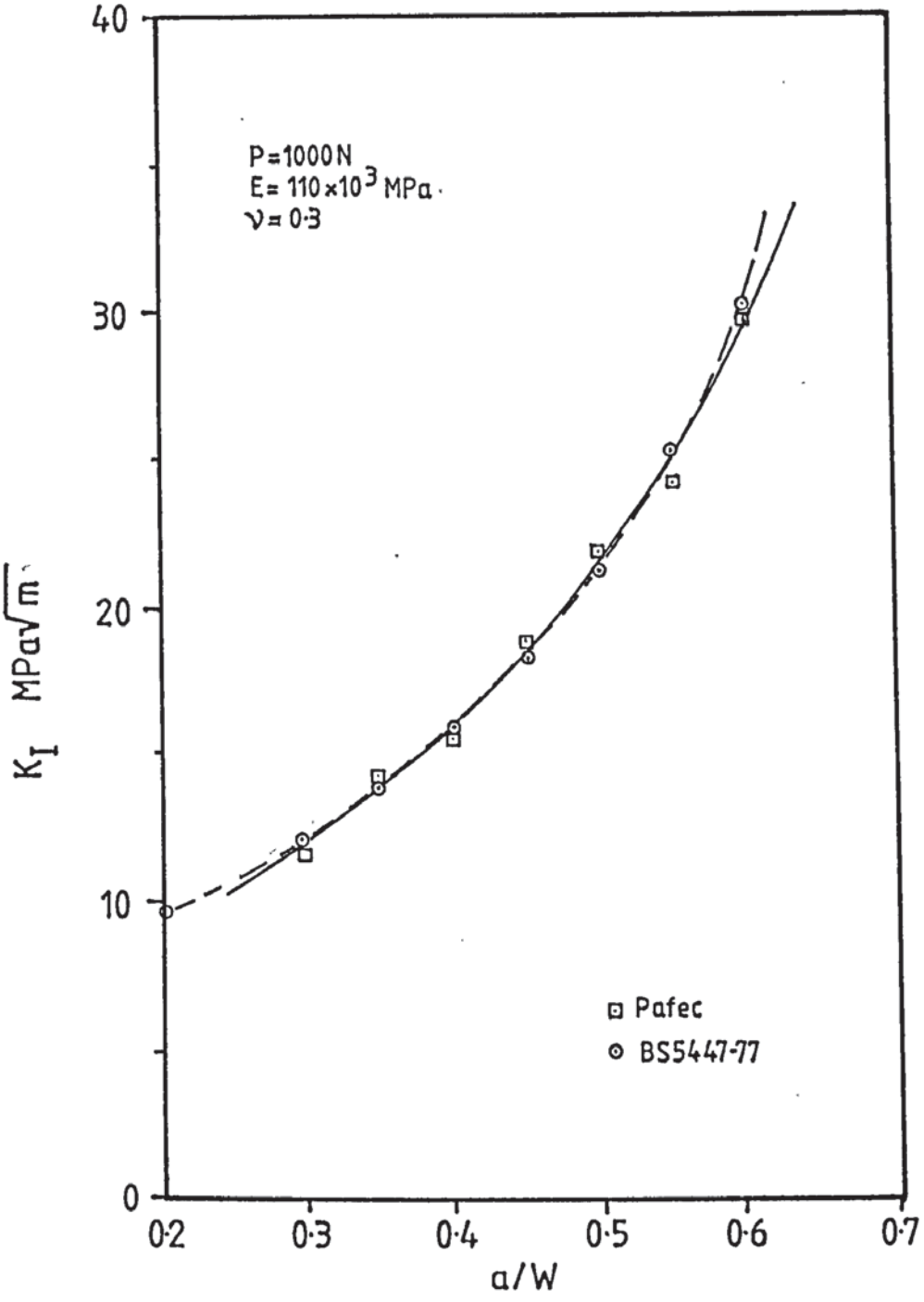

Figure 4.24 Stress intensity calibration for fixed load under three point bending using S/W= 4:1

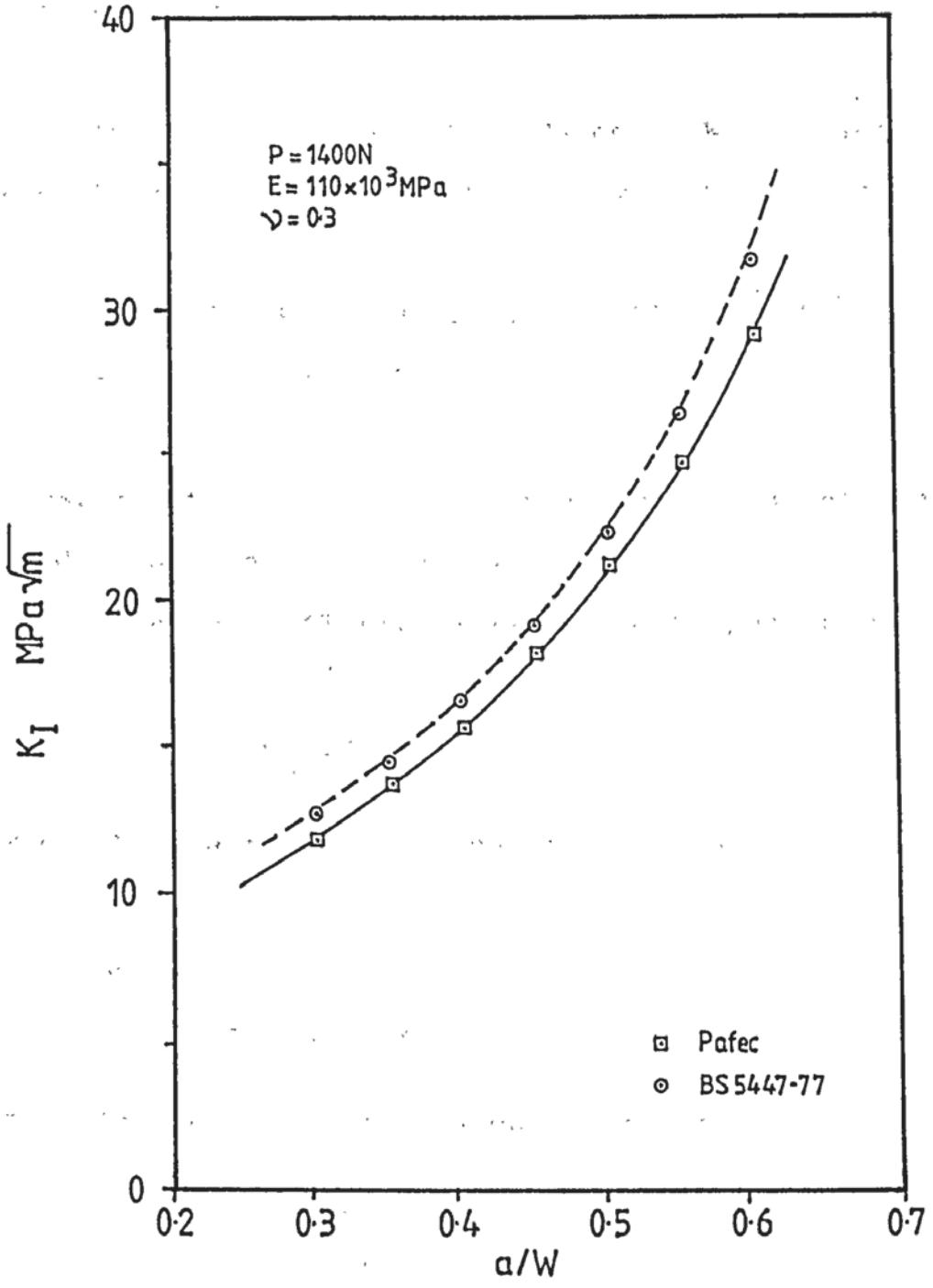

Figure 4.25 Stress intensity calibration for fixed load and three point bending using S/W= 3:1

discrepancy between the two calibrations has increased to approximately 5-6% with the Pafec analysis giving consistently lower results.

In the case of the Pafec S/W=3:1 analysis, the results may be described by a polynomial of the form:

$$K = -1060.9(a/W)^4 + 2032.1(a/W)^3 - 1328.5(a/W)^2 + 401.9(a/W) - 35.42 \quad \ldots\ldots(4.9)$$

However, this result is for a fixed load of 1400N. To produce a general polynomial for all loads we use the fact that equation 2.47 may be expressed in the form:

$$K = \frac{P}{BW} . Y \sqrt{a} \quad \ldots\ldots(4.10)$$

Where Y is a polynomial function of a/W.

Let $Y' = Y \sqrt{a}$

Then $Y' = f(a/W) \times \frac{BW}{P}$ $\ldots\ldots(4.11)$

Therefore equation 4.9 is multiplied by:

$$\frac{0.005 \times .01}{0.0014} = 0.0357$$

To produce Y'. This polynomial is shown graphically in figure 4.26. In use the stress intensity is obtained by using:

$$K = \frac{P}{BW} . Y' \quad \ldots\ldots(4.12)$$

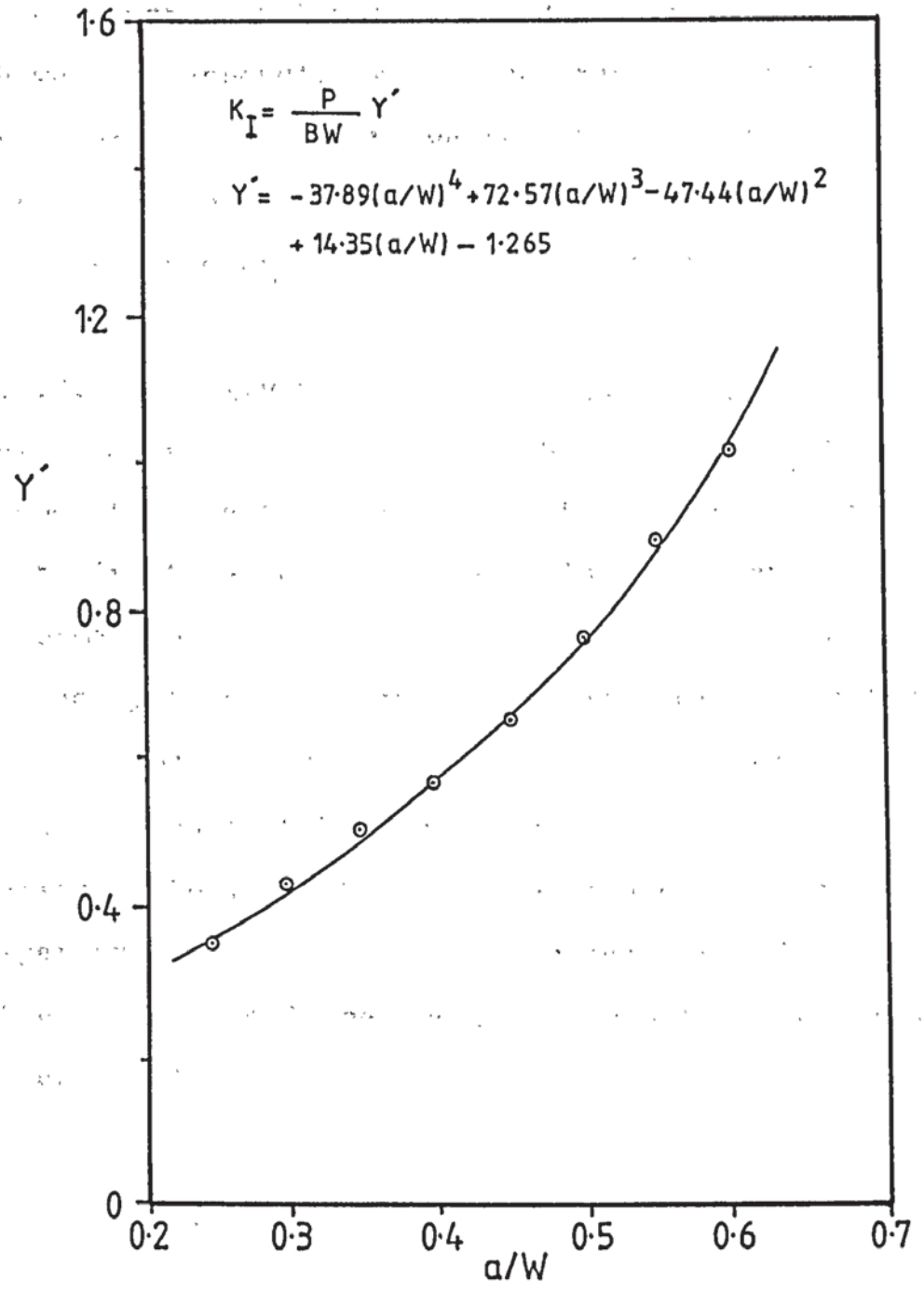

Figure 4.26 Pafec theoretical stress intensity calibration for three point bending using S/W= 3:1

4.5.3 Analysis of fatigue propagation results

Fatigue propagation results were analysed by use of a 7 point incremental polynomial data reduction program, as shown in appendix 4. The results were illustrated graphically as da/dN versus ΔK. As ΔK is an elastic parameter, an investigation was carried out to identify any results not conforming to LEFM behaviour.

4.5.3.1 Identifying the onset of general yield

The major limitation to the use of LEFM for high temperature testing is the onset of general yielding before fast fracture of the remaining ligament. For most deformation theories the material is assumed to be a perfectly elastic/plastic material, that is having a linear elastic behaviour up to yield where a sharp transition to totally plastic behaviour is encountered. In this case, a general rule is that during fatigue elastic conditions are experienced up to 80% of the general yield load. For a three point bend specimen, the general yield load P_{gy} is given by (104):

$$P_{gy} = 1.5\ \sigma_y \frac{B}{S} (W-a)^2 \qquad \ldots\ldots (4.13)$$

Where 1.5 is the notch constraint factor, σ_y is the 0.2% proof stress, B is the specimen thickness, W is the specimen width, S is the loading span and a is the crack length. If the maximum load during fatigue is P_{max} then:

$$\text{Let } P_{max} = 0.8\ P_{gy}$$

$$P_{max} = 0.8 \times 1.5\ \sigma_y \frac{B}{S} (W-a)^2 \qquad \ldots\ldots (4.14)$$

Using values for 0.2% proof stress given in table 2.4 for alloy SRR 99, the maximum permissible crack length for a specimen with dimensions of B=5mm, W=10mm a=2mm and a loading span of 30.31 mm was calculated for a range of maximum fatigue loads. The results are given in table 4.11 for test conditions of 750°C and 850°C.

Table 4.11 Calculation of onset of general yield

Load P_{max} KN	750°C			850°C		
	W-a mm	a/W	Δa/a	W-a mm	a/W	Δa/a
2.8	3.63	0.637	2.18	4.18	0.58	1.91
2.9	3.70	0.63	2.15	4.25	0.575	1.87
3.0	3.76	0.624	2.12	4.33	0.567	1.835
3.1	3.82	0.618	2.09	4.40	0.56	1.80
3.2	3.88	0.611	2.057	4.47	0.55	1.75
3.3	3.94	0.606	2.03	4.54	0.546	1.73
3.4	4.00	0.600	2.00	4.61	0.539	1.695
3.5	4.06	0.594	1.97	4.67	0.533	1.665

4.5.3.2 Analysis of maximum plastic zone size

Elastic fracture mechanics is based upon the assumption that the plastic zone produced around a notch or crack tip is contained entirely within an elastic stress field. In order to ensure this, the ASTM standard for fracture toughness testing (75) recommends that the plastic zone size be no greater than 1/50th of the specimen thickness.

Fatigue crack closure during unloading leads to the production of a reversed plastic zone which reduces the size of the plastic zone produced during the loading cycle. The resultant plastic zone of reversing deformation is one quarter of the maximum plastic zone size, and is given by :

$$r_{yf} = \frac{1}{2\pi} \times \left[\frac{\Delta K}{2\sigma_y}\right]^2 \qquad \ldots\ldots (4.15)$$

In the case of alloy SRR 99 fatigue specimens, the maximum permissible size for the plastic zone is:

$$r_{yf} = \frac{B}{50} = \frac{1}{50} \times 0.005 = 0.0001m$$

At 750°C the 0.2% proof stress for alloy SRR 99 is 1071MPa giving a maximum permissible ΔK of 53.7MPa$\sqrt{m}$. Use of σ_y=809MPa in equation 4.15 produces a maximum ΔK for specimens tested at 850°C of 40.6MPa$\sqrt{m}$.

4.5.4 Fatigue crack propagation results

Three specimen orientations as shown in figure 3.2 were examined. In order to simplify reference to the results, the specimens have been denoted by the following codes :

PL1 Propagation test at 750°C (001)-(100) orientation
PL2 Propagation test at 750°C (001)-(210) orientation
PL3 Propagation test at 750°C (001)-(110) orientation

PH1 Propagation test at 850°C (001)-(100) orientation
PH2 Propagation test at 850°C (001)-(210) orientation
PH3 Propagation test at 850°C (001)-(110) orientation

The codes are the same as those used for smooth fatigue specimens with the exception of the prefix. The complete specimen code also contains the specimen number and the frequency used for the test. For example, PH3/2H is the second specimen to be tested at 850°C having an orientation of (001)(top face)-(110)(transverse face). The H suffix denotes that the specimen was subjected to hold times by use of the trapezoidal waveform shown in figure 3.16b; a Z suffix indicating the use of the triangular waveform.

The fatigue results are shown graphically in figure 4.27 as the increment of crack growth per cycle: da/dN, versus the cyclic stress intensity factor range: ΔK. Details of specimen and test conditions are given in table 4.12.

For each specimen, the breakdown of LEFM conditions were analysed by use of techniques described in section 4.5.3, using specimen details given in table 4.12. Where necessary the point is illustrated on the graph; $0.8P_{gy}$ denoting the estimated onset of general yielding, and r_{yf} indicating that the fatigue plastic zone size had become larger than 1/50th of the specimen thickness. The calculations were based on data obtained from Rolls-Royce Ltd. Values of 0.2% proof stress for specimens tested in the [001] direction were used together with an approximate value of K_{Ic} of 60-70 MPa$\sqrt{m}$, a value of 65 being used. The values are denoted by a solid line.

In the case of (001)-(210) and (001)-(110) specimens, the end face orientations are similar to the side faces and therefore if the tensile component of the applied force is considered to operate along the axis of the bar ie the <210> and <110> respectively (see discussion), the value of the yield stress for these orientations is needed. As the values were not available for alloy SRR 99, use was made of the work carried out by Kear et al (38,57) on the orientation dependence of yielding in Mar-M200 single crystals. The authors found that the yield stress for specimens with both [210] and [110] tensile axis were similar and is approximately 18% lower than the value for [001] specimens at both 750°C and 850°C. Calculations based on a 18% reduction of the [001] yield stress for alloy SRR 99 are shown in figure 4.27 as a dotted line.

Table 4.12 Fatigue crack propagation specimen details

Specimen	Cast No	Temp °C	Nominal Orientation	Dimensions a_o mm	B mm	W mm	Init P.D µV	P_{min} KN	P_{max} KN
	TRIANGULAR WAVEFORM ZERO HOLD 1.25Hz								
PL1/1Z	S38233-12/4	750	(001)-(100)	2.04	5.035	9.97	223	0.3	3.00
PL1/2Z	S38233-12/1	750	(001)-(100)	2.04	5.04	9.97	169	0.3	3.00
PL2/1Z	S38233-16/3	750	(001)-(210)	1.98	5.035	9.98	219	0.30	3.00
PL2/2Z	S38233-16/2	750	(001)-(210)	2.00	5.065	9.98	172	0.28	2.80
PL3/1Z	S38233-9/3	750	(001)-(110)	1.94	5.03	9.97	190.5	0.32	3.20
PL3/2Z	S38233-9/1	750	(001)-(110)	1.97	5.03	9.95	203	0.32	3.20
PH1/1Z	S38233-12/6	850	(001)-(100)	2.13	5.04	9.91	210	0.28	2.80
PH1/2Z	S38233-12/7	850	(001)-(100)	2.06	5.05	9.92	196	0.28	2.80
PH2/1Z	S38233-16/7	850	(001)-(210)	1.99	5.01	9.97	168.5	0.28	2.80
PH2/2Z	S38233-16/4	850	(001)-(210)	1.95	5.02	9.98	177.5	0.30	3.00
PH3/1Z	S38233-9/7	850	(001)-(110)	2.00	5.01	9.96	199	0.28	2.80
PH3/2Z	S38233-9/6	850	(001)-(110)	1.95	5.02	9.98	158.5	0.28	2.80
	TRAPEZOIDAL WAVEFORM 1.6 SECOND HOLD 0.25Hz								
PL1/1H	S38233-15/2	750	(001)-(100)	1.84	5.03	10.0	187	0.32	3.20
PL1/2H	S38233-15/1	750	(001)-(100)	1.92	5.02	9.95	223.5	0.32	3.20
PL2/1H	S38233-20/1	750	(001)-(210)	1.95	5.02	10.0	214	0.32	3.20
PL2/2H	S38233-16/5	750	(001)-(210)	1.95	4.88	9.96	193.5	0.30	3.00
PL3/1H	S38233-14/1	750	(001)-(110)	1.92	5.03	10.0	131.5	0.34	3.40
PL3/2H	S38233-9/5	750	(001)-(110)	1.94	5.01	9.97	191.5	0.30	3.00
PH1/1H	S38233-15/5	850	(001)-(100)	1.86	5.03	10.0	165	0.30	3.00
PH1/2H	S38233-15/1	850	(001)-(100)	1.96	5.03	9.92	175.5	0.30	3.00
PH2/1H	S38233-20/5	850	(001)-(210)	1.96	5.04	9.99	201	0.30	3.00
PH2/2H	S38233-20/4	850	(001)-(210)	1.96	5.04	9.99	159.5	0.30	3.00
PH3/1H	S38233-14/5	850	(001)-(110)	1.94	5.00	9.95	172	0.30	3.00
PH3/2H	S38233-14/4	850	(001)-(110)	1.92	5.01	9.98	175	0.30	3.00

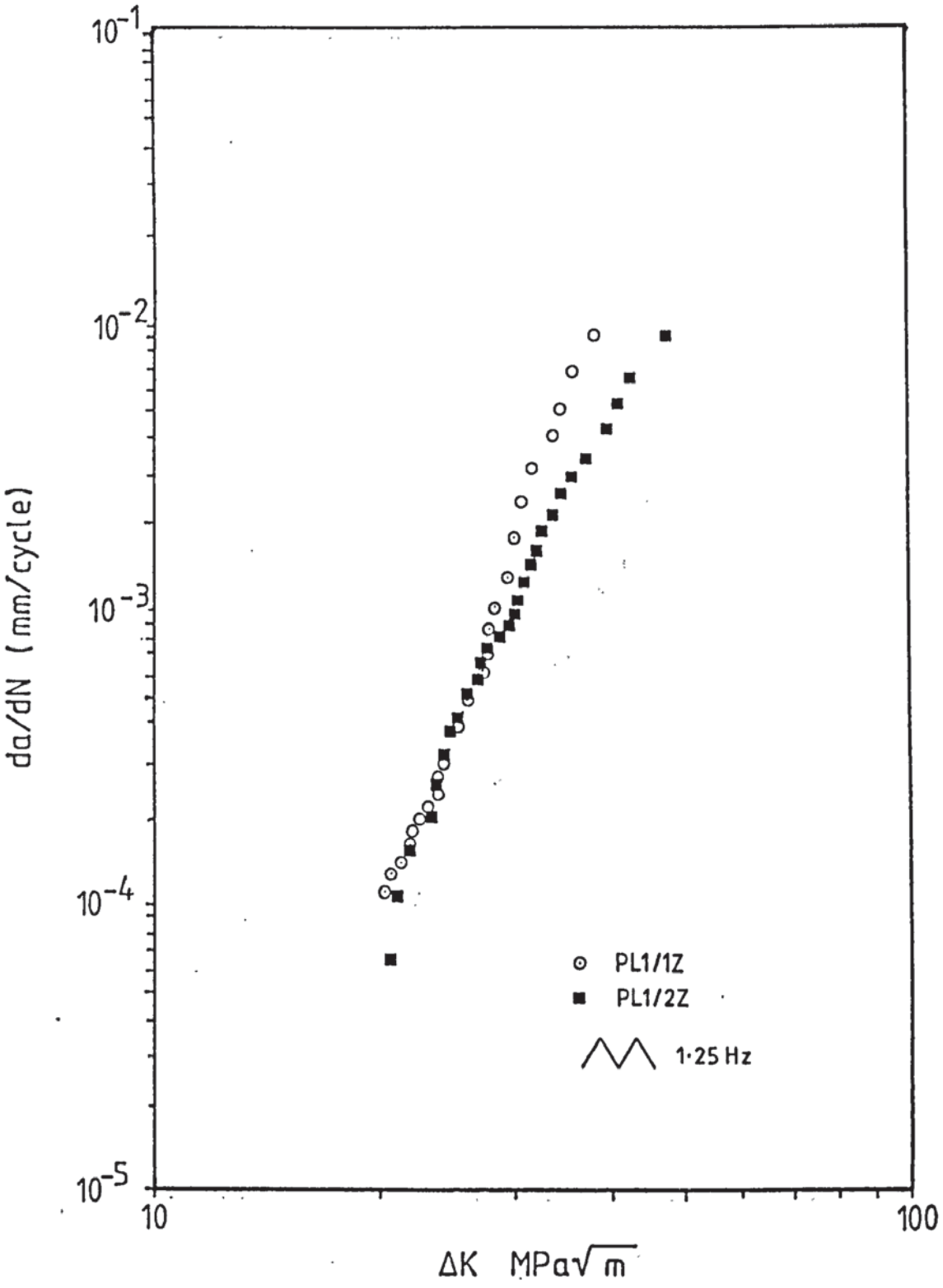

Figure 4.27a Fatigue crack growth data for (001)-(100) specimens tested at 750°C Frequency 1.25Hz

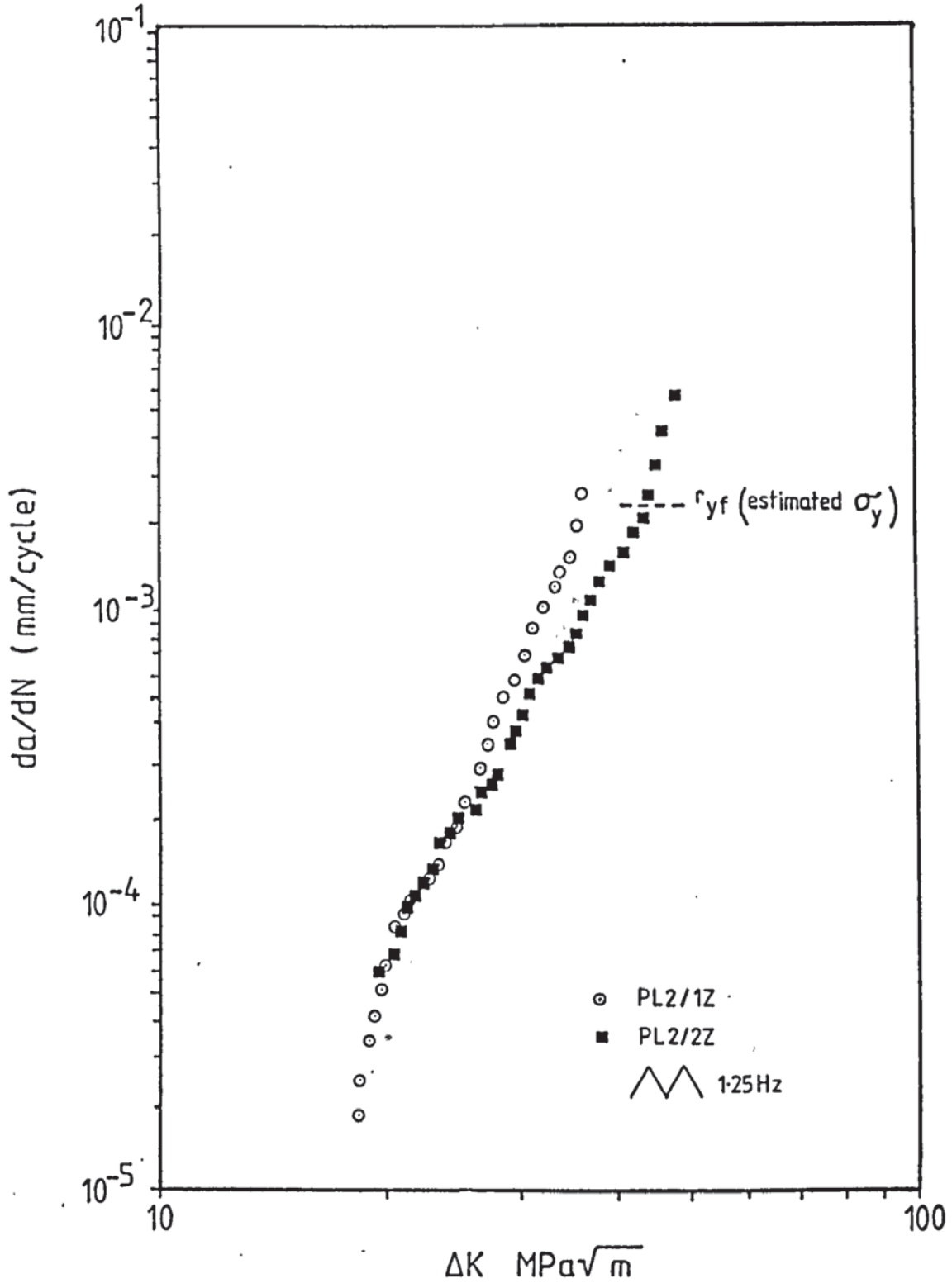

Figure 4.27b Fatigue crack growth data for (001)-(210) specimens tested at 750°C Frequency 1.25Hz

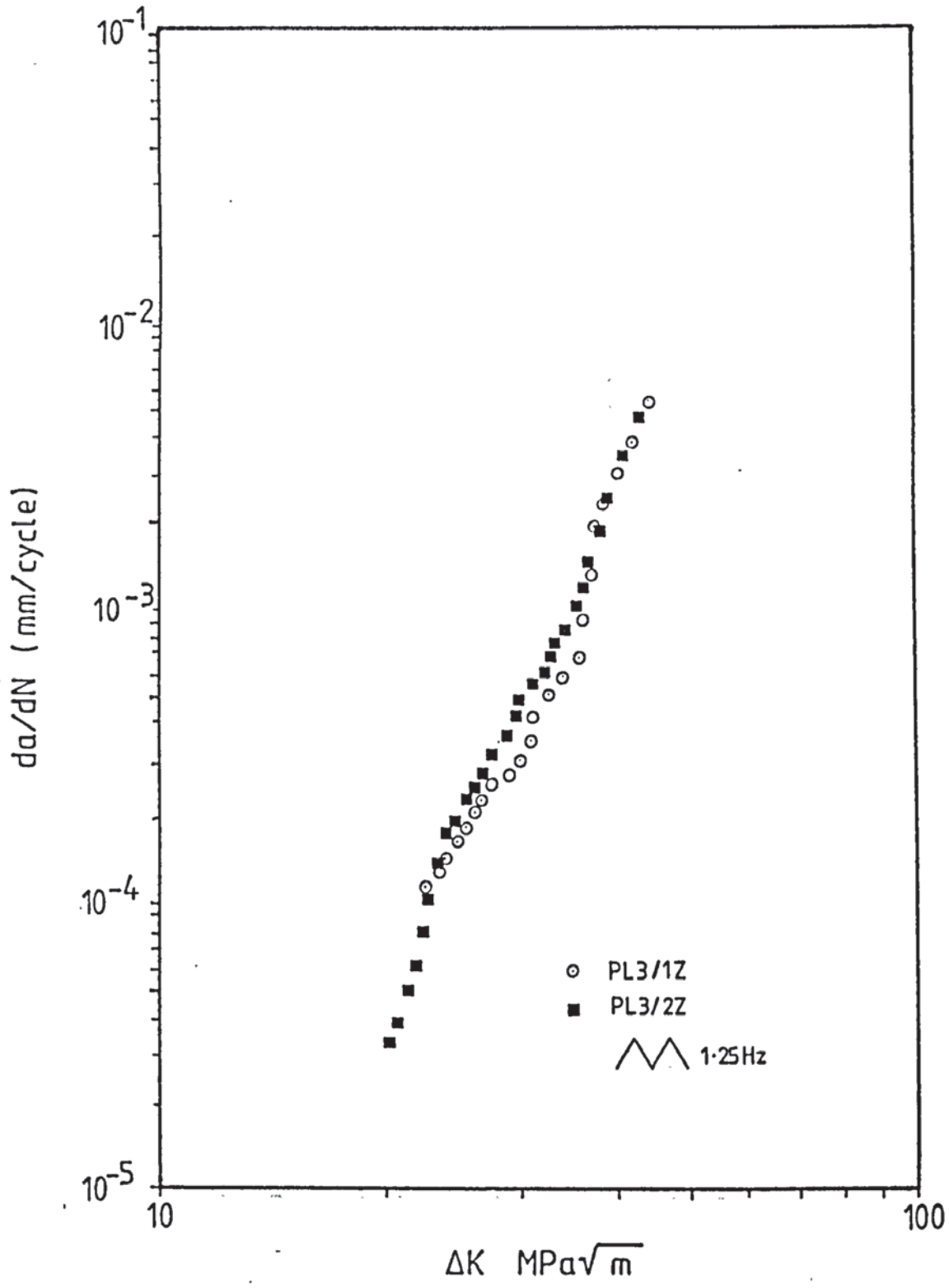

Figure 4.27c Fatigue crack growth data for (001)-(110) specimens tested at 750°C Frequency 1.25Hz

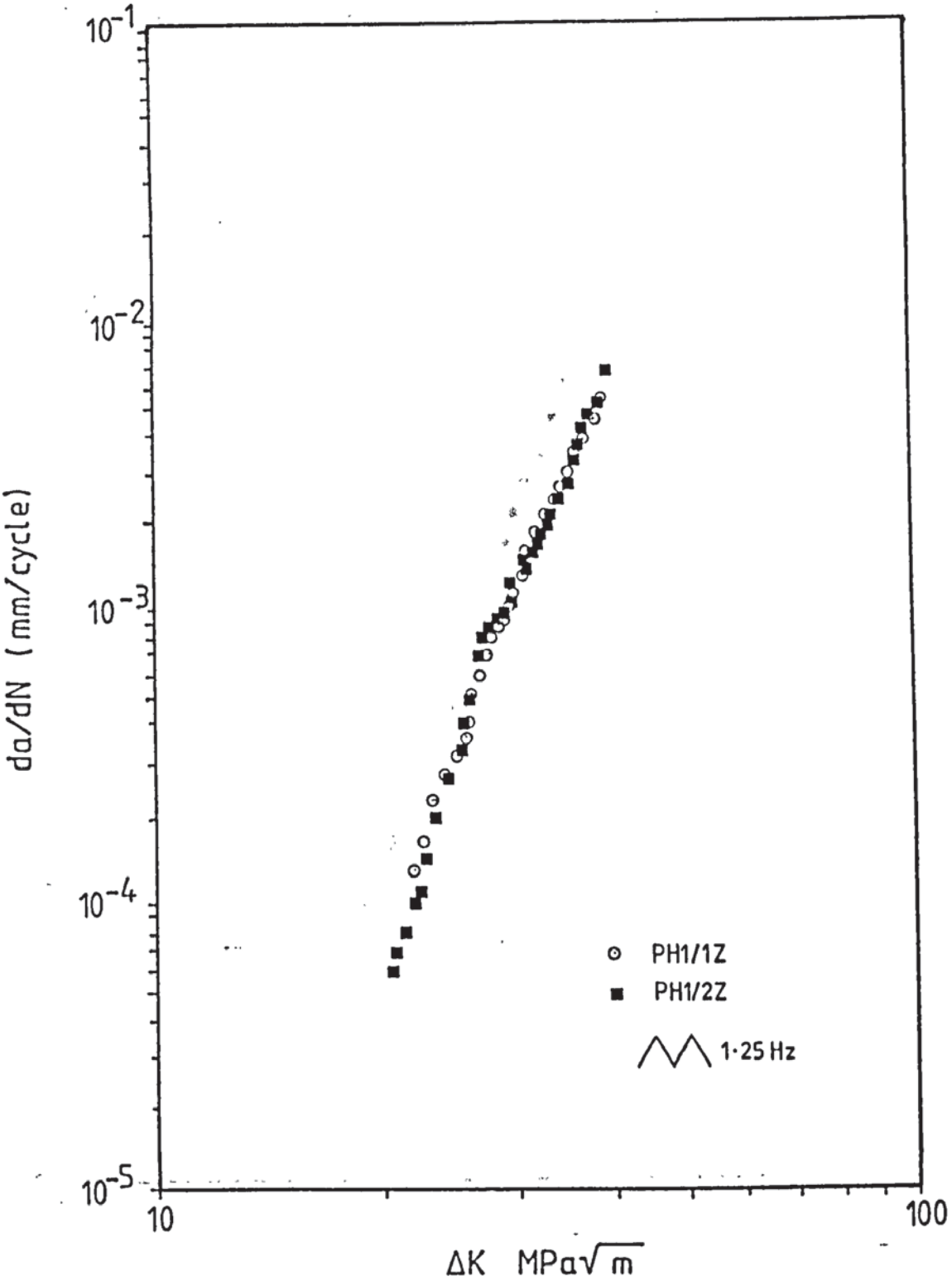

Figure 4.27d Fatigue crack growth data for (001)-(100) specimens tested at 850°C Frequency 1.25Hz

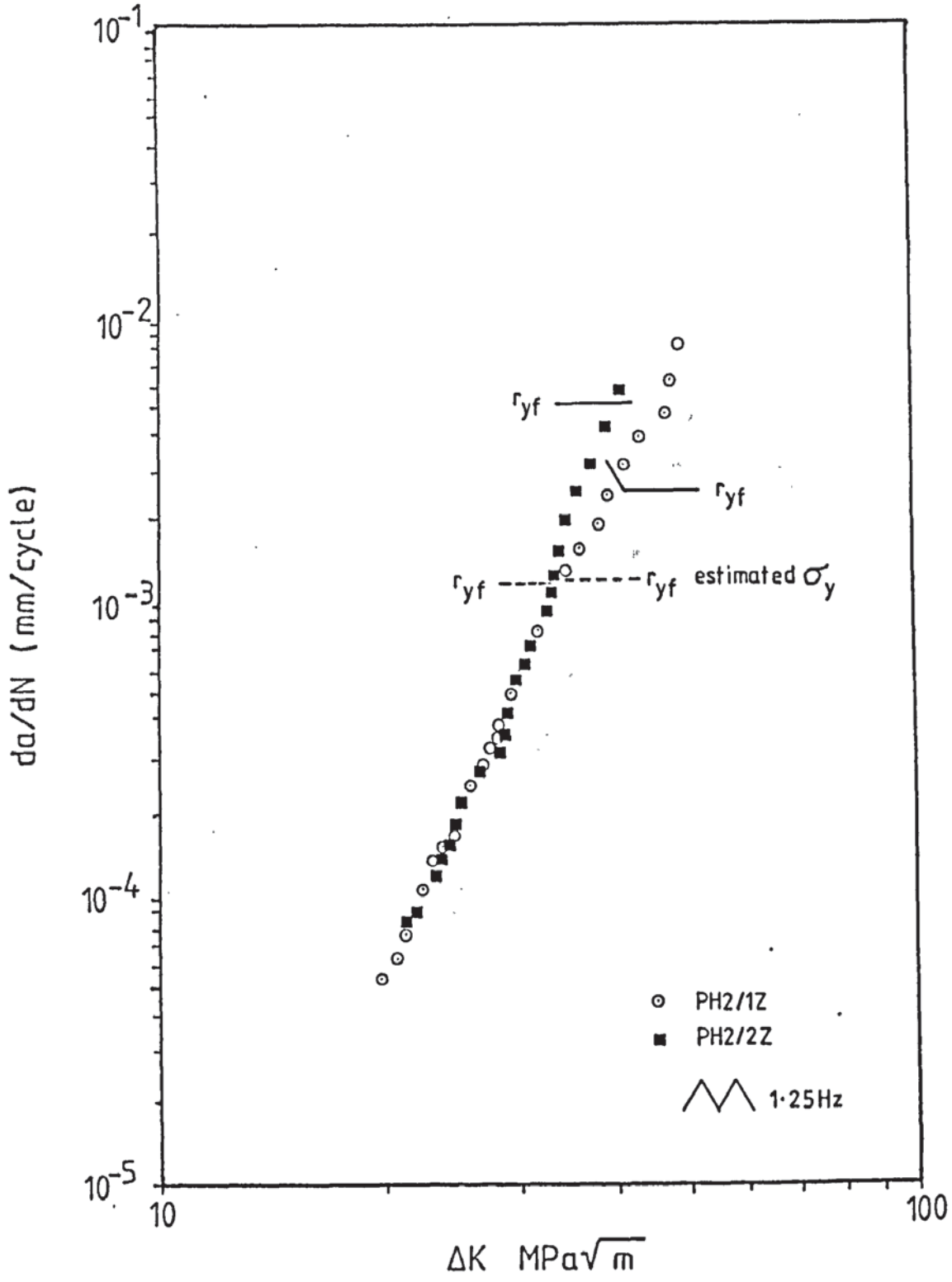

Figure 4.27e Fatigue crack growth data for (001)-(210) specimens tested at 850°C Frequency 1.25Hz

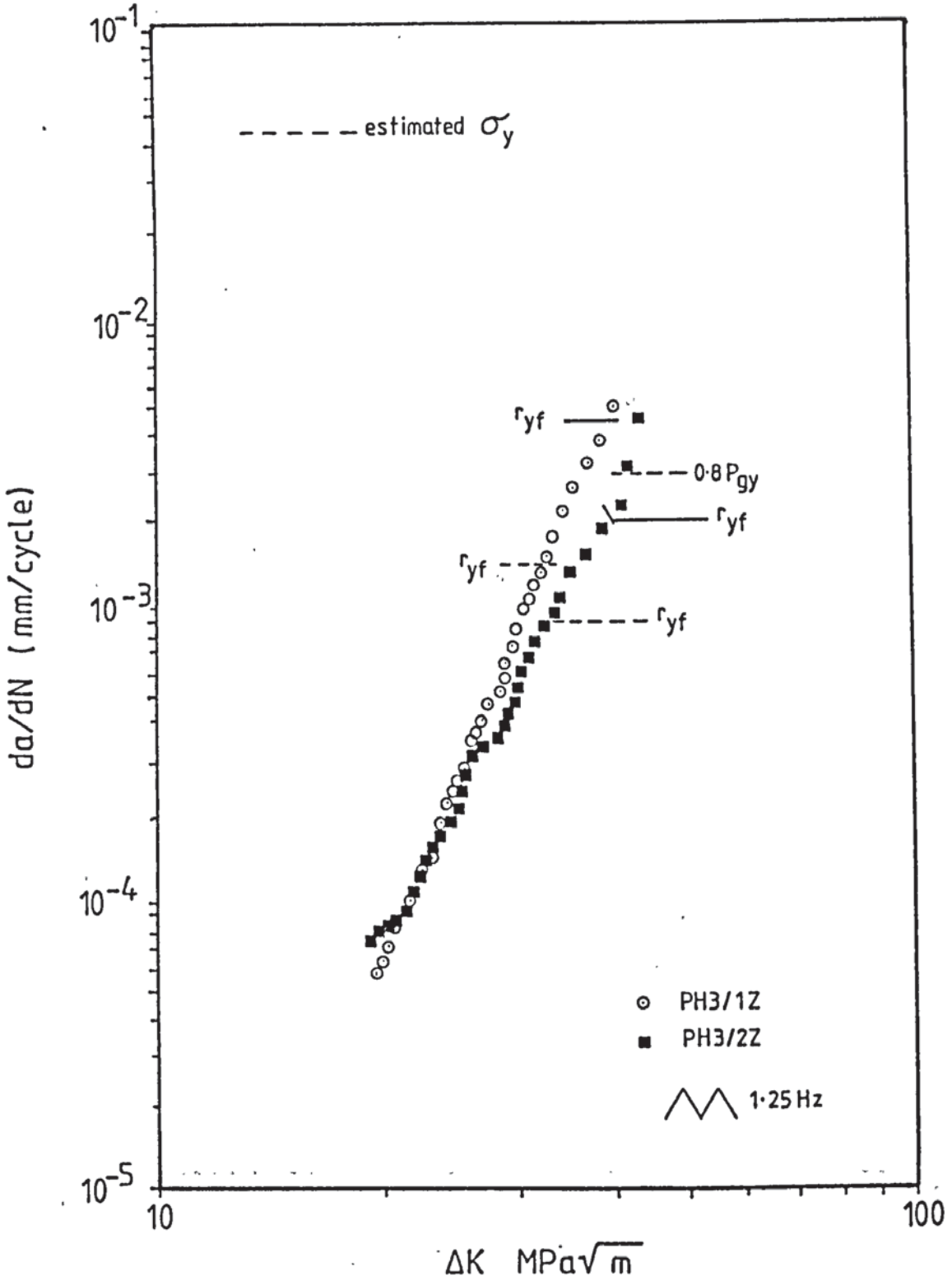

Figure 4.27f Fatigue crack growth data for (001)-(110) specimens tested at 850°C Frequency 1.25Hz

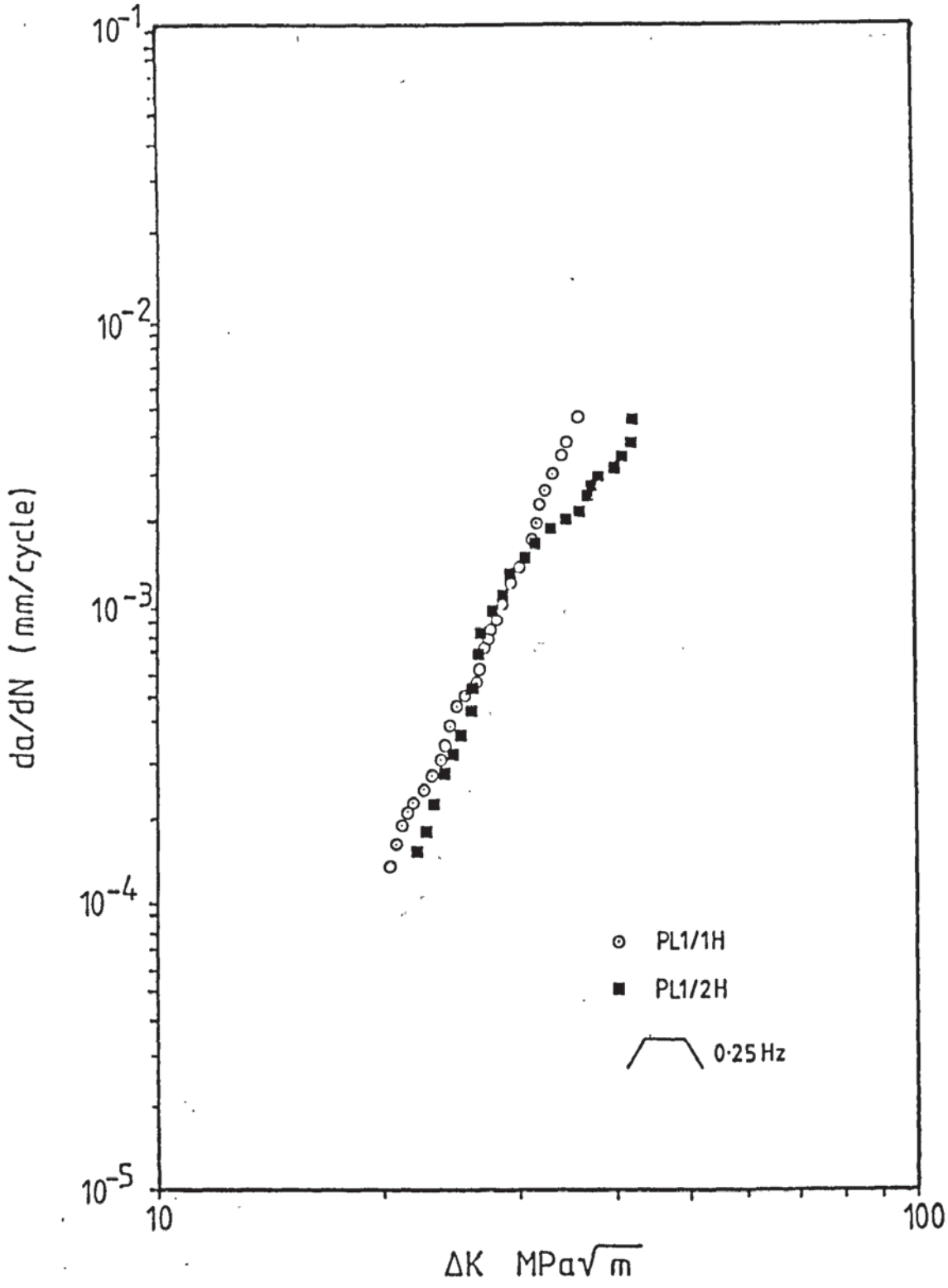

Figure 4.27g Fatigue crack growth data for (001)-(100) specimens tested at 750°C Frequency 0.25Hz

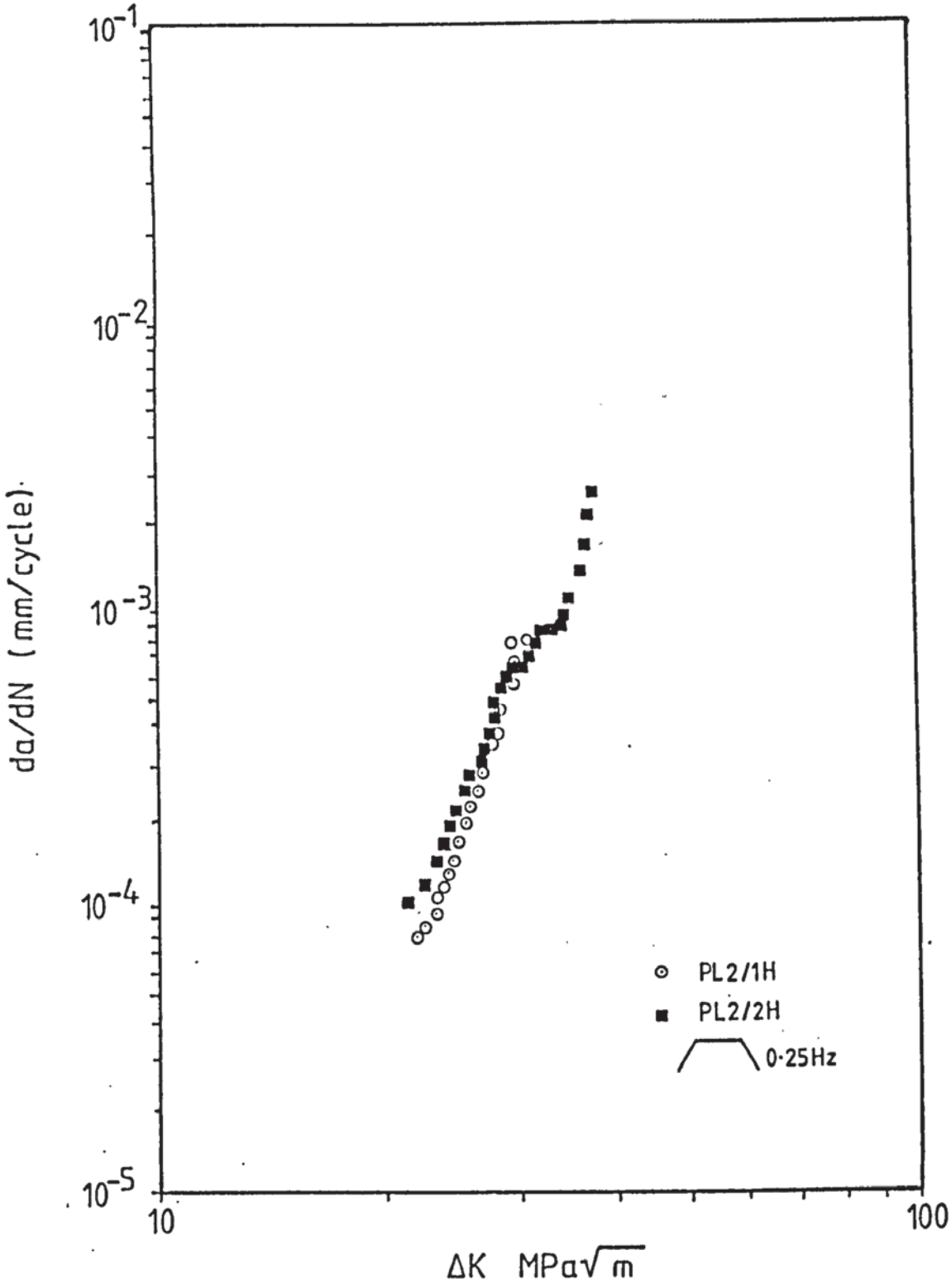

Figure 4.27h Fatigue crack growth data for (001)-(210) specimens tested at 750°C Frequency 0.25Hz

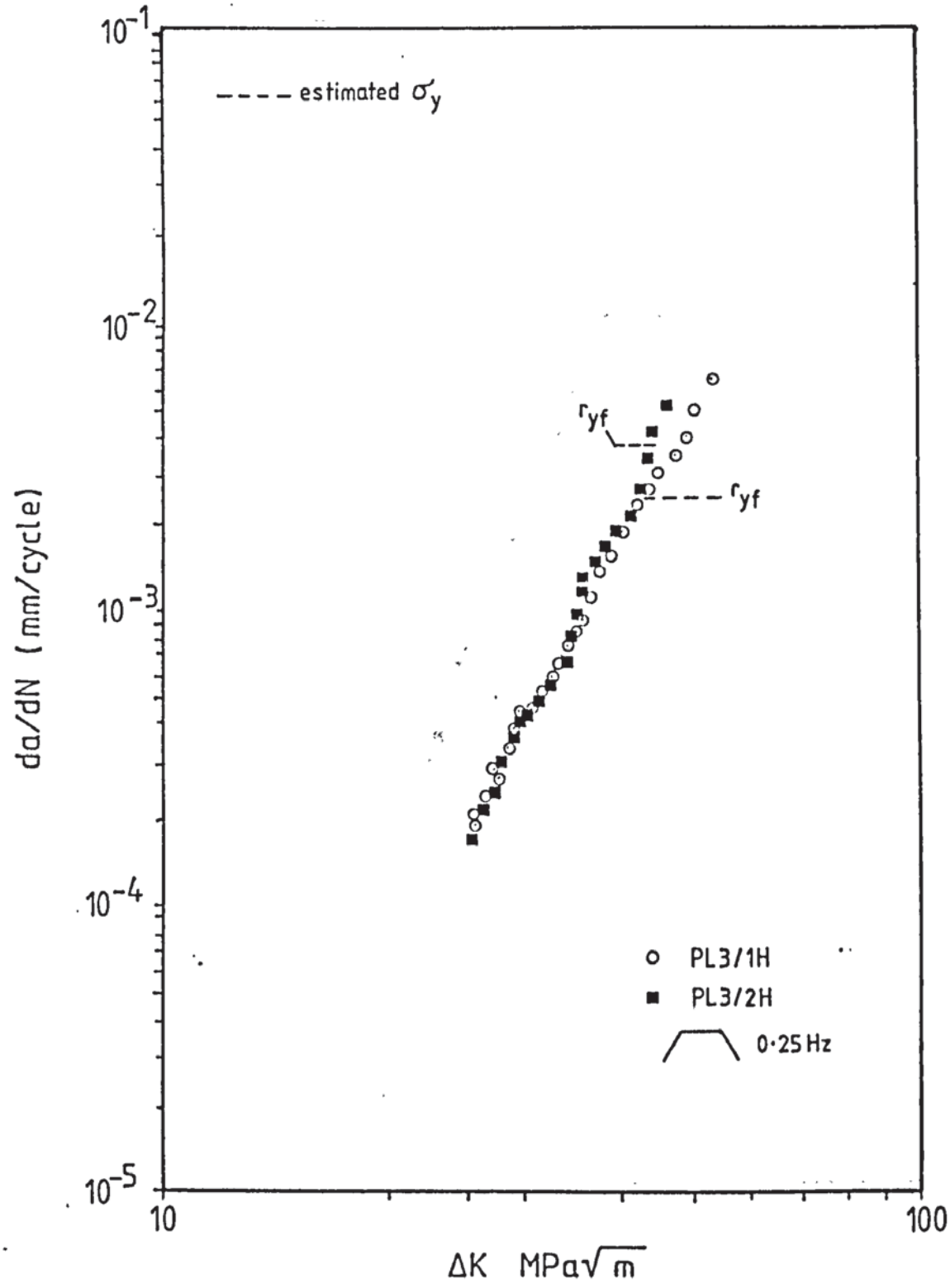

Figure 4.27i Fatigue crack growth data for (001)-(110) specimens tested at 750°C Frequency 0.25Hz

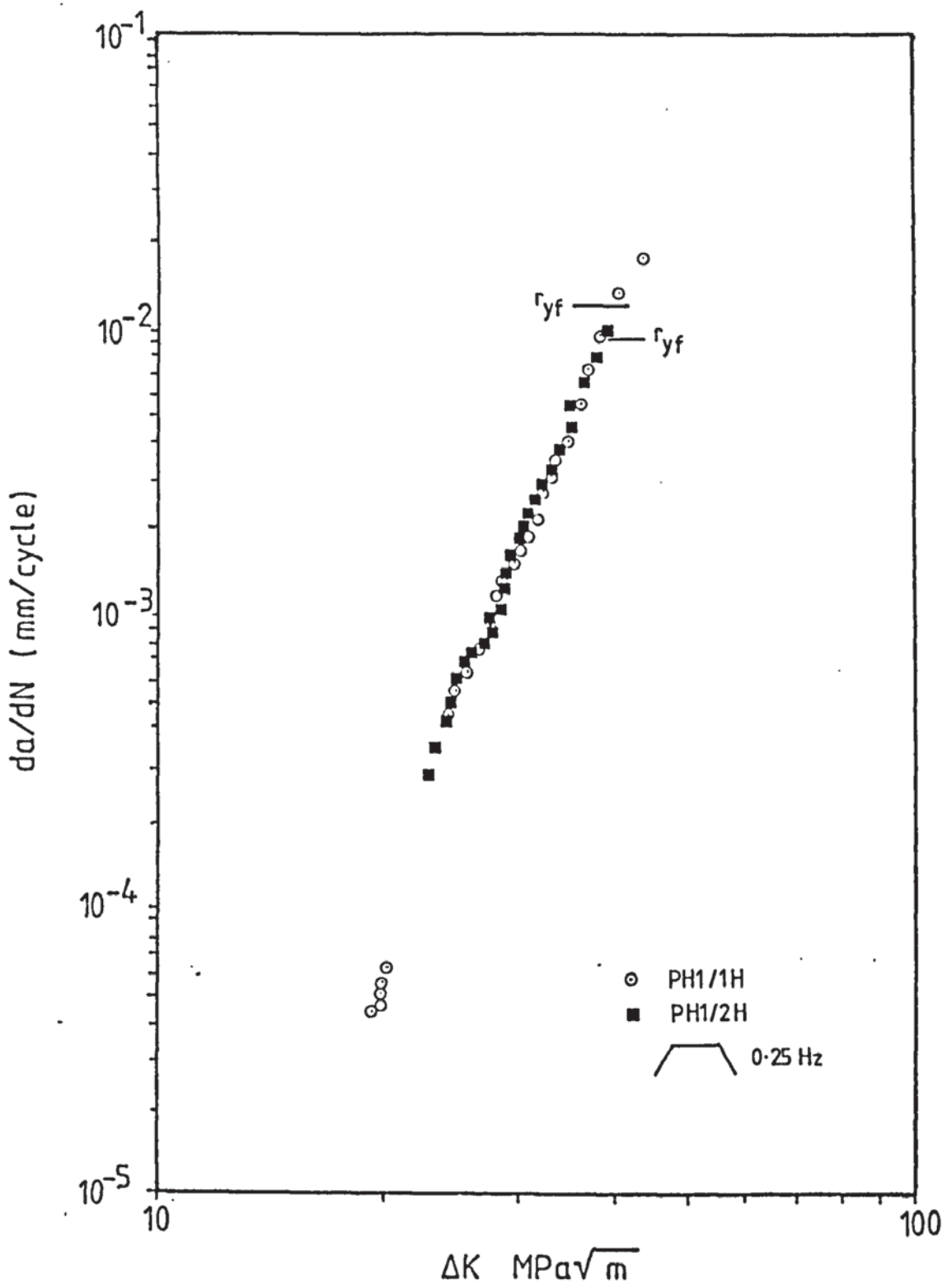

Figure 4.27j Fatigue crack growth data for (001)-(100) specimens tested at 850°C Frequency 0.25Hz

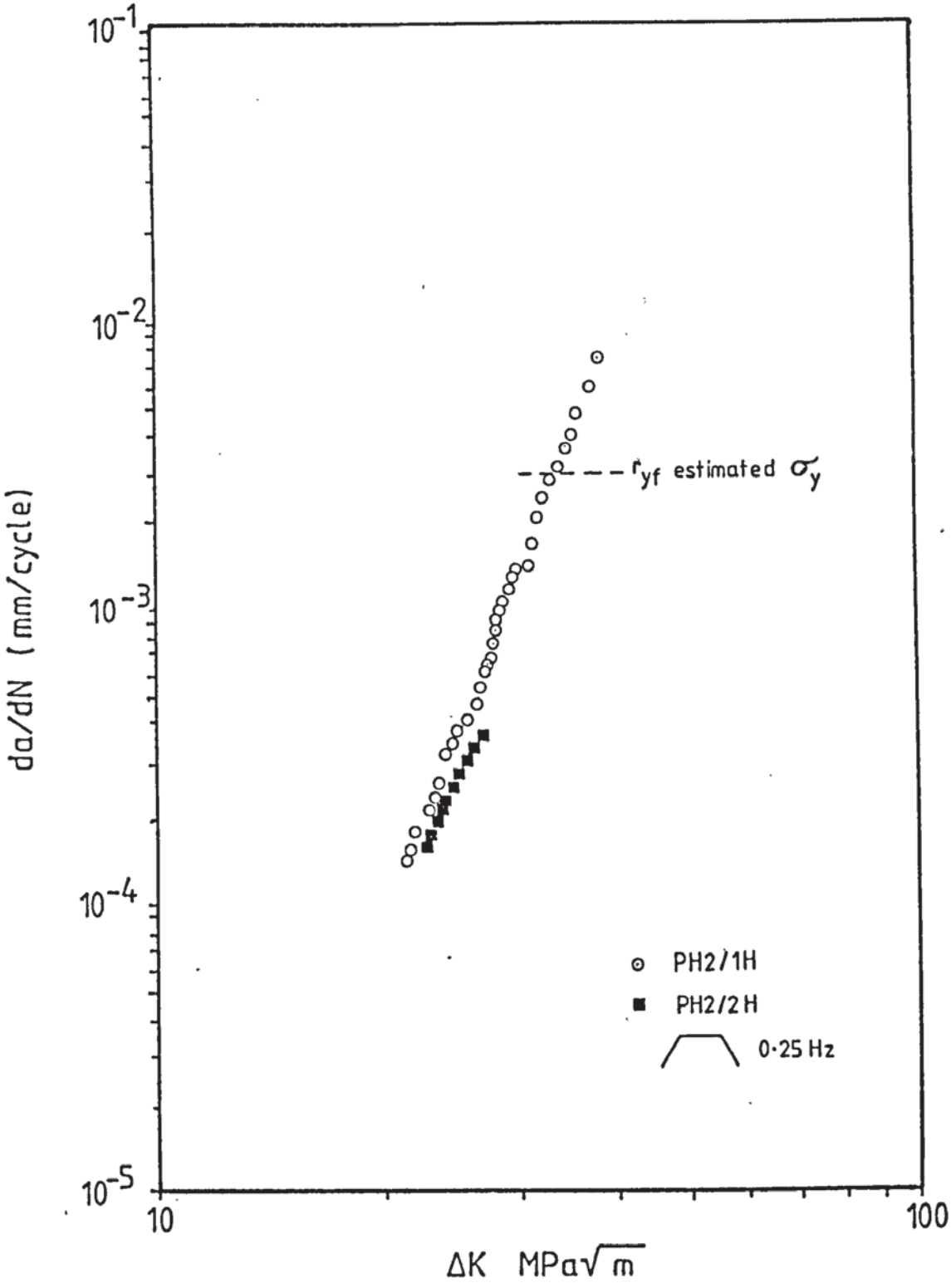

Figure 4.27k Fatigue crack growth data for (001)-(210) specimens tested at 850°C Frequency 0.25Hz

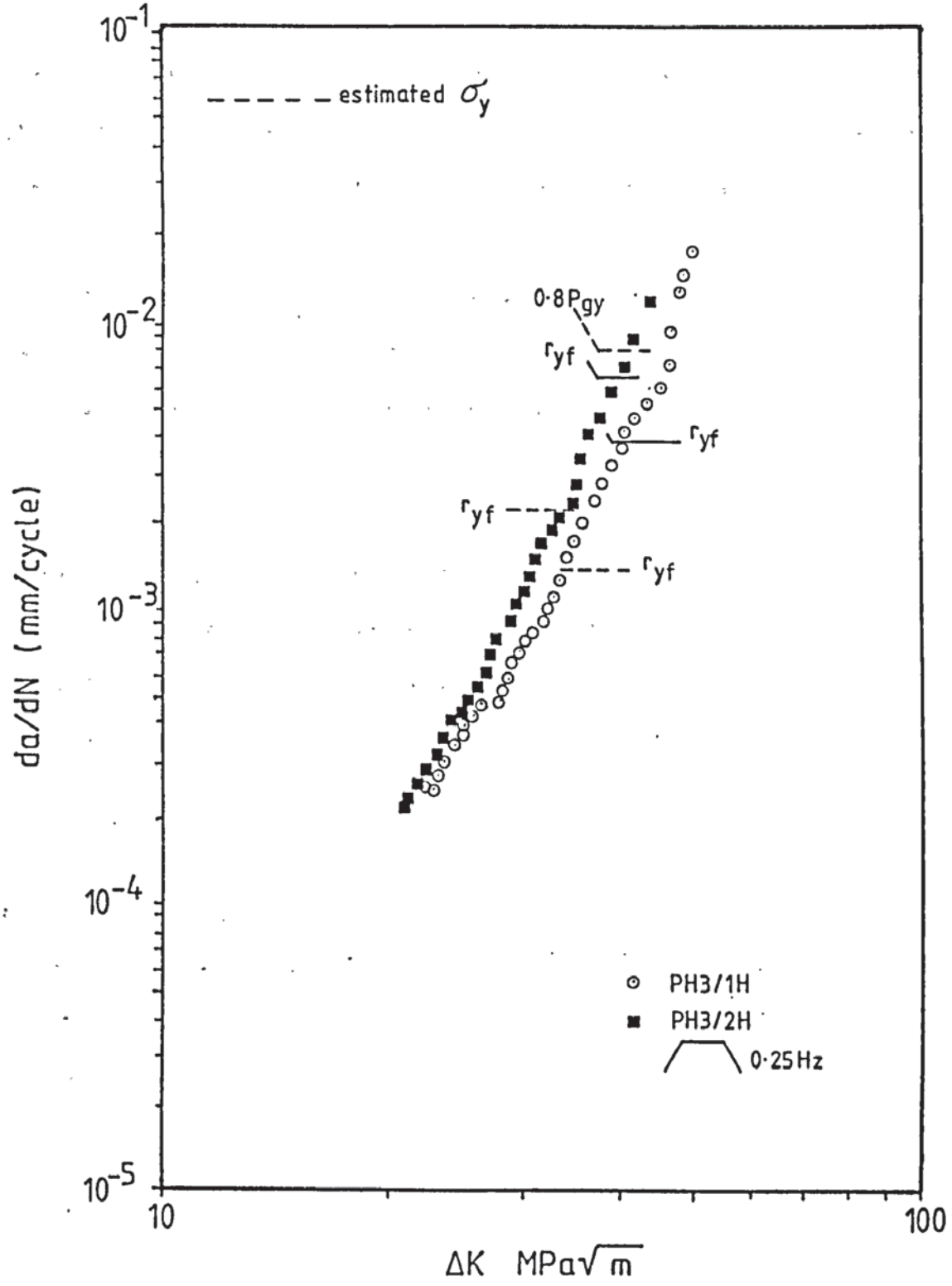

Figure 4.27l Fatigue crack growth data for (001)-(110) specimens tested at 850°C Frequency 0.25Hz

4.5.4.1 Linear regression analysis of fatigue crack growth data

Linear regression analysis was carried out on the data illustrated in figure 4.27. Only data up to the lowest possible LEFM breakdown point was used in order to prevent the inclusion of geometrical or plasticity effects.

Table 4.13 gives the linear regression results for the fatigue crack propagation data shown in figure 4.27. The results were obtained using values of Log da/dN versus Log ΔK.

Two specimens were tested at each condition as shown in figures 4.27a-l. In most cases the tests show good correlation at low to moderate crack growth rate, any variation starting at higher crack growth rates.

Figures 4.28a-d portray the data compiled in terms of temperature, orientation and frequency in order to illustrate the effect of these parameters on fatigue crack growth rate. Where data produced under the same conditions was found to vary, an average result has been plotted.

Table 4.13 Linear regression analysis of fatigue crack propogation results

Specimen	Cast No	Temp °C	Nominal Orientation	constant	exponent	Regression coefficient(R)
TRIANGULAR WAVEFORM ZERO HOLD 1.25Hz						
PL1/1Z	S38233-12/4	750	(001)-(100)	-30.62	7.05	0.995
PL1/2Z	S38233-12/1	750	(001)-(100)	-25.24	5.354	0.990
PL2/1Z	S38233-16/3	750	(001)-(210)	-28.24	6.154	0.994
PL2/2Z	S38233-16/2	750	(001)-(210)	-22.22	4.254	0.998
PL3/1Z	S38233-9/3	750	(001)-(110)	-25.89	5.308	0.976
PL3/2Z	S38233-9/1	750	(001)-(110)	-26.74	5.588	0.991
PH1/1Z	S38233-12/6	850	(001)-(100)	-27.53	6.100	0.996
PH1/2Z	S38233-12/7	850	(001)-(100)	-29.29	6.610	0.992
PH2/1Z	S38233-16/7	850	(001)-(210)	-26.32	5.554	0.999
PH2/2Z	S38233-16/4	850	(001)-(210)	-26.55	5.611	0.994
PH3/1Z	S38233-9/7	850	(001)-(110)	-28.03	6.136	0.997
PH3/2Z	S38233-9/6	850	(001)-(110)	-23.71	4.752	0.994
TRAPEZOIDAL WAVEFORM 1.6 SECOND HOLD 0.25Hz						
PL1/1H	S38233-15/2	750	(001)-(100)	-26.83	5.955	0.997
PL1/2H	S38233-15/1	750	(001)-(100)	-22.26	4.520	0.957
PL2/1H	S38233-20/1	750	(001)-(210)	-31.51	7.110	0.994
PL2/1H	S38233-16/5	750	(001)-(210)	-24.46	4.988	0.989
PL3/1H	S38233-14/1	750	(001)-(110)	-24.06	4.787	0.997
PL3/2H	S38233-9/5	750	(001)-(110)	-26.48	5.489	0.994
PH1/1H	S38233-15/5	850	(001)-(100)	-27.90	6.281	0.996
PH1/2H	S38233-15/1	850	(001)-(100)	-27.98	6.328	0.996
PH2/1H	S38233-20/5	850	(001)-(210)	-28.02	6.287	0.992
PH2/2H	S38233-20/4	850	(001)-(210)	-24.06	4.939	0.994
PH3/1H	S38233-14/5	850	(001)-(110)	-19.99	3.785	0.993
PH3/2H	S38233-14/4	850	(001)-(110)	-23.346	4.884	0.994

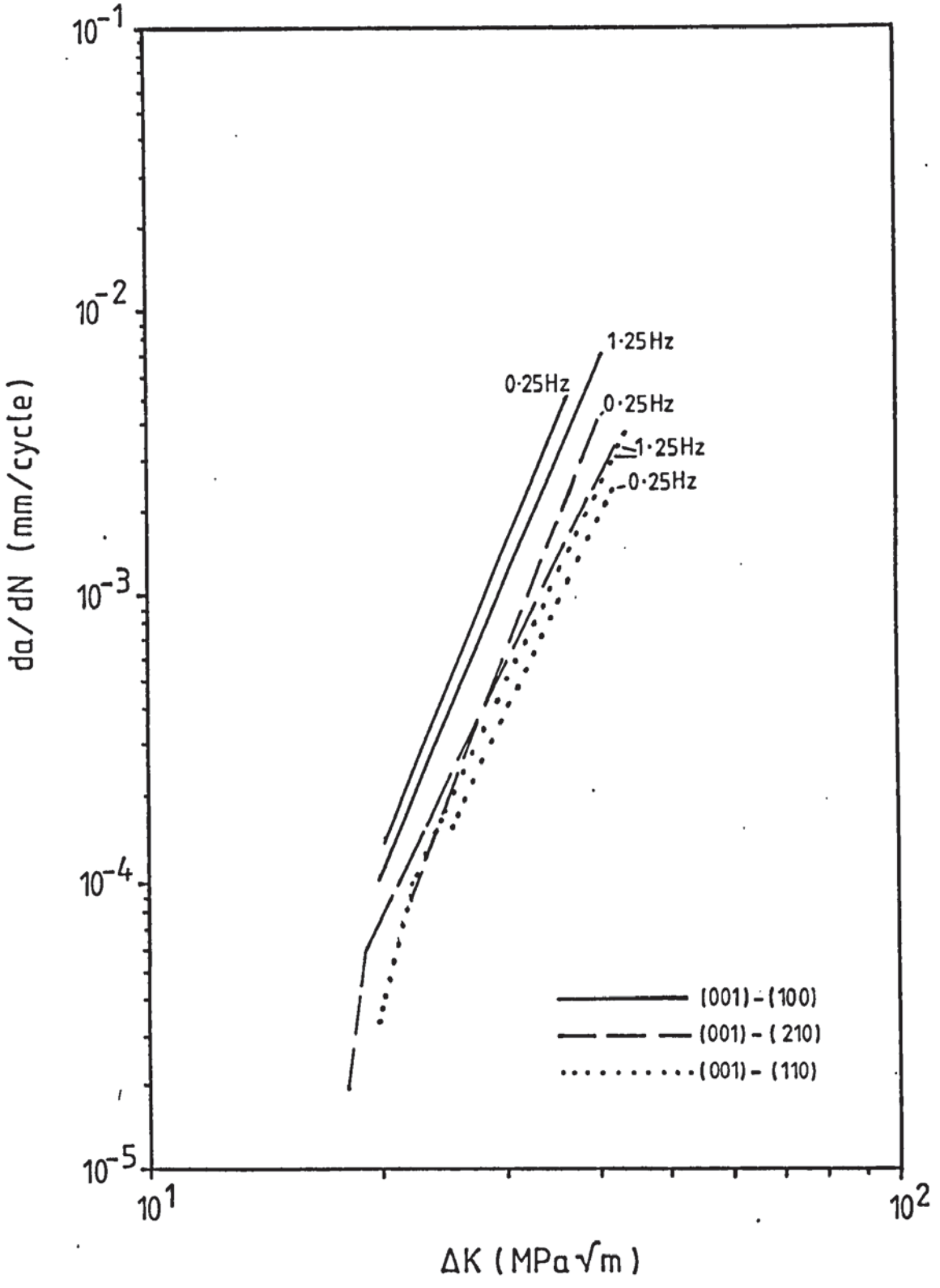

Figure 4.28a Effect of orientation and frequency on fatigue crack growth in alloy SRR 99 tested at 750°C

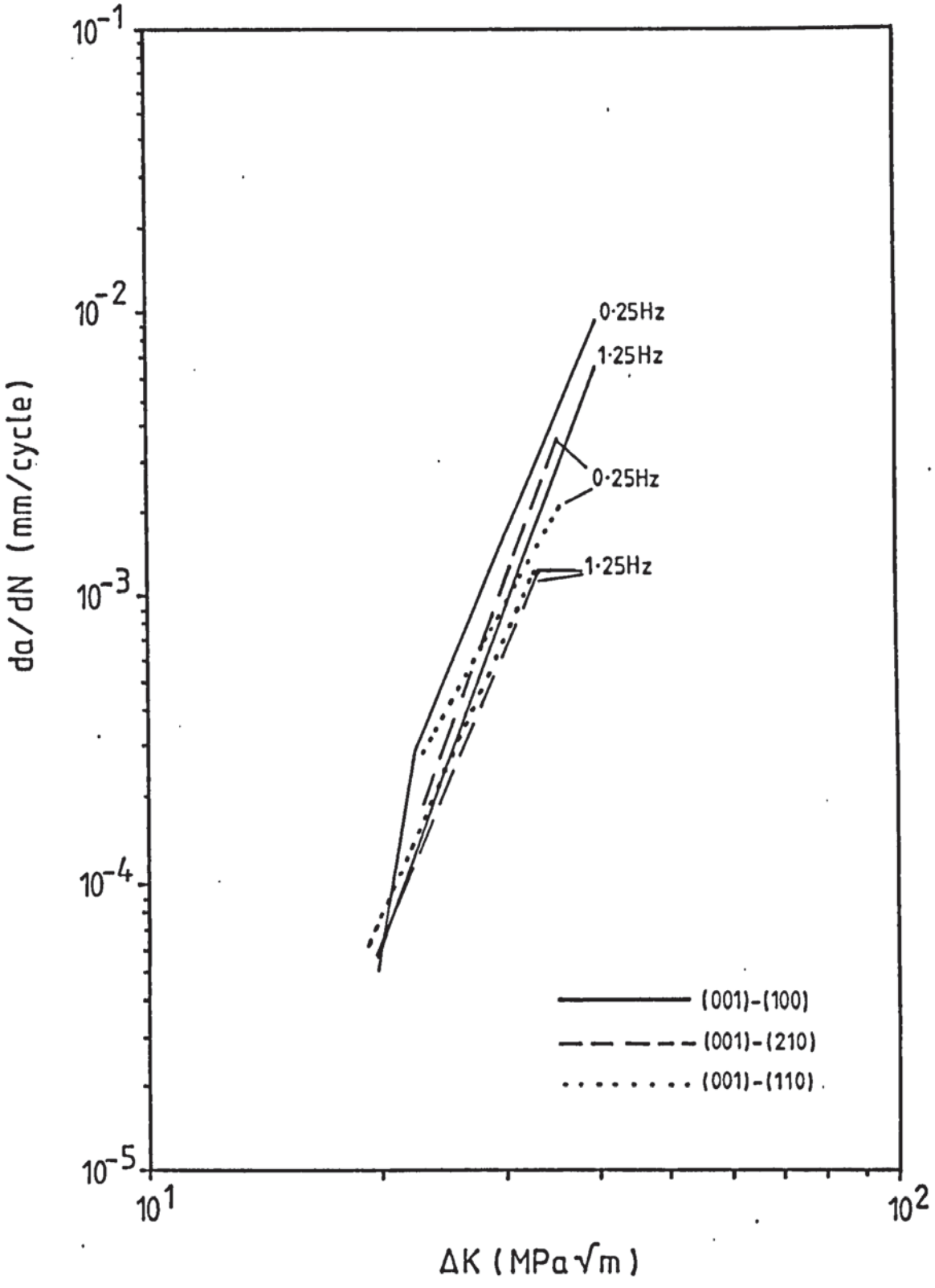

Figure 4.28b Effect of orientation and frequency on fatigue crack growth in alloy SRR 99 tested at 850°C

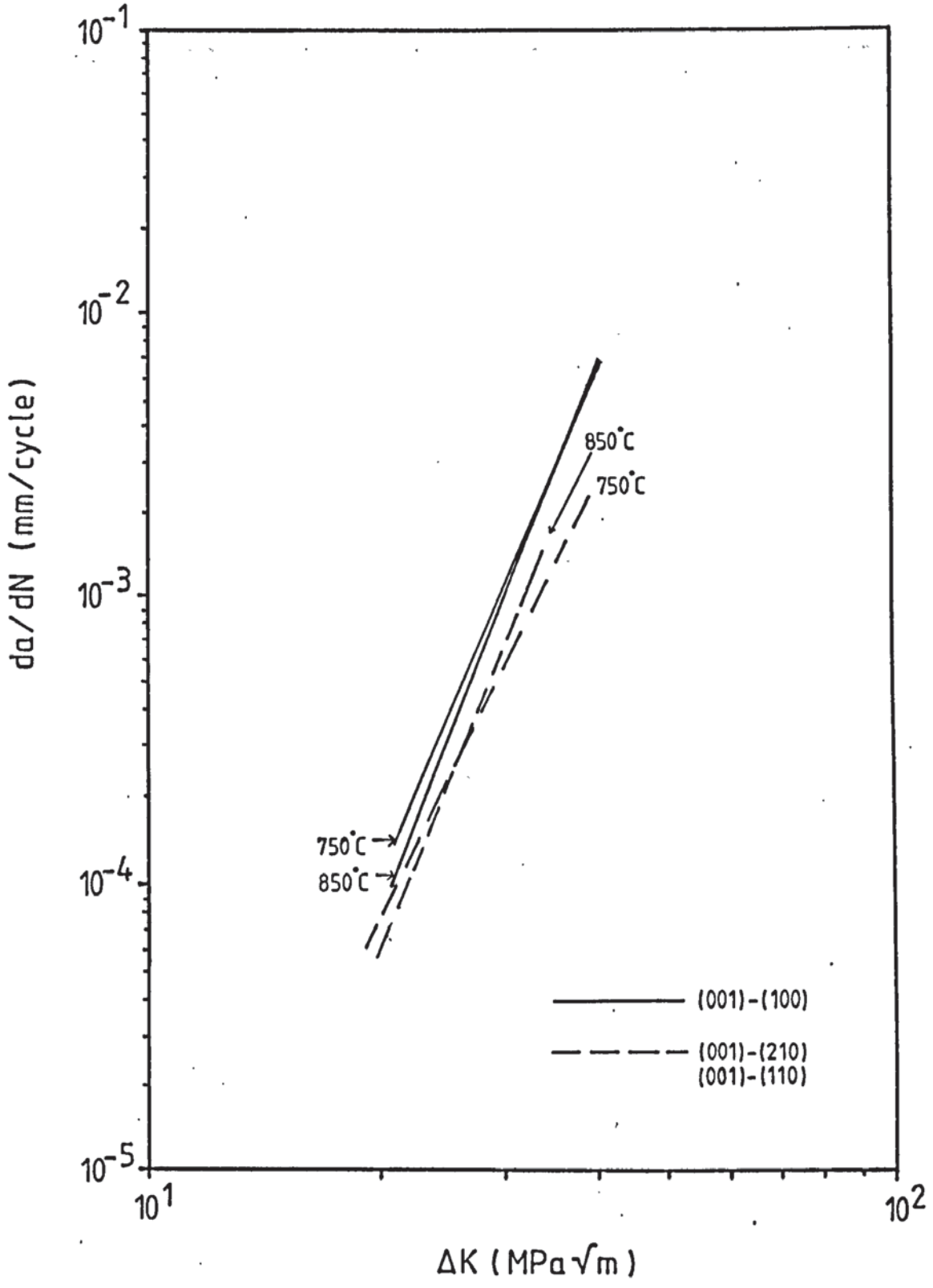

Figure 4.28c Effect of temperature and orientation on fatigue crack growth in alloy SRR 99 tested at 1.25Hz

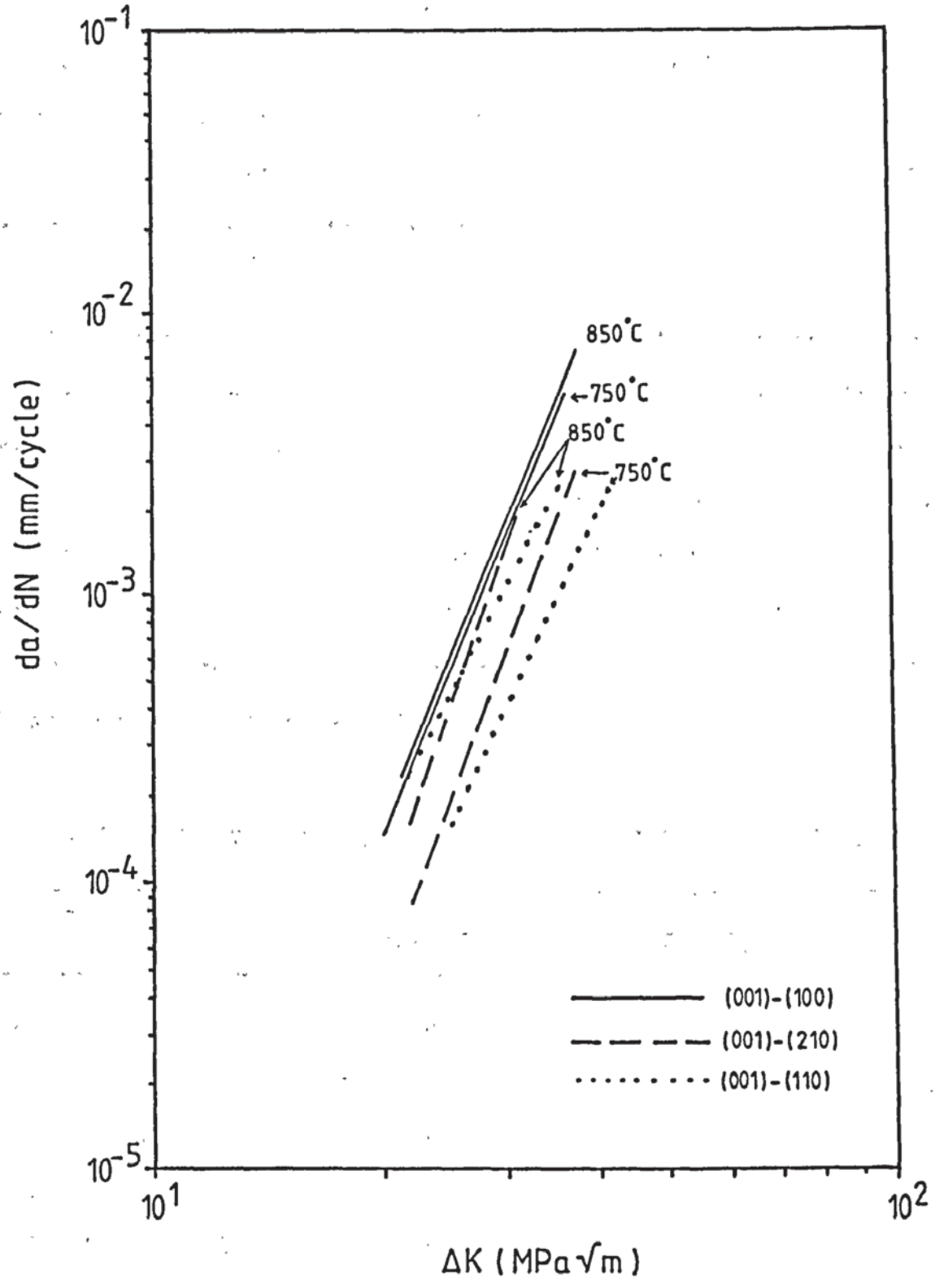

Figure 4.28d Effect of temperature and orientation on fatigue crack growth in alloy SRR 99 tested at 0.25Hz

4.5.5 Orientation analysis for fatigue crack propagation specimens

Fatigue crack propagation specimens were supplied in three nominal orientations, as illustrated in figure 3.2. In all cases the crack growth direction is [001], ie parallel to the main dendrite growth direction.

In order to confirm that the orientations were close to those specified, Laue back reflection x-ray analysis was carried out to determine both top and transverse face orientations. Table 4.14 gives the results of the orientation analysis in terms of position within a unit stereographic triangle, described by the parameters θ and φ as used in figure 4.6. The orientations are illustrated schematically in figure 4.29.

Table 4.14 Fatigue crack propagation specimen orientations

Specimen	Cast No	nominal orientation	Top face		Side face	
			θdegrees	φdegrees	θdegrees	φdegrees
PL1/2Z	S38233-12/1	(001)-(100)	1.5	0	5	8
----	S38233-12/5	(001)-(100)	1	25	4.8	43.5
PH1/1H	S38233-15/5	(001)-(100)	2	1	1	0
PH2/1H	S38233-20/5	(001)-(100)	3.5	0	30	8
PL2/2Z	S38233-16/2	(001)-(210)	3.5	23	28	4.5
PL2/2H	S38233-16/5	(001)-(210)	1.5	1	28	4
PL3/2H	S38233-9/5	(001)-(110)	5	21	35.5	7
PH3/1H	S38233-14/5	(001)-(110)	3	16.5	45	7
PL3/2Z	S38233-9/1	(001)-(110)	5	45	38	9

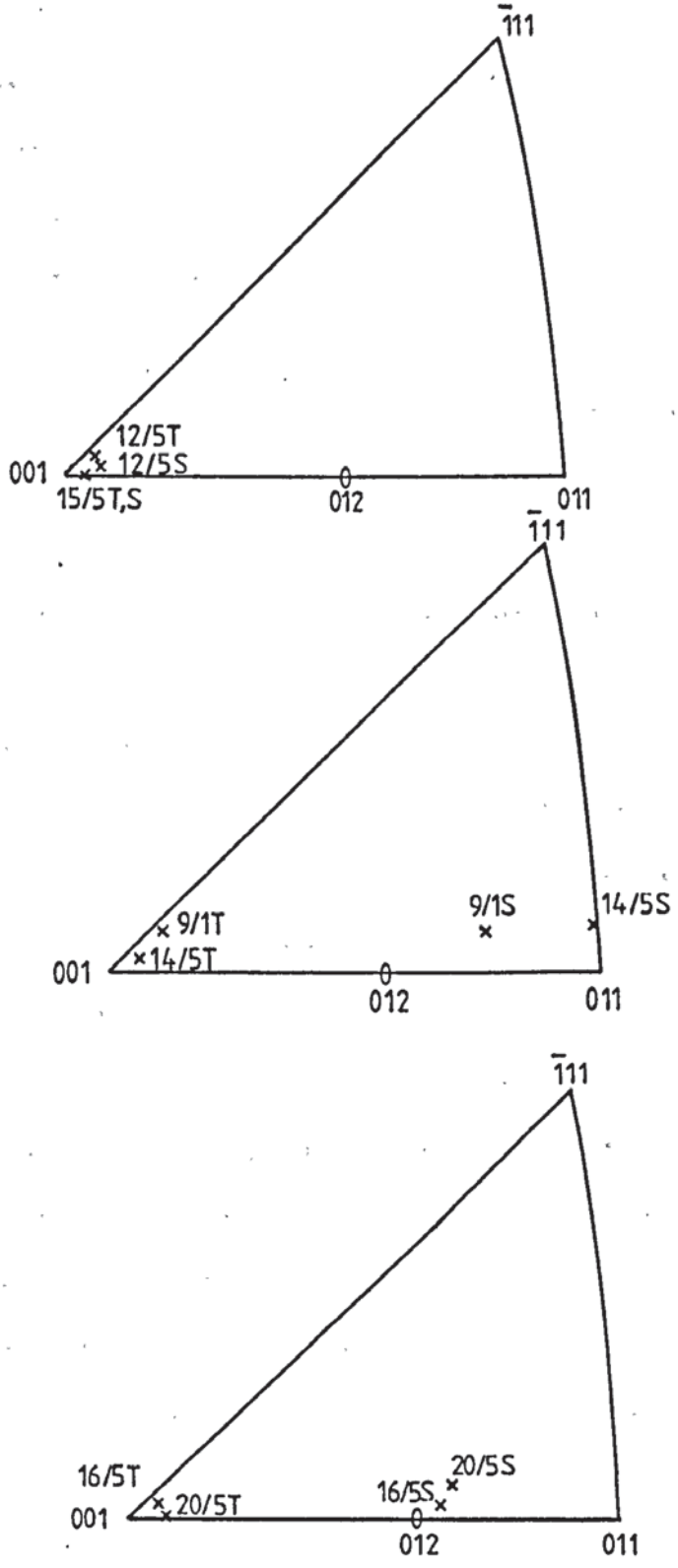

Figure 4.29 Laue orientation analysis results for fatigue crack propagation specimens

4.5.6 Examination of SRR 99 fatigue crack propagation fractures

Figures 4.30 and 4.31 illustrate the fracture surfaces produced by the fatigue crack propagation testing of alloy SRR 99. In all cases the crack propagation direction is [001], that is along the main dendrite growth direction. The specimens were observed in a scanning electron microscope with the notch root parallel to the bottom edge of the screen, so that the [001] is vertical.

To assist with the examination, figures 4.32a-c illustrate schematically the three nominal specimen orientations used for smooth bar fatigue and fatigue crack propagation testing. Figure 4.32d illustrates the forces acting on a beam in three point bending. The predominant force may be assumed to be tensile, operating along the axis of the bar. There is also a shear component which is zero on the surface of the bar and and reaches a maximum at the neutral axis. By inspection of figures 4.32a-c it can be seen that the specimens differ in orientation by a lateral rotation about the [001] and therefore the end face orientation is of the same type as the transverse face (assuming the normal to the top face is exactly [001]). As mentioned previously in section 4.5.4 the tensile axis for the (001)-(210) and (001)-(110) specimens are <210> and <110> respectively and therefore the yield strength of the crystal in these directions is important when considering LEFM breakdown conditions.

Examination of the fracture surfaces of (001)-(100) specimens tested at temperatures of 750°C and 850°C at a frequency of 1.25Hz (figure 4.30a) showed the presence of crystallographic facets. The facets were found to be parallel to the notch root, ie in the [100] direction (see figure 4.32a) and approximately 30μm high. The macroscopic crack growth plane is normal to the stress axis, ie {100}. The transition between planes was sharp with undercutting of the facet plane, as shown in figure 4.30a/1.

Figure 4.30b is a montage of the first 0.5mm crack growth produced at a temperature of 750°C and a frequency of 1.25Hz in a (001)-(210) specimen. The general crack growth plane was found to be normal to the stress axis ie {210}, as illustrated in figure 4.32b. Crystallographic ridges were found in the 1.25Hz propagation region although the 40Hz propagation region (bottom of montage) was found to be completely planar.

Figure 4.30c illustrates fatigue fracture surfaces produced by crack propagation testing (001)-(110) specimens at 750°C and 850°C at a frequency of 1.25Hz. The area marked in figure 4,30c/2 by a white box indicates the 40Hz propagation region which was used to avoid notch effects and to ensure that the crack would continue to grow at the lower frequency. The macroscopic crack growth planes were found to be slightly curved for specimens tested at both temperatures, though the general trend was to be normal to the stress axis . Although ridges were observed on the

crack plane (figure 4.30c/1) they did not appear to have an exact crystallographic direction.

Figure 4.31a shows fatigue fracture surfaces produced by crack propagation testing at 750°C and a frequency of 0.25Hz. Due to the increased amount of oxide present on the fracture surfaces only examination at low magnifications was possible. Details of any crystallographic features were not as well defined as those observed in specimens tested at the higher frequency, although some facets were observed in the (001)-(100) specimen (figure 4.31a/1).

Figure 4.31b shows fracture sufaces produced by fatigue crack propagation testing at 850°C and 0.25Hz. Both (001)-(100) and (001)-(210) specimens showed clear crystallographic facets, the (001)-(110) specimen being too oxidised for accurate analysis. The (001)-(210) specimen exhibited crystallographic ridges of the type seen in samples tested at 1.25Hz. Facets observed for the (001)-(100) specimens however appeared as cubic blocks rather than the terraces seen in specimens tested at 1.25Hz

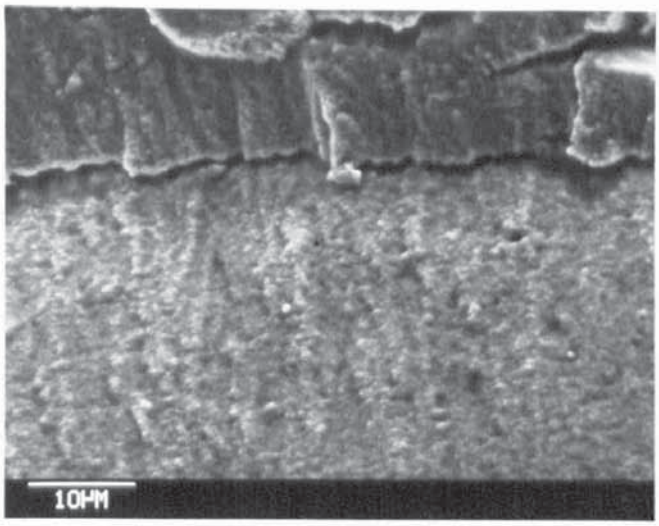

S38233-12/1
(001)-(100)
750°C
Mag'n x1400

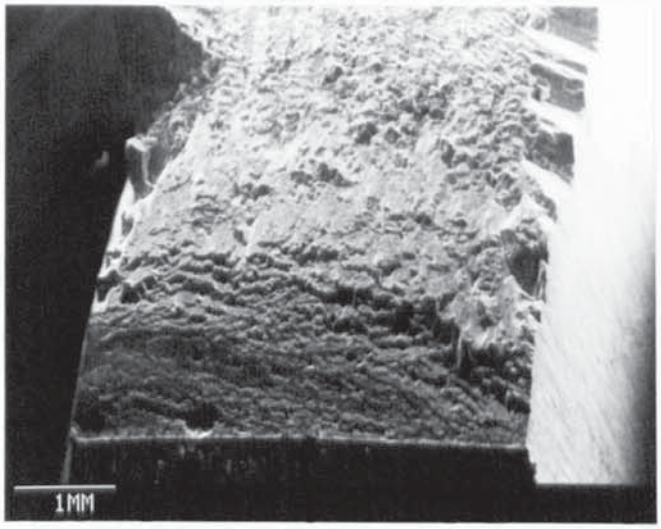

S38233-12/7
(001)-(100)
850°C
Mag'n x13

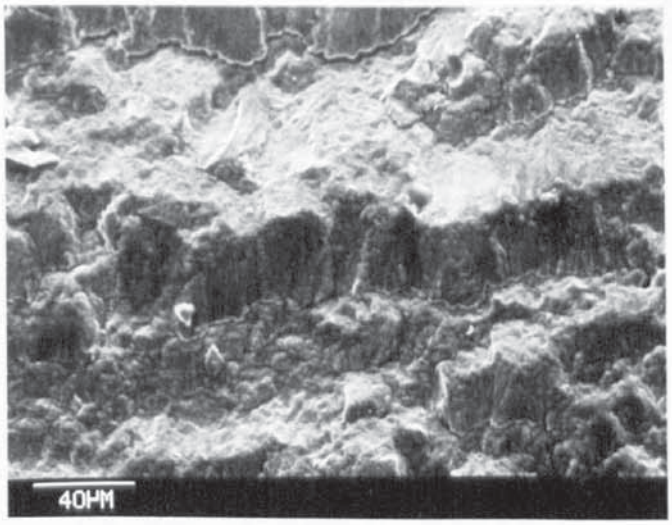

S38233-12/7
(001)-(100)
850°C
Mag'n x325

Figure 4.30a Fracture surfaces for(001)-(100) fatigue crack propagation specimens tested at 1.25Hz

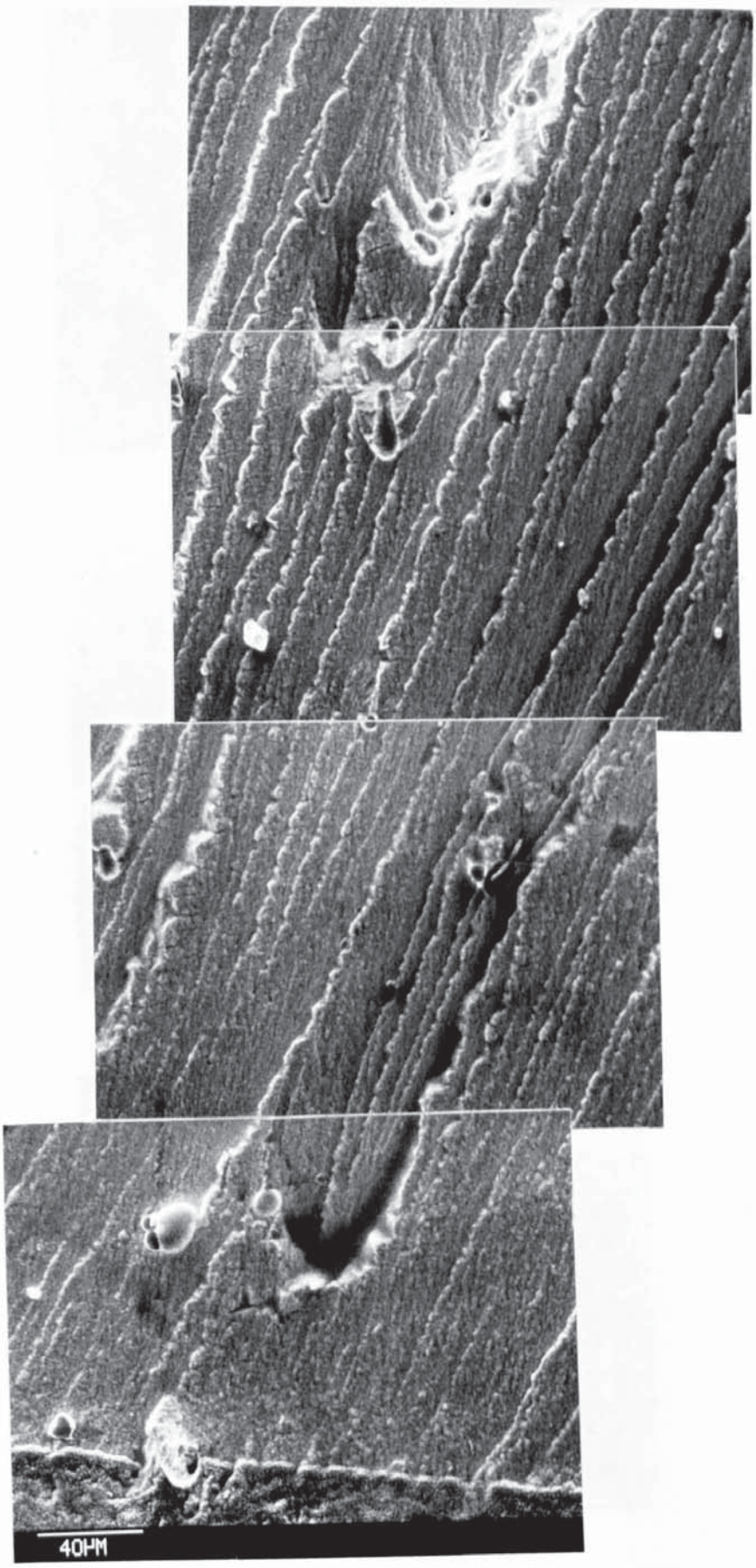

Figure 4.30b Fracture surface for(001)-(210) fatigue crack propagation specimen tested at 1.25Hz

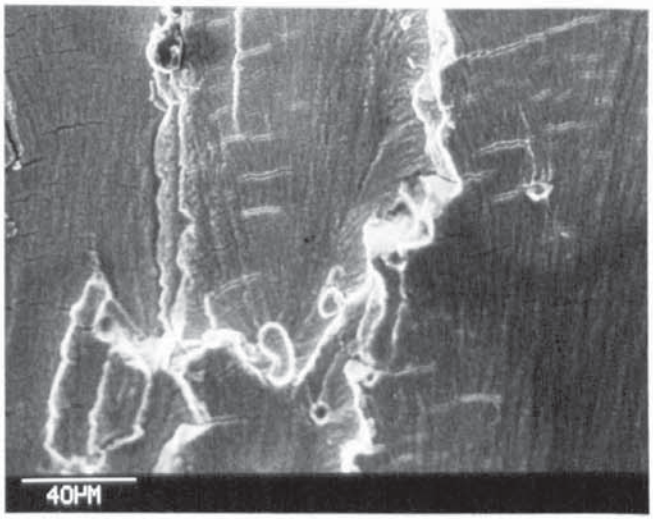

1) S38233-9/1
(001)-(110)
750°C
Mag'n x375

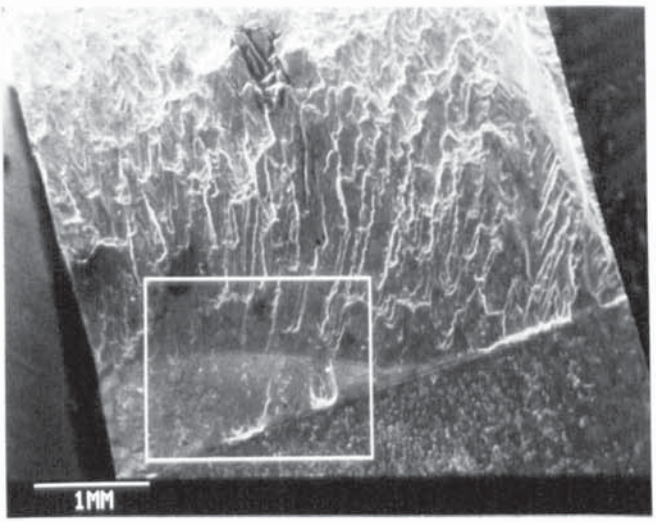

2) S38233-9/1
(001)-(110)
750°C
Mag'n x15

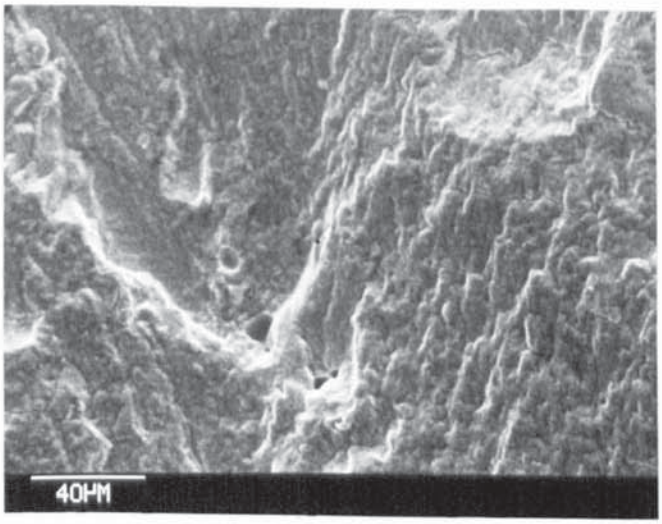

3) S38233-9/7
(001)-(110)
850°C
Mag'n x375

Figure 4.30c Fracture surfaces for(001)-(110) fatigue crack propagationspecimens tested at 1.25Hz

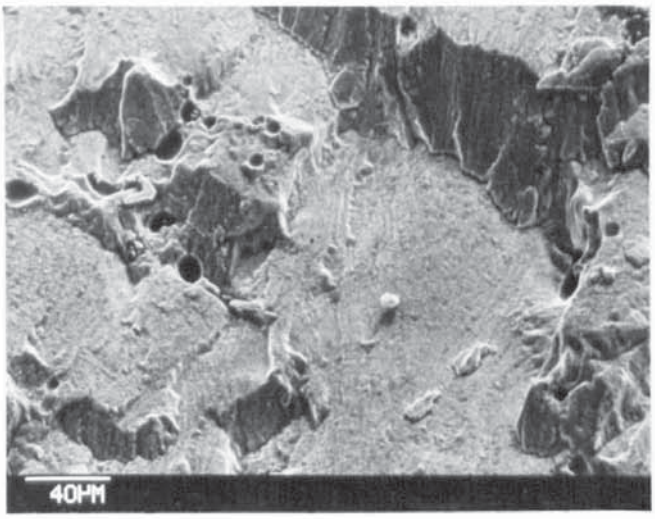

1) S38233-15/2
(001)-(100)
750°C
Mag'n x275

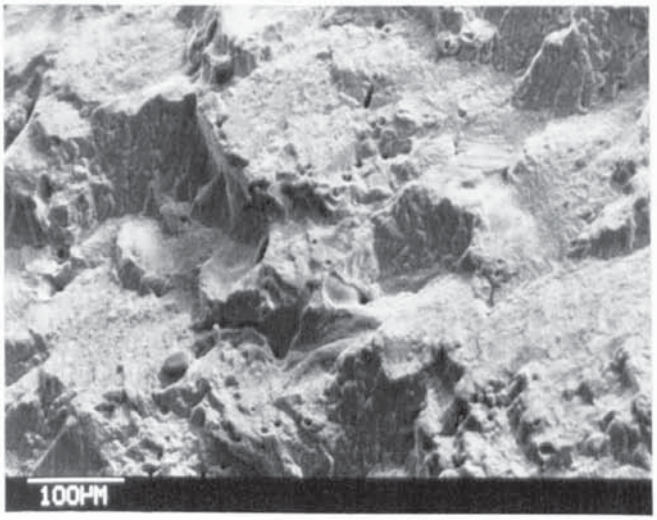

2) S38233-16/5
(001)-(210)
750°C
Mag'n x130

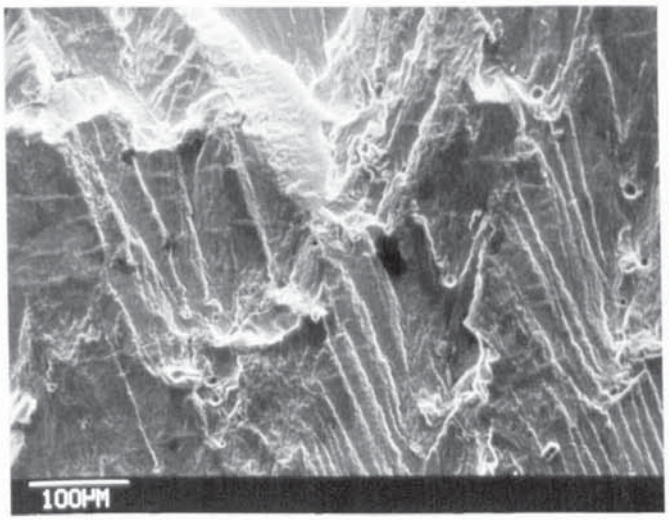

3) S38233-9/5
(001)-(110)
750°C
Mag'n x130

Figure 4.31a Fracture surfaces of fatigue crack propagation specimens tested at 750°C and 0.25Hz

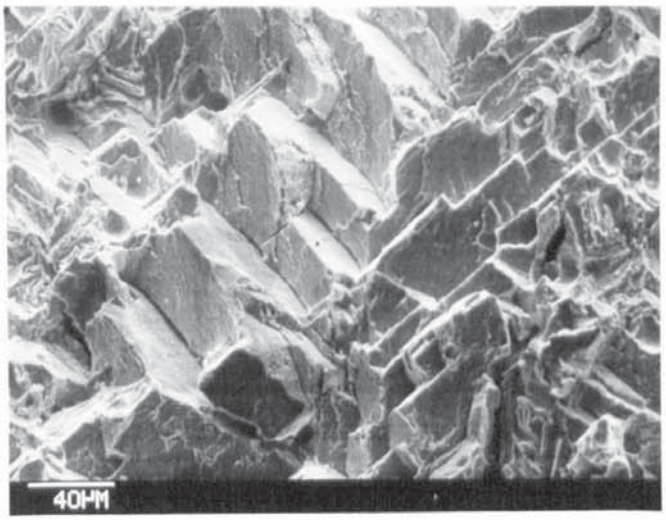

1) S38233-12/2
(001)-(100)
850°C
Mag'n x275

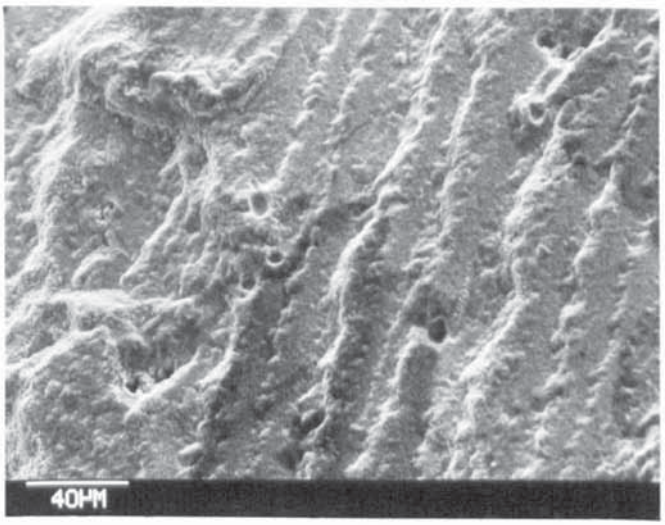

2) S38233-20/4
(001)-(210)
850°C
Mag'n x325

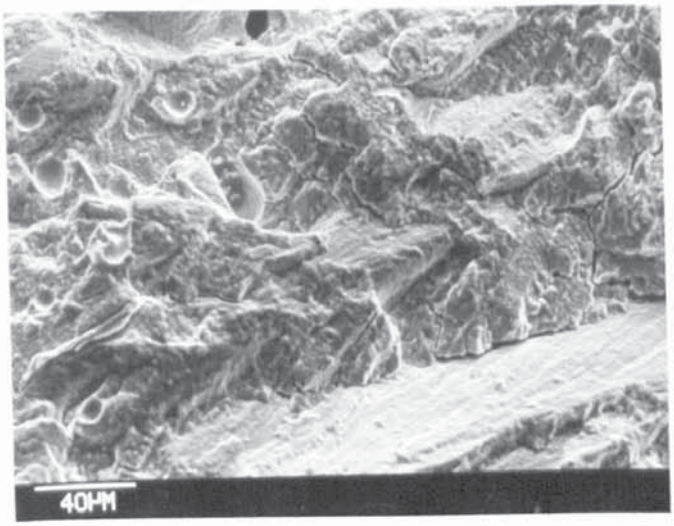

3) S38233-14/5
(001)-(110)
750°C
Mag'n x325

Figure 4.31b Fracture surfaces of fatigue crack propagation specimens tested at 850°C and 0.25Hz

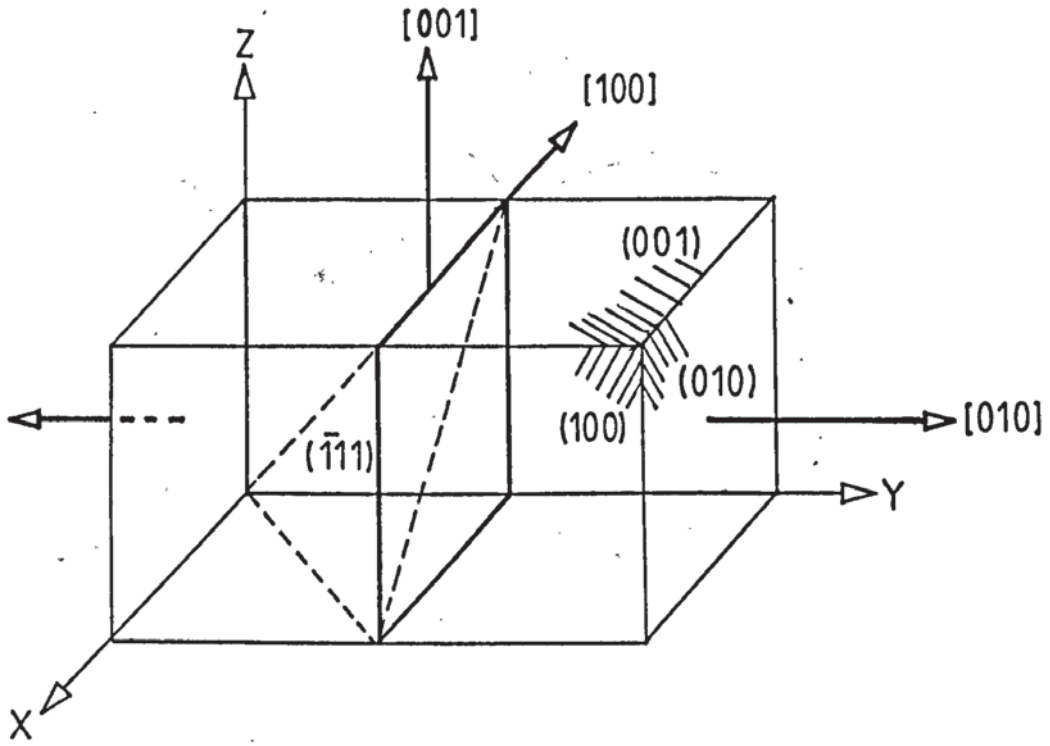

Figure 4·32a Orientation of (001) - (100) fatigue specimens

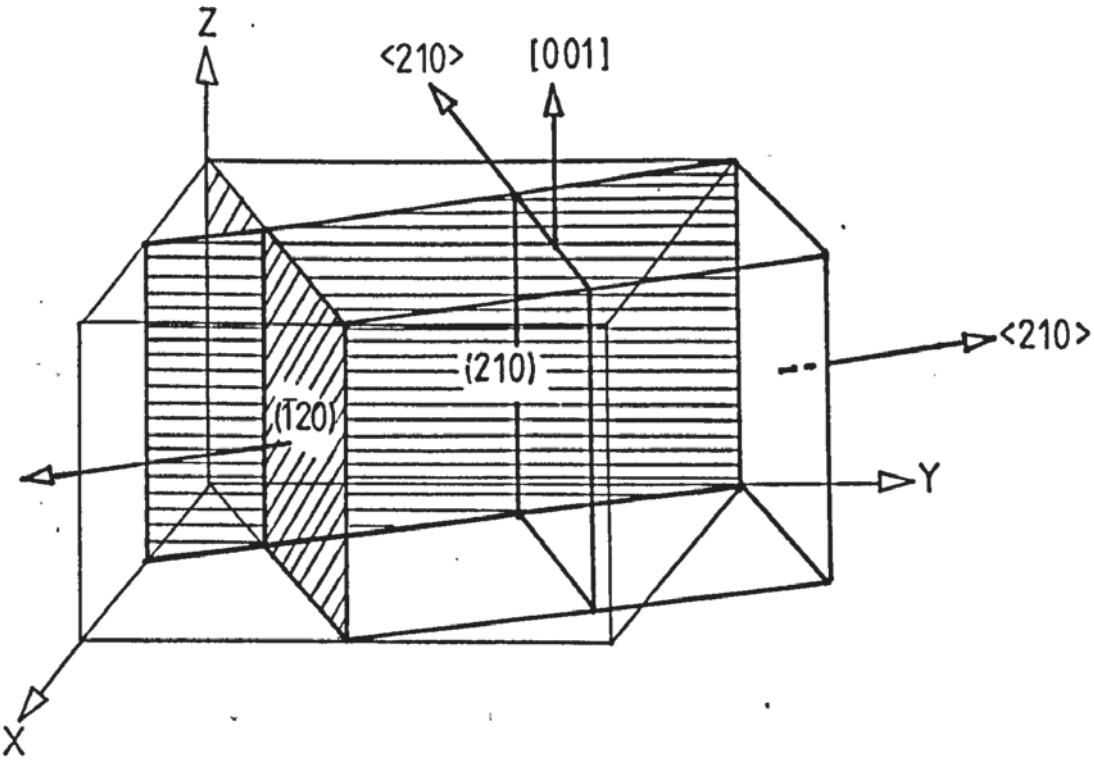

Figure 4·32b Orientation of (001) - (210) fatigue specimens

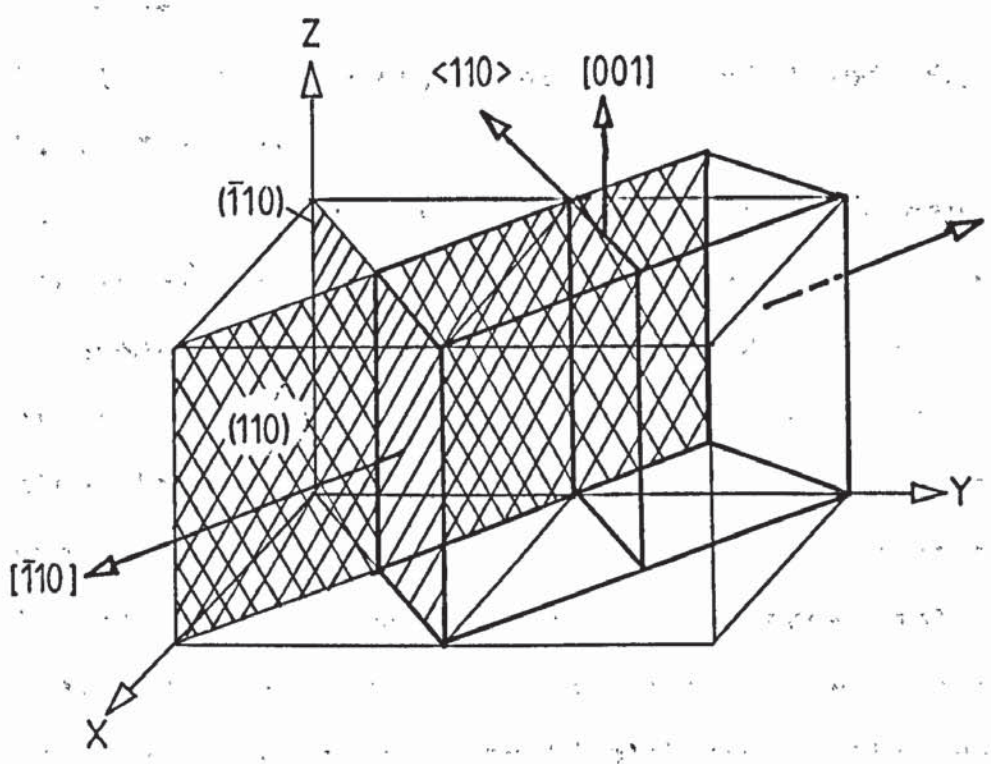

Figure 4·32c Orientation of (001) - (110) fatigue specimens

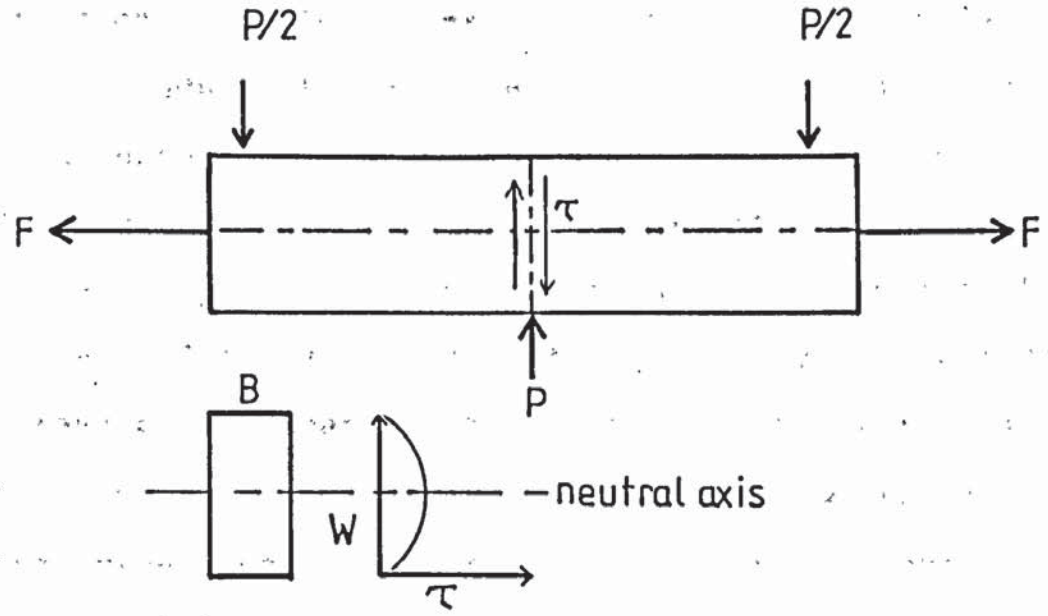

Figure 4·32d Forces acting upon a beam in three point bending

5 Discussion

5.1 The creep properties of alloy SRR 9 and SRR 99

5.1.1 Test procedure

Several approaches have been made to the creep testing of single crystals. In general, single crystal specimens are produced in small sizes. This is dictated by the expense of producing large single crystals for destructive tests. Also the high creep resistance exhibited by nickel base superalloy single crystals requires testing at high stress in order to produce failure within a acceptable time, and therefore the cross sectional area of the test piece has to be small in order to avoid problems in the selection of material for the specimen grips. Use of specimens with short gauge lengths increases the problems of accurate strain measurement.

In order to simplify the manufacture and testing of single crystals, research has been carried out using cylindrical specimens tested in compression (105). This greatly reduces the time involved in machining specimens and the problems in producing specimen grips. There is the added advantage that extensometer attachments may be attached to the plattens rather than the specimen itself. The main drawback associated with creep testing in compression is that the height to diameter ratio must be kept low to avoid specimen buckling. However, use of a large cross sectional area increases the probability of friction between specimen and platten which produces complex stress distributions in the specimen.

In this study Pre-machined tensile specimens were obtained from Rolls-Royce Ltd.. Two geometries as illustrated in figure 3.1 were supplied, the flat specimens being produced in SRR 9, an early development alloy. As the specimens required different gripping arrangements, a strain measuring technique was required which may be easily converted for differing specimen geometries.

The use of a non contact device was considered to be an inexpensive and flexible measuring system for use in situations where non standard specimens are being used. The use of an infra red extensometer was prevented by the small gauge length, and the fact that reference points could not be applied to the gauge length by use of reflective paint due to the high temperature and large displacements involved. It was decided therefore to investigate the use of a photographic technique for the measurement of strain in comparative testing of specimens.

The system used is described in section 3.5 and shown in figure 3.8. An analysis of the strain measurement accuracy obtained by this technique has been carried out in order to identify the main sources of error.

5.1.2 Analysis of strain measurement accuracy

In order to assertain the accuracy of measurement of length from a film negative by the use of a Nikon measurescope, the following experiments were undertaken.

5.1.2.1 Comparison of photographic method with direct measurement

A steel tensile specimen was covered with engineering blue and marked with two 15mm gauge lengths, the size used in creep tests employing SRR 9 $2mm^2$ rectangular specimens (figure 3.9). The camera unit was set up to photograph the specimen at approximately the same magnification as that used in the creep experiments. The specimen gauge lengths were measured by use of a travelling microscope and photographed in order to record the initial gauge lengths. The specimen was then placed in an Instron tensile testing machine, strained, unloaded then removed and measured by both methods. The process was repeated several times before failure of the specimen. The results obtained are shown in table 5.1

Table 5.1 Strain accuracy results

Measure-ment	gauge length 1			gauge length 2		
	travelling microscope ε_1	photographic negative ε_2	diff $\varepsilon_2-\varepsilon_1$	Travelling microscope ε_1	Photographic negative ε_2	diff $\varepsilon_2-\varepsilon_1$
1	0.0504	0.0573	0.0069	0.0492	0.0528	0.0036
2	0.1002	0.1091	0.0088	0.0982	0.1037	0.0055
3	0.1548	0.1646	0.0097	0.1543	0.1614	0.0071
4	0.2379	0.2473	0.0094	0.2364	0.2486	0.0122

The difference in strain values for the two methods was found to vary, the photographic technique giving consistently higher values. The discrepancy between the two results was found to increase with higher values of strain. The difference between the two gauge lengths may be taken as an indication of the measurement variation involved in each technique. The average variation in readings produced by use of a travelling microscope is 0.0013ε, whereas for photographic technique gives an average variation of 0.0036ε.

5.1.2.2 Analysis of graphical scatter bands

For each creep specimen tested, the results were portrayed graphically in terms of true strain versus time as illustrated in figures 4.3, 4.8, and 4.9. Scatter bands were drawn onto the linear portion of some curves to encompass all the data points, as shown in figure 4.3d. Table 5.2 gives the size of the scatter bands in terms of true strain for both SRR 9 and SRR 99 data.

The average scatter band size for both specimen geometries is approximately $\Delta\varepsilon=0.007$, indicating that overall accuracy is not related to specimen configuration. The initial gauge lengths of the specimens was approximately 15mm in the case of the flat SRR 9 specimens and 12mm for the round SRR 99 stress rupture specimens.

The values presented will include all variations including measurement errors, temperature fluctuation and the error due to the inability to measure strain within the parallel gauge length.

Table 5.2 Scatter band values for creep tests

SRR 9		SRR 99	
specimen	$\Delta\varepsilon$	specimen	$\Delta\varepsilon$
9L/4	0.007	99L1/1	0.006
9L/5	0.010	99L1/2	0.006
9L/6	0.008	99L1/3	0.004
9L/7	0.005	99H1/1	0.015
9L/8	0.006	99H1/2	0.007
9L/9	0.008	99H1/3	0.008
average	0.0073	average	0.0076

5.1.2.3 Measurement accuracy for photographic technique

An analysis was carried out in order to obtain an average error value for the photographic strain measuring technique. Table 5.3 gives two sets of measurements for specimen 9L/6 , with the third column giving the difference between the strain values for each frame. These strain values, $\Delta\varepsilon$, have been classified in table 5.4

The assumption made in using the average strain difference or error to describe the technique is that there is no difference between batches . In this case a batch is the series of lengths measured for each frame. If the

error involved in measuring the length of the specimen from the negative is the same for photographs taken at the start of the test as for those taken just before specimen failure;(ie the value of strain measured has little effect on overall accuracy) then the distribution of errors obtained will be normal.

Pearson's second coefficient of skewness gives an empirical value of the measure of asymmetry of the distribution:

$$\text{Skewness} = \frac{3\ (\text{mean}-\text{median})}{\text{Standard deviation}} \qquad \ldots\ldots\ (5.1)$$

In the case of specimen 9L/6 $\bar{x}$=0.3369, σ_{n-1} =0.3686 and the median=0.2965 giving a skew coefficient of +0.3285 indicating that the distribution has a moderate positive skew.

A more quantitative method of testing the observed frequency with that of a normal distribution is the chi-squared test (106). Using classified data the statistic χ^2 is given by the sum of the relative squared differences for each cell:

$$\chi^2 = \Sigma \frac{(O_i - E_i)}{E_i} \qquad \ldots\ldots\ (5.2)$$

Where O_i is the observed frequency of the ith class and E_i is the expected frequency for that class.

Table 5.3 Measurement variation using photographic technique (specimen 9L/6)

Frame	Measurement1 $\varepsilon 1(x10^{-2})$	Measurement2 $\varepsilon 2(x10^{-2})$	Difference $\Delta\varepsilon(x10^{-2})$
1	1.034	1.144	0.110
2	1.033	1.268	0.235
3	1.359	2.114	0.755
4	1.067	1.259	0.192
5	1.166	1.401	0.235
6	0.944	1.174	0.230
7	0.952	1.336	0.384
8	1.211	1.567	0.356
9	1.307	1.601	0.294
10	1.681	1.926	0.245
11	1.745	1.872	0.127
12	1.359	2.601	1.062
13	1.700	2.338	0.638
14	2.130	2.538	0.408
15	2.809	2.689	-0.120
16	3.219	3.115	-1.040
17	3.152	3.117	-0.035
18	2.309	3.273	0.964
19	3.003	3.593	0.590
20	3.260	3.750	0.490
21	3.454	3.912	0.458
22	3.932	4.218	0.268
23	4.087	4.426	0.339
24	4.448	5.036	0.588
25	4.537	5.361	0.824
26	5.290	5.496	0.206
27	5.493	6.116	0.623
28	5.967	6.174	0.207
29	6.163	6.694	0.531
30	6.663	6.755	0.092
31	6.863	6.756	-0.107
32	7.464	7.780	0.316
33	7.778	7.990	0.212
34	8.751	9.050	0.299
35	9.646	9.896	0.250
36	10.608	11.509	0.901
		mean	0.337
		σ_{n-1}	0.369

Table 5.4 Classified data for specimen 9L/6 used in Chi-squared test

Δε	Class boundary	Zfor class boundaries	Area under normal curve	Area for each class	expected freq	Observed freq
(x10-²)			0 to Z			
	-1.005	-3.641	0.499			
-1to-0.8				0.001	0.036(0)	1
	-0.795	-3.071	0.4989			
-0.79to-0.6				0.0044	0.158(0)	0
	-0.595	-2.528	0.4945			
-0.59to-0.4				0.0178	0.641(1)	0
	-0.395	-1.986	0.4767			
-0.39to-0.2				0.0516	1.858(2)	0
	-0.195	-1.443	0.4251			
-0.19to 0				0.109	3.93(4)	3
	0.005	-0.9	0.3159			
0.01to 0.2				0.175	6.311(6)	5
	0.205	-0.358	0.1406			
0.21to 0.4			ADD	0.216	7.776(8)	13
	0.405	0.193	0.0754			
0.41to 0.6				0.1919	6.91(7)	7
	0.605	0.727	0.2673			
0.61to 0.8				0.1307	4.705(5)	3
	0.805	1.270	0.398			
0.81to 1				0.067	2.408(2)	3
	1.005	1.813	0.465			
1.01to 1.2				0.026	0.936(1)	1
	1.205	2.355	0.491			

χ^2 is a measure of the discrepancy in the hypothesis that error values from different frames are normally distributed, ie no differences between samples. This hypothesis may be tested at various levels of confidence and if found to fail indicates that there is a size factor involved.

Table 5.4 gives the classified data for the strain difference values $\Delta\varepsilon$ given in table 5.3. Columns 3,4 and 5 produce frequency values for each cell which would be expected if the distribution were normal. Using the χ^2 distribution, the expected frequency in each category (cell) must be at least 5, therefore the first five cells and the last 4 cells have been combined to give:

Table 5.5 Frequency values for χ^2 test

O_i	4	5	13	7	7
E_i	6.62	6.31	7.78	6.91	8.05

Hence,with use of equation 5.2

$$\chi^2 = \frac{(4-6.62)^2}{6.62} + \frac{(5-6.31)^2}{6.31} + \frac{(13-7.78)^2}{7.78} + \frac{(7-6.91)^2}{6.91} + \frac{(7-8.05)^2}{8.05}$$

$$= 1.04 + 0.27 + 3.50 + 0 + 0.14 = 4.95$$

The degrees of freedom = Number of cells-1-m, where m is the number of parameters estimated to compute the table of expected frequencies, in this case μ and σ for the normal distribution, so:

V= degrees of freedom= 5-1-2=2

The hypothesis that the observed frequency is normal was tested at $\chi^2 0.05$ level of significance and also at $\chi^2 0.95$ level to test that the result is not so good as to be unbelievable. From tables of percentile values for chi-squared distribution (107):

$$V=2 \quad \chi^2 0.05 = 5.99$$
$$V=2 \quad \chi^2 0.95 = 0.103$$

As $5.99 > 4.95 > 0.103$, it can be said that the fit of the data to a normal distribution is good, but not so good as to be unbelievable. Now, assuming the distribution of measurement error for the 36 frames tested is normal, it can be said that the measurement errors for the technique are at a 95% level of significance (see table 5.3):

$$x \pm 1.96\sigma$$
$$0.337 \pm 0.722 \ (\times 10^{-2}) \quad \text{ie} \quad \Delta\varepsilon = 1.059 \times 10^{-2}$$

As the distribution may be considered normal, then the sample means will be normally distributed. This allows the use of a one way analysis of variance technique. Using the film data for specimen 99H1/3, the first 12 frames were measured three times and the corresponding strain calculated. The analysis of variance is given by (106):

$$\frac{\sum_{i=1}^{k}\sum_{j=1}^{n} Xij^2 - \sum_{i=1}^{k}\left(\sum_{j=1}^{n} Xij\right)^2 /n}{(n-1)} = \sigma_o \quad \ldots\ldots (5.3)$$

Table 5.6 Analysis of variance for SRR 99 creep specimen (99H1/3)

	measurement			sum=S	crude sum of squares	$S^2/3$	difference	degrees of freedom	range
	1	2	3						
					(1)	(2)	(1-2)		
1	1.067	0.088	0.843	1.998	1.857	1.331	0.526	2	0.979
2	1.496	1.264	0.942	3.708	4.723	4.568	0.155	2	0.554
3	1.527	1.554	1.004	4.085	5.755	5.562	0.192	2	0.55
4	1.726	1.890	1.203	4.819	7.998	7.741	0.257	2	0.687
5	1.618	1.585	1.341	4.554	6.928	6.883	0.046	2	0.277
6	2.045	1.905	1.921	5.871	11.501	11.489	0.018	2	0.140
7	2.274	1.966	1.769	6.009	12.166	12.036	0.130	2	0.505
8	2.335	2.118	1.967	6.420	13.807	13.739	0.068	2	0.368
9	2.517	2.345	2.043	6.905	16.008	15.893	0.115	2	0.474
10	2.759	2.527	2.119	7.405	18.488	18.278	0.210	2	0.640
11	2.804	2.557	2.225	7.586	19.351	19.182	0.169	2	0.579
			TOTAL	55.572	118.58	116.70	1.88	22	
								MEAN RANGE	0.523

NOTE: all numbers have been multiplied by 10^2 except for degrees of freedom

The first term of the numerator is the sum of squares of each of the nk observations, the second being the sum of squares of each sample total divided by n. Table 5.6 gives an analysis for the first 11 frames, three measurements being made from each frame:

Sum of squares of the deviations of the observations from sample means (sum of squares between samples	= 1.88
degrees of freedom within samples	= 22

The experimental error variance is given by the sum of squares between samples divided by the degrees of freedom. Hence 1.88/22 gives σ_o^2 = 0.085, giving a value of standard deviation of σ = 0.292.

Now taking the value of mean range (table 5.6) to produce an average error value at 95% confidence:

$$\Delta\varepsilon = X \pm 1.96\sigma$$
$$= 0.532 \pm 0.572$$
$$\Delta\varepsilon_{max} = 1.095\times10^{-2}$$

This value compares with a value of $\Delta\varepsilon_{max}$ = 1.059x10-2 obtained by chi-squared analysis on a flat SRR 9 specimen. Comparing the scatter band results for specimen 99H1/3 with

the analysis of variance result it may be noted that analysis of variance indicates that the measurement accuracy is of the same level as the scatter band. The staircase effect seen on some creep curves (eg 99H1/2) may therefore be attributed to the measurement technique.

The results presented are for tests showing above average scatter band sizes in order to define the maximum error of the system. It was found that correct lighting of the specimen and strict control of film development produced negatives of high contrast and clarity, greatly improving ease of measurement.

The test equipment shown in figure 3.8.is not ideal. The viewing port in the furnace was horizontal and of small dimensions thus leaving little room for specimen extension and creating problems with shadows from the sides of the port. A vertical viewing port would have enabled more even illumination of the specimen, however the use of a small port with a glass window did allow accurate temperature control. The other major problem involved the lack of gauge marks on the specimens, with measurements being made from the shoulder positions.

It is considered that use of flat specimens with clearly marked gauge lengths and a larger viewing port to enable use of ring flash lighting would improve the accuracy of this technique.

The discrepancy between direct measurement and the photographic technique with an overestimation of strain increasing with increasing extension indicates an instability of the film base relative to the start of the film ie film shrinkage is not even throughout the roll. This may be assessed by use of a known length comparison photographed with the gauge length which may be used to correct for shrinkage.

The photographic technique may be considered to be an inexpensive approach to the problems of strain measurement at high temperature, especially with the advent of motorised automatic 35mm cameras with in built timing facilities which negates the use of a separate timer unit.

The technique used has scope for improvement, the main requirements being a viewing window large enough to allow correct illumination of the specimen and a clearly marked gauge length on the specimen. The main drawback with the technique is the time consuming process of measuring the gauge lengths from the film, compared to continuous data recording by use of a displacement transducer/chart recorder system.

5.1.3 The creep properties of SRR 9

Single crystal creep specimens of alloy SRR 9 were supplied by Rolls-Royce Ltd in the fully aged condition. The specimens were from the same cast and produced to the standard orientation control;ie the tensile axes controlled to within 7° from [001] but no control is placed on the direction of the deviation. As nickel-base single crystals are known to exhibit significant anisotropy between 750°c and 860°C, with small variations in orientation from the [001] producing significant variation in creep life (59,61,62), investigation of the creep properties of alloy SRR 9 were undertaken at both 750°C and 850°C. The effect of orientation variation within the standard quality control limits has been examined.

The general appearance of the creep curves obtained for alloy SRR 9 can be seen in figures 4.3a-m. Specimens 9L/1 and 9L/2 were interrupted tests used to investigate the photographic strain measuring technique. Specimens 9L/3 and 9H/2 were tested to failure, but in each case equipment malfunction meant that some data was lost.

The creep curves are of conventional shape, that is a primary creep region leading to a steady state then a tertiary stage of accelerating creep rate leading to failure. An exception to this is specimen 9L/6 (figure 4.3f) which exhibited an incubation period of low strain rate before the steady state period.

The value of initial plastic strain appears to have little correlation to time to rupture or minimum creep rate, however three specimens with similar orientations; 9L/4, 9L/5 and 9L/6 had identical initial plastic strain values. By examination of table 4.2 and figure 4.31, it may be seen that the minimum creep rates obtained for specimens tested at 750°C are similar, ranging from 2.2×10^{-3}/hr to 3.9×10^{-3}/hr. The minimum creep rate obtained for specimen 9L/2 is suspect due to problems with temperature control during the test. At 850°C a larger variation in minimum creep rate was noted ranging from 2.71×10^{-3} /hr to 15.3×10^{-3}/hr, rupture times being 5.3 to 22.4 hours.

The creep properties have been related to crystal orientation and rotation. Figures 4.6 and 4.7 illustrate the initial and final orientations of the SRR 9 specimens tested, together with the times to rupture. Orientations were determined by the Laue back reflection method. Due to the difficulty in measuring rotations of less than 2°, especially for orientations near [001] ie. near the centre of the stereographic projection, crystal rotation for specimens very close to the [001] may be inaccurate. A general indication of the crystal rotations involved, rather than individual results have been used.

For specimens tested at 750°C, the trend is for a rotation towards the [001]-[011] boundary, generally towards the [001]. Specimen 9L/3 was found to be outside the quality control region, however this enabled an

accurate crystal rotation analysis. The specimen showed significant rotation towards the [001], in accordance with figure 2.15b which illustrates crystal rotations for the $(1\bar{1}1)[\bar{1}12]$. It is also interesting to note that specimen 9L/1 which was originally oriented in a position of multiple slip for the {111}<110> system (ie along the [001]-$[\bar{1}11]$ boundary), rotated towards the [001]-[011] boundary. This rotation is also in accordance with the $(1\bar{1}1)[\bar{1}12]$ system. As the [001]-[011] boundary in the region near [001] is a position of duplex slip on $(1\bar{1}1)[\bar{1}12]$ and $(\bar{1}\bar{1}1)[112]$, it appears that primary slip on the {111}<112> system is dominant at 750°C.

At 850°C, the trend is for rotation towards [001]. Rotations along the [001]-[011] boundary may be caused by both {111}<110> and {111}<112> systems, however specimens oriented towards the centre of the stereographic triangle such as specimen 9H/4 would be expected to rotate towards the [001]-$[\bar{1}11]$ if {111}<110> slip systems were dominant during primary slip.

Two specimens were found to have orientations approximately 16° from [001] positioned close to the [001]-$[\bar{1}11]$ boundary, as shown in figure 4.7. Specimen 9H/2 had the longest time to rupture of all specimens tested at 850°C of 22.4 hours. This is contrasted by the similarly oriented specimen 9H/3 which had a rupture time of 11.2 hours. The Schmid factor for the $(111)[\bar{1}01]$ slip system for this orientation is approximately 0.46 (figure 2.14a),

whereas the Schmid factor for the $(1\bar{1}1)[\bar{1}12]$ system is 0.49. It may be expected that the {111}<110> system would dominate if no other factors are involved. Comparison of crystal rotations for these two specimens indicate a marked difference in primary creep mechanism. In order to explain these results, a review of possible creep mechanisms is required.

During creep at low and intermediate temperatures with high stress levels, the main deformation mechanism will be the shearing of γ' precipitates by superlattice dislocation pairs. Kear et al (15,16,22) have shown that shear of the γ' by an array of partial dislocations having a net Burgers vector a<112> may take place at intermediate temperatures. The driving force for this mechanism is the replacement of antiphase boundaries with stacking faults, the stacking fault energy of the alloy being low. The mechanism is dependent on cooperative movement of the partial dislocations and therefore at high strain rates becomes less favourable than shear by {111}<110> dislocation pairs. At high temperature, due to the reduction of APB by local diffusion it is expected that primary creep deformation will be by pairs of {111}<110> dislocations. At higher temperatures and lower stress levels dislocation climb over precipitates will become more favourable than shearing mechanisms.

Several investigators (58-61) have noted a change in primary creep mechanism from {111}<112> systems at 750°C to

{111}<110> systems at 850°C. At both temperatures TEM analysis has shown (59) that secondary or steady state creep is controlled by the recovery of {111}<110> dislocations in the networks formed around γ' particles. Where {111}<112> slip is operative during primary creep, the transition to second stage creep occurs due to intersection of {111}<112> slip systems strain hardening the material. During steady state creep shear of γ' precipitates by {111}<110> occurs, the rate of deformation being regulated by recovery at the interfacial networks. Analysis has shown that specimens oriented along the [001]-[$\bar{1}$11] boundary have more stable dislocation networks due to favourable dislocation junction reactions (59) than specimens oriented along the [001]-[011]. It may be considered therefore that where specimens require small rotations for multiple slip, specimens oriented along the [001]-[$\bar{1}$11] will exhibit longer creep lives.

The creep properties of SRR 9 may now be explained with reference to possible slip mechanisms. At 750°C crystal rotations are in agreement with {111}<112> slip. Specimens 9L/2, 9L/4 and 9L/6 all rotated to the [001], requiring little primary slip to reach a position where multiple slip is favourable. This is illustrated in figure 4.3 where the creep curves for these specimens show insignificant primary creep stages. Specimen 9L/1 originally oriented in a position favourable for multiple slip on {111}<110>, rotated to the [001]-[011] boundary by slip on the (1$\bar{1}$1)[$\bar{1}$12] system, confirming the dominance of

{111}<112> slip during primary creep at this temperature.

The accuracy of the Laue back reflection technique becomes suspect for orientations close to the [001], however specimens within 2° of the [001] will require very small rotation to reach stable multiple slip positions; demonstrated by the absence of primary creep regions for near [001] specimen. The crystal rotation observed for Specimen 9L/5 does not conform to those expected for either slip systems, and it is concluded that the rotation measurement may be in error. Specimen 9L/3 which was oriented 8° from the [001] away from either stereographic boundary had a significant primary creep period of 4 hours. This is reflected by the large crystal rotation indicating the influence of primary creep on the $(1\bar{1}1)[\bar{1}12]$ before attaining a duplex slip position on the [001]-[011] boundary. This produced a lower rupture time than for specimens near the [001] in positions favourable for multiple slip.

At 850°C the specimens oriented close to the [001] ie. 9H/1, 9H/4 and 9H/5 rotated towards the [001]-[011] denoting primary slip on the {111}<112> system. By reference to figure 4.3m it may be seen that there is an early transition to tertiary creep, indicating that microstructural damage accumulation started early in the life of the specimens. The two specimens which had orientations 16° from the [001] were found to have marked differences in creep properties.

The creep curve for specimen 9H/3 (figure 4.3i) shows the presence of a primary creep stage. The specimen was also found to have a large crystal rotation, as shown in figure 4.7. The specimen originally oriented on the [001]-[111] boundary, a position favourable for multiple slip on {111}<110> systems, exhibited a large rotation in accordance to the $(1\bar{1}1)[\bar{1}12]$. In the case of specimen 9H/2 (figure 4.3h) the rotation indicated slip on the $(111)[\bar{1}01]$. Little rotation was required to reach an orientation enabling multiple slip on the {111}<110>, leading to the early formation of stable dislocation networks. The creep curve for specimen 9H/2 is incomplete, however it can be seen that the period of primary creep is negligible and the creep rate for the first four hours of testing is comparatively low.

The increase in rupture life for specimen 9H/2 when compared to 9H/3 is due to the small period of primary creep required before the production of dislocation networks caused by dislocation interactions due to the operation of multiple slip systems. In specimen 9H/3 extensive slip on the $(1\bar{1}1)[\bar{1}12]$ system was required before the onset of multiple slip. The improvement in rupture life for specimens 9H/2 and 9H/3 over specimens with orientations near [001] may be explained by use of the observations of Leverant et al (59). For specimens oriented along the $[001]-[\bar{1}11]$ the operating slip systems are $(111)[\bar{1}01]$ and $(\bar{1}\bar{1}1)[011]$ leading to dislocation reactions of the type:

$$a/2[10\bar{1}]+a/2[011] > a/2[011] \quad \ldots\ldots (5.4)$$

Specimens along the [001]-[011] boundary are oriented favourable for slip on (111)[101] and (111)[$\bar{1}$01] slip systems, producing reactions of the type:

$$a/2[101]+a/2[\bar{1}01] > a/2[001] \quad \ldots\ldots (5.5)$$

The latter reaction is not energetically favourable, therefore crystals oriented along the [001]-[011] are slower to form stable dislocation networks than those oriented along the [001]-[$\bar{1}$11].

5.1.4 The creep properties of alloy SRR 99

The creep results obtained by testing alloy SRR 99 specimens may be seen in section 4.3. The results are presented in table 4.4 and shown graphically in figures 4.8 and 4.9. A range of stresses were used at each temperature to investigate the effect of stress on creep properties and to allow analysis of the stress exponent for each temperature. Premature failure of the specimen grips however prevented the completion of this analysis. Due to the low number of results, the creep exponent values have been used to indicate the typical rather than precise values. Due to the anisotropic nature of single crystals, step testing of a single specimen would be advised to avoid orientation differences.

The testing regimes of 850°C and an initial stress of 550MPa and 750°C and a stress of 850Mpa were chosen to give rupture times of approximately 100 hours (108). The creep results obtained show reasonable agreement with predicted values, an average rupture time of 150 hours for the 750°C/850MPa tests and 85 hours for the 850°C/550MPa test.

Specimens tested at 750°C and 850MPa produced similar rupture times and minimum creep rate values, the latter being between 0.3-0.45x10^{-3}/Hr. The specimen tested at an initial stress of 825Mpa had a similar minimum creep rate of 0.37x10^{-3}/Hr. At 800MPa the minimum creep rate was found to be about 0.25x10^{-3}/Hr giving a rupture time approximately twice that attained for specimens tested at 850Mpa. The stress exponent n in the first term of equation 2.27 was calculated by measuring the slope of the log minimum creep rate versus log stress curve. The stress exponent calculated by using average minimum creep rate values was approximately 8. Using one specimen at each stress with similar orientation, ie 99L1/1, 99L2/1, and 99L3/1, gives a stress exponent of 8.7. The results are in agreement with data published for single crystal nickel base superalloys between 750°C and 1000°C (105,109).

The creep curves at 750°C all show a conventional response, having a primary creep period of about 4 hours for specimens 99L1/1 and 99L1/4, and about 1 hour for

specimens 99L1/2 and 99L1/3. Specimen 99L2/1 tested at 750°C and 825MPa exhibited an extensive primary period of approximately 10 hours. Most curves show the start of the tertiary stage commencing at approximately 50% of the rupture life.

Crystal rotation data was limited for alloy SRR 99 due to the difficulty of obtaining a clear Laue photograph from the deformed gauge length. Figure 4.13 shows the initial orientations for specimens tested at 750°C and 850MPa. All specimens gave similar rupture times, indicating a relitively low level of anisotropy. Specimen 99L1/4 oriented 5° from the [001] and mid way between the [001]-[$\bar{1}$11] and [001]-[011] boundaries gave a similar rupture time to specimens oriented near the [001]. Specimen 99L1/2 was found to rotate to the [001]-[011] without movement towards the [001]. Specimen 99L1/1 which exhibited the lowest rupture time had an initial orientation on the [001]-[$\bar{1}$11] boundary. Analysis showed that the crystal rotated the [001]-[011], in accordance to the (1$\bar{1}$1)[$\bar{1}$12] illustrated in figure 2.15b. As the [001]-[$\bar{1}$11] boundary is a stable multiple slip orientation for {111}<110> systems and a position producing stable interfacial dislocation networks in secondary creep; it may be considered that the {111}<112> slip system is significant during the primary creep stage. The crystal rotations observed correspond to the deformation mechanism of shearing the γ' particles by partial dislocation arrays having a net Burgers vector of a<112> during the initial

stages of creep.

Creep curves for specimens tested at 850°C and 550MPa are shown in figures 4.9a-d and figure 4.9g. All curves show a low level of initial plastic strain and a short primary creep period. Specimen 99H1/1 shows a deviation at the initial creep stage which is considered to be due to measurement error, possibly due to uneven film shrinkage.

Specimen 99H1/2 exhibits an incubation period rather than the standard primary period of steadily decreasing creep rate. The incubation period was found to be a region of very low creep rate of about 15 hours duration. The presence of an incubation period has been identified as being due to a low number of mobile dislocations in the crystal (50). This is due to the stability of dislocations in subgrain networks. Prior straining or working of the crystal has the effect of releasing dislocations for slip, thus removing the incubation period.

Specimens tested at 850°C and an initial stress of 500MPa were also found to have low initial plastic strain values and an insignificant primary creep stage. Specimen 99H2/1 indicates that a reduction of initial stress level of 50MPa produces a doubling of creep life, similar to tests carried out at 750°C. The stress exponent obtained using average minimum creep rate values is 2.8, the maximum value obtainable being 7.8. The results suggest that the creep mechanisms are similar at both temperatures.

The initial orientations and rupture lives for specimens of alloy SRR 99 tested at 850°C are shown in figure 4.14. Specimen 99H1/1 which produced the lowest rupture time on testing at an initial stress of 550MPa was found to undergo a significant rotation towards the [001], in accordance with the $(1\bar{1}1)[\bar{1}12]$ slip system. Specimen 99H1/2 rotated towards the [001]-[011] also in accordance with this system. Specimen 99H1/4 initially oriented very near to the [001] was found to have a shorter creep life than specimens 99H1/2 and 99H1/3. Crystal rotation analysis indicated a move away from the [001], the direction similar to that portrayed in figure 2.14b suggesting the dominance of slip on the $(111)[\bar{1}01]$ system during primary creep.

The results indicate that the {111}<112> slip system is still active in the early stages of creep deformation at a temperature of 850°C, therefore the shear of γ' precipitates may be considered to be the operative mechanism for the early stages of deformation. There are also indications of the introduction of {111}<110> slip during the primary creep stage at this temperature suggesting a reduction in APB energy, reducing the advantage of deformation by the more complex partial dislocation array utilising stacking faults.

5.1.5 Comparison of the creep properties of alloy SRR 9 and SRR 99

5.1.5.1 Comparison of microstructure

Alloy SRR 9 and SRR 99 are based on the nickel based casting alloy Mar M200. The compositions and heat treatments of the alloys are given in section 3.1.

The removal of grain boundary strengthening elements such as boron, carbon, hafnium and zirconium, has increased the incipient melting point of the alloys (1), allowing the use of higher solution temperatures. This has led to the reduction in microsegregation, coarse γ' and eutectic islands. Beneficial effects have also been found in the precipitation of the γ' phase with the more homogeneous solid solution allowing the even precipitation of a high volume fraction of even sized precipitates.

Alloy SRR 99 is an evolution of alloy SRR 9 with strict control of carbon and residual levels with the lowest content possible aimed for. The alloy also has a multi-stage solution treatment which has been introduced to improve microsegregation and the solution of high temperature phases.

Figures 4.1 and 4.2 show the main microstructural features of the alloys. Both alloys were found to contain a similar high volume fraction of γ', with cube dimensions of 0.25-0.5μm. The main difference in microstructure is that alloy SRR 9 contains a higher volume of primary MC

carbide particles, and the γ' particles appear to be slightly less cuboidal. On macro etching, the dendritic solidification nature of the alloy was clearly observed in alloy SRR 9. At higher magnification, the interdendritic areas were found to contain coarser γ' particles.

Alloy SRR 9 was found to contain a number of larger particles not observed in alloy SRR 99, as shown in figures 4.2b and c. These particles are considered to be eutectic nodules which were not taken into solution during heat treatment. Energy dispersive analysis (EDAX) has been carried out in order to identify the microconstituents of this feature by use of a Link system analyser, used in conjunction with a Joel 900 scanning electron microscope. The areas examined using 'spot analysis' are indicated in figure 4.2c. The analysis was carried out in semi-quantitative mode. The presence and estimate of concentration of an element was determined by use of the characteristic x-ray peaks obtained from excitation of electrons in the surface layers of the specimen, caused by collision of electrons from the primary beam. Where possible, secondary characteristic peaks were checked for presence in order to distinguish between elements with similar primary peaks.

The accuracy of the analysis is determined by several factors. The use of a lithium fluoride detector prevents the analysis of elements with atomic numbers below 8; ie oxygen, nitrogen, carbon and boron. The variation of

background energy levels and the modest resolution obtained by a scanning electron microscope leads to a widening of the characteristic peaks, therefore creating problems in identifying the energy level corresponding to the tip of the peak. Another problem encountered during this analysis was the detection of tungsten and tantalum, due to the elements having similar characteristic x-ray spectra. Due to this problem, the value obtained for tungsten was taken to indicate the proportion of both tungsten and tantalum.

The results obtained from the analysis are shown in table 4.1. The dark area at the centre of the nodule was found to contain a concentration of tungsten (and tantalum), titanium and zirconium and a reduced concentration of chromium and aluminium when compared to a general EDAX analysis from a general area of the matrix (position F). Examination of the light central areas and acicular regions (B and C in figure 4.2c) indicated the presence of iron at significant levels. The casting composition of SRR 9 is given in table 3.1 and by comparison of this composition with the EDAX results It can be seen that zirconium and iron are impurity elements in this alloy which have concentrated in the eutectic islands.

Alloy SRR 9 may therefore be considered to have higher levels of microsegregation and retention of eutectic islands due to incomplete solution treatments, which may be

aggravated by the lowering of safe solution treatment temperature by the presence of impurity elements and low melting point constituents. Reduction of low melting point forming elements and multi-stage solution treatments for alloy SRR 99 has led to a simplified and homogeneous microstructure.

5.1.5.2 Comparison of creep properties

The creep life of alloy SRR 9 was found to be considerably lower than for alloy SRR 99 when tested under the same conditions; 750°C and 850MPa and 850°C and 550MPa. In general SRR 9 specimens had lives a factor of 10 less than SRR 99 specimens, ie. a rupture times of about 10 hours compared to rupture times around 100 hours for SRR 99.

Crystal rotation experiments however indicated that the alloys had very similar deformation mechanisms. In fact both alloys show the same variation of mechanism with temperature; with {111}<112> slip systems operating in the early stage of creep deformation at 750°C, and the appearance of {111}<110> slip systems during primary creep at 850°C.

Examination of the creep fractures for SRR 99 specimens (figures 4.10-4.12) indicate that there is no major effect of stress on the fracture mechanism at 750°C or 850°C. All specimens retained a circular cross section indicating that the majority of deformation occurred by slip on several systems. The creep fractures appeared to be faceted and on closer examination square facets were

found to be associated with microporosity, as illustrated in figure 4.12. The intermediate areas were smooth cleavage type surfaces indicating crack propagation along slip planes. No appreciable necking was apparent in any specimens. The onset of cracking associated with micropores is consistent with the findings of Nathal and Ebert (48) for single crystals of Nasair 100 at 1000°C. Using interrupted tests, the authors found that crack propagation from micropores was only initiated during the latter stages of tertiary creep. Creep fractures for SRR 9 as shown in figures 4.4 and 4.5 also exhibited crack facets surrounding micropores, however generally the fractures exhibited larger areas of smooth crack propagation. The results obtained for SRR 9 and SRR 99 indicate the operation of similar deformation mechanisms and a similar response to temperature.

Specimen 9H/2 which was observed to have several transverse cracks in various positions along the gauge length and was found to contain several eutectic nodules. Figure 4.5 shows one of the transverse cracks. The radial feature associated with the crack has a dimension similar to the eutectic nodules observed in alloy SRR 9, however further metallographic analysis is needed to confirm this observation.

In summary, both alloys exhibit the same deformation and fracture mechanisms. Creep deformation is by shear of the γ' precipitates by {111}<112> dislocations during primary creep and by {111}<110> dislocations during steady

state creep. Creep rupture is by initiation of cracks from microporosity and large microstructural features such as γ/γ' eutectic nodules and MC carbides. This is due to the stress concentrations associated with these features producing a local increaes in creep rate, as both alloys exhibit a high dependence of creep rate on applied stress ($n\sim7$). Linking of crack initiation sites in both alloys was found to be by crack growth on crystallographic planes. Crack growth of this nature is considered to be due to the concentration of slip on one plane with little climb or cross slip onto other planes causing a build up of shear and normal stresses, leading to slip band decohesion (85). Deformation and failure mechanisms for both alloys were found to be unaffected by a temperature increase from 750°C to 850°C.

Although both SRR 9 and SRR 99 exhibit the same deformation mechanisms and variation of properties with temperature, SRR 9 was found to have creep rupture times an order of magnitude lower than SRR 99. This is considered to be due to the chemical and microstructural differences between the alloys. SRR 9 was found to have a much higher level of microsegregation and coarser dendritic structure. The alloy upon heat treatment contains microstructural features such as large MC carbides and eutectic nodules which are significantly larger than observed in alloy SRR 99. These large features will produce significant stress concentrations and thus crack initiation will occur earlier in SRR 9, leading to a reduction of creep life.

5.2 The fatigue properties of un-notched specimens of alloy SRR 99

The results of load controlled fatigue tests carried out on unnotched specimens of alloy SRR 99 under sinusoidal loading at a frequency of 40Hz have been reported in section 4.4. To avoid variation in surface conditions between specimens, the top face of each specimen was mechanically polished to 1μm finish then electropolished.

Three orientations of specimens were tested, all having a top (polished) face of (001). the side and end face orientations were; (100), (210) and (320). The orientations are described schematically in figures 3.2 and 4.32. The (001)-(320) specimens were produced whilst attempting to cast (001)-(110) specimens.

The S-N curve obtained by testing at 750°C is shown in figure 4.15 and 4.17. In general only three specimens were available for each orientation, however the results for both (001)-(100) and (001)-(210) specimens were found to fit the same curve which may be described by the equation:

$$\Delta\sigma = 5258.2\ N_f^{-0.158} \qquad \ldots\ldots (5.6)$$

Data for (001)-(320) specimens showed an increase in fatigue life over the other orientations with the greatest improvement in fatigue life obtained at higher stress levels.

Figure 4.16 illustrates the S-N curve obtained by testing at 850°C. The variation of fatigue life with orientation was found to be less significant at this temperature, with all specimens relating to a curve described by the equation:

$$\Delta\sigma = 3093\ N_f^{-0.104} \qquad \ldots\ldots (5.7)$$

The upper bound of the results was described by the (001)-(320) specimens, although due to the low number of specimens tested the difference is not significant enough to be conclusive.

Figure 4.17 shows the effect of temperature and crystal orientation on the fatigue life of SRR 99. The prime observation is that fatigue life increased with an increase in temperature from 750°C to 850°C. The maximum increase in life is approximately $5x10^5$ and occurred for tests carried out under a stress range of 750MPa.

It is interesting to note that (001)-(320) specimens tested at 750°C and a stress range above 800MPa have fatigue lives consistent with those obtained for specimens tested at 850°C. The specimen tested at a stress range of 746MPa was found to have an intermediate life between the 750°C and 850°C S-N curves for (001)-(100) and (001)-(210) specimens.

As stated previously in section 4, the yield stress in nickel-base superalloys is known to be anisotropic, with the 0.2% proof stress for [012] and [011] oriented crystals being approximately 18% lower than for [001] crystals at 750°C (38,57). As the tests were carried out in three point bending, the forces acting upon the specimens may be approximated, as illustrated in figure 4.32d, as a tensile force acting along the bar, and a shear force acting on the plane normal to the tensile force. The shear force has a maximum value at the neutral axis and is zero at the surface of the ligament and therefore has a minor effect on initiation. The tensile force acts in a direction equivalent to the transverse orientation of the specimen; ie for a (001)-(210) specimen, the tensile component of the force acts in a <210> direction. It is to be expected therefore that the yield strength in this direction will be important in determining the onset of plasticity in the specimen. If a reduction of 18% on the [001] yield strength is assumed for (001)-(210) and (001)-(320) specimens, then tests carried out using a stress range above 790MPa may have experienced plasticity in the surface of the ligament.

At 850°C, the stress range required to exceed the fibre stress for (001)-(100) specimens is indicated in figure 4.17. At this temperature, the difference in yield strength with orientation will be smaller than at 750°C due to the general decrease in strength above 800°C as illustrated in figure 2.11.

The fatigue fractures were examined in order to observe the crack growth mechanism and to identify any variation of crack growth with temperature and specimen orientation.

At 750°C the (001)-(100) and (001)-(210) specimens exhibited considerable crystallographic crack growth producing a quasi-cleavage style fracture appearance. The facets were found to be smooth, planar areas on which the dendrite arm positions could be clearly seen. This effect is illustrated in figure 4.21b.

The (001)-(320) specimens were found to have less crystallographic fracture surfaces. The majority of the fracture was found to be on a plane normal to the tensile force and contained vertical ridges which appear to indicate the positions of the dendrite arms. In the case of specimen FL3/2, a smooth area corresponding to the initiation site can be seen (figure 4.21c) where the dendrite ridges have been removed indicating a plastically deformed region.

At 850°C both (001)-(100) and (001)-(210) specimens retain significant areas of facets, however the latter have a more mixed mode of fracture, with initial crystallographic crack growth leading to areas of ductile fracture. (001)-(320) specimens tested at 850°C were predominantly non crystallographic in nature with only

small regions of facets observed.

A summary of the fracture surfaces is given in table 4.9, which also gives the number of different types of planes observed in the crystallographic region. The crystallographic crack growth occurred predominantly on one type of plane, but frequently smaller facets were observed on other planes as illustrated in figures 4.19a and 4.21b. Two trace analysis as described in section 4.4.3 determined that the facets observed were {111} planes, indicating crack growth along active slip planes in the crystal. Crystallographic crack growth has been observed frequently in nickel-base single crystals (110-114), especially at low and intermediate temperatures.

Crystallographic crack growth, termed stage I according to Forsyth (63) is related to deformation mechanisms in the crystal. Nickel-base superalloys have low levels of stacking fault energy which produces extended dislocations, having wide spacing of partial dislocations. This spacing of partial dislocations inhibit cross slip and therefore at low and intermediate temperatures deformation tends to be concentrated into coarse planar bands (110,111).

The presence of stage I crack growth is dependent on the temperature and frequency of cycling used. Stage I is favoured by low temperature and high frequency. High temperatures and low frequencies which assist the

dispersal of dislocations reduce the tendency for stage I growth (111). Although the fracture surface has the appearance consistent with cleavage, crack growth rates in stage I may be relatively low with fracture only occurring after appreciable propagation.

Sadananda has proposed two models for the faceted mode of fatigue growth observed in materials exhibiting planar slip (85,115). The models are illustrated in figure 5.1. Figure 5.1a illustrated how cumulative plastic strain along a restricted number of slip planes may cause the formation of a crack on a cleavage plane. Figure 5.1b illustrates crack formation along a slip plane. Reversed slip occurring on adjacent planes produces a high density of dislocation dipoles creating intense local dilatation, separation occurring by the action of local shear and normal stresses. Crack growth normal to the applied stress axis may be maintained by slip concentrating on a second, more favourable oriented plane after extension along the primary plane. As the two trace analysis results indicate faceting on {111} slip planes, the results are consistent with the model shown in figure 5.1b.

In order to assess the effect of slip plane orientation on crack growth, the Schmid factors (equation 2.38) for the main {111}<110> systems in the three specimen orientations have been calculated and are given in table 5.7.

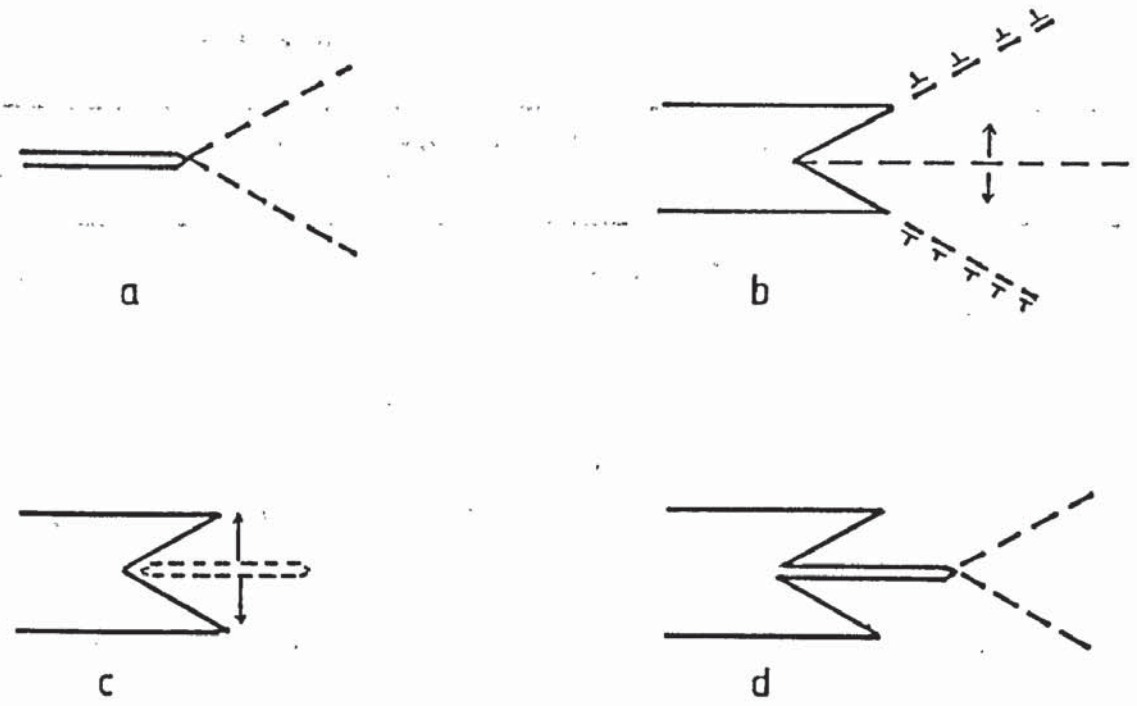

Figure 5.1a Model for faceted fatigue crack growth on clevage planes (85)

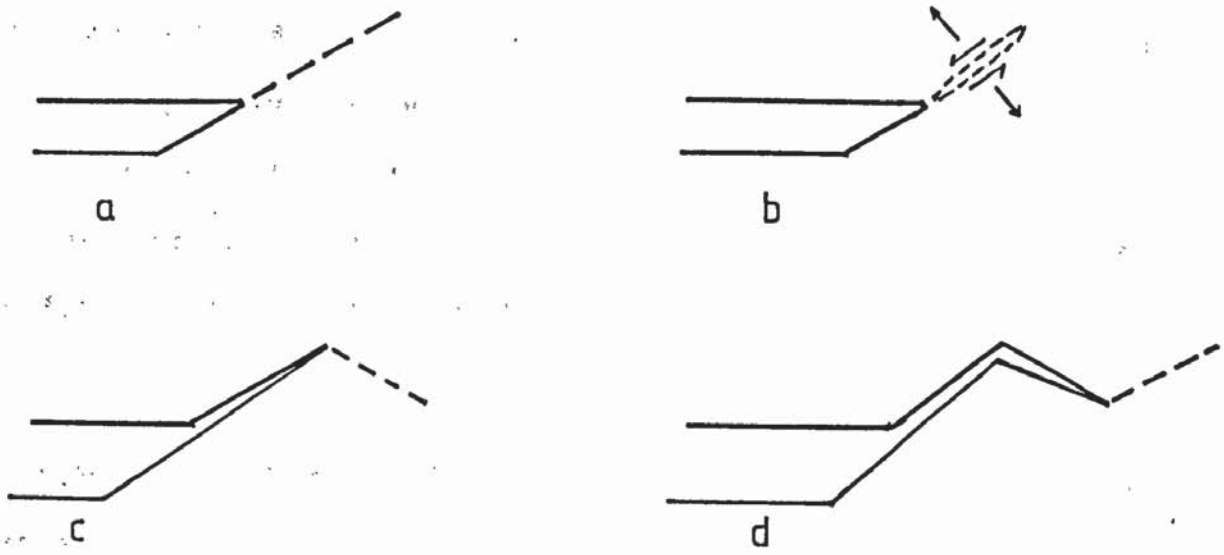

Figure 5.1b Model for faceted fatigue crack growth on slip planes (85)

Table 5.7 Schmid factors for {111}<110> systems in Fatigue specimens

Specimen orientation	Tensile force Orientation	Slip system	Schmid Factor
(001)-(100)	<1 1.71 11.63>	(111)[0$\bar{1}$1]	0.417
		(111)[$\bar{1}$01]	0.417
		($\bar{1}$11)[101]	0.457
		(1$\bar{1}$1)[011]	0.427
		($\bar{1}\bar{1}$1)[101]	0.33
		($\bar{1}\bar{1}$1)[011]	0.35
(001)-(210)	<0.18 1 2.16>	(111)[$\bar{1}$01]	0.474
		($\bar{1}$11)[101]	0.499
		(1$\bar{1}$1)[011]	0.303
(001)-(320)	<0.01 1 1.6>	(111)[1$\bar{1}$0]	0.47
		(111)[$\bar{1}\bar{1}$0]	0.47
		(111)[$\bar{1}$01]	0.314
		($\bar{1}$11)[101]	0.314

The results indicate that for (001)-(100) oriented specimens The possibility of slip systems operating on three {111} planes is possible with Schmid factors of 0.43,0.42 and 0.46. (001)-(210) specimens are oriented for one slip system to be favourable on two {111} planes. (001)-(320) specimens however, have two operating systems both acting on the same plane, with slip on other planes less favourable due to a significantly lower Schmid factor.

Schmid factor analysis indicates that all specimen orientations have favourable {111}<110> slip systems. There is no definite correlation between the number of planes containing slip systems with high Schmid factors and the number of facet types observed. It also appears that

the possibility of slip on several planes does not inhibit stage I crack growth.

The fatigue crack initiation sites observed have been given in table 4.9. Generally the initiation sites were at or near the surface of the ligament, however internal initiation was observed in several (001)-(320) specimens. Analysis of the fracture surfaces by scanning electron microscope indicated that initiation sites were associated with surface defects and microporosity which is consistent with previous findings (112,116).

An increase of fatigue endurance limit with temperature has been noted previously in load controlled high cycle fatigue of both polycrystalline and single crystal nickel- base superalloys (117,118). The improvement of fatigue life has been attributed to the prevention of reversed slip in slip offsets at the surface due to oxide growth, thus retarding surface initiation of cracks by the intrusion/extrusion mechanism. The mechanism also explains the tendency for sub-surface initiation observed at high temperatures. In addition, at high temperatures a higher level of slip dispersal may retard the formation of cracks at carbides and micropores by reducing the amount of deformation in planar slip bands. The development of homogeneous slip would also promote the transition to stage II cracking observed in specimens tested at 850°C.

In this study, load controlled fatigue has been used in the transition region between high and low cycle fatigue. Consequently, variation of yield stress with orientation and temperature will have an important effect on fatigue life. The elastic modulus is also known to vary with temperature and orientation. Variation of fatigue life with orientation in strain controlled low cycle fatigue has been found to be related to the variation in stress generated in the specimens due to difference in elastic modulus (112,113,117).

In conclusion, it is considered that the oxide mechanism cannot explain the observed temperature and orientation effects. The improvement of fatigue life with increase in temperature is thought to be due to an increase in the level of plasticity at the crack tip, leading to lower crack propagation rates due to crack tip blunting. This effect, and the dispersal of slip onto other operating planes by climb and cross slip, also promotes crack growth normal to the applied stress by a ductile rupture mechanism, as observed in the fracture surfaces of specimens tested at 850°C. The effect of orientation on fatigue life may be explained by the variation of yield strength with temperature, the (001)-(320) orientation having a lower yield strength and therefore greater crack tip plasticity. At higher temperatures, this variation is reduced due to the sharp decrease in strength with increase in temperature above 800°C (figure 2.11), which is observed for all orientations (57).

5.3 Fatigue crack propagation in SRR 99 single crystals

Fatigue crack propagation studies were carried out using notched specimens of the same dimensions and orientations as those used for smooth bar fatigue tests. The orientation are described schematically in figures 4.32a-c. The test method and subsequent analysis of results has been discussed previously.

The orientations were chosen to investigate the effect of orientation on crack growth in terms of variation of mechanical properties and crack growth plane. In all cases the crack growth direction was maintained at <001> in order to remove dendritic growth effects. Experiments on directionally solidified nickel base superalloys (119) has shown that crack growth perpendicular to the main solidification direction may lead to crack branching and growth along interdendritic regions at high temperature.

The results have been compiled in figures 4.28a-d. Only data considered to be obtained within the linear elastic fracture mechanics regime has been shown. In general, the repeat tests show good correlation for low to moderate levels of ΔK, as illustrated in figures 4.27a-l. Where a variation was noted, an average result has been portrayed.

In each case, fatigue cracks have been initiated from the notch at the test temperature using a sinusoidal

waveform with a frequency of 40Hz. The base of the notch was marked with a 'spark erosion' etching pen in order to introduce thermal damage into the notch root and thus produce an smaller effective notch root radius. Propagation studies were not started until the fatigue crack had propagated approximately 0.6mm in order to avoid notch proximity effects and to ensure re-initiation upon starting the test after the frequency change.

Figure 4.28a illustrates the results obtained for specimens tested at 750°C. For tests conducted using a triangular waveform with a frequency of 1.25Hz, (001)-(210) and (001)-(110) specimens were found to behave similarly. The results for these specimens indicate the onset of near threshold crack growth behaviour at values of ΔK around 15MPa$\sqrt{m}$. Results obtained for (001)-(100) specimens show a significantly higher crack growth rate at all levels of ΔK.

The dependence of crack growth rate on stress intensity range was similar for (001)-(210) and (001)-(110) orientations, with a slight increase noted for (001)-(100) specimens. This is demonstrated by the values obtained for the Paris law exponent (equation 2.52), produced by linear regression analysis of the log da/dN versus log ΔK data. The average value for the exponent n is 6.2 for (001)-(100) and about 5.3 for (001)-(210) and (001)-(110) orientations.

The effect of the introduction of a 1.6 second hold time at minimum and maximum load, producing a frequency of 0.25Hz, on fatigue crack growth rate at 750°C may also be seen in figure 4.28a. A slight reduction in crack growth rate for (001)-(210) and (001)-(110) specimens is indicated, with a slight increase in crack growth rate for (001)-(100) specimens. The results obtained for (001)-(210) specimens show a slight increase in stress dependency with an change in Paris law exponent of ~5 to 5.5. The variation of results with change of frequency however may be regarded as minimal compared to the normal scatter bands observed in crack growth rate data.

At 850°C, the variation of crack propagation rate with orientation is less significant. Results obtained using the 1.25Hz triangular waveform indicate that at low values of ΔK the crack growth rates are similar. At higher levels of ΔK, due to a higher dependence of crack propagation rate on stress intensity, the stress intensity exponent n being 6.3 compared to 5.5, (001)-(100) specimens exhibit a slightly higher crack propagation rate.

The effect of the 1.6 second trapezoidal waveform is to increase the crack propagation rates slightly for all specimen orientations. The maximum increase observed is a factor of 2 for (001)-(100) specimens at low levels of ΔK. There is also indication of near threshold crack growth behaviour in (001)-(100) specimens at ΔK levels below 20MPa$\sqrt{m}$.

The effect of increasing temperature from 750°C to 850°C can be seen in figure 4.28c for specimeens tested under triangular loading waveform at 1.25Hz and in figure 4.28d for specimens tested with a trapezoidal waveform at 0.25Hz.

For tests carried out at 1.25Hz the effect of increasing temperature was found to be minimal in all specimen orientations. For tests carried out at 0.25Hz however, a significant increase in crack growth rates for (001)-(210) and (001)-(110) specimens was observed. The (001)-(100) specimens exhibited no change in crack growth rate with increase in temperature.

The net effect of the increase in temperature for tests carried out at 0.25Hz appears to be a reduction of orientation variation with crack growth rates for both (001)-(210) and (001)-(110) specimens increasing to the level of (001)-(100) specimen crack growth rates.

The fracture surfaces of the fatigue crack propagation specimens have been detailed in section 4.5.6. Generally, the fracture surfaces followed a direction normal to the maximum applied stress. Deviation away from normal crack growth direction was observed in slow propagation regions, especially in (001)-(210) specimens, but these were generally less than 10° and for short distances.

In the fast propagation region, evenly spaced vertical ridges were observed on the fracture surface. These are similar to the features seen in fracture surfaces obtained from smooth bar fatigue tests. As the preferred growth direction in FCC materials is <100>, the vertical ridges observed running vertically down the fracture planes in all specimen orientations ie <001> indicate that the ridges denote the positions of the main dendrite arms.

Examination of the fracture surfaces by scanning electron microscope indicated the presence of crystallographic features. Orientation analysis of these facets has not been undertaken in the present experimental programme.

Faceted crack growth behaviour is known to occur in nickel base superalloys both in single and polycrystals during fatigue crack propagation from notches. (120-122). Crystallographic crack growth may be experienced at all cyclic frequencies for temperatures up to 750°C. The dominant mode of failure at ambient temperatures appears to be crack growth on a single {111} plane or on a combination of {111} planes (120). The mechanism is thought to be due to coplanar slip relaxing the shear stress component at the crack tip without affecting the normal stresses, due to the lack of displacements normal to the crack plane. This condition leads to a build up of normal stresses on planar slip bands ahead of the crack tip.

Crompton and Martin (122) have identified a change in crack growth behaviour with temperature for single crystals of Mar-M200 tested at frequencies between 0.1 and 10Hz. At room temperature crack growth was found to occur on {111} planes but at temperatures of 650°C and 850°C, crack growth was found parallel to {100}. This was believed to be due to the morphology and distribution of the γ' precipitates . The strength of γ' is known to increase in this temperature region (9,19) and therefore dislocations in the crack tip are contained in the γ matrix with crack propagation by plasticity failure of the matrix occurring. Although different crack propagation directions were examined, all specimens appear to have been tested so that the plane normal to the maximum stress was a {100} plane, therefore the observation of crack growth on this plane does not distinguish between orientation or maximum stress effect.

Chan and Leverant (121), have examined fatigue crack growth in several orientations at 982°C and found that at a test frequency of 10Hz, fatigue crack propagation was entirely non crystallographic for most orientations.

The effect of orientation on crack propagation rate has been found to be minimal at elevated temperatures (121,122), and the effect of frequency has been found to be minor at temperatures between 600°C and 850°C (122), which is in agreement with the present results.

In the present findings, the presence of crystallographic crack growth has been found to be dependent on frequency and applied stress intensity. In all orientations, the initial fatigue crack propagation carried out at 40Hz was found to be completely planar with no evidence of facets. The crystallographic facets were also found to increase in size and number with distance away from the notch, ie with increase in stress intensity. This effect has been noted previously (122).

In conclusion, the effect of orientation on fatigue crack growth is similar to that observed in un-notched specimens. At 750°C, the lowest crack growth rates were observed in (001)-(110) specimens. This is considered to be due to the lower yield strength in this orientation, producing an increase in crack tip plasticity and therefore in crack tip blunting. At 850°C, due to the decrease in yield strength observed in all orientations, the variation of yield strength with orientation becomes minor and the effect of orientation on fatigue crack growth rate is not observed.

Fatigue crack growth observed in notched specimens appears to be by a ductile mechanism in a direction normal to the applied stress. Small scale faceting was observed on the fracture surfaces which indicate local areas of stage I crystallographic grack growth. The predominance of stage II crack growth is considered to be due to the increased amount of normal to shear stresses below the notch.

6. Conclusions

1. The photographic strain measurement technique has been found to be an economic and practical solution to the problems of measuring creep rates at elevated temperature.

2. Crystal rotation analysis of Alloy SRR 9 and SRR 99 has indicated the presence of {111}<112> slip mechanisms during primary stages of creep deformation at temperatures of 750°C and 850°C.

3. Variation in orientation produced by normal casting practices was found to be not significant for both alloy SRR 9 and SRR 99.

4. Examination of creep fracture surfaces of alloy SRR 9 and SRR 99 by scanning electron microscope showed the presence of cracks associated with microporosity. Failure was attributed to multiple initiation of cracks, followed by crystallographic crack growth until failure.

5. Under similar conditions, the creep rupture life of alloy SRR 99 was found to be a factor of 10 greater than SRR 9. As crystal rotation results and fracture appearance are similar for the two alloys, it is considered that the difference in properties be attributable to larger microstructural features found in SRR 9, such as carbides and eutectic islands.

6. Fatigue crack initiation in electropolished un-notched specimens of alloy SRR 99 was found to be from microporosity or surface defects. Sub surface initiation was observed at both 750°C and 850°C.

7. Failure in smooth bar (un-notched) fatigue specimens of alloy SRR 99 was predominantly by crystallographic crack growth along {111} slip planes.

8. All specimen orientations of alloy SRR 99 tested under load controlled fatigue at a frequency of 40Hz exhibited an increase in fatigue life with increase in temperature from 750°C to 850°C.

9. The use of linear elastic fracture mechanics to describe fatigue crack growth in alloy SRR 99 was found to be acceptable for temperatures up to 850°C at frequencies of 1.25 and 0.25Hz.

10. During fatigue crack propagation at 750°C and a frequency of 1.25Hz, (001)-(100) oriented specimens exhibited a moderate increase in crack growth rate over (001)-(210) and (001)-(110) oriented specimens. A reduction of frequency to 0.25Hz did not affect this situation. At 850°C, the effect of orientation is minimal at both frequencies. the reduction in frequency to 0.25Hz has the effect of slightly increasing crack growth rates in all specimen orientations.

11. The effect of an increase in temperature from 750°C to 850°C is minimal for tests carried out at 1.25Hz. At 0.25Hz however the effect is minimal on (001)-(100) oriented specimens but produces an increase in crack growth rate in (001)-(210) and (001)-(110) specimens The net effect of the temperature increase at test frequencies of 0.25Hz is to remove the observed orientation effects.

12. Although, in general, macroscopic crack growth was normal to the applied stress, small crystallographic facets were observed on examination of the fracture surfaces of fatigue crack propagation specimens tested at both 750°C and 850°C.

13. The effect of orientation on the fatigue properties of both notched and un-notched specimens could be explained by the variation of yield strength with temperature and orientation. At 750°C, orientations with the lowest yield strength were found to have the longest fatigue lives, thought to be due to crack tip blunting effects. At 850°C, the yield strengths of all crystal orientations decrease to a similar level and therefore variations due to crack tip plasticity are reduced.

7. Further work

The present investigation into the creep properties of alloy SRR 99 may be extended to cover other temperatures and stress levels, to enable the measurement of creep exponent and activation energy. Creep Experiments using specimens oriented away from <001> will assist in understanding the effect of orientation on creep properties.

In order to fully understand the results obtained from the fatigue testing of un-notched specimens, knowledge of the yield strengths for the specimen orientations used are required for the temperatures studied.

Fatigue crack propagation tests have been carried out using a triangular waveform in order to obtain base-line data for the investigation into the effect of hold times on fatigue crack propagation. Knowledge of the creep constants for alloy SRR 99, together with further studies using longer hold times, will enable the prediction of hold time effects by the method proposed by Saxena et al (90). Investigation of fatigue crack growth at higher temperatures than those studied in the present work may require the use of the cyclic elastic plastic parameter, ΔJ.

The present work may be extended to include the examination of dislocation and crack growth mechanisms by electron microscopical techniques such as T.E.M. analysis.

8. Appendix 1

8.1 Laue film digitising program for Tektronix 4020A Computer

The program assumes a square film and a specimen to film distance of 3cm. For other distances alter line 1150.

DEVICE NUMBERS

@1	PLOTTER
@32	SCREEN
@4	PRINTER
@8	DIGITISING TABLET

```
400  INIT
405  PRINT "GG"
410  PRINT "INPUT SPECIMEN NUMBER"
420  INPUT X$
500  Z$= "SPECIMEN No"
510  PRINT@4:"        SINGLE CRYSTAL ORIENTATION ANALYSIS"
520  PRINT@4:"J"
525  IMAGE 10X,11A,3X,9A
530  PRINT @4: USING 525:Z$,X$
535  PRINT @4:"J"
540  PRINT @4:"                        DIGITISING CO-ORDINATES"
550  PRINT @4:"J"
560  IMAGE 25X,4A,14X,4A
570  Q$="Xval"
580  W$="Yval"
590  PRINT @4: USING 560:Q$,W$
600  PRINT @4: "J"
610  PRINT "DIGITISE BOTTOM LEFT CORNER"
620  INPUT @8:A1,B1,C$
630  PRINT"GG"
640  PRINT "DIGITISE BOTTOM RIGHT CORNER"
650  INPUT @8:A2,B2,C$
660  PRINT "GG"
670  PRINT "DIGITISE TOP RIGHT CORNER"
680  INPUT @8:A3,B3,C$
690  PRINT "GG"
700  DIM  X(100), Y(100)
710  DIM  X1(100), Y1(100)
720  N=1
730  PRINT "DIGITISE THE POINTS(EXIT OFF X AXIS. . .)"
740  INPUT @8:X (N),Y(N),Z$
750  IF X(N)>A3 OR Y(N)>B3 THEN 790
760  N=N+1
770  PRINT"GG"
780  GO TO 740
790  ALFA=ATN((B2-B1)/(A2-A1))
```

```
800  REM  *SHIFT TABLET ORIGIN TO FILM CENTRE*
810  FOR I=1 TO N-1
820       X(I)=X(I)-A1
830       Y(I)=Y(I)-B1
840  NEXT I
850  REM *ADJUST FOR FILM TILT ON TABLET*
860  FOR I=1 TO N-1
870       D8=X(I)
880       D9=Y9(I)
890       X(I)=D8*COS(ALPHA)+D9*SIN(ALPHA)
900       Y(I)=-D8*SIN(ALPHA)+D9*COS(ALPHA)
910  NEXT I
920  REM  *SCALE THE POINTS*
930  Xmin=-50
940  Xmax=50
950  Ymin=-50
960  Ymax=50
970  Xlen=SQR((B2-B1)^2+(A2-A1)^2)
980  Ylen=SQR((B3-B2)^2+(A3-A2)^2)
990  FOR I=1 TO N-1
1000      X1(I)=X(I)*(Xmax-Xmin)/Xlen+Xmin
1010      Y1(I)=Y(I)*(Ymax-Ymin)/Ylen+Ymin
1020 NEXT I
1030 PRINT "GGGGGGALL DONE!"
1040 FOR I= 1 TO N-1
1050      PRINT @4: USING 1070:I,X1(I),Y1(I)
1060 NEXT I
1070 IMAGE     3X,2D,15X,5D.3D,10X,5D.3D
1080 REM  *CONVERT X,Y INTO GAMMA,DELTA*
1090 DIM GAMMA(N)
1100 DIM DTA(N)
1110 SET DEGREES
1120 FOR I=1 TO N-1
1130 OS=SQR(Y1(I)^2+X1(I)^2)
1140 MU=ASN(X1(I)/OS)
1150 SGMA=0.5*ATN(OS/30)
1160 GAMMA(I)=ATN(TAN(SGMA)*COS(MU))
1170 DTA(I)=ATN(TAN(MU)*SIN(GAMMA(I)))
1180 IF Y1<0 THEN
1190      GAMMA(I)=GAMMA(I)*-1
1200      GO TO 1220
1210   END IF
1220 NEXT I
1225 PRINT @4:"JJ"
1230 PRINT @4:"          VALUES OF GAMMA AND DELTA"
1240 PRINT @4:"J"
1250 IMAGE 24X,5A,12X,5A
1260 Q$="GAMMA"
1270 W$="DELTA"
1280 PRINT @4: USING 1250:Q$,W$
1290 PRINT @4:"J"
1300 FOR I=1 TO N-1
1310      PRINT @4: USING 1070:I,GAMMA(I),DTA(I)
1320 NEXT I
1330 END
```

9. APPENDIX 2

9.1 Laue stereographic projection program for Tektronix 4020A

Note: This program has been converted for an Apple II computer but has been found to be unsuitable. This is due to inaccurate trigonometrical functions which make it impossible to create great circles which are near to straight lines ie $\alpha > 90°$.

DEVICE NUMBERS

@1	PLOTTER
@32	SCREEN
@4	PRINTER
@8	DIGITISING TABLET

```
400  INIT
405  PRINT "GG"
410  PRINT "INPUT SPECIMEN NUMBER"
420  INPUT X$
500  Z$= "SPECIMEN No"
510  PRINT@4:"        SINGLE CRYSTAL ORIENTATION ANALYSIS"
520  PRINT@4:"J"
525  IMAGE 10X,11A,3X,9A
530  PRINT @4: USING 525:Z$,X$
535  PRINT @4:"J"
540  PRINT @4:"                    DIGITISING CO-ORDINATES"
550  PRINT @4:"J"
560  IMAGE 25X,4A,14X,4A
570  Q$="Xval"
580  W$="Yval"
590  PRINT @4: USING 560:Q$,W$
600  PRINT @4: "J"
610  PRINT "DIGITISE BOTTOM LEFT CORNER"
620  INPUT @8:A1,B1,C$
630  PRINT"GG"
640  PRINT "DIGITISE BOTTOM RIGHT CORNER"
650  INPUT @8:A2,B2,C$
660  PRINT "GG"
670  PRINT "DIGITISE TOP RIGHT CORNER"
680  INPUT @8:A3,B3,C$
690  PRINT "GG"
700  DIM  X(100), Y(100)
710  DIM  X1(100), Y1(100)
720  N=1
730  PRINT "DIGITISE THE POINTS(EXIT OFF X AXIS. . .)"
740  INPUT @8:X (N),Y(N),Z$
750  IF X(N)>A3 OR Y(N)>B3 THEN 790
```

```
760  N=N+1
770  PRINT"GG"
780  GO TO 740
790  ALFA=ATN((B2-B1)/(A2-A1))
800  REM  *SHIFT TABLET ORIGIN TO FILM CENTRE*
810  FOR I=1 TO N-1
820       X(I)=X(I)-A1
830       Y(I)=Y(I)-B1
840  NEXT I
850  REM *ADJUST FOR FILM TILT ON TABLET*
860  FOR I=1 TO N-1
870       D8=X(I)
880       D9=Y9(I)
890       X(I)=D8*COS(ALPHA)+D9*SIN(ALPHA)
900       Y(I)=-D8*SIN(ALPHA)+D9*COS(ALPHA)
910  NEXT I
920  REM  *SCALE THE POINTS*
930  Xmin=-50
940  Xmax=50
950  Ymin=-50
960  Ymax=50
970  Xlen=SQR((B2-B1)^2+(A2-A1)^2)
980  Ylen=SQR((B3-B2)^2+(A3-A2)^2)
990  FOR I=1 TO N-1
1000      X1(I)=X(I)*(Xmax-Xmin)/Xlen+Xmin
1010      Y1(I)=Y(I)*(Ymax-Ymin)/Ylen+Ymin
1020 NEXT I
1030 PRINT "GGGGGGALL DONE!"
1040 FOR I= 1 TO N-1
1050      PRINT @4: USING 1070:I,X1(I),Y1(I)
1060 NEXT I
1070 IMAGE      3X,2D,15X,5D.3D,10X,5D.3D
2000 REM  *STEREOGRAPHIC PROJECTION*
2005 N=N-1
2010 PAGE
2020 PRINT @32:"STEREOGRAPHIC PROJECTION PLOTS"
2030 REM  *DATA FOR CIRCLE*
2040 DIM X(72),Y(72),XP(35),YP(35),H(35),K(35),L(35)
2041 DIM H2(15),K2(15),L2(15)
2050 SET DEGREES
2060 FOR I=1 TO 72
2070      X(I)=50*COS(I*5)
2080      Y(I)=50*SIN(I*5)
2090 NEXT I
2100 REM  *CONVERT X1 AND Y1 TO PLOTTING VALUES*
2110 A=0
2111 B=0
2112 C=1
2113 D=1
2114 E=0
2115 F=0
2116 U=0
2117 V=1
2118 W=0
2119 RC=50
2120 IC=30
```

```
2125 FOR I=1 TO N
2130      SQ=SQR(X1(I)^2+Y1(I)^2)
2140      SG=0.5*ATN(SQ/IC)
2150      R=RC*TAN(SG/2)
2160      XP(I)=X1(I)*R/SQ
2170      YP(I)=Y1(I)*R/SQ
2180 NEXT I
2190 REM  *INDEX POINTS AND PRINT*
2200 REM  *DUMMY PROJECTION ON 001*
2211 PRINT @4:"DUMMY INDICES ON [001]"
2212 PRINT @4:
2213 PRINT @4:"VALUES OF [HKL]
2214 PRINT @4:
2220 FOR I=1 TO N
2230      RS=RC*RC
2240      P2=XP(I)*XP(I)+YP(I)*YP(I)
2250      CA=RS-P2
2260      CA=CA/(RS+P2)
2270      CD=-2*YP(I)*RC
2280      CD=CD/(RS+P2)
2290      CU=2*XP(I)*RC
2300      CU=CU/(RS+P2)
2310      L(I)=CA
2320      K(I)=CU
2330      H(I)=CD
2400 PRINT @4:I,H(I),K(I),L(I)
2410 NEXT I
2500 REM  *DRAW PROJECTION*
2510 PRINT"INPUT DEVICE No"
2520 INPUT Z1
2530 PAGE
2540 WINDOW -50,50,-50,50
2550 VIEWPORT 45,115,15,85
2560 REM  *DRAW CIRCLE*
2563 PRINT @1,32:"BY";30
2565 MOVE @Z1:X(72),Y(32)
2570 FOR I=1 TO 72
2580      DRAW @Z1:X(I),Y(I)
2590 NEXT I
2601 WINDOW 30,130,0,100
2610 MOVE @Z1:76,-4
2620 PRINT @Z1:"100";
2630 MOVE @Z1:130,49
2640 PRINT @Z1:"010";
2650 MOVE @Z1::81,50
2660 PRINT @Z1:"001";
2670 HOME
2680 J=0
2700 REM  *PLOT POINTS*
2710 FOR I=1 TO N
2720      MOVE @Z1:XP(I)+80,YP(I)+50
2730      SCALE 1,1
2740      RMOVE @Z1:-0.5*1.55,-0.5*1.88
2750      PRIINT @Z1:"+";
2760      RMOVE @Z1:0.5*1.55,0.5*1.88
2770      WINDOW 30,130,0,100
2780      MOVE @Z1:XP(I)+80,YP(I)+50
```

```
2785      PRINT @1,32:"S";1.55;1.88
2790      PRINT @Z1:I
2791      PRINT @1,32:"S";1.55;1.88
2792 NEXT I
2795 M=0
2800 HOME
2810 MOVE @32:0,100-2*J
2815 REM  *GREAT CIRCLE ROUTINE"
2820 PRINT @32:"CIRCLE POINTS?"
2825 PRINT @32:"INPUT 0,0 TO EXIT"
2830 INPUT S,T
2832 IF S=0 AND T=0 THEN
2833      GO TO 4000
2834 END IF
2835 M=M+1
2837 PRINT @4:"GREAT CIRCLE ";M;" IS BETWEEN ";S;"  AND ";T.
2840 PU=K(S)*L(T)-K(T)*L(S)
2850 PV=L(S)*H(T)-L(T)*H(S)
2860 PW=H(S)*K(T)-H(T)*K(S)
2861 H2(M)=PU
2862 K2(M)=PV
2863 L2(M)=PW
2865 O2=PU^2+PV^2+PW^2
2870 AL=PW/SQR(O2)
2880 BE=PU/SQR(O2)
2890 GA=PV/SQR(O2)
2900 XG=RC*GA/(1+AL)
2910 YG=-RC*BE/(1+AL)
2920 ACS(AL)
2930 IF LP=90 OR LP=270 THEN
2935      REM  *STRAIGHT LINE PLOT*
2936      AA=ATN(YG/XG)
2940      XT=-RC*SIN(AA)
2950      YT=RC*COS(AA)
2960      XB=-1*XT
2970      YB=-1*YT
2990      MOVE @Z1:XT+80,YT+50
3000      DRAW @Z1:XB+80,YB+50
3020      J=J+3
3030      GO TO 2800
3040 END IF
3050 CR=RC/AL
3060 OC=RC*TAN(LP)
3070 HY=SQR(XG^2+YG^2)
3080 TH=ATN(YG/XG)
3085 TA=TH
3090 TH=TH+180
3100 IF TA<0 THEN
3110      TH=TH+180
3120 END IF
3130 SF=OC/HY
3140 XC=XG*SF
3150 YC=YG*SF
3160 AL=ACS(AL)
3170 SA=TH-(90-AL)
3180 EA=TH+(90-AL)
3190 QQ=SA
```

```
3200 IF EA<QQ THEN
3210      BA=SA
3220      SA=EA
3230      EA=BA
3235 END IF
3240 QQ=(EA-SA)/20
3250 FOR I=SA TO EA+QQ/2 STEP QQ
3260      XX=COS(I)*CR
3270      YY=SIN(I)*CR
3280      XX=XX+XC
3281      YY=YY+YC
3290      XX=XX+80
3291      YY=YY+50
3300      QQ=SA
3310      IF I<>QQ THEN
3320           GO TO 3360
3330      END IF
3340      MOVE @Z1:XX,YY
3350      GO TO 3370
3360      DRAW @Z1:XX,YY
3370 NEXT I
3380 GO TO 2800
4000 REM  *ANGULAR DIFFERENCE CALCULATIONS*
4010 INPUT Z$
4011 IF Z$<>" " THEN
4012      GO TO 4020
4013 END IF
4020 PAGE
4030 PRINT @32:"CENTRE OF PROJECTION IS No 30"
4032 H(30)=1.0E-6
4033 K(30)=1.0E-6
4034 L(30)=1
4035 PRINT "ANGLES BETWEEN SPOTS ONLY"
4040 PRINT"No OF FIRST SPOT"
4041 INPUT S
4050 PRINT "No OF SECOND SPOT?"
4051 INPUT T
4060 W1=H(S)*H(T)+K(S)*K(T)+L(S)*L(T)
4070 W2=H(S)^2+K(S)^2+L(S)^2
4080 W3=H(T)^2+K(T)^2+L(T)^2
4090 W4=SQR(W2*W3)
4100 AN=W1/W4
4200 NG=ACS(AN)
4210 PRINT @4:"ANGLE BETWEEN ";S;" AND ";T;" IS= ";NG
4220 PAGE
4230 PRINT @32:"ANOTHER PAIR?"
4232 INPUT Z$
4240 IF Z$="Y" OR Z$="y" THEN
4250      GO TO 4010
4260 END IF
4265 PAGE
4270 PRINT @32:"INDICES OF GREAT CIRCLE INTERSECTIONS"
4280 PRINT
4290 PRINT "No OF FIRST CIRCLE(FROM PRINTER LISTING)?"
4298 INPUT S
4300 INPUT T
```

```
4310 CU=K2(S)*L2(T)-K2(T)*L2(S)
4320 CV=L2(S)*H2(T)-L2(T)*H2(S)
4330 CW=H2(S)*K2(T)-H2(T)*K2(S)
4335 PRINT @4:"INDICES OF INTERSECTION";S;",";T;"="CU,CV,CW
4370 PAGE
4380 PRINT "ANOTHER INTERSECTION?"
4382 INPUT Z$
4390 IF Z$="Y" OR Z$="y" THEN
4400      GO TO 4265
4410 END IF
4420 END
```

10. Appendix 3

10.1 Pafec program for three point bend specimen with half span to width ratio of 3:1

```
C CRACK-TIP ELEMENT AND ISOPARAMETERS
CONTROL
          !PLANE.STRAIN
C STOP
CONTROL.END

NODES
NODE      X         Y
1         .002      0
2         .00225    0
3         .00250    0
4         .00275    0
5         .003      0
6         .00325    0
7         .00350    0
8         .00375    0
9         .004      0
10        .00425    0
11        .00450    0
12        .00475    0
13        .005      0
14        .00525    0
15        .00550    0
16        .00575    0
17        .006      0
18        .0065     0
19        .007      0
20        .0075     0
21        .008      0
22        .0085     0
23        .009      0
24        .0095     0
25        .010      0
26        0         0.001155
27        .003      .004
28        .007      .004
29        .010      .0035
30        0         .010
31        .003      .010
32        .007      .010
33        .010      .010
34        0         .015
35        .003      .015
36        .007      .015
37        .010      .015
```

```
PAFBLOCKS
ELEMENT.TYPE = 36210
PROPERTIES = 1
TYPE = 1
BLOCK.NUMBER    N1    N2    TOPOLOGY
     1          1     1      1  9 26 27
     2          1     1      9 17 27 28
     3          1     1     17 25 28 29
     4          1     1     26 27 30 31
     5          1     1     27 28 31 32
     6          1     1     28 29 32 33
     7          1     1     30 31 34 35
     8          1     1     31 32 35 36
     9          1     1     32 33 36 37

MESH
REFERENCE       SPACING.LIST
     1               4

PLATES.AND.SHELLS
PLATE.OR.SHELL.NUMBER=1
THICKNESS=.005

MATERIAL.NUMBER
7

LOADS
CASE NODE DIRECTION VALUE
 1    34       1      700

RESTRAINTS
NODE.NUMBER     DIRECTION
     17              2
     18              2
     19              2
     20              2
     21              2
     22              2
     23              2
     24              2
     25              2
     25              1
CRACK.TIP
LIST
17
END.OF.DATA
```

NOTE: The above program was run under plane stress conditions and the final results multiplied by $1/1-\nu^2$ to convert to plane strain. This could have been avoided by the insertion of PLANE.STRAIN as indicated in the listing(97).

Printout from Phase 7 for this example 3:1 a/W=0.6

CASE 1 NODE NUMBER	TRANSLATIONS MULTIPLIED BY 1E6 UX	UY	RESULTANT TRANSLATION MULTIPLIED BY 1E6 U HISTOGRAM	SCALED COORDINATES MULTIPLIED BY 1E6 X	Y
1	-4.296	42.690	42.906***	0.002	0.00
2	-4.300	40.600	40.827***	0.002	0.00
3	-4.302	38.501	38.740***	0.003	0.00
4	-4.303	36.388	36.641***	0.003	0.00
5	-4.300	34.259	34.528***	0.003	0.00
6	-4.295	32.113	32.399**	0.003	0.00
7	-4.282	29.947	30.252**	0.004	0.00
8	-4.270	27.756	28.083**	0.004	0.00
9	-4.244	25.533	25.885**	0.004	0.00
10	-4.222	23.279	23.659**	0.004	0.00
11	-4.184	20.975	21.388**	0.004	0.00
12	-4.166	18.586	19.047*	0.005	0.00
13	-4.111	16.080	16.597*	0.005	0.00
14	-4.119	13.530	14.143*	0.005	0.00
15	-3.955	10.592	11.307*	0.006	0.00
16	-3.496	4.691	5.850	0.006	0.00
17	-3.644	*	3.644	0.006	0.00
18	-1.387	*	1.387	0.006	0.00

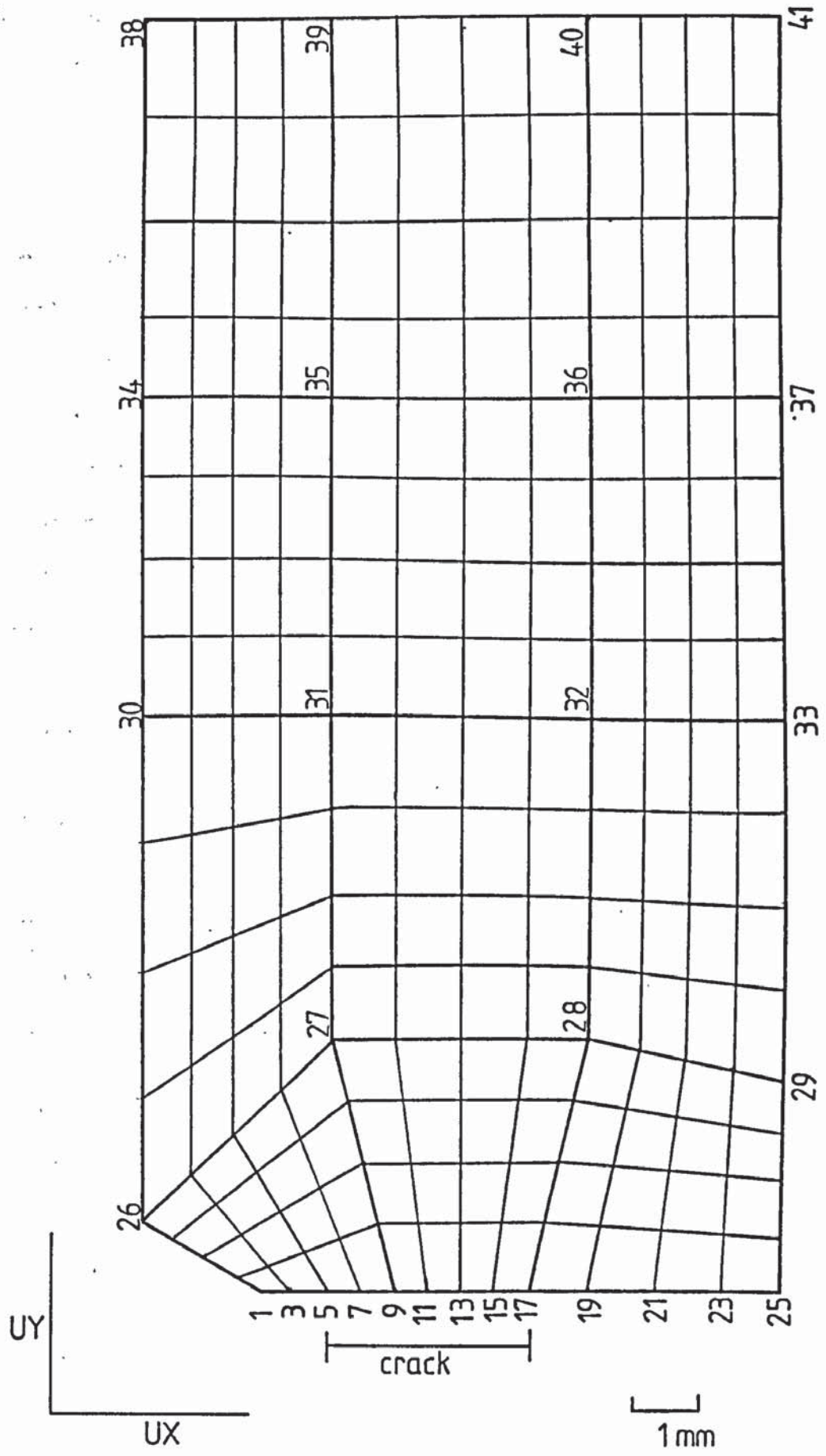

Figure A3.1 Schematic of mesh used in PAFEC analysis

II. APPENDIX 4

II.1 ASTM 7 Point polynomial data reduction program for fatigue propagation analysis Macintosh (Microsoft basic)

The program expects the data to have been typed in using Cricket graph or a similar program with data handling routines. The data consisting of two columns, cycles and voltage, are transferred onto the clip·board. The basic interpreter and the program are loaded and run. The program will read the data from the clipboard and write the results, da/dN and ΔK, back onto the clipboard so that they may be read into the Cricket graph table and saved. The technique is simplified by use of the Switcher utility to hold Cricket graph and Basic in memory simultaneously.

```
REM astm 7 point polynomial data reduction
DIM a(200),c(200),b(3),d(200),k(200),g(100),h(100),v(200)
PRINT:INPUT "no of data pairs?";n
PRINT:INPUT "PMAX";p1
INPUT "PMIN";p2
INPUT "BREADTH(metres)";b
INPUT "WIDTH(metres)";w
INPUT "INITIAL CRACK LENGTH ";a0
INPUT "value for V0 ";v0
PRINT
REM retrieve data
OPEN "clip:" FOR INPUT AS#1
FOR i=1 TO n
INPUT #1,c(i),v(i)
NEXT i
CLOSE #1
REM pd calibration
FOR i=1 TO n
v(i)=(v(i)-v0)/v0
a(i)=.9752*v(i)+.19725
a(i)=(a(i)*a0)+a0
NEXT i
n=n-6
FOR i=1 TO n
l=0
k=k+1
k1=k+6
```

```
FOR j=k TO k1
l=l+1
g(l)=a(j)
h(l)=c(j)
NEXT j
c1=.5*(h(1)+h(7))
c2=.5*(h(7)-h(1))
s1=0
s2=0
s3=0
s4=0
s5=0
s6=0
s7=0
FOR m=1 TO 7
x=(h(m)-c1)/c2
y=g(m)
s1=s1+x
s2=s2+x^2
s3=s3+x^3
s4=s4+x^4
s5=s5+y
s6=s6+x*y
s7=s7+y*(x^2)
NEXT m
d1=7*(s2*s4-s3^2)-s1*(s1*s4-s2*s3)+s2*(s1*s3-s2^2)
t1=s5*(s2*s4-s3^2)-s6*(s1*s4-s2*s3)+s7*(s1*s3-s2^2)
b(1)=t1/d1
t2=7*(s6*s4-s7*s3)-s1*(s5*s4-s7*s2)+s2*(s5*s3-s6*s2)
t3=7*(s2*s7-s3*s6)-s1*(s1*s7-s3*s5)+s2*(s1*s6-s2*s5)
b(3)=t3/d1
y1=s5/7
r1=0
r2=0
FOR q=1 TO 7
x=(h(q)-c1)/c2
y2=b(1)+b(2)*x+b(3)*(x^2)
r1=r1+(g(q)-y2)^2
r2=r2+(g(q)-y1)^2
NEXT q
r3=1-(r1/r2)
d(i)=b(2)/c2+2*b(3)*(h(4)-c1)/(c2^2)
u=1+3
REM pafec k calibratiion
com1=-37.889*((a(u)/w)^4)+72.57*((a(u)/w^3)-47.44*((a(u)/w^2)
com1=com1+14.35*(a(u)/w)-1.265
k(i)=((p1-p2)/(b*w))*com1
NEXT i
REM paste to clipboard
OPEN "clip:" FOR AS#1
FOR i=1 TO n
WRITE #1,d(i),k(i)
NEXT i
CLOSE #1
PRINT "processing terminated.  Data residing in clipboard"
END
```

12. REFERENCES

1. M. Gell, D.N. Duhl and A.F. Giamei, The development of single crystal superalloy turbine blades, Superalloys 1980, Proceedings of the fourth int. symposium on superalloys, A.S.M, 1980, pp. 205-214.

2. M.R. Winstone and J.F. Northwood, An investment casting technique for the control of single crystal orientation and the effect of orientation on the properties of a nickel-base superalloy, Int. congress on metals engineering, The University of Aston in Birmingham, september 1981, paper6.

3. B. Chalmers, Principles of solidification, John Wiley & sons, 1964.

4. R.W.K. Honeycombe, The plastic deformation of metals, second edition, Edward Arnold, 1984, ch.2.

5. C.T. Sims and W.C. Hagel, The superalloys, John Wiley & sons,1972..

6. M.V. Nathal and L.J. Ebert, The influence of cobalt, tantalum and tungsten on the microstructure of single crystal nickel-base superalloys, Met Trans, volume 16A, october1985, pp. 1849-1862.

7. A.F. Giamei and B.N. Kear, On the nature of freckles in nickel-base superalloys, Met Trans, volume 1A, August 1970, pp. 2185-2192.

8. G.W. Meetham, The contribution of materials to the development of the gas turbine engine, The Metallurgist and materials technologist, November 1976, pp. 589-602.

9. P.A. Flinn, Theory of deformation in superlattices, Trans. Metallurgical society of A.I.M.E, volume 218, February 1960, pp. 145-154.

10. M.J. Whelan, Dislocation interaction in FCC metals, Proc. Royal society, series a, volume 249, 1959, pp. 115-137.

11. J.P. Hirth and J. Lothe, Theory of dislocations, McGraw-Hill Book company, New York, 1968, p. 291.

12. A.H. Cottrell, Interactions of dislocations and solute atoms, Relation of properties to microstructures, A.S.M, 1954, pp. 131-163.

13. M.J. Marcinkowski, N. Brown and R.M. Fisher, Dislocation configurations in AuCu3 and AuCu type superlattices, Acta Met, volume 9, February 1961, pp. 129-137.

14. B.H. Kear, A.F. Giamei, J.M. Silcock and R.K. Ham, Slip and climb processes in γ' precipitation hardened nickel-base alloys, Scripta Met, volume 2, 1968, pp. 287-294.

15. B.H. Kear, A.F. Giamei, G.R. Leverant and J.M. Oblak, On intrinsic/extrinsic stacking fault pairs in the L12 lattice, Scripta Met, volume 3, 1969, pp. 123-130.

16. B.H. Kear, A.F. Giamei, G.R. Leverant and J.M. Oblak, Viscous slip in the L12 lattice, Scripta Met, volume 3, 1969, pp. 455-460.

17. N. Thompson, Dislocation nodes in Face-Centered cubic lattices, Proc. Physical society (London), volume 66B, 1953, pp. 481-492.

18. J.P. Hirth, On dislocations in the FCC lattice, J. applied physics, volume 32, number 4, April 1961, pp. 700-706.

19. R.G. Davies and N.S. Stoloff, On the yield strength of aged Ni-Al alloys, Trans. Metallurgical society of AIME, volume 233, April 1965, pp. 715-719.

20. P.H. Thornton, R.G. Davies and T.L. Johnson, The temperature dependence of the flow stress of the γ' phase based upon Ni3Al, Met. Trans. volume 1A, January 1970, pp. 207-218.

21. S.M. Copley and B.H Kear, Temperature and orientation dependence of the flow stress in off-stoichiometric Ni3Al (γ' phase)., Trans. Metallurgical society of A.I.M.E, volume 239, 1967, pp. 977-984.

22. B.H. Kear, G.R.Leverant and J.M. Oblak, An analysis of creep induced intrinsic/extrinsic fault pairs in a precipitation hardened nickel-base alloy, Trans. A.S.M, volume 62, 1969, pp. 639-650.

23. R.F. Decker, Strengthening mechanisms in nickel-base superalloys, Climax Molybdenum company symposium, Steel strengthening mechanisms, Zurich, 5-6th May, 1969, pp. 147-170.

24. R.M.N. Pelloux and N.J.Grant, Solid solution and second phase strengthening of nickel alloys at high and low temperatures. Trans. Metallurgical society of A.I.M.E, volume 218, April 1960, pp. 232-237.

25. B.E.P. Beeston, I.L. Dillamore and R.E. Smallman, The stacking-fault energy of some nickel-cobalt alloys, Metal science journal, volume 2, 1968, pp. 12-14.

26. R.W. Guard and J.H. Westbrook, Alloying behaviour of Ni3Al (γ'phase), Trans. Metallurgical society of A.I.M.E, volume 215, 1959, pp.807-814.

27. V.A. Phillips, Coherency hardening in Ni-Al.Ti alloys, Scripta Met., volume 2, 1968, pp. 147-152.

28. R.F. Decker and J.R. Mihalisin, Coherency strains in γ' hardened nickel alloys, Trans. A.S.M, volume 62, 1969, pp. 481-489.

29. V.Gerold and H. Haberkorn, On the critical resolved shear stress of solid solutions containing coherent precipitates, Physica status solidi, volume 16, 1966, pp. 675-684

30. J.Friedel, Dislocations, english edition, Pergamon press, 1964.

31. E.Orowan, Symposium on internal stresses in metals & alloys, Discussion, session III, Institute of metals, London, 1948, pp. 451-453.

32. M.F. Ashby, Results and consequences of a recalculation of the Frank-Read and the Orowan stress, Letters to the editor, Acta Met., volume 14, May 1966, pp. 679-680.

33. R.K. Ham, Ordered alloys : structural applications and physical metallurgy, Claitors, Baton Rouge, louisiana, 1970, pp. 365-373.

34. L.M. Brown and R.K. Ham, Dislocation-particle interactions, Strengthening methods in crystals, edited by A. Kelly and R.B. Nicholson, Chapter 2, Elsevier publishing company Ltd, 1971, pp. 10-35.

35. H. Gleiter and E. Hornbogen, Theory of the interaction of dislocations with coherent ordered zones (II),Physica status solidi, volume 12, number 1, 1965, pp. 251-264.

36. S.M. Copley and B.H. Kear, A dynamic theory of coherent precipitation hardening with application to nickel-base superalloys, Trans. Metallurgical society of A.I.M.E, volume 239, July 1967, pp. 984-993.

37. P. Beardmore, R.G. Davies and T.L. Johnston, On the temperature dependence of the flow stress of nickel-base alloys, Trans. Metallurgical society of A.I.M.E, volume 245, July 1969, pp. 1537-1545.

38. S.M. Copley, B.H. Kear and G.M. Rowe, The temperature dependence of yielding in Mar-M200 single crystals. Materials science Engineering, volume 10, 1972, pp. 87-91.

39. Mrs. J. Hooker, Internal data, Rolls-Royce Ltd, Elton Road, PO Box 31, Derby, DE2 8BJ, 1984.

40. A.K. Mukherjee, J.E. Bird and J.E. Dorn, Experimental correlations for high-temperature creep, Trans.A.S.M, volume 62, 1969, pp. 155-179.

41. J.H. Gittus, Development of a theoretical equation for steady state dislocation creep and comparison with data, Acta Met., volume 22, June 1974, pp. 789-791.

42. H. Burt, J.P. Dennison and B. Wilshire, Friction stress measurements during creep of Nimonic 105, Metal science, May 1979, pp. 295-300.

43. R.A. Stevens and P.E.J. Flewitt, The dependence of creep rate on microstructure in a γ' strengthened superalloy, Acta Met., volume 29, 1981, pp. 867-882.

44. J.D. Parker and B. Wilshire, Friction stress measurements during high-temperature creep of polycrystalline copper, Metals science, October 1978, pp. 453-458.

45. M.McLean, The measurement of friction stress in high temperature creep, Scripta Met., volume 13, May 1979, pp. 339-344

46. M.McLean, On the threshold stress for dislocation creep in particle strengthened alloys, Acta Met., volume 33, number 4, 1985, pp. 545-556.

47. D. Pearson, F.D. Lemkey and B.H. Kear, Stress coarsening of γ' and its influence on creep properties of a single crystal superalloy, Superalloys 1980, Proc. fourth international symposium on superalloys, A.S.M, 1980, pp. 513-521.

48. M.V. Nathal and L.J. Ebert, Elevated temperature creep-rupture behaviour of the single crystal nickel-base superalloy Nasair 100, Met. Trans., volume 16A, 1985, pp. 427-439.

49. R.A. MacKay and L.J. Ebert, The development of γ-γ' lamellar structures in a nickel-base superalloy during elevated temperature mechanical testing, Met. Trans., volume 16A, 1985, pp. 1969-1981.

50. C. Carry and J.L. Strudel, Apparent and effective creep parameters in single crystals of nickel-base superalloy- 1 Incubation period, Acta Met., volume 25, 1977, pp. 767-777.

51. G.A, Webster and B.J. Piearcey, An interpretation of the effects of stress and temperature on the creep properties of a nickel-base superalloy, Metals Science, 1967, volume 1, pp. 97-104.

52. B.F. Dyson and M. McLean, Particle coarsening, σ_o and tertiary creep, Acta Met., volume 31, 1983, pp.17-27.

53. P.J. Henderson and M. McLean, Microstructural contributions to friction stress and recovery kinetics during creep of the nickel-base superalloy IN 738LC, Acta Met., volume 31, 1983, pp. 1203-1219.

54. J.R. Moon, Worked examples in stereographic projection, The Institute of Metallurgists, Chameleon press Ltd,Monograph number 2, 1978.

55. B.D. Cullity, Elements of x-ray diffraction, second edition, Addison-Wesley publishing company, INC, 1978, chapter 8, pp. 233-268.

56. E. Schmid and W. Boas, plasticity of crystals with special reference to metals, F.A. Hughes and Co. Ltd, 1950, chapter 6.

57. B.H. Kear and B.J. Piearcey, Tensile and creep properties of single crystals of the nickel-base superalloy Mar-M200, Trans. Metallurgical society of A.I.M.E, volume 239, August 1967, pp. 1209-1215.

58. G.R. Leverant and B.H. Kear, The mechanism of creep in gamma prime precipitation-hardened nickel-base alloys at intermediate temperatures, Met. Trans., volume 1, February 1970, pp. 491-498.

59. G.R. Leverant, B.H. Kear and J.M. Oblak, Creep of precipitation-hardened nickel-base alloy single crystals at high temperatures, Met. Trans., volume 4, January 1973, pp. 355-362.

60. R.A. MacKay, R.L. Dreshfield and R.D. Maier, Anisotropy of nickel-base superalloy single crystals, Superalloys 1980, Proc. fourth international symposium on superalloys, A.S.M, 1980, pp. 385-394.

61. R.A. MacKay and R.D. Maier, The influence of orientation on the stress rupture properties of nickel-base superalloy single crystals, Met. Trans., volume 13A, October 1982, pp. 1747-1754.

62. M. Plumbridge and D. Ryder, The metallography of fatigue, Metallurgical reviews, volume 14, 1969, pp. 119-142.

63. P.J.E. Forsyth and D.A. Ryder, Some results of the examination of aluminium alloy specimen fracture surfaces, Metallurgica, volume 63, March 1961, pp. 117-124.

64. P.J.E. Forsyth, The physical basis of metal fatigue, American Elsevier publishers, New York, 1969, pp. 36-38.

65. P.J.E. Forsyth, C. Stubbington and D.Clark, Clevage facets observed on fracture surface in aluminium alloys, J. Institute of metals, volume 90, 1961-1962, pp. 238-239.

66. C. Laird, The influence of metallurgical structure on the mechanism of fatigue, A.S.T.M, STP 415, 1967, pp.131-169.

67. J.T. Barnby, Fatigue, Mills and Boon Ltd., 1972

68. R.W. Landgraf, The resistance of metals to cyclic deformation. Achievement of high fatigue resistance in metals and alloys, A.S.T.M, STP 467, 1970, pp. 3-36.

69. A. Griffith, The phenomena of rupture and flow in solids, Philosophy transactions of the royal society, volume 221A, 1921, pp. 163-197.

70. G.R. Irwin, Fracturing of metals, A.S.M, Clevland, Ohio, 1949, pp 147-148.

71. H.M. Westergaard, Bearing pressures and cracks, J. applied mechanics, volume 6A, 1939, pp. 29-49.

72. G.R. Irwin, Analysis of stresses and strains near the end of a crack traversing a plate, J. applied mechanics, volume 24, pp. 361-364.

73. D.J. Cartwright and D.P. Rooke, Evaluation of stress intensity factors. J. strain analysis, volume 10, number 4, October 1975, pp. 217-225.

74. G.R. Irwin, Plastic zone near a crack and fracture toughness, Proc. 7th Sagamore conference, 1960, pp. IV-63.

75. Standard method for plane strain fracture toughness of metallic materials, A.N.S.I/ A.S.T.M E399-78a, part 10, 1978, A.S.T.M annual standards.

76. P. Paris and F. Erdogan, a critical analysis of crack propagation laws, Trans. American society of mining engineers, series D, volume 85, 1963, pp. 528-534.

77. J.R. Rice, A path independent integral and the approximate analysis of strain concentrations by notches and cracks, J. applied mechanics, volume 35, 1968, pp. 379-386.

78. J.R. Rice, P.C. Paris and J.G. Merkle, Some further results of J integral analysis and estimates, Progress in flaw growth and fracture toughness testing,A.S.T.M, STP 536, Philadelphia, pp.231-235.

79. N.E. Dowling and J.A. Begley, Fatigue crack growth during gross plasticity and the J-integral, Mechanics of crack growth, A.S.T.M STP 590, Philadelphia, 1976, pp. 83-104.

80. K. Sadananda and P. Shahinian, A fracture mechanics approach to high temperature fatigue crack growth in Udimet 700, Engineering fracture mechanics, volume 11, 1970, pp.73-86.

81. J.G. Merkle and H.T. Corten, A J-integral analysis for the compact specimen, considering axial forces as well as bending effects, J.pressure vessel technology, Trans. A.S.M.E, volume 96, 1976, pp. 286-292.

82. K. Sadananda and P. Shahinian, High-temperature crack-growth behaviour in Nimonic PE16 and alloy 718, Metals Technology, January 1982, pp. 18-25

83. K. Sadananda and P. Shahinian, Creep crack growth in Udimet 700, Met. Trans, volume 9A, January 1978, pp. 79-84.

84. G.J. Lloyd, High temperature fatigue and creep-fatigue crack propagation: Mechanics, mechanisms and observed behaviour in structural materials, Fatigue at high temperatures, edited by R.P. Skelton, Applied science publishers, London, chapter 5, pp. 187-259.

85. K. Sadananda and P. Shahinian, Creep-fatigue crack growth, Cavities and cracks in creep and fatigue, edited by J.Gittus, Applied science publishers, London, chapter 5, pp. 109-197.

86. K. Sadananda and P. Shahinian, Creep crack growth in Alloy 718, Met. trans, volume 8A, March 1977, pp. 439-449.

87. R. Koterazawa and T. Mori, Applicability of fracture mechanics parameters to crack propagation under creep condition. Trans. A.S.M.E, series H, J. engineering materials and technology, October 1977, pp. 299-303.

88. A. Saxena, Evaluation of C* for the characterisation of creep-crack growth behaviour in 304 stainless steel; Fracture mechanics: Twelfth conference, A.S.T.M STP 700, 1980, pp. 131-151.

89. K. Sadananda and P. Shahinian, Evaluation of J* parameter for creep crack growth in type 316 stainless steel, Fracture mechanics: Fourteenth symposium- Volume II: Testing and applications, A.S.T.M STP 791, J.G. Lewis and G. Sines ,editor, 1983, pp. 182-196.

90. A. Saxena, R. S. Williams and T. T. Shih, A model for representing and predicting the influence of hold time on fatigue crack growth behavior at elevated temperature, Fracture mechanics: Thirteenth conference, A.S.T.M STP 743, R. Roberts editor, 1981, pp. 86-99.

91. H. Riedel and J. R. Rice, Tensile cracks in creeping solids, Fracture mechanics: Twelfth conference, A.S.T.M STP 700, 1980, pp. 112-130.

92. D. Driver, Single crystal orientation measurements - definition of characteristic angles, Rolls-Royce internal report, DRV/BXR, Rolls-Royce Ltd, Elton Road, PO BOX 31, Derby, DE2 8BJ.

93. A.B. Greninger, Determination of orientations of metallic crystals by means of back-reflection Laue photographs, Trans. Metallurgical society of A.I.M.E, Volume 117, 1935, pp. 61-71.

94. T.H. Kosel, Computational techniques for stereographic projection, J. Materials Science, Volume 19, 1984, pp. 4106-4118.

95. H. Tada, P.C. Paris and G.R. Irwin, The stress analysis of cracks handbook, Del Research, Hellertown, Pa, 1973.

96. C. Sih, Handbook of Stress intensity factors for researchers and engineers, Institute of fracture and solid mechanics, Leigh University, Bethlehem. Pennsylvania, 1973.

97. R.D. Hanshell, Pafec 75, Get started manual, Pafec Limited, October 1979.

98. Che-yu Li and R.P. Wei, Calibrating the electrical potential method for studying slow crack growth, Materials research & standards, Volume 6, Number 8, August 1966, pp. 392-394.

99. D.M. Gilbey and S. Pearson, Measurement of the length of a central or edge crack in a sheet of metal by an electrical resistance method, Royal Aircraft establishment, Technical report, Number 66402, December 1966.

100. H.H. Johnson, Calibrating the electric potential method for studying slow crack growth, Materials research & standards, Volume 5, 1965, pp. 442-445.

101. S.T. Rolfe and J.M. Barsom, Fracture and fatigue control in structures, Applications of fracture mechanics, Prentice-Hall Inc, 1977, pp. 208-267.

102. J.T. Fong and N.E. Dowling, Analysis of fatigue crack growth rate data from different laboratories, Fatigue crack growth measurements and data analysis, A.S.T.M STP 738, S.J Hudak and R.J Bucci, Eds, 1981, pp. 171-193.

103. Plane strain fracture toughness testing, BS5447, British standards institute, 1977.

104. J.T. Barnby, Fracture and fatigue, compiled notes, Internal report, The University of Aston in Birmingham, pp 44-45.

105. M. Khobaib, The effect of orientation and chemistry on creep in a Ni-base superalloy, Ph.D thesis, Connecticut University, 1974

106. O.L. Davies and P.L. Goldsmith. Statistical methods in research and production, Oliver& Boyd, chapter 6, 1971

107. H. T. Hayslett, Statistics made simple, W. H. Allen & Co Ltd, London, 1978.

108. J. Hooker, Rolls-Royce Ltd, Elton Road, Derby, Private communication. 1982.

109. N. V. Nathal and L. J. Ebert, The influence of cobalt, tantalum and tungsten on the elevated temperature mechanical properties of single crystal nickel-base superalloys, Met. trans, Volume 16A, October 1985, pp. 1863-1870.

110. M. Gell, G.R. Leverant and C.H. Wells, The fatigue strength of nickel-base superalloys, Achievement of high fatigue resistance in metals and alloys, A.S.T.M STP 467, 1970, pp. 113-153.

111. M. Gell and G.R Leverant, Mechanisms of high temperature fatigue, Fatigue at elevated temperatures, A.S.T.M STP 520, 1973, pp. 37-67.

112. D.L. Anton, Low cycle fatigue characteristics of <001> and randomly aligned superalloy single crystals, Acta. Met, volume 32, Number 10, 1984, pp. 1669-1679.

113. T.P. Gibb, J. Gayda and R.V. Miner, Orientation and temperature dependence of some mechanical properties of the single-crystal nickel-base superalloy Rene N4: Part II: Low cycle fatigue behaviour, Met. trans, Volume 17A, March 1986, pp. 497-505.

114. D.J. Duuqette and M. Gell, The effect of the enviroment on the mechanism of stage I fatigue fracture, Met. trans, Volume 2, May 1971,pp. 1325-1331.

115. K. Sadananda, Theoretical aspects of fatigue and creep crack growth, Advances in fracture research, Proceedings of the 6th Int. conference on Fracture (ICF6), New Dehli, India, December 1984, pp. 211-234.

116. P. K. Wright and A. F. Anderson, The influence of orientation on the fatigue of directionally solidified superalloys, Superalloys 1980, Proceedings of the fourth int. symposium on superalloys, A.S.M, 1980, pp. 689-698.

117. G. F. Paskiet, D. H. Boone and C. P. Sullivan, Effect of aluminide coating on the high-cycle fatigue behaviour of a nickel-base high temperature alloy, J. Institute of Metals, Volume 100, 1972, pp. 58-62.

118. D. J. Duquette and M. Gell, The effects of the enviroment on the elevated temperature fatigue behaviour of nickel base superalloy single crystals, Met. Trans, Volume 3A, July 1972, pp. 1899-1905.119.K. S. Chan, J. E. Hack and G. R. Leverant, Fatigue crack growth in Mar-M200 single crystals, Met. trans, Volume 18A, April 1987, pp. 581-591.

119. R. B. Scarlin, Fatigue crack propagation in a directionally solidified nickel-base alloy, Met. trans, Volume 7A, October 1976, pp. 1535-1541.

120. K. S. Chan, J. E. Hack and G. R. Leverant, Fatigue crack growth in Mar-M200 single crystals, Met. trans, Volume 18A, April 1987, pp. 581-591.

121. K. S. Chan and G. R. Leverant, Elevated-temperature fatigue crack growth behavior of Mar-M200 single crystals, Met. trans, Volume 18A, April 1987, pp. 593-602.

122. J. S. Crompton and J.W. Martin, Crack growth in a single crystal superalloy at elevated temperature, Met. trans, Volume 15A, September 1984, pp. 1711-1719.